AN EXPERIMENTAL STUDY OF FLOW OVER A 6 TO 1 PROLATE SPHEROID AT INCIDENCE

by

Seungki Ahn

Dissertation submitted to the Faculty of the

Virginia Polytechnic Institute and State University

in partial fulfillment of the requirements for the degree of

DOCTOR OF PHILOSOPHY

in

Aerospace Engineering

APPROVED:

Roger L. Simpson, Chairman

Joseph A. Schetz

Frederick H. Lutze

William H. Mason

Dana A. Walker

October, 1992

Blacksburg, Virginia

AN EXPERIMENTAL STUDY OF FLOW OVER A 6 TO 1 PROLATE SPHEROID AT INCIDENCE

by

Seungki Ahn

Committee Chairman : Roger L. Simpson

Aerospace Engineering

(ABSTRACT)

In two-dimensional flow, the point of flow separation from the surface coincides with the point at which the skin friction vanishes. However, in three-dimensional flow, the situation is much more complex and the flow separation is rarely associated with the vanishing of the wall shear stress except in a few special cases. Though the effects of cross-plane separation are substantial and have been recognized for some time, the phenomenon of flow separation over three-dimensional bodies is still far from being completely understood. The flow is so complex that no completely satisfactory analytical tools are available at the moment. In an attempt to logically identify the various effects and parametric dependence while simultaneously minimizing configuration dependent issue, the flow over a 6 to 1 prolate spheroid, which is a generic three-dimensional body, is investigated.

For the identification of the general flow pattern and better understanding of the flow field, surface-oil-flow visualization tests and force and moment tests were performed. The angle of attack effect and Reynolds number effect on the separation

location are studied with natural transition. Forces and moments tests, surface pressure distribution measurements as well as the surface presure fluctuations, and mini-tuft flow visualization tests were made to document the flow characteristics on the surface of the body with an artificial boundary layer trip.

It was found that there exists a critical Reynolds number at which the flow characteristics of the afterbody changes. This critical Reynolds number was also confirmed by the force and moment tests. Above this Reynolds number, as the Reynolds number increases, the separation lines do not change their circumferential location but stretch to the upstream of the body. For the low supercritical Reynolds number range, the angle of attack effect on the location of the primary separation is not as prominent as in the higher Reynolds number range where the cross-flow component effect becomes dominant. Surface pressure fluctuation data and surface pressure spectra were measured and documented for the first time for this type of three-dimensional flow.

For the extension of the study to unsteady transient motion effects, a new Dynamic-Plunge-Pitch-Roll (DyPPiR) model mount was designed and developed to generate required transient motions. The measurements carried out during this study are to be used as reference data to identify the unsteady transient effect of the flow field undergoing unsteady transient maneuvers.

ACKNOWLEDGEMENTS

The author would like to express his deep appreciation to his advisor, Dr. Roger L. Simpson who gave invaluable guidance and assistance throughout this study. Without his encouragement, support and guidance, it would have been difficult to accomplish this work. He would like to thank Dr. Joseph A. Schetz for the continued support for the DyPPiR project. He also would like to thank Dr. Frederick H Lutze, Dr. William H. Mason, and Dr. Dana A. Walker for serving on the Advisory Committee and for their helpful comments and suggestions on this study. The author would like to extend his appreciation to Dr. James L. Thomas and Ms. Sherrie Krist of NASA Langley Analytical Methods Branch for the numerical calculations.

He wishes to thank all the people who were directly and indirectly involved in the DyPPiR project for their job well done. He also wishes to thank his fellow graduate students who shared their time in everyway. Finally, a very special thanks are to his wife Namhee, his daughter Heajoon, and son Jongwoo for their help and patience during this study.

This study was supported by the Office of Naval Research under contract no. N00014-87-K-0816-P04. This support and the continued interest and encouragement of the Technical Monitor, Mr. James A. Fein, is greatfully acknowledged.

TABLE OF CONTENTS

LIST OF FIGURES

LIST OF TABLES

NOMENCLATURE

c – speed of sound

C_M – pitching moment coefficient $= \frac{PM}{qSd}$

C_N – yawing moment coefficient $= \frac{YM}{qSd}$

C_p – pressure coefficient $= \frac{P}{qS}$

C_R – rolling moment coefficient $= \frac{RM}{qSd}$

C_Y – side force coefficient $= \frac{SF}{qS}$

C_Z – normal force coefficient $= \frac{NF}{qS}$

D_H – diameter of pinhole

d – diameter of model

f – frequency

f_c – cut-off frequency

f_n – system natural frequency

k – system stiffness

L – length of model = 2a

l – pinhole length, distance between transducers

m – system mass

P – pressure

p_{rms} – root mean square pressure fluctuation

$p(t)$ – pressure signal

Q, q – freestream dynamic pressure

r – radius of pressure transducer

R_N – Reynolds number based on the length of model

S – reference area of model $= \pi r^2$

T – temperature

U_c – wave speed

U_e – boundary layer edge velocity

U_∞ – reference approach velocity

V – freestream velocity or cavity volume

x – longitudinal location of the model

Greekcharacters

α – angle of attack

β – bulk fluid modulus of oil

δ – boundary layer thickness

Φ – power spectrum

ϕ – circumferential angle

ρ – fluid density

τ – period

ω – circular frequency

ω_n – natural frequency

1. INTRODUCTION

The phenomenon of flow separation over three-dimensional bodies is still far from being completely understood. Boundary layer separation of any kind is fundamentally a three-dimensional, unsteady, viscous phenomenon. For bodies such as submarines and torpedos, cross-plane separation is particularly important in determining the velocity field near the stern in order to determine its effect on propulsion. It is also necessary in determining the pressure distribution on the body and its influence on maneuverability and control. At high angles of attack, the leeward separation on an axisymmetric body is exceedingly complex and progress in forming the basis for describing and modeling how vorticity is shed from the body to the leeward wake has depended crucially upon experiment (Orlik-Rückemann, 1987).

The problem becomes more complicated for a vehicle executing a circular turning motion. In this case, the local angle of attack varies significantly along the length of the body (Hoerner, 1975). Though the effects of cross-plane separation are substantial and have been recognized for some time, the flow is so complex that no completely satisfactory analytical tools are available. A comprehensive method would need to calculate the boundary layer development up to the separation lines, then calculate vortex sheet lift-off, and its trajectory, as well as its influence on the outer potential flow, requiring a viscous-inviscid interaction calculation capability. Computational fluid dynamics has not yet progressed to the stage where reliable and affordable calculations can model unsteady, turbulent, separated flow over three-dimensional bodies. The Navier-Stokes equations have been

accepted as a correct mathematical model for complex flow problems including separated flow fields, and their solutions hold promise for complete and accurate predictions. However, the computer resources required for acceptable resolution of three-dimensional separated flows over such bodies are still large at the present time. More over, solutions to these equations will be limited by the accuracy of turbulence modeling of complex and interacting flows.

In an attempt to logically identify the various effects and parametric dependence while simultaneously minimizing the configuration uniqueness issue, the flowfield around a 6 to 1 prolate spheroid, which is a generic three-dimensional body, is investigated in this study. Even with this comparatively simple shape in a steady flow, the problem is complex with regions of laminar, transitional, turbulent and separated flow on the spheroid depending upon the angle of attack(Cebeci and Meier, 1987). This study is performed for the establishment of a steady case reference data base for the future unsteady measurements.

For the unsteady measurements, a special apparatus called the Dynamic Plunge-Pitch-Roll (DyPPir) model support system is developed. A detailed description of the system is presented in Appendix A.

2. BACKGROUND

2.1 Three-Dimensional Flow Separation in Steady Flow

In two-dimensional steady flow, the point of flow detachment or separation from the surface coincides with the point at which the skin friction vanishes. However, in three-dimensional flow, the situation is much more complex and the flow separation is rarely associated with the vanishing of the wall shear stress except in a few special cases.

After the work of Maskell (1955), who attempted a rational interpretation of experimental observations shown in Figure 2, considerable progress has been made in physical understanding of separated three-dimensional flows by the work of Legendre (1956) and Lighthill (1963). In particular, these authors introduced equivalent concepts of limiting streamlines and skin friction lines. The limiting streamline is the limit position of the streamline as its distance to the wall becomes zero and the skin friction line is the line of force of the field of vectors formed by the skin friction. Using the pattern of these skin friction lines, it is possible to interpret most of the experimental observations by introducing a limited number of singularities. This introduction of limited singularities is a powerful tool for rationally interpreting the surface oil flow visualizations which is somtimes extremely complex. Inspired by the work of Poincare (Chanetz, 1988) on the singular points of differential systems, Legendre considered isolated points where the friction vectors vanishes as singular points of the surface flow pattern. These points are of

the node, focus, and saddle point types as shown in Figure 3. Lighthill (1963) has shown that the range of possible overall patterns of skin friction and vortex lines on a smooth surface are subject to a topological law, namely the number of nodal points must exceed the number of saddle points by two. Based on the works of Legendre and Lighthill, Peake and Tobak (1980) then formulated simple topological rules governing the set of nodes and saddle points contained in the flow.

Any separated three-dimensional flow has at least one saddle point through which two particular 'separator' streamline pass. Such streamlines separate and delimit different domains in the surface flow such as friction lines running along either side of the separator line, starting out infinitely adjacent and then moving a finite distance from each other as they approach the saddle point. It is also observed that certain friction lines belonging to each of these domains are likely to converge rapidly toward a separation line without coming into contact with it. This convergence phenomenon, which is not a truly distinctive property of a separation line, occurs when a separation 'sheet' forms as the result of the dissipative part of the flow surging into the irrotational flow field, according to a mechanism revealed by Lighthill (1963). The symmetrical process of reattachment or attachment may then be defined in similar manners, except that now the skin friction lines diverge to either side of the particular line, which becomes an attachment separator line.

According to certain authors such as Wang (1983) and Tobak and Peake (1982), the above definition of three-dimensional separation should be modified in consideration of experimental observations that apparently confilict with it. That is, we should make a distinction between the "global" separation and the "local"

separation. The local approach is the one in which an attempt is made to recognize separations as it happens, seeking to identify it in terms of the behavior of the limiting streamlines. The global approach is that in which the various elements of the total flow such as boundary layers and vortices are brought together in the understanding of the entire flow field.

One of the first to investigate the boundary layer developing on a prolate spheroid at an angle of attack and the correlative problem of separation is undoubtedly Eichelbrenner (1957) who proposed a three-dimensional laminar boundary layer computation method. Due to the very limited computation resources available at the time, the method used relatively extensive simplifying assumptions. At the same time, to validate the theory, valuable data were obtained by Werle (1957, 1962) on three-dimensional separation, collected in a large number of water tunnel tests. Later, much work was devoted to developing methods to compute three-dimensional boundary layers, first laminar and then turbulent. Cousteix (1974) proposed an integral method which, after consecutive improvements, is widely used to compute laminar and turbulent boundary layers. Integral methods have been investigated by many researchers such as Smith (1982), Stock (1978, 1980), and Rotta (1977). Le Balleur and Lazareff (1984) developed a three-dimensional integral method based on a multizonal marching technique. Wang (1975) investigated the computation of the boundary layer on a 4 to 1 prolate spheroid by an implicit finite difference method based on the Crank-Nicholson scheme. Particularly, Wang considered the problem of zones of influence and dependency in formulating his algorithm. Ragab (1982) conducted computations by a finite difference method

whose formulation takes into account zones of influency and dependency. His discretizing scheme is similar to the characteristic box scheme successfully used by Meier and Cebeci (1984). In this scheme, the discretization takes into account the local direction of the external streamline. Another approach for computing the three-dimensional boundary layer is that of Patel and Baek (1987) who used Alternating Direction Implicit type descretizing.

Computations of flows around a body with its vortices are still largely based on ideal fluid models employing the concepts of vortex sheets with descretization, and by several methods such as doublets (Hunt,1978), vortex filaments (Katz,1981), and vortex particles (Rechbach,1977). Computations are also made by direct solution of the Euler equations, which offers the advantage of automatically "capturing" the discontinuity surfaces (Rizzi and Eriksson, 1984; Manie *et al.*, 1984). In the ideal fluid models, the separation line is an input that must first be found by a boundary layer computation, so that to find the solution a coupling technique has to be used to account for the interaction between the supposedly inviscid outer flow field and the viscous boundary layer. Finally, with the progress in computers and numerical techniques, it is now possible to perform a full computation of the flow by solving the Reynolds-averaged Navier-Stokes equations. Such examples are the works done by Van Dalsem and Steger (1985), Kordulla *et al.* (1986), Pan and Pulliam (1986), and Vatsa and Thomas (1989).

On the experimental side, well-planned research was carried out at DFVLR, West Germany, on a 2.4 meter long 6 to 1 prolate spheroid model and yielded a precise characterization of the surface flow visualization and skin friction measurements (Vollmers *et al.*,1983; Meier *et al.*, 1981, 1982, 1983(a), 1983(b), 1984(a),

1984(b), 1987). The cooperative research between DFVLR and ONERA (Chanetz, 1988; Chanetz and Delery, 1988; Barberis and Chanetz, 1986) and Sino-Italian co-operative research program (Iuso *et al.*, 1980) also provided a detailed and well documented data. Especially, the experiments of Meier and Kreplin (1978) and their collegues on a 6 to 1 prolate spheroid is the test case which is relatively widely used by many researchers. Also AGARD Fluid Dynamics Panel Working group 10, which was assembled to investigate the limits of boundary layer methods for the calculations of three-dimensional turbulent separated flows, used DFVLR 6 to 1 prolate spheroid data as a test case (Yoshihara, 1990). Other related references are also listed in Bibliography.

2.2 Surface Pressure Fluctuations

The surface pressure fluctuations that develop beneath a turbulent boundary layer have been studied over the past three decades. These research efforts were aimed at solving the problems associated with the acoustic noise and flow induced vibrations which are generated by the pressure fluctuations in a turbulent boundary layer (Agarwal and Simpson, 1989). Willmarth (1975) and Blake (1970) reviewed numerous previous studies. Panton and Linebarger (1974) developed a numerical solution in two-dimensional turbulent boundary layer based on assumed forms of the mean flow and turbulent structure. Recently, Kim (1989) performed a direct numerical simulation on a turbulent channel flow. Majority of the work reported is on the pressure fluctuations in two-dimensional flows. A comprehensive review on the previous works on the two-dimensional flows can be found in Horne (1990).

The pressure field in a turbulent flow is produced by a summation of contributions from the turbulent velocity fluctuations (Willmarth, 1975). For an incompressible flow the pressure fluctuations are related to the velocity fluctuations through Poisson's equation, obtained from the divergence of the momentum equation.

$$\frac{\partial^2 P}{\partial {x_i}^2} = -\rho q$$

where q is given by the following

$$q = \frac{\partial^2 V_i V_j}{\partial x_i \partial x_j}$$

Pressure fluctuations at a point are produced by momentum fluctuations at many other points. Ideally, the wall pressure fluctuations measured would have negligible contributions from the free-stream turbulence intensity and no acoustic background noise. Experimental data are usually contaminated by the facility related noise in the low frequency range and spatial resolution of the pressure transducer limits high frequency range. The pressure sensors should be sufficiently small to resolve turbulent scales of the order of ten viscous lengths. Various investigators have circumvented this difficulty by measuring the pressure spectrum using noise cancellation techniques (McGrath and Simpson, 1987; Agarwal and Simpson, 1989; Horne, 1990). Bull and Thomas (1976) concluded that the use of pinhole sensors in air led to errors in the measured spectra. However, Farabee and Casarella (1991) concluded that pin-hole sensors are effective for wall pressure measurement. In this study, in order to improve the spatial resolution, pin-hole transducers are used.

3. EXPERIMENTAL FACILITY AND INSTRUMENTATION

Instrument transducers are almost always thought of as devices which convert the quantity to be measured into an electrical analog of some kind. These electric signals, even though very small, are amplified and processed with relative ease. Thus the amplifiers and signal processing equipment are essential parts of most measuring systems and they must be carefully matched with the transducing device. However, it is generally the mechanical behavior of the transducer which limits the performance of a measuring system. Furthermore, unsteady quantities may be regarded as 'quasi-periodic' or 'transient'. Generally items such as sensitivity and range, frequency response, linearity, repeatability, calibration, *etc.* should be considered carefully for unsteady quantity measurements. In this section, some instrumentation problems considered during this study will be discussed along with detailed descriptions of the tunnel and model used.

3.1 Virginia Tech $6' \times 6'$ Stability Wind Tunnel

The measurements were conducted in the Virginia Polytechnic Institute and State University $6' \times 6'$ Stability Wind Tunnel shown in Figure 4. The Wind Tunnel is a continuous, closed test section, single return subsonic wind tunnel with 25 feet long interchangable round and square test sections. The tunnel is powered by a 600 HP D.C. motor driving 14 foot propeller with eight wooden blades and provide a maximum speed of 220 ft/sec and unit Reynolds number of 1.33×10^6 per foot

in the normal $6' \times 6'$ cross-section configuration used here. Higher speeds can be achieved with a reduced test section. Tunnel speed is regulated by an Emerson VIP ES-6600 SCR Drive which is interfaced with the tunnel's computer data acquisition system.

The 9:1 contraction ratio and the seven anti-turbulence screens mounted in the stilling chamber, result in very low turbulence levels. The turbulence levels are on the order of 0.05% or less and varies slightly with speed (Choi and Simpson, 1987). The temperature stabilization is provided by the air-exchange tower located between the stilling chamber and the fan mounted in the diffuser section. Another unique feature of the wind tunnel consists of its ability to produce curved flows in a square section with walls which can be curved, and rolling flows in a round section with an upstream rotor.

3.2 6 to 1 prolate spheroid model

The 6 to 1 prolate spheroid model used in the experiment has a 54 inch long major axis ($L = 2a$) and 9 inch minor axis. The model, which is shown in Figure 5, is composed of double cylinder center body and interchangable forward and after body with nose and tail ring at the respective ends. In order to achieve a high strength and minimum weight construction, the inside structure consists of 8 bulkheads and 16 longerons machined from aluminum 7075-T6. The skin which is bonded to this aluminum structure is made of fiberglass reinforced plastic. It was composed of 5 different layers and machined to 0.125 inches thick with gel coat on both inside and outside surfaces. The model was mounted on a sting-strut model support system.

For the measurements of the transient and fluctuating pressures acting on the surface of the 6 to 1 prolate spheroid model, the pressure transducers were mounted through pinhole cover adaptors bonded to the inside surface of the fiberglass skin of the model. The pressure tap locations given in Table 1 are along the model on a meridian to reduce the possible number of test runs using the rolling capability of the DyPPiR. The total weight of the model is 58.76 lbs.

3.3 5-Component Internal Balance

To achieve higher stiffness and higher natural frequency, the axial element was eliminated from the balance and a rugged single piece moment-beam type 5-component internal strain gage balance as shown in Figure 6 was designed, fabricated, and calibrated. Acording to a simple one-dimensional beam analysis, the natural frequencies of this balance are 25 Hz and 18 Hz for normal force and side force direction, respectively. The design loads are as follows.

- Normal Force 1400 LB.
- Side Force 800 LB.
- Pitching Moment 3000 in-LB.
- Yawing Moment 1500 in-LB.
- Rolling Moment 600 in-LB.

The design is of a conventional type. A cruciform type flexure with main web and two side webs is used for the rollimg moment measurement. 17-4 PH stainless steel was selected for the balance material due to its good fatigue life, elastic quality, and ease of machining. Micro Measurement Group 350 Ohm foil type strain gages are used for the bridge elements due to their long fatigue life. The calibrated standard deviation of each component based on all loads was within 0.25 % full scale range.

To correct and verify the effect of higher harmonics, dynamic calibration of the 5-component balance was also performed using the impact hammer and frequency analyzer system. Detailed description of the design, fabrication, and static and dynamic calibration of the 5-component internal balance is presented in Appendix D.

3.4 Pressure Transducer and Calibration

In their review on wind tunnel pressure measuring techniques, Bynum *et al.* (1970) give a comprehensive account of pressure transducers. Particular attention to unsteady pressure measurements is also given in a review by Willmarth (1971) and both contain very extensive bibliographies on a number of relevant topics.

Where the static pressure on a surface is to be measured, the flush-mounted diaphragm-type transducer is an obvious choice. If the sensitivity of the transducer is adequate, it does not need a cavity behind a small orifice, which introduces phase lag and amplitude errors as a Helmholtz resonator. Mounting of the transducer also assumes importance if the surface forms part of a structure which is subject to vibration. Also the acceleration sensitivity of a transducer should be as small as possible. O-rings make fairly good vibration isolators as well as excellent seals (Bynum *et al.*, 1970).

With these considerations, ENDEVCO 8510B-2 2 psid piezoresistive pressure transducers were chosen for the surface pressure measurements. This transducer utilizes a silicon pressure sensing diaphragm and incorporates four piezoresistive silicon elements diffused on to the diaphragm together with the connections for a four-arm, fully active, Wheatstone bridge. The natural frequency of this transducer is virtually that of the unloaded diaphragm, which is proportional to

$$\frac{thickness}{(diameter)^2}$$

The diffusion of the silicon elements avoids some of the problems associated with the bonding of gages to the diaphragm normally used for static pressure measurements. The high gage factor of semi-conductors enable adquate sensitivities to be

obtained with thick small diameter diaphragms, and natural frequency of around 70 KHz with sensitivity of $2.5\mu V/Pa$. The integrated nature of the transducer gives good thermal stability unless severe temperature gradient exist. Acceleration sensitivity is also small compared to other similar-type transducers as well as other-type transducers. It has a sensing element of 3.86 mm (.152 inch) in diameter and has a O-ring seal which works as a good vibration isolator.

Static calibration was made using a TSI-1125 hot-wire calibrator connected to a pressure chamber which houses the transducers to be calibrated. The pressure inside the chamber was monitored by the Datametrics Barocel precision pressure transducer connected to a digital manometer giving a comparison calibration. The signal was amplified by Measurement Group 2310 Straingage Amplifier and then acquired through the R/C Electronics ISC-16 12-bit A/D converter, with simultaneous sample and hold, connected to a microcomputer. Individual calibration curve was made for each pressure transducer and their standard deviation is within 0.1 % full scale range.

Since the fluctuating pressure on a surface is an integral of the velocity fluctuation in a certain volume of the flow field, the spatial resolution problem is considered to improve the measurement resolution. Due to this spatial integration, 3dB damping point usually occurs at $\omega_n \approx 1$ (Corcos, 1963). For the 0.1 inch dia. sensing area of the transducer at $U_e = 150ft/sec$ with an assumption that $U_c = 0.6U_e$, the cut-off frequency of the transducer becomes

$$f_c = \frac{U_c}{2\pi r} \approx 3.438Khz$$

The use of a pinhole cover will give us better spatial resolution and high enough effective frequency range. If the orifice and cavity should be used, the length of the hole between the cavity and the surface should be kept small, while the orifice itself should be as large as the smallest required spatial resolution and the disturbance to the flow allow. With a reasonable fabrication method, a pin-hole with a size of $D_H = 0.074cm$ (0.029 inch dia.) can easily be made. This has resulted in a design as shown in Figure 7. Since the medium is air, this cavity will act as a Helmholtz-Resonator with a natural frequency (Blake, 1983)

$$f_n = \left[\frac{\pi r^2 c^2}{V(l + \frac{1}{2}\sqrt{\pi^2 r^2})} \right]^{\frac{1}{2}}$$

The natural frequency f_n of this design is approximately 11.85 KHz, a lot higher than the flush mounted transducer. But, it is safe to use the limiting frequency as $f_c = \frac{1}{2} f_n$ to eliminate the possible over amplification problem close to the resonant frequency (Blake, 1983). This will reduce the effective frequency range to about 6 KHz.

Unfortunately the pressure transducer has its own cavity and the same size of pinhole on top of the cavity will cause the natural frequency of the resulting Helmholtz resonator drop to down to approximately 4.8 Khz. Thus, it was decided to calibrate the whole assembly dynamically and obtain the transfer function of the individual setup. Amplitude response in frequency domain is also quite important and even though there are several different methods available for dynamic calibration (Crites and Frey, 1968; Kendall and Crites, 1969; Godt and Pyle, 1970; Kendall, 1970; Simpson and Gatley, 1970; Kendall, 1971), comparison calibration

was performed in order to verify the frequency characteristics of the pinhole cover and transducer combination.

Dynamic calibration of each pinhole cover and transducer combination was performed in a $48in \times 48in \times 48in$ anechoic chamber using Bruel and Kjaer 4135 microphone as a reference standard. The frequency response of this particular microphone is flat up to 10 KHz. Acoustic sound pressure field is generated by a 3 inch dia. midrange tweeter which has a flat frequency response range from 700 Hz to 27 KHz. White noise signal ($20Hz \sim 20KHz$) is generated from the Bruel and Kjaer type 1024 Sine-Random Generator and low-pass filtered by Krohn-Hite model 3202 filter at 20 KHz. The speaker is driven by this random noise through a 100W power amplifier.

Since the pinhole cap was integrated as a part of the surface of the model, a segment of the model was placed in the anechoic chamber with the reference microphone. The signal from the reference microphone is amplified by a Bruel and Kjaer type 2619 preamplifier and type 2801 power supply, then by the Measurement Group type 2310 signal conditioning Amplifier. The signal from the individual pressure transducer was amplified from the type 2310 signal conditioning amplifier. These two signals were then analysed on a Data 6000 Model 611 Universal Waveform Analyzer the get the transfer function. The data are stored on a floppy disk by Model 681 disk drive as a final form. The test set-up is as shown in Figure 8.

The transfer functions were corrected for the acoustic signature and its harmonics due to the standing wave and flutter echo effects (Hassall and Zaveri, 1979)

resulted in by the experimental set-up. Typical transfer function is as shown in Figure 9.

3.5 Data Acquisition

Data acquisition was performed using a microcomputer which is equipped with 16 channel single ended, 12-bit resolution A/D converter board. This R/C electronics ISC-16 A/D converter board has simultaneous sample and hold features and can sample up to 1 MHz sampling rate. The input signals were conditioned to ± 10 volt range using appropriate signal conditioning amplifiers. Each record was comprised of 4096 points of measurements. The sampling frequency of the pressure measurements were set at 20,000 KHz in order to get the power spectrum up to 10 KHz with low pass filter set at 10 KHz for anti-alising and the force measurements were made at 500 Hz with a filter set at 10 Hz because of the natural frequency of the balance and model combination.

3.6 Angle of Attack System

The usual way to get the angle of attack information from a sting mounted model is either by a precalibrated load - sting and balance deflection relation or from an inertial package directly mounted onboard the model. The former has a large uncertainty in the measured angle of attack due to the propagated uncertainties from the measured forces and moments, sting and balance deflection coefficients, and unwanted hysteresis due to the free play in the joints throughout the model support. The latter, which is a combination of an onboard electrolytic bubble and several accelerometers, gives direct information. But it also has its own drawbacks when used under these severe conditions due to the limitations of the fragile bubble and the accelerometers because of their slow response of the order of a second, intensive labor requirement for mounting and alignment, and large package size and number of wires inside the model (Young, 1982). In this study, onboard electronic servoinclinometer was used to measured the angle of attack of the model. This unit covers $\pm$ 90 deg. range and has a cut off frequency of 40 Hz.

4. EXPERIMENTAL TECHNIQUES AND TEST CONDITIONS

In this section, detailed description of the experimental techniques used will be given along with the test conditions.

4.1 Test conditions

In order to identify the flow characteristics of the flow around the body, surface oil flow visualization tests were performed. The conditions for these tests are as shown in Table 2. Forces and moments measurements were also made at the same conditions. Once the separation locations and behavior of the forces and moments at various Reynolds numbers and angles of attack with natural transition are identified, it was decided to run all the tests at highest Reynolds number possible. The tests were performed at $R_N = 4.2 \times 10^6$ with an artificial boundary layer trip at $x/L = 0.2$.

4.2 Experimental Techniques

Measurements cover surface oil flow visualization, mini-tuft flow visualization, force and moment measurements, and mean surface pressure distribution measurement. Surface pressure fluctuations were also measured. No other attempt was made at this time to measure the boundary layer related characteristics which were measured by Barber (1990).

4.2.1 Artificial Boundary Layer Trip

Although much progress has been made, in the last ten years or so, to identify and understand receptivity, much still remains to be done. The detailed character of free-stream turbulence as observed in wind tunnels has yet to be measured and the finer points of its signature in the boundary layer leading to excitation of Tollmein-Schlichting waves clarified. Environmental effects have been neglected and not been studied systematically in an organized manner. Yet with the need of increased accuracy required from the recent wind tunnel measurements and the need for reduced discrepancies of the experimental data obtained from different wind tunnels, the wind tunnel environmental effects have to be accurately assessed. The work recently done by Meier and Michel (1987) to investigate the free-stream turbulence effect on the boundary layer transition location on a 6 to 1 prolate spheroid in three different European wind tunnels is one such example. Looking at the breadth and delicacy both from experimental and theoretical point of view, the subject of environmental effects on boundary layer transition and its characteristics appears to be a challanging one.

In view of the relatively low critical values of Re_d for the lateral modes of transition, it is inferred that natural, untripped transition will occur even on the forward portion of typical missile and fuselage models after the angle of attack is increased to only moderate levels. A sudden forward movement of transition may then occur and the experimenter should be watchful for related changes in separation and aerodynamic coefficients.

Tests performed by Meier *et al.* (1982, 1983) show that the boundary layer trip does not change the separation location on the after body of the 6 to 1 prolate

spheroid. But this is true only for the cases that the Reynolds number is sufficiently large to ensure turbulent separation prevailing on the after body. According to the surface oil flow test performed (Ahn and Simpson, 1992), there exists a critical Reynolds number, at around $R_N = 2.5 \times 10^6$, which changes the flow characteristics on the after body of the 6 to 1 prolate spheroid. The test shows total laminar flow and laminar separation at Reynolds number $R_N = 2.0 \times 10^6$ and shows turbulent separation on the after body at Reynolds number $R_N = 2.8 \times 10^6$ at moderate angles of attack. In order to stabilize the flow and achieve turbulent separation on the after body of the model, the boundary layer on the 6 to 1 prolate spheroid should be artificially tripped using a trip device. Moreover, the boundary layer trip is necessary to eliminate the facility dependency of the separation location due to the change in the turbulence level as shown by Meier *et al.* (1987). The boundary layer trip was applied at x/L = 0.2. Trip disk method adopted from Boeing Commercial Airplane Co. (Smith, 1989) was used to trip the boundary layer. The disks were 0.046 inch in diameter, 0.028 inch high, and 0.1 inch apart. Detailed techniques used to generate the trip device is described in Appendix C.

4.2.2 Force and Moment Measurement

Forces and moments acting on the body were measured to investigate the effect of Reynolds number and angle of attack. 5-component internal balance developed for the DyPPiR was used. Due to the low level of the balance signal, it was required to amplify the signal at a gain of 10000. Each test points were measured separately for the zeros and data. The signals were simultaneously sampled at 500 Hz over 4096 points and averaged. The angle of attack was varied from -3 degree to +35 degrees.

4.2.3 Surface-Oil-Flow Visualization

In order to identify the flow characteristics on the surface of a 6 to 1 prolate spheroid, surface-oil-flow visualization tests were performed. Surface-oil-flow visualization method are widely used for steady cases to visualize the surface skin friction lines (Maltby and Keating, 1962). The main purpose of these tests are to observe the general flow pattern so that better understanding on the flow arround a 6 to 1 prolate spheroid can be attained and the locations which needs extensive studies are to be identified. The angle of attack effect and Reynolds number effect are also to be studied with natural transition to aid the high Reynolds number flow simulation with artificial boundary layer transition.

Tests were performed, as shown in Table 2, at 5 different angles of attack from 0 degree to 20 degrees with 5 degrees increament and at 5 different Reynolds numbers ranging from 1.4×10^6 to 4.2×10^6. Out of 25 conditions tested, only 14 cases show distinct flow patterns including separation lines. The axisymmetric flow conditions do not show high enough skin friction to effectively overcome and prevent the effect of the gravity acting on the oil mixture. Low angles of attack and low Reynolds number cases show similar characteristics.

A mixture of kerosene, titanium dioxide, and oleic acid was used for visualization and the mixture ratio was varied much from a lean solution to a thick paste-like mixture according to the tunnel speed and the flow characteristics on the model surface. A thin layer of kerosene was left on the model and, before it dries, a layer of oil mixture was applied on the whole surface of the model. To avoid brush marks which can be mistaken as skin-friction lines, the mixture was

applied with spanwise strokes with a soft sponge brush. After the mixture was applied the tunnel was brought up to a desired speed as quickly as possible and then was run until the oil was dry enough not to alter the oil flow pattern on the model. Still pictures were taken during and after each run. For better contrast, the model surface was painted flat black with white grid lines and then satin clear lacquer was coated and polished to protect the painted surface. As the flow passes over the body, the oil mixture flows along the skin-friction lines. Since skin friction is related to the velocity gradient normal to the wall, the limiting-streamlines also give some indication of the near-wall velocity field. It can be presumed that the regions of higher shear stresses, which appears as darker regions on the oil-flow visualization patterns, are also regions of higher near-wall velocities. A detailed discussion of the interpretation of the surface-oil-flow visualization can be found in Peake and Tobak (1982).

4.2.4 Mini-Tuft Surface-Flow Visualization.

A completely different method should be used for the limiting-streamline pattern visualization formed on the body because of the finite mass and inertia effects of the indicators normally used for the steady cases. A non-intrusive method called mini-tuft originally developed by Crowder (1977, 1980(a), 1980(b), 1983(a), 1983(b)) and Crowder *et al.* (1980) was prepared for the surface flow visualization during the unsteady transient motions. The method successfully used for steady cases by other investigators, such as Dobny *et al.* (1986), O'leary and Drew (1987), has been proven to be effective for the unsteady cases as well. The method uses

very fine nylon nonofilaments which are made visible by coating them with fluorescent dye and illuminating them with a powerful ultra-violet light source. The method was used for steady cases measurements.

The material used for the tuft is a 15-denier nylon-66 monofilament fiber supplied by DuPont and de Nemoir co.. The diameter of the monofilament is 0.0015 inch. The fluorescent dye used was Acid Yellow 7, Brilliant Flavine FFA supplied by Melody Chemicals, Inc. in a powder form. A solution was made up of 1 % powder, by weight, in water with 2 cubic centimeters of concentrated formic acid added to each liter of the solution. The acid attacks the surface of the nylon monofilament and increase the amount of the dye absorbed. The "raw" monofilament was wound on a large diameter glass bobin and boiled in the solution for two hours and rinsed with water and dried. The model surface was coated with black gel coating to get the best possible contrast with the yellow color emitted from the mini-tufts when illuminated by ultra violet light. Duco cement in a hypodermic syringe was used to attach the mini-tufts on the surface of the model. Detailed analysis on the glue effect on the boundary layer can be found in Dobney *et al.* (1986).

The very thin minitufts were made visible for photographic purpose by illuminating them with strong ultra-violet light. Then the optical diameter of the tuft becomes 30 to 40 times larger and they can easily be photographed. For a short duration illumination, Norman Enterprises XT-4000 strobo flash light was used. It emmits 4000 Joules of illumination during 4.5 msec. In order to block the visible light and pass only the ultra-violet light, Corning Glass Works Filter no. 5970 ultra-violet passing filter was used in front of the flash light. The center wavelength of the filter is around 360 nm which is close to the excitation wavelength of

the dye. The ground flat filter was cut to 1 inch by 1 inch pieces and then glued together with a high temperature RTV. This prevents shattering of the glass filter due to the thermal expansion of the glass by absorbing the light energy. Excited in this way, the fluorescent dye emits visible spectrum of light momentarily so that the tufts can be photographed normally. Photographic films are, however, very sensitive to UV light. Therfore, the UV light must be filtered before it reaches the photographic emulsion. For this purpose, Kodak Wratten 2A UV blocking filter was placed in front of the camera lens. This filter absorbes light below 400 nm. The filter characteristics are shown in Figure 10. The flash light was synchronized to the camera in order to use the maximum power of the flash light.

4.2.5 Surface Pressure Measurement

The pressure field in a turbulent flow is produced by a summation of contributions from the turbulent velocity fluctuations (Willmarth, 1975). For an incompressible flow the pressure fluctuations are related to the velocity fluctuations through Poisson's equation, obtained from the divergence of the momentum equation.

Pressure fluctuations at a point are produced by momentum fluctuations at many other points. Therefore, the pressure at a given point will not be highly correlated with the velocity fluctuations at any one neighboring point. A large diameter of pressure transducer diaphragm causes a reduction in the rms pressure measured by the transducer because of the small-scale pressure fluctuations produce an attenuated signal owing to the cancellation of pressure change on the face of the

transducer. In order to overcome this problem and enhance the spatial resolution of the pressure measurements, pinhole caps described in chapter 3 were used. The data were simultaneously sampled at 20 Khz over 4096 points. 50 temporal records, each 0.2048 sec long, were stored for post data processing. The process was repeated for 41 roll locations to cover the range of 180 degree roll angles. The signal was monitored on an oscilloscope to visualize the change of the signal pattern.

5. SIGNAL PROCESSING AND DATA REDUCTION

5.1 Force and Moment Data Reduction

Forces and Moments data were reduced using the body axes system as a reference system. The data were converted to physical quantities using the balance equations and averaged over a 4096 samples. The detailed description of the balance equation can be found in Appendix D. Through a balance misalignment correction, measured data were transformed from balance axes to body axes. Sting cavity pressure was measured but the symmetry of the internal surface along the balance axis induced no corrections. Maximum cross-section area was used as a reference area and maximum diameter was used as a reference length.

5.2 Surface Pressure Data

The mean value of the pressure was obtained by averaging each time record composed of 4096 points and over 50 time records totalling 204800 points. The noise signature of the tunnel was removed using two different methods. The first one is the subtraction of noise spectrum suggested by Blake (1983) to get the power spectrum purely due to the turbulent pressure fluctuation.

$$\Phi_{true} = \Phi_{measured} - \Phi_{acoustic}$$

The second noise cancellation algorithm is a varient of well accepted two dimensional flow technique.

In a two dimensional turbulent boundary layer, if the contaminating noise is acoustic in origin and could be assumed to propagate as a plane wave, the temporal subtraction scheme works very well, provided pressure signals are dealt with (Simpson *et al.*; 1987). There is one very important implicit assumption within this temporal subtraction method. The sensitivities of each individual pressure transducer must be equal. The very subtle misconception related to transducer output and sensitivity is due to the fact that we are dealing with the voltage signals in the laboratory instead of actual pressure signals. Assume a simple 2 pressure transducer arrangement which are separated transverse to the flow velocity. The distance between the transducers l is very large ($l >>> 0$) such that the signal due to the turbulence at transducer 1 is not correlated with the turbulence at transducer 2. Furthermore, an assumption is made that the contaminating noise, whether narrow band acoustic in origin or wide band random phenomena, is fully correlated at each location with itself but not with the signals due to turbulence. If we express the two pressure signals as

$$p_1(t) = p_{t_1} + p_{n_1}$$

$$p_2(t) = p_{t_2} + p_{n_2}$$

The desired power spectrum $\Phi_{(p_1-p_2)(p_1-p_2)}$ can be expressed by

$$\Phi_{(p_1-p_2)(p_1-p_2)} = \Phi_{p_{t_1}p_{t_1}} + \Phi_{p_{t_2}p_{t_2}} - 2\Phi_{p_{t_1}p_{t_2}}$$
$$+ \Phi_{p_{n_1}p_{n_1}} + \Phi_{p_{n_2}p_{n_2}} - 2\Phi_{p_{n_1}p_{n_2}}$$

The last three terms cancel out resulting in

$$\Phi_{(p_1-p_2)(p_1-p_2)} = 2\Phi_{p_{t_1}p_{t_1}}$$

In three dimensional flow, the above cancellation technique breaks down due to the distance required for the transducers to uncorrelate the signal due to turbulence. Agarwal and Simpson (1989) proposed a technique with a pair of microphones closely located but the second signal with a finite time delay. This method was proven effective in a three dimensional flow such as wing-body junction flow. Ölçmen and Simpson (1992) further applied this technique to the same type wing-body junction flow with a single microphone and the time delay of its temporal signal to cancel the acoustic noise in the flow. This method yield

$$\Phi_{(p(t)-p(t-\tau))(p(t)-p(t-\tau))} = 2\Phi_{p_{t_1}p_{t_1}}$$

assuming that the coherent acoustic and vibrational component cancel out for the specific frequency $f = 1/\tau$. Here, the single microphone technique is used as the second method.

These FFT's were corrected through the frequency response function to get the true FFT's by removing the false amplification and attenuation caused by the pinhole cap existing in front of the pressure transducer. Then the FFT's were integrated to get the true rms pressure fluctuation values.

In order to minimize the effort required to scale the pressure fluctuation spectrum data, integral boundary layer properties such as boundary layer thickness, velocity profile, and local skin friction values, etc were obtained through a computer simulation. A computer code, **cfl3d**, was used to calculated these properties at the same experimental flow conditions. This code developed by Thomas is described in Vatsa *et al.* (1987) in detail. It shows a good agreement with the data obtained by Meier *et al.* (1984, 1985) on the same 6 to 1 prolate spheroid. This

code was also compared with other codes by Rudy *et al.* (1988). The calculation, performed on the CRAY-2 Navier at the Numerical Simulator at NASA Ames Research Center, was provided by the Analytical Methods Branch of NASA Langley Research Center. The calculation was made on a fine grid of 49×49 points in the crossflow direction and 73 points in the axial direction, which is a C-O type grid, mapped on a 6 to 1 prolate spheroid mounted on a sting. The calculation simulated the test condition of $R_N = 4.2 \times 10^6$ and angles of attack of 10 deg. and 30 deg. with the boundary layer tripped at x/L = 0.2. The data used to normalize the pressure fluctuation spectrum is tabulated in Table 3.

5.3 Wall Interference Correction

Wall interference correction was estimated. The result suggested minimal interference due to the nature of the model shape. No special attempt was made to incorporate any correction. Detailed analysis is presented in Appendix E.

5.4 Uncertainties of Measurements

An attempt has been made to identify the different sources and magnitude of the uncertainties associated with the various measurements. Uncertainties of measured and calculated quantities were estimated using the fractional deviation method of error propagation (Holman, 1978; Beers, 1962; Cline and McClintock, 1953; Moffat, 1982). The estimated uncertainties of the measured quantities are presented in Figure 4.

6. EXPERIMENTAL RESULTS AND DISCUSSION

6.1 Surface-oil Flow Visualization for Steady Flow

6.1.1 General Description of the Flow

Surface-oil-flow results are presented in Figures 11 to 25. A typical oil-flow pattern with no boundary layer trip is as shown in Figure 19. The skin friction lines show two distinct patterns in the range of Reynolds number and angles of attack tested. Since the oil flow pattern left on the body usually shows all the transient traces occuring during the run and because of its relatively crude resolution, it is quite difficult to check the detailed flow structure from this pattern unless it is a dominant large structure separation. At moderate angles of attack, around 10 degrees, the flow shows laminar forebody separation and turbulent afterbody separations. The laminar flow around the nose, at $x/L \approx 0.3$ and circumferential angle $\phi \approx 115$ degrees, makes a transition into a turbulent flow at the inflection point of the forebody separation line which in turn coalese into the turbulent primary separation line on the afterbody. This turbulent separation line is a line where the separation sheet contacts the surface of the body. And the beginning of the separation line was defined as a point where the skin friction lines coalese at a finite angle to this separation line. This separation sheet formed by the coalesing skin friction lines is stretched and rolls up into a vortical type flow. Induced by this

vortical type flow formed by the primary separation sheet, there appears secondary counter rotating separation sheet between the primary separation line and the lee-side attachment line. The topological structure of the cross-flow is illustrated in Figure 26.

The forebody laminar separation, within the range of angle of attack tested, is an open separation. It is started from a regular point as indicated by the skin friction lines shown in Figure 19. According to previous calculations on the laminar boundary layer on the lee-side symmetry plane (Wang, 1970; Cebeci *et al.*, 1980; Stock, 1980; Grundmann, 1982; Ragab, 1982), the critical angle of attack for the boundary layer on this symmetry line to separate is about 42 degrees for the case of the 6 to 1 prolate spheroid. The critical angle of attack calculated by Grundmann shows that it is a function of geometry. Recent tests carried out at the DLR of Germany (Hornung, 1986) showed that nose bluntness governs the type of separation on the forebody. As the nose bluntness increases, the critical angle of attack to get the closed separation decreases. Their surface oil flow result clearly shows an open separation at 30 degrees of angle of attack which is well below the critical angle of attack for the symmetry plane separation calculated previously. Also, Cebeci and Su (1988) recently confirmed this open separation in their calculations. Ragab (1982) obtained the same results in his calculation arround the nose of the 6 to 1 prolate spheroid.

As can be seen in Figure 19, this laminar open separation located at $x/L = 0.1 \sim 0.3$ reattaches at slightly higher circumferential location on the leeside of the body closer to the symmetry plane, $\phi \approx 135$ degrees, and converges to the skin friction line which is the beginning of the afterbody turbulent separation line. A little

further downstream at $x/L \approx 0.4$, this laminar separation undergoes a transition to a turbulent boundary layer and the separation line is moved further leeside starting at $\phi \approx 135$ degrees. This sudden delay of cross flow separation is similar to that of a circular cylinder in a critical flow region, but the critical Reynolds number for the transition is somewhat lower than the circular cylinder. There has been some effort to derive a three-dimensional relationship for this critical Reynolds number for the transition directly from the two-dimensional results but it is unconvincing (Poll, 1986).

While the flow from the reattached laminar separation and the flow from the windward attachment line after the transition coalese to the turbulent afterbody separation line, the flow on the leeward side of the turbulent separation line is still parallel to the separation line. This low shear flow is originated from the nose stagnation point and follows the leeside of the body. Soon this low shear flow moves closer to the separation sheet emenating from the body which forms into a vortical type flow. Induced by this vortical type flow, the low shear flow on the leeside of the body now begins to coalese to the afterbody primary turbulent separation line. The main source of the energy which makes this low shear flow turn its direction and coalese to the turbulent separation line is the vortical type flow bringing the higher momentum fluid close to the surface. As the primary separation becomes stronger, it induces another separation which is called secondary separation. Now the low momentum fluid on the leeside of the body begins to coalese to the secondary separation and only the portion ahead of the secondary separation coaleses to the primary separation line forming a narrow stream of skin friction lines. Between the two separation lines there appears a reattachment line which divides the flow. Upon

close examination during the test, a tertiary vortex system is observed between the separation lines and reattachment line at angles of attack of 15 and 20 degrees. They do not persist enough to set up a distinct pattern as in the case of the cylindrical afterbodies in a cross-flow (Chanetz, 1988; Peake and Tobak, 1982).

6.1.2 Reynolds Number Effects

From the series of the surface oil flow tests conducted with natural transition, it is found that there exists a "critical" Reynolds number where the flow characteristics and separation pattern on the afterbody go from laminar to transitory or turbulent. Up to the Reynolds number $R_N = \frac{UL}{\nu} = 2.08 \times 10^6$, the whole body is covered by laminar separation followed by a turbulent reattachment line further on the leeside of the body. Above this Reynolds number, the flow changes to turbulent separation from the rear part of the body progressing to upstream as the Reynolds number increases, which is already observable at $R_N = 2.85 \times 10^6$. The "critical" Reynolds number is located between those two Reynolds numbers at about 2.5×10^6.

The separation lines at subcritical Reynolds numbers are shown in Figure 27 for 20 degrees angle of attack. In this low Reynolds number range, the primary separation line is located circumferentially below $\phi = 90°$ for $x/L \geq 0.4$. This is similar to the case of a circular cylinder in a cross-flow. Still, as the Reynolds number increases, the separation line moves close to $\phi = 90°$. Another important characteristic worth mentioning is that the location of the reattachment line of this primary laminar separation is identical for those two cases even though the

location of the primary separation lines are different. The same phenomena were observed at lower angles of attack, but the separation pattern does not show a distinct pattern as in the case of the higher angles of attack due to the low surface shear stress.

For supercritical Reynolds numbers, as the Reynolds number increases the primary separation line does not change its circumferential location but stretches to the upstream of the body as shown in Figures 28,29, and 30 for angles of attack 10, 15, and 20 degrees, respectively. For angle of attack 10 degrees, the separation lines were compared with the surface skin friction measurement of Meier *et al.* (1982) performed at $R_N = 7.2 \times 10^6$. The primary separation lines from the present oil flow tests show excellent agreement with the lines where the circumferential component of the skin friction vanishes. As expected, this line also stretches further upstream because of the increase in the Reynolds number. Due to the large change in the curvature of the body, which is unfolded on a rectangular grid, data points after $x/L = 0.9$ have relatively large error in their location. The locations are on the leeside of the body unlike the laminar separation. It can be clearly seen from Figure 30 that the separation lines suddenly move to the leeside of the body as the Reynolds number increase through the critical range.

For the 15 degree and 20 degree angle of attack cases, the secondary separation lines also show the same behavior as the primary separation lines stretching further upstream as the Reynolds number increases. At 20 degrees shown in Figure 30, the secondary separation lines show excellent agreement.

An interesting feature noticeable is that a tertiary vortex system shows up between the primary and secondary separation lines at angles of attack above 15

degrees. The more dominant tertiary vortex systems were also observed on the cylindrical afterbody by Chanetz (1988) in a low speed test and by Boersen (Peake and Tobak; 1982) in a supersonic flow. The flow field shown in Figure 26 meets the topological law applied for stream lines on a two-dimensional plane cutting a three-dimensional body (Peake and Tobak; 1980). The sum of the nodes is greater than the sum of the saddles by 1.

In Figures 31 and 32, these separation lines are shown for $R_N = 3.45 \times 10^6$ and $R_N = 4.20 \times 10^6$ for angles of attack of 15 and 20 degrees, respectively. As can be seen, the separation lines, including secondary and tertiary separation lines, and reattachment lines are almost at the same circumferential angle and stretch upstream as the Reynolds number insreases. The stretching effect is not that dominant in angle of attack 20 degree case.

6.1.3 Angle of Attack Effects

The separation lines at Reynolds number $R_N = 2.85 \times 10^6$ are shown in Figure 33. As the angle of attack increases, the separation line stretches to upstream location and the leeside of the body. On the afterbody, $x/L = 0.8 \sim 1.0$, the primary separation line moves gradually to the leeward of the body, which shows the increased cross-flow velocity effect. Secondary separation lines also show the same trends.

At $R_N = 3.45 \times 10^6$ the separation pattern shows exactly the same behavior as in the case of $R_N = 2.85 \times 10^6$. As shown in Figure 34, the locations of the separation lines are almost identical to those of $R_N = 2.85 \times 10^6$ and stretching toward upstream.

From Figure 35, it can be clearly seen that the separation lines not only stretch to the upstream of the body but also change their location to the lower circumferential location with increasing angle of attack. The separation line at $\alpha = 20°$, $R_N = 2.85 \times 10^6$ almost coincides with the separation line at $R_N = 3.45 \times 10^6$ case. The general behavior of the separation line on the body after $x/L = 0.8$ is the same as in the lower Reynolds number cases mentioned above.

The starting point of the nose laminar separation seems to be dependent on angle of attack rather than Reynolds number. However, the length of this separation line is highly Reynolds number dependent as one can expect. At an angle of attack 10 degrees, the starting point of this nose separation was roughly around 25 % length from the nose. As the angle of attack is increased, this point moves further upstream to 15 % and 10 % for 15 degree and 20 degree angles of attack, respectively.

6.1.4 Boundary Layer Trip Effects

In order to investigate the boundary layer trip effect on the separation location, the boundary layer was tripped on the forebody at $x/L \approx 0.1$. The trip locations were derived from the measurement of Meier and Kreplin (1980). Boundary layer profiles were measured with single-wire probe at several locations on the body in order to check the boundary layer characteristics. The boundary layer profiles measured at an angle of attack 15 degrees are shown in Figure 36. The boundary layer profile on the leeside attachment line 1″ downstream of the transition strip ($x/L \approx 0.166$) and Reynolds number $R_N = 1.4 \times 10^6$ clearly shows laminar

boundary layer profile which is in excellent agreement with Blasius laminar profile. The turbulence level and the hot-wire signal also indicated steady laminar flow at this location. This shows not only the trip strip which was designed to work at $R_N = 4.2 \times 10^6$ didn't work at this low Reynolds number but also the boundary layer profile is still laminar at this location.

At $R_N = 4.2 \times 10^6$, the profile at this location shows a complete transition to the turbulent boundary layer. The boundary layer profile ahead of the trip strip already shows transitory profile at this Reynolds number. The profile at $1''$ downstream of the trip strip shows a complete transition to the turbulent boundary layer. This profile shows almost same shape as the profile measured on the side of the model just before the primary separation at $x/L = 0.8$ and $\phi = 90$ degrees, as shown in Figure 36. No noticeable change in the pattern and location of the primary separation was found after the boundary layer was tripped. This was also confirmed by the measurement of Meier and Kreplin (1980) and the calculation of Rotta (1980), which showed little difference in the momentum thickness, which was within the experimental uncertainties.

High Reynolds number simulation test using a circular trip at x/L =0.2 shows very close agreement with the skin friction measurements of Meier and Kreplin (1980) and is shown in Figure 37. The surface oil flow results are shown in Figures 38 and 39 for the angles of attack 10 and 30 degrees, respectively. At an angle of attack of 30 degrees, shown in Figure 40, the separation location on the mid-body approaches that of a two dimensional cylinder and only the nose and tail region show strong three-dimensional effects.

6.2 Mini-Tuft Surface-Flow Visualization

Mini-tuft surface flow visualization results are shown in Figures 41 to 47 for different angles of attack. A total of 3862 tufts were applied on the surface of the 6 to 1 prolate spheroid model. Each tuft has a length of 0.6 inches and spaced with a $\Delta\phi = 10$ degrees. The results show the same flow characteristics as obtained by the surface-oil-flow technique except that no cleaning is necessary and can be used in unsteady flow situations. Considering the number of tufts required to visualize the flow, the resolution of the tufts in the lateral direction is not enough to detect any meaningful crossflow component of the separation.

6.3 Force and Moment Measurement

Tests were performed at five different Reynolds numbers and one with the boundary layer tripped at x/L = 0.2 in order to simulate a high Reynolds number situation. Up to the angle of attack of 10 degrees, the normal force coefficient C_Z, given in Figure 48, does not change as the Reynolds number increases. At the lowest Reynolds number tested, $R_N = 1.39 \times 10^6$, C_Z has the highest value which becomes smaller as the Reynolds number increases to 2.83×10^6. At $R_N = 2.83 \times 10^6$, the C_Z slope does not change as the angle of attack increases above 10 degrees. The normal force coefficient increase again as the Reynolds number increases above 2.83×10^6. The recovery of the normal force coefficient is only about the half that it had at low Reynolds number. This is due to the change of the primary separation area. As shown in Figure 30, the primary separation line moves quite a distance, about

$\Delta\phi = 50$ deg., while the Reynolds number changes from 1.4×10^6 to 2.85×10^6, thus reducing the total normal force. At Reynolds numbers above 2.83×10^6, the separation region stretches to the forward portion of the body, which has large contribution to the normal force.

The pitching moment coefficient C_M, given in Figure 49, shows different trends. At Reynolds numbers below 2.0×10^6, the C_M curve changes its direction at 18 degrees. This also can be found in measurements of Iuso *et al.* (1988) at $R_N = 1.0 \times 10^6$. The sudden drop of this pitching moment coefficient C_M is believed to be due to the absence of the suction because of laminar separation. This laminar separation can be seen in surface pressure measurements, Figure 56, which shows rather large increase in p_{rms}/Q on top of the nose region. As the Reynolds number increases the C_M curve increases to its maximum at $R_N = 2.83 \times 10^6$ and comes down a little, in contrast to the normal force curve. The trends at angles of attack above 20 degrees are due to the nose separation. This can be seen by comparing the results at $R_N = 4.19 \times 10^6$ with no trip and $R_N = 4.25 \times 10^6$ with trip. Up to angle of attack 18 degrees, these cases show the same C_Z and C_M values. But as the α increases above 20 degrees, the nose separation with natural transition has lower normal force but higher pitching moment. The pitching moment coefficient shows large effect of Reynolds number.

Side force C_Y, yawing moment C_N, , which are shown in Figures 50 and 51, respectively, do not show any Reynolds number and angle of attack dependence except some fluctuations at angle of attack higher than 10 degrees. The nonzero values at lower angle of attack is due to misalignment of the model and flow angularity. Rolling moment coefficient C_R, shown in Figure 52, does not change through

the range of the angle of attack tested. Another interesting feature worth mentioning is that the change in the normal force coefficient slope and pitching moment coefficient curve slope is related to the variation of the sting cavity pressure shown in Figure 53. The case of $R_N = 4.25 \times 10^6$ is presented in Figure 54. As can be seen, there exist three distinct regions. From angle of attack 0 to 10 degrees, the cavity pressure coefficient C_{pc} decreases and C_Z and C_M have almost a linear slope. The change in the primary separation location in this range is confined to the tail region which is very small compared to the whole body. Also the separation line breaks up from a closed separation to an open separation at an angle of attack around 5 degrees as shown by Cebeci and Su (1988). Between 10 degrees and 20 degrees, the separation lines stretch to the forward body and above 20 degrees, the separation line moves to windward side as shown in Figure 40.

6.4 Surface Pressure Measurements

6.4.1. Mean Pressure Distribution

The mean pressure coefficients are presented in Figures 55 to 74 for the angles of attack of 10 and 30 degrees along with the rms pressure fluctuations and potential flow solutions. The potential flow solution is derived in Appendix B. The mean pressure coefficients are also compared to the data measured by Meier *et al.* (1986) at 10 and 30 degrees angle of attack (Ragab, 1989).

At 10 degrees of angle of attack, overall mean values are slightly higher than those of Meier *et al.* (1986). The difference in terms of pressure coefficient is

$\Delta C_p = 0.01$. Meier *et al.* (1986) obtained the data in an open jet wind tunnel whereas the present data are obtained in a closed test section wind tunnel. The correction applied for an uncertain tunnel reference pressure (Meier *et al.*, 1986) might have caused this discrepancy which is consistent throughout the measured data, even at 30 degree angle of attack. The mean pressure distribution closly follow the potential flow solution down to x/L = 0.565. Starting from x/L = 0.689 and further downstream, the measured distribution is off from the potential flow which indicates viscous and separating flow.

At 30 degrees of angle of attack, the mean pressure distribution clearly shows the location of the separation. At x/L = 0.108, which is in front of the boundary layer trip and shown in Figure 66, the laminar separation can be seen at $\phi = 135$ degrees. At x/L = 0.232, downstream of the boundary layer trip, turbulent separation can be seen at $\phi \approx 145$ degrees. The laminar separation seen at the upstream location still exists at $\phi \approx 135$ degrees. From x/L = 0.440, the suction peak due to the vortical flow rolled up from the body surface shows up. The constant pressure region due to the flow separation becomes wider as we go downstream and matches well with the surface oil flow result. The deviation between the present measurement and the measurement of Meier *et al.* (Ragab, 1989) is slightly bigger than 10 degrees angle of attack case but show excellent agreement.

6.4.2. Root-Mean-Square Pressure Fluctuation

For the attached flow at 10 degrees angle of attack, the root-mean-square pressure fluctuation p_{rms}/Q is close to 0.01 as found by Schewe (1983). At 30

degrees of angle of attack, p_{rms}/Q is lower than 0.01 which indicates large d^+ due to the finite size of the pinhole. The rms pressure fluctuation becomes higher as the separation line is approached. As shown in Figures 71 and 72, not only the primary separation line but also the secondary separation and reattachment lines can be identified by the peaks in p_{rms}/Q. These peaks match very well with the separation location obtained through the surface oil flow tests.

6.4.3. Surface Pressure Spectra

The temporal signal of the pressure is shown in Figure 75. These signal are measured at x/L = 0.896, 0.108, and 0.689 and angle of attack 0 degrees without the boundary layer trip. At x/L = 0.689, the pressure signal shows intermittent burst due to the boundary layer transition. At x/L = 0.896, the signal shows turbulent fluctuation. The data measured at x/L = 0.108 are used as the tunnel acoustic noise and the spectra are shown in Figure 76 for the circumferential angles of 0, 30, 60, 90, 120, 150, 180 degrees. The high peak at around 50 Hz is the fan blade passing frequency at the flow speed tested and also strong successive harmonics of this fundamental frequency. At 1.25 KHz, there exists a huge peak which seems to be the characteristic frequency of the tunnel. This hissing noise was observed throughout the tests. In Figure 77, the two different methods used are compared to each other. The acoustic noise spectrum subtraction technique and the single microphone technique show good agreement.

The pressure spectra measured at angle of attack 30 degrees are presented in Figures 78 to 95. These data were smoothed using the locally weighted regression

method (Cleveland and Devlin, 1988). The acoustic noise subtraction technique gives lower magnitude in an attached flow region and higher low frequency magnitude in a separated flow region. The variation of the magnitude of the power spectrum is somewhat different depending on the location of the measurement but it maintains general trends as shown in Figure 83. In windward attached flow region ($\phi = 0, 30, 60$ degrees), at frequency around 300 Hz, the slope of the spectrum is $f^{-1.3}$ compared to f^{-1} of two dimensional flow. As the separation region is approached ($\phi = 90$ degrees), the low frequency fluctuation below 400 Hz becomes high. Once the separation line is crossed ($\phi = 120, 150$ degrees), the high pressure fluctuation extends further from 400 Hz to $\approx$ 3 KHz range and form $f^{-1.3}$ to $f^{-1.5}$ slope. At the leeside reattachment line ($\phi = 180$ degrees), this spectrum goes back to the value of windward attached flow region except that it still has higher magnitude fluctuation at around 200 to 300 Hz. The single microphone technique gives the same trends but the variation is a little smaller than the acoustic noise spectrum subtraction technique. These can be seen from Figures 86 to 93.

The pressure fluctuation spectra measured at $\phi = 90$ degrees are normalized using outer variables. They are shown in Figures 94 and 95 for the acoustic noise spectrum subtraction technique and for the single microphone with time delay technique, respectively. Although the displacement thickness δ_* is an integral length scale for the boundary layer, it is not a direct measure of the outer length scale of the boundary layer. Here, the boundary layer thickness δ, the local boundary layer edge velocity U_e, and freestream dynamic pressure Q are used to normalize the pressure fluctuation spectrum. The acoustic noise spectrum subtraction technique again shows higher low frequency contents as shown in Figure 94. The spectrum

measured at x/2a = 0.2135 was somewhat contaminated by the post boundary layer trip which was located at x/2a =0.2. At x/2a = 0.342, 0.440, 0.565, the pressure fluctuation spectra collapse together up to $\omega\delta/U_e \approx 2 \times 10^{-2}$ and the slope of the spectra are (-1) power of the frequency as normally found in a two-dimensional turbulent boundary layer (McGrath and Simpson, 1987). This shows that the flow on the windward side is colateral as in the case of a two-dimensional boundary layer.

As the location moves further downstream, getting closer to the separation location, the pressure fluctuation spectra get higher in the low frequency range. Since the contributions at low frequencies are from the turbulent velocity fluctuations across the entire boundary layer, this increase of the energy content in low frequency range is due to the flow separation. The p_{rms}/Q values at these locations also indicate the deviation from a normal turbulent boundary layer. Due to the uncertainties of the subtracted acoustic noise spectrum, high frequency results are not reliable. The amount of contribution from the spectra above 4 KHz is about 9 precent of the total value. The single microphone with time delay technique also shows the same trends except that it under corrects the noise contents. It shows an extended (-1) power region and the variation in the low frequency region is small compared to the acoustic noise spectrum subtraction case.

7. CONCLUSION

The flow over a 6 to 1 prolate spheroid was investigated. Surface oil flow visualization tests, mini-tuft flow visualization tests, force and moment tests, surface pressure measurements including the pressure fluctuations were carried out to investigate this flow. From these measurements, the following can be concluded.

The cross-flow separation on a 6 to 1 prolate spheroid is characterized. There exists a critical Reynolds number at around 2.5×10^6, which changes the characteristics of the afterbody separation. Above this critical Reynolds number, the after body separation is a turbulent boundary layer separation. Below this Reynolds number, the after body separation is mostly a laminar boundary layer separation. Above this critical Reynolds number, the Reynolds number effect on the primary separation location is very small. But, the angle of attack effect on the location of the primary separation is dominant at all Reynolds numbers tested.

Forces and moments can be directly related to the variation of the separation location through the range of the angle of attack tested. Force and moment measurements also show the existance of the critical Reynolds number. Above this Reynolds number, at an angle of attack, the normal force coefficient increases as the Reynolds number increases. Below this value, the normal force coefficient decreases to the minimum value as the Reynolds number increases to the critical Reynolds number. The variation in the pitching moment coefficient is the opposite of the normal force coefficient.

Surface pressure measurements show a very good agreement on the mean values with other available data. The variation of the mean pressure coefficient around the circumferential angle shows the location of the separated region.

For the first time, the pressure fluctuations in the flow of this kind is reported. The root-mean-square pressure fluctuation normalized by the free-stream dynamic pressure clearly reveals the locations of the primary, the secondary separation and the reattachment line. To measure the surface pressure fluctuations in the frequency domain, the acoustic noise spectrum subtraction method and the single microphone with time delay technique were used. They show very good agreement but the single microphone with time delay technique requires further verification to be used in a three-dimensional flow field. In the separated flow region, the low frequency pressure fluctuation below 500 Hz is high. The power spectra show $f^{-1.0}$ region in the attached flow region. The spectrum normalized by the outer flow scaling show good collapse at low frequencies and the intensity gets high as the separation is approached.

For the future unsteady measurements, the Dynamic Plunge-Pitch-Roll (DyP-PiR) model support was designed and developed.

BIBLIOGRAPHY

Agarwal, N. K., and Simpson, R. L., "A New Technique for Obtaining the Turbulent Pressure Spectrum from the Surface Pressure Spectrum," *Journal of Sound and Vibration*, Vol. 135, No. 2, pp. 346-350, 1989.

Ahn, S., and Simpson, R. L., *Cross Flow Separation on a Prolate Spheroid at Angle of Attack*, AIAA Paper No. 92-0428, 1992.

Armco Stainless Steel Products, *ARMCO 17-4PH Precipitation-Hardening Stainless Steel*, Product Data Bulletin No. S-22, 1986.

Atraghji, E. G., *Surface Flow Visualization, Surface Pressure and Surface Preston Pitot Pressure Measurement over a 6 : 1 Ellipsoid at Incidence at M=0.3 and M=0.74*, 5x5 Ft Trisonic Blowdown Wind Tunnel Project Report 5x5/0032, NAE, NRC, Ottawa, Canada, 1968.

Band, E. G. U., and Payne, P. R., "The Pressure Distribution on the Surface of an Ellipsoid in Inviscid Flow," *Aeronautical Quarterly*, February, 1980.

Barber, K. M., *Mean Velocity and Turbulence Measurements of Flow around a 6 to 1 Prolate Spheroid*, MS thesis, Aerospace Engineering, Virginia Polytechnic Institute and State University, 1990.

Barberis, D., "3-D Boundary Layer Computation on Arbitrary Obstacles with Direct and Inverse Methods," *La Recherche Aérospatiale*, No. 3, pp. 1-27, 1986.

Barberis, D., and Chanetz, B., "Decollement en Ecoulement Incompressible Tridimensionnel: Experiences de Validation et Modelisation," *29ème Colloque D'Aérodynamique Appliquée, Aussois*, November, 1986.

Beers, Y., *Introduction to the Theory of Error*, Addison-Wesley, Massachusetts, 1957.

Bendat, J. S., and Piersol, A. G., *Random Data - Analysis and Measurement Procedures*, John Wiley and Sons, 1986.

Bippes, H., "Experimental Study of the Flow Along a Body of Revolution," *Boundary Layer Effect - Proceedings of the 7th US/FRG Data Exchange Agreement Meeting*, AFFDL-TR-78-111, 1978.

Blake, W. K., "Turbulent Boundary Layer Wall Pressure Fluctuations on Smooth and Rough Walls," *Journal of Fluid Mechanics*, Vol. 44, pp. 637-660, 1970.

Blake, W. K., "Differential Pressure Measurement," *Fluid Mechanics Measurements*, Ed. Goldstein, R. J., 1983.

Bradshaw, P., "'Inactive' Motion and Pressure Fluctuations in Turbulent Boundary Layers," *Journal of Fluid Mechanics*, Vol. 30, Part 2, pp. 241-258, 1967.

Braslow, A. L., Hicks, R. M., and Harris, R. V., Jr, *Use of Grit Type Boundary-Layer-Transition Trips on Wind Tunnel Models*, NASA TN D-3579, September, 1966.

Braslow, A. L., and Knox, E. C., *Simplified Method for Determination of Critical Height of Distributed Roughness Particles for Boundary-Layer Transition at Mach Numbers from 0 to 5*, NACA TN 4363, September, 1958.

Bull, M. K. and Thomas, A. S. W., "High Frequency Wall-Pressure Fluctuations in Turbulent Boundary Layers," *The Physics of Fluids*, Vol. 19, No. 4, pp. 597-599, April, 1976.

Bynum, D. S., Ledford, R. L., and Smotherman, W. E., *Wind Tunnel Pressure Measuring Techniques*, AGARD-AG-145-70, December, 1970.

Cebeci, T., Khattab, A. K., and Stewartson, K., "Prediction of Three-Dimensional Laminar and Turbulent Boundary Layers on Bodies of Revolution at High Angles of Attack," *2nd Symposium on Turbulent Shear Flows*, Imperial College, London, July, 1979.

Cebeci, T., Khattab, A. K., and Stewartson, K., "On Nose Separation," *Journal of Fluid Mechanics*, Vol. 97, Part 3, pp. 435-454, 1980.

Cebeci, T., Khattab, A. K., and Stewartson, K., "Three-Dimensional Laminar Boundary Layer and the O.K. of Accessibility," *Journal of Fluid Mechanics*, Vol. 107, pp. 57-87, 1981.

Cebeci, T., and Meier, H. U., *Problems Associated With the Calculation of the Flow Around Bodies of Revolution at Incidence*, DFVLR IB 222-81/A 09, 1981.

Cebeci, T., and Meier, H. U., "A Note on the Specification of Freestream Velocity Calculation of the Boundary Layer Flow around Bodies of Revolution at Incidence," *Z. Flugwiss. Weltraumforschung*, pp. 416-418, 1982.

Cebeci, T., and Meier, H. U., *Turbulent Boundry Layers on a Prolate Spheroid*, AIAA Paper No. 87-1299, June, 1987.

Cebeci, T., and Su, W., "Separation of Three-Dimensional Laminar Boundary Layer on a Prolate Spheroid," *Journal of Fluid Mechanics*, Vol., 191, pp. 47-77, 1988.

Cebeci, T., and Su, W., *The Birth of Open Separation on a Prolate Spheroid*, Report No. MDC K0171, Douglas Aircraft Co., McDonnell Douglas Corp., September, 1988.

Chanetz, B., *Contribution a L'Etude du Decollement Tridimensionnel en Ecoulement Turbulent Incompressible*, These de Doctorate d'Eat de L'Universite Claude Bernard de Lyon, September, 1988.

Chanetz, B., and Délery, J., "Experimental Analysis of Turbulent Separation on an Oblate Ellipsoid-Cylinder," *La Recherche Aérospatiale*, No. 3, pp. 59-77, 1988.

Chang, M.-S., and Purtell, L. P., "Three-Dimensional Flow Separation and the Effect of Appendages," *16th Symposium on Naval Hydrodynamics*, pp. 352-370, Berkeley, Ca., July, 1982.

Chang, R. C., and Muirhead, V. U., "Effect of Sink Rate on Ground Effect of Low-Aspect-Ratio Wings," *Journal of Aircraft*, Vol. 24, No. 3, pp. 176-180, March, 1987.

Choi, K. and Simpson, R. L., *Some Mean Velocity, Turbulence, and Unsteadiness Characteristics of the VPI & SU Stability Wind Tunnel*, Aerospace and Ocean Engineering Dept. Report, Virginia Polytechnic Institute and State University, December, 1987.

Christophe, J., *A New Rig for Flight Mechanics Studies in the ONERA Aerothermodynamic Test Center of Modane*, AIAA-80-0464, AIAA 11th Aerodynamic Testing Conference, 1980.

Cleveland,W. S., and Devlin, J. S., "Locally Weighted Regression: An Approach to Regression Analysis by Local Fitting," *Journal of the American Statistical Association*, Vol. 83, pp. 596-610, 1988.

Corcos, G. M., "Resolution of Pressure in Turbulence," *The Journal of the Acoustical Society of America*, Vol. 35, No. 2, pp. 192-199, February, 1963.

Corcos, G. M., "The Structure of the Turbulent Pressure Field in Boundary-Layer Flows," *Journal of Fluid Mechanics*, Vol. 18, Part 3, pp. 353-378, 1964.

Corcos, G. M., "The Resolution of Turbulent Pressureat the Wall of a Boundary Layer," *Journal of Sound and Vibration*, Vol. 6, No. 1, pp. 59-70, 1967.

Coulter, S. M., and Buchanan, T. D., "Description of a new High-Alpha, High-Load, Pitch-Yaw Dynamic Stability Test Mechanism at AEDC," *AIAA Paper 80-0451*, AIAA 11th Aerodynamic Testing Conference, 1980.

Coulter, S. M., and Marquart, E. J., "Cross and Cross-Coupling Derivative Measurements on the Standard Dynamic Model at AEDC," *AIAA Paper 82-0596*, AIAA 12th Aerodynamic Testing Conference, 1982.

Cousteix, J., *Analyse Théoreque et moyens de prévision de la couche limite turbulente tridimensionnelle*, Thèse de Doctorat, Université de Paris-6, 1974.

Crites, R. C., and Frey, R. C., *Experiments with Acoustical Measurements in the McDonnell Polysonic Wind Tunnel*, Engineering Laboratories, McDonnell Aircraft Co., April, 1968.

Crowder, J. P., *Fluorescent Mini-Tufts for Non-Intrusive Flow Visualization*, McDonnell-Douglas Report MDC J7374, 1977.

Crowder, J. P., "Add Fluorescent Minitufts to the Aerodynamicist's Bag of Tricks," *Astronautics and Aeronautics*, pp. 54-56, November, 1980.

Crowder, J. P., "Fluorescent Minituft for Nonintrusive Surface Flow Visualization," *Flow Visualization II*, Merzkirch, W. Ed., Proceedings of the Second International Symposium on Flow Visualization, pp. 663-667, September, 1980.

Crowder, J. P., "Fluorescent Minituft for Flow Visualization on Rotating Surfaces," *Flow Visualization III*, Yang, W. J. Ed., Proceedings of the Third International Symposium on Flow Visualization, pp. 55-64, September, 1983.

Crowder, J. P., "Flow Visualization Techniques Applied to Full Scale Vehicles," *Flow Visualization IV*, Véret, C. Ed., Proceedings of the Fourth International Symposium on Flow Visualization, pp. 15-24, August, 1983.

Crowder, J. P., Goldhammer, M. I., and Smyth, D. N., *STOL Aircraft Transient Ground Effects; Part II. Experimental Techniques Feasibility Study*, NASA CR 137767, 1975.

Crowder, J. P., Hill, E. G., and Pond, C. R., "Selected Wind Tunnel Testing Developments at the Boeing Aerodynamics Laboratory," *AIAA Paper 80-0458*, AIAA 11th Aerodynamic Testing Conference, 1980.

Davis, D. D., and Sweberg, H. H., *Investigation of Some Factors Affecting Comparisons of Wind-Tunnel and Flight Measurements of Maximum Lift Coefficients for a Fighter-Type Airplane*, NACA TN 1639, June, 1948.

den Boer, R. D., Houwink, R., and Zwaan R. J., "Requirements and Capabilities in Unsteady Wind Tunnel Testing," *Aerodynamic Data Accuracy and Quality: Requirements and Capabilities in Wind Tunnel Testing*, AGARD-CP-429, October, 1987.

Dobney, D. G., Hanson, P., and Fiddes, S. P., "The 'Minituft' Surface Flow Visualisation Method; Experence of Use in the RAE 5m pressurised Low-Speed Wind Tunnel," *The Aeronautical Journal*, January, 1986.

Dubois, M., " Six-Component Strain-Gage Balances for Large Wind Tunnels," *Experimental Mechanics*, pp. 401-407, November, 1981.

Edwards, H. B., " Design Requirements in Multi-Component Strain Gage Balances," *ISA 29th Annual Meeting*, pp. 227-235, 1983.

Edwards, J. W., *Analysis of an Electrohydraulic Aircraft Control-Surface Servo and Comparison with Test Results*, NASA TN D-6928, August, 1972.

Eichelbrenner, E. A., *Décollement laminaire en trois dimensions sur un obstacle fini*, Publication ONERA No. 89, 1957.

Eichelbrenner, E. A., "Three-Dimensional Boundary Layers," *Ann. Rev. Fluid Mech.*, Vol. 5, pp. 339-360, 1973.

Ericsson, L. E., *Vortex-Induced Effects on Aircraft Dynamics*, AIAA Paper No. 86-2279, AIAA Atmospheric Flight Mechanics Conference August, 1986.

Eward, B., " The Development of Electron Beam Welded, Strain-Gaged Wind Tunnel Balances," *Journal of Aircraft*, Vol. 16, No. 5, pp. 349-352, 1979.

Eward, B., and Graewe, E., " Development of Internal Balances for Cryogenic Wind Tunnels," *ICIASF '87 Record*, 1987.

Eward, B., and Krenz, G., " The Accuracy Problems of Airplane Development Force Testing in Cryogenic Wind Tunnels," *AIAA Paper 86-0776*, AIAA 14th Aerodynamic Testing Conference, 1986.

Farabee, T. M., and Casarella, M. J., "Spectral Features of Wall Pressure Fluctuations Beneath Turbulent Boundary Layers," *The Physics of Fluids, A* , Vol. 3, No. 10, ' 1991.

Faulkner, S. M., Hess, J. L., Smith, A. M. O., and Liebeck, R. H., *Charts and Formulas for Estimating Velocity Fields in Incompressible Flow*, Report No. LB32707, Douglas Aircraft Company, July, 1968.

Fuchs, H., "Prediction of Dynamic Derivatives," *Stability and Control of Tactical Missile Systems*, Paper No. 6, AGARD-CP-451, March, 1989.

Fussey, D. A., "Dynamic Force Measurement Design Parameters Associated with Wind Tunnel Powered Models," *ISA 20th Annual Meeting*, Vol. 11, 1974.

Gadeberg, B. L., *The Effect of Rate of Change of Angle of Attack on the Maximum Lift Coefficient of a Persuit Airplane*, NACA TN 2525, October, 1951.

Gad-el-Hak, M., "Visualization Techniques for Unsteady Flows: An Overview," *Journal of Fluids Engineering*, Vol. 110, pp. 231-243, September, 1988.

Gallaway, C. R. and Osborn, R. F., *Aerodynamic Perspective of Supermaneuverability*, AIAA-85-4068, AIAA 3rd Applied Aerodynamics Conference, Oct., 1985.

Garner, H. C., Rogers, E. W. E., Acum, W. E. A., and Maskell, E. C., *Subsonic Wind Tunnel Wall Corrections*, AGARDograph 109, AGARD, NATO, October, 1963.

Geyer, L. H., *Controlled Damping Through Dynamic Pressure Feedback*, Technical Bulletin 101, Moog, Inc., June, 1958 (Revised Apr., 1972).

Godt, P. W. and Pyle, H. S., *The Application of a Laser Interferometer System for Calibrating Accelerometers and Dynamic Pressure Transducers*, Engineering Laboratories, McDonnell Aircraft Co., April, 1970.

Goodman, A., *Experimental Techniques and Methods of Analysis Used in Submerged Body Research*, Third Symposium on Naval Hydrodynamics; High Performance Ships, Sep., 1960.

Goodman, A., Brown, C. E., and Altmann, R. J., *An Experimental Study to Determine the Flow and the Subsonic Static and Dynamic Stability Characteristics of Aircraft Operating at High Angles-of-Attack*, AIAA 87-2560, AIAA Atmospheric Flight Mechanics Conference, August, 1987.

Gourjienko, G. A., *Method of Curved Models and Its Application to the Study of Curvilinear Flight of Airships*, Rpt 182, Part I and Part II, Central Aero-Hydro-Dynamical Institute, Moscow, Reprinted as NACA TM 829 and 830, 1934.

Grundmann R., "Kritischer Anstellwinkel bei der Umströmung von Rotationsellipsoiden," *Z. Flugwiss. Weltraumforsch.*, Vol. 6, No. 6, pp. 441-442, 1982.

Han, T., and Patel, V. C., "Flow Separation on a Spheroid at Incidence," *Journal of Fluid Mechanics*, Vol. 92, Part 4, pp. 643-657, 1979.

Hansen, R. M., *Mechanical Design and Fabrication of Strain-Gage Balance*, - AGARD Report 9, 1956(a).

Hansen, R. M., *Evaluation and Calibration of Wire-Strain-Gage Balance under Load*, AGARD Report 13, 1956(b).

Harper, P. W., and Flanigan, R. E., *The Effect of Change of Angle of Attack on the Maximum Lift of a Small Model*, NACA TN 2061, March, 1950.

Hassall, J. R., and Zaveri, K., *Acoustic Noise Measurements*, Brüel and Kjær, January, 1979.

Herbst, W. B., "Future Fighter Technologies," *Journal of Aircraft*, Vol. 17, No. 8, pp. 561-566, August, 1980.

Hirsh, R. S. and Cebeci, T., *Calculation of Three-Dimensional Boundary Layers with Negative Cross Flow on Bodies of Revolution*, AIAA paper No. 77-683, June, 1977.

Hoerner, S. F., and Borst, H. V., *Fluid-Dynamic Lift*, 1975.

Holman, J. P., *Experimental Methods for Engineers*, 1978.

Horne, M. P., *Physical and Computational Investigation of the Wall Pressure Fluctuations in a Channel Flow*, NRL Memorandum Report 6628, April, 1990.

Hornung, H., *Institut für Experimentelle Strömungsmechanik 1980-1985: 2. Auflage* , DFVLR IB 222-85 A 44, March, 1986.

Hunt, B., *The Panel Method for Subsonic Aerodynamic Flows.*, VKI Lecture Series 1978-4 on Computational Fluid Dynamics, 1978.

Iuso, G., Onorato, M., Oggiano, M. S., De Ponte, S., Yuzhong, B., and Xiaodi, Z., "Experimental Investigation of the Complex 3-D Flow Around a Body of Revolution at Incidence /A Sino-Italian Cooperative Research Program," *ICAS-88-4.9.1*, pp. 1382-1391, 16th Congress of the International Council of the Aeronautical Sciences, 1988.

Johnson, G. I., "Some Design Considerations Regarding Multicomponent Transducers for Static and Dynamic Load Measurements," *ICIASF '83 Record*, 1983.

Jumper, E. J., Schreck, S. J., and Dimmick, R. L., "Lift-Curve Characteristics for an Airfoil Pitching at Constant Rate," *Journal of Aircraft*, Vol. 24, No. 10, pp. 680-687, October, 1987.

Katz, J., "A Discrete Vortex Method for the Non-Steady Separated Flow over an Airfoil," *Journal of Fluid Mechanics*, Vol. 102, pp.315 - 328, 1981.

Kendall, D. N., *Dynamic Calibration of Pressure TRansducers*, Engineering Laboratories, McDonnell Aircraft Co., May, 1970.

Kendall, D. N., *Application of Miniature Pressure Transducers to the Measurement of Buffet Phenomena*, Engineering Laboratories, McDonnell Aircraft Co., May, 1971.

Kendall, D. N., and Crites, R. C., *Measurement of Fluctuating Pressures*, Engineering Laboratories, McDonnell Aircraft Co., April, 1969.

Kim, J., "On the Structure of Pressure Fluctuations in Simulated Turbulent Channel Flow," *Journal of Fluid Mechanics*, Vol. 205, pp. 421-451, 1989.

Kline, S. J., and McClintock, F. A., "Describing Uncertainties in Single-Sample Experiments," *Mechanical Engineering*, Vol. 75, No. 1, pp. 3 - 8, January, 1953.

Ko, J. S., *Analysis of Dynamic Stability Derivatives for Aircraft at High Angle of Attack*, Ph.D. Dissertation, Aerospace Engineering, Virginia Polytechnic Institute and State University, 1985.

Kordulla, W., Vollmers, H., and Dallmann, U., "Simulation of Three-Dimensional Transonic Flow with Separation Past a Hemisphere-Cylinder configuration," *Application of Computational Fluid Dynamics in Aeronautics.* AGARD-CP-412, AGARD NATO, 1986.

Kraft, E. M., "Boundary Layer Manipulation," *Boundary Layer Simulation and Control in Wind Tunnels*, Report of the Fluid Dynamics Panel Working Group 09, AGARD-AR-224, AGARD NATO, April, 1989.

Kreplin, H.-P., and Meier, H. U., "Experimentelle Untersuchungen von Ablösephanomenen an einem Rotationssymmetrischen Köpper," *Erscheiut im DGLR Jarbuch 1979*, DFVLR IB 251-79 A 25, pp. 71.1-71.10, 1979.

Kreplin, H.-P., Meier, H. U., and Landhäußer, A., *Wall Shear Stress Measurements on a Prolate Spheroid at Zero Incidence in the DNW Wind Tunnel*, DFVLR-Mitt. 86-06, February, 1986.

Kreplin, H. P., Meier, H. U., Mercker, E., and Landhäußer, A., *Wall Shear Stress Measurements on a Prolate Spheroid at Zero Incidence in the DNW Wind Tunnel*, Data Report, DFVLR IB 222-85/A 11, 1985.

Kreplin, H. P., and Vollmers, H., "Preliminary Turbulence Measurements in Three-Dimensional Boundary Layers on a Prolate Spheroid," *Viscous and Interacting Flow Field Effects; Proceedings of the 6th US/FRG Data Exchange Agreement Meeting*, DFVLR IB 222-81/CP1, pp. 218-229, 1981.

Kreplin, H.-P., Vollmers, H., and Meier, H. U., "Experimental Determination of Wall Shear Stress Vectors on an Inclined Prolate Spheroid," *Vicous and Interacting Flow Field Effects; 5th US-FRG-DEA Meeting*, AFFDL-TR-80-3088, pp. 315-332, June, 1980.

Kreplin, H.-P., Vollmers, H., and Meier, H. U., "Measurements of the Wall Shear Stress on an Inclined Prolate Spheroid," *Z. Flugwiss. Weltraumforschung*, Vol. 6, No. 4, pp. 248-252, 1982.

Kreplin, H.-P., Vollmers, H., and Meier, H. U., "Wall Shear Stress Measurements on an Inclined Prolate Spheroid in the DFVLR 3M X 3M Low Speed Wind Tunnel Göttingen," Data Report, IB 222-84 A33 DFVLR, AVA Göttingen, Jan., 1985.

Lamb, H., *Hydrodynamics*, 6th edition, Dover Publicationc, 1945.

Lang, J. D. and Francis, M. S., *Unsteady Aerodynamics and Dynamic Aircraft Maneuverability*, Paper no. 29, Unsteady Aerodynamics-Fundamentals and Applications to Aircraft Dynamics AGARD-CP-386, 1985.

Le Balleur, J. C., and Lazareff, M., *A Multi-Zonal-Marching Integral Method for 3D Boundary Layer with Viscous-Inviscid Interaction*, 9th International Conference on Numerical Methods in Fluid Dynamics, 1984.

Legendre, R., "Séparation de l'Écoulement Laminaire Tridimensionnel," *La Recherche Aéronautique*, No. 54, Nov.-Dec., pp. 3-8, 1956.

Lighthill, M. J., "Attachment and Separation in Three-Dimensional Flows," *Laminar Boundary Layers*, Ed. Rosenhead L., Oxford Univ. Press, 1963.

Mabey, D. G., "On the Prospects for Increasing Dynamic Lift," *Aeronautical Journal*, May, 1988.

Maltby, R. L., and Keating, R. F. A., "The Surface Oil Flow Technique for Use in Low Speed Wind Tunnels," *Flow Visualization in Wind Tunnels Using Indicators*, AGARDograph 70, pp. 29-74, 1962.

Manie, F., Neron, M., and Schmitt, V., "Experimental and Computational Investigation of the Vortex Flow on a Swept Wing," *Proceedings of the 14th ICAS Congress*, 1984.

Maskell, E. C., *Flow Separation in Three-Dimensions*, RAE Aero. Report 2565, Nov. 1955.

Mason, W. H., *Basic Subsonic Aerodynamics*, Aerodynamic Calculation Methods for Programmable Calculators and Personal Computers, 1981.

McCroskey, W. J., "Some Current Research in Unsteady Fluid Dynamics," *Journal of Fluids Engineering*, Vol. 99, pp. 8-39, March, 1977.

McGrath, B. E., and Simpson, R. L., *Some Features of Surface Pressure Fluctuations in Turbulent Bouadary Layers with Zero and Favorable Pressure Gradients*, NASA CR 4051, 1987.

Meier, H. U., and Cebeci, T., *Flow Characteristics of a Body of Revolution at Incidence*, DFVLR IB 222-84/A 44, 1984.

Meier, H. U., and Gronau, K. H., "Viscous and Interacting Flow Field Effects," *Viscous and Interacting Flow Field Effects; Proceedings of the 6th US/FRG Data Exchange Agreement Meeting*, DFVLR IB 222-81/CP1, 1981.

Meier, H. U., and Kreplin, H. P., "Pressure Distributions and Flow Visualizations on an Ellipsoid 1:6 Designed for Three-Dimensional Boundary Layer Investigations," *Boundary Layer Effect - Proceedings of the 7th US/FRG Data Exchange Agreement Meeting*, AFFDL-TR-78-111, 1978.

Meier, H. U., and Kreplin, H. P., "Influence of Free Stream Turbulence on Boundary Layer Development," *AIAA Journal*, Vol. 18, No. 1, pp. 11-15, January, 1980.

Meier, H. U., and Kreplin, H.-P., "Experimental Investigation of the Boundary Layer Transition and Separation on a Body of Revolution," *Z. Flugwiss. Weltraumforschung*, Vol. 4, No. 2, pp. 65-71, 1980.

Meier, H. U., and Kreplin, H. P., "Experimental Study of Boundary Layer Velocity Profiles on a Prolate Spheroid at Low Incidence in the Cross Section $X_0/L = 0.64$," *Viscous and Interacting Flow Field Effects; Proceedings of the 5th US/FRG Data Exchange Agreement Meeting*, AFFDL-TR-80-3088, pp. 169-189, June, 1980.

Meier, H. U., and Kreplin, H. P., "Boundary Layer Separation Due to "Weak" and "Strong" Viscous-Inviscid Interaction on an Inclined Body of Revolution," *Viscous and Interacting Flow Field Effects; Proceedings of the 8th US/FRG Data Exchange Agreement Meeting*, DFVLR IB 222-84/A 19, 1984.

Meier, H. U., Kreplin, H. P., and Landhäußer, A., *Wall Pressure Measurements on a 1:6 Prolate Spheroid in the DVFLR 3m x 3m Low Speed Wind Tunnel($\alpha = 10°$, $U_\infty = 55$ m/s, Artificial Transition)* Data Report, DFVLR IB 222-86 A 04, 1986.

Meier, H. U., Kreplin, H. P., Landhäußer, A., and Baumgarten, D., *Mean Velocity Distributions in Three-Dimensional Boundary Layers, Developing on a 1:6 Prolate Spheroid with Natural Transition*, Data Report, DFVLR IB 222-4/A 10, 1984.

Meier, H. U., Kreplin, H. P., Landhäußer, A., and Baumgarten, D., *Mean Velocity Distributions in Three-Dimensional Boundary Layers, Developing on a 1:6 Prolate Spheroid with Artificial Transition*, Data Report, DFVLR IB 222-4/A 11, 1984.

Meier, H. U., Kreplin, H.-P., and Ming, X., *Problems Associated with Artificial Boundary Layer Transition*, AIAA Paper No. 83-1673, July, 1983.

Meier, H. U., Kreplin, H. P., and Vollmers, H., "Velocity Distributions in 3D-Boundary Layers and Vortex Flows Developing on an Inclined Prolate Spheroid," *Viscous and Interacting Flow Field Effects; Proceedings of the 6th US-/FRG Data Exchange Agreement Meeting*, DFVLR IB 222-81/CP1, pp. 202-217, 1981.

Meier, H. U., Kreplin, H.-P., and Vollmers, H., *The Effect of Artificial Transition on the Boundary Layer Development on an Inclined Body of Revolution*, DFVLR-AVA IB 222-82 A 18, April, 1982.

Meier, H. U., Kreplin, H.-P., and Vollmers, H., "Develpment of Boundary Layers and Separation Pattern on a Body of Revolution at Incidence," *2nd Symposium on Numerical and Physical Aspects of Aerodynamic Flows* , State University, Long Beach, CA, January, 1983.

Meier, H. U., Michel, U., and Kreplin, H. P., "The Influence of Wind Tunnel Turbulence on the Boundary Layer Transition," *Perspectives in Turbulence Studies*, pp. 26-46, 1987.

Michel, U. and Froebel, E., "Flow Unsteadiness in Three Low-Speed Wind Tunnels," *Aerodynamic Data Accuracy and Quality: Requirements and Capabilities in Wind Tunnel Testing*, AGARD-CP-429, October, 1987.

Moffat, R. J., "Contributions to the Theory of Single-Sample Uncertainty Analysis," *Journal of Fluids Engineering*, Vol. 104, pp. 250 - 260, June, 1982.

Moor, S. B., *The Design and Evaluation of an Internal Six Component Strain Gage Balance*, MS Thesis, Southern Methodist University, January, 1961.

Ölçmen, S. M., and Simpson, R. L., *Influence of Wing Shapes on the Surface Pressure Fluctuations of a Wing-Body Junction*, AIAA Paper No. 92-0433, 1992.

O'Leary, C. O., and Drew, W., "Flow Visualisation on Rolling Models using Minitufts," *The Aeronautical Journal*, pp. 269-274, June/July, 1987.

Orlik-Rückemann, K. J., "Review of Techniques for Determination of Dynamic Stability Parameters in Wind Tunnels," *Dynamic Stability Parameters*, AGARD-LS-114 May, 1981.

Orlik-Rückemann, K. J., "Aircraft Dynamics - Aerodynamic Aspects and Wind Tunnel Techniques," *Special Course on Fundamentals of Fighter Aircraft Design*, AGARD-R-740, October, 1987.

Pan, D., and Pulliam, T. H., *The Computation of Steady 3-D Separated Flows over Aerodynamic Bodies at Incidence and Yaw*, AIAA Paper No. 86-0109, January, 1986.

Panton, R. L. and Linebarger, J. H., "Wall Pressure Spectra Calculations for Equilibrium Boundary Layers," *Journal of Fluid Mechanics*, Vol. 65, Part 2, pp. 261-287, 1974.

Patel, V. C., and Baek, J. H., "Boundary Layers in Planes of Symmetry, Part II: Calculations for Laminar and Turbulent Flows," *AIAA Journal*, Vol. 25, No. 6, pp. 812-818, June, 1987.

Peake, D. J., and Tobak, M., *Three-Dimensional Interactions and Vortical Flows with Emphasis on High Speeds*, AGARDograph 252, 1980.

Peake, D. J., and Tobak, M., "Three-Dimensional Separation and Reattachment," *High Angle of Attack Aerodynamics*, AGARD Lecture Series 121, December,1982.

Perry, C. C., and Lissner, H.R., *The Strain Gage Primer* , McGraw-Hill, 1955.

Poll, D. I. A., *On the Effect of Boundary-Layer Transition on a Cylindrical Afterbody at Incidence in Low-Speed Flow*, Aeronautical Journal, Oct., 1985.

Pope, A., and Harper, J. J., *Low Speed Wind Tunnel Testing*, John Wiley and Sons, 1966.

Ragab, S. A., *A Method for the Calculation of Three-Dimensional Boundary Layers with Circumferential Reversed Flow on Bodies*, AIAA Paper No. 82-1023, June, 1982.

Ragab, S. A., *Euler/Boundary Layer Solutions for Vortex Separation from Smooth Surfaces*, AIAA Paper No. 85-0016, January, 1985.

Ragab, S. A., *Steady and Unsteady Boundary Layers on Prolate Spheroids at High Incidence*, AIAA Paper No. 85-1708, July, 1985.

Ragab, S. A., *Private communication*, 1989.

Rechbach, C., "Calcul numérique d'écoulement tridimensionnels instationaires avec nappes tourbillonnaires," *La Recherche Aérospatiale*, No. 5, pp. 289-298, 1977.

Ringel M., and Levin, D., "Improved Drag Element for Wind Tunnel Sting Balances," *Journal of Aircraft*, Vol. 22, No. 11, pp. 979-982, November, 1985.

Rizzi, A. W., and Eriksson, L. E., "Computation of Flow Around Wings Based on the Euler Equations," *Journal of Fluid Mechanics*, Vol. 148, pp. 45-71, 1984.

Rotta, J. C., "Theoretical Investigations of Three-dimensional Tuebulent Boundary Layers on Swept Wings," *Viscous and Interacting Flow Field Effects; Proceedings of the 5th US/FRG Data Exchange Agreement Meeting*, AFFDL-TR-77-61, 1977.

Rotta, J. C., "A Theoretical Treatment of the Free Stream Turbulence Effects on the Turbulent Boundary Layer," *Viscous and Interacting Flow Field Effects; Proceedings of the 5th US/FRG Data Exchange Agreement Meeting*, AFFDL-TR-80-3088, pp. 118-140, June, 1980.

Rudy, D. H., Kumar, A., Thomas, J. L., and Gnoffo, P. A., "A Comparative Study and Validation of Upwind and Central-Difference Navier-Stokes Codes for High-Speed Flows," *Validation of Computational Fluid Dynamics*, Vol. 1, AGARD-CP-437, May, 1988.

Russo, G. P., "Techniques for Boundary Layer Tripping and Control," *Boundary Layer Simulation and Control in Wind Tunnels*, Report of the Fluid Dynamics Panel Working Group 09, AGARD-AR-224, AGARD NATO, April, 1989.

Schewe, G., "On the Structure and Resolution of Wall-Pressure Fluctuations associated with Turbulent Boundary-Layer Flow," *Journal of Fluid Mechanics*, Vol. 134, pp. 311-328, 1983.

Schnabl F., "Entwicklung eines Algorithmus zur Auswertung der Eichversuche an 6-Komponenten-DMS-Waagen," *Z. Flugwiss. Weltraumforschung*, Vol. 11, No. 3, pp. 342-346, 1987.

Schneider, G. R., "Calculation of Three-Dimensional Boundary Layers on Bodies of Revolution at Incidence," *Viscous and Interacting Flow Field Effects; Proceedings of the 5th US/FRG Data Exchange Agreement Meeting*, AFFDL-TR-80-3088, pp. 287-314, June, 1980.

Schneider, G. R., "Calculation of Three-Dimensional Boundary Layers in the Plane of Symmetry of a Prolate Spheroid at Incidence including Laminar-Turbulent Transition," *Viscous and Interacting Flow Field Effects; Proceedings of the 8th US/FRG-Data Exchange Agreement Meeting*, BWVg-FBWT 83-4, pp. 39-48, May, 1983.

Seidel, M. Ed., *Design, Manufacturing, Calibration of the German-Dutch Wind Tunnel*, DNW, May, 1982.

Sevik, M., *The Lift on an Oscillating Body of Revolution*, Ph.D. Thesis, Pennsylvania State University, 1963.

Simpson, J. P., and Gatley, W. L., *Dynamic Calibration of Pressure Measuring Systems*, MDC 70-010, McDonnell Aircraft Company, 1970.

Simpson, R. L., Ghodbane, M. G., and McGrath, B. E., "Surface Pressure Fluctuations in a Separating Turbulent Boundary Layer," *Journal of Fluid Mechanics*, Vol. 177, pp. 167-186, 1987.

Sjörs, I., "Experimental Design for Calibration of Wind Tunnel Balances," *ICIASF '83 Record*, 1983.

Smith, D. G., *Private Communication*, Aerodynamics Laboratory, Boeing Commercial Airplanes, October, 1989.

Smith, L. H., and Nunn, R. H., *Aerodynamic Characteristics of an Axisymmetric Body undergoing a Uniform Pitching Motion*, AD-A007553, Naval Postgraduate School, February, 1975.

Smith, L. H., and Nunn, R. H., "Aerodynamic Characteristics of an Axisymmetric Body undergoing a Uniform Pitching Motion," *Journal of Spacecraft*, Vol. 13, No. 1, pp. 8-14, January, 1976.

Smith, P. D., *Numerical Computation of Three-Dimensional Turbulent Boundary Layers*, RAE Tech Memo Aero 1945, 1982.

Statler, I. C., Tufts, O. B. and Hirtreiter, W. J., *The Development and Evaluation of the CAL/Air Force Dynamic Wind-Tunnel Testing System*, Part 1, AFFDL-TR-66-153, 1966.

Stock, H. W., "Three Dimensional Boundary Layers on Wings and Bodies of Revolution," *Boundary Layer Effect - Proceedings of the 7th US/FRG Data Exchange Agreement Meeting*, AFFDL-TR-78-111, 1978.

Stock, H. W., *Computation of the Boundary Layer and Separation Lines on Inclined Ellipsoids and of Separated Flows on Infinite Swept Wings*, AIAA Paper No. 80-1442, July, 1980.

Szebehely, V. G., and Niederer, O. C., *Unsteady and Amplitude Effects on the Moment Derivatives of a Prolate Spheroid*, DTMB Report 828, December, 1953.

Tcheng, P., "The Dynamic Characteristics of a Five Component Oscillating Balance," ISA Vol 17. pp 184-190. 1980.

Thomas, A. S. W. and Bull, M. K., "On the Role of Wall-Pressure Fluctuations in Deterministic Motions in the Turbulent Biundary Layer," *Journal of Fluid Mechanics*, Vol. 128, pp. 283-322, 1983.

Tobak, M. and Peake, D. J., "Topology of Three-Dimensional Separated Flows," *Ann. Rev. Fluid Mech.*, Vol. 14, pp. 61-85, 1982.

Van Dalsem, W., and Steger, J. L. *The Efficient Simulation of Three-Dimensional Viscous Flows Using the Bounadry Layer Equations*, AIAA Paper 85-4064, AIAA 3rd Applied Aerodynamics Conference, 1985.

Vatsa, V. N., Thomas, J. L., and Weden, B. W., *Navier-Stokes Computations of Prolate Spheroids at Angle of Attack* , AIAA Paper 87-2627, AIAA Atmospheric Flight Mechanics Conference, Montrey, CA, August, 1987.

Vollmers, H., "Integration of Streamlines from Measured Static Pressure Fields on a Surface," *Viscous and Interacting Flow Field Effects; Proceedings of the 6th US/FRG Data Exchange Agreement Meeting*, DFVLR IB 222-81/CP1, pp. 259-270, 1981.

Vollmers, H., Kreplin, H.-P., Meier, H. U., and Kühn, A., *Measured Mean Velocity Field Around a 1:6 Prolate Spheroid at Various Cross Sections*, Data Report, DFVLR IB 221-85 A 08, 1985.

Wang, K. C., "Three-Dimensional Boundary Layer near the Plane of Symmetry of a Spheroid at Incidence," *Journal of Fluid Mechanics*, Vol. 43, Part 1, pp. 187-209, 1970.

Wang, K. C., "Laminar Boundary Layer over a Body of Revolution at Extremely High Incidence," *The Physics of Fluids*, Vol. 17, No. 7, pp. 1381-1385, July, 1974.

Wang, K. C., "Boundary Layer over a Blunt Body at Low Incidence with Circumferential Reversed Flow," *Journal of Fluid Mechanics*, Vol. 72, Part 1, pp. 49-65, 1975.

Wang, K. C., "On the Current Controversy about Unsteady Separation," *Numerical and Physical Aspects of Aerodynamic Flows*, Ed. Cebeci, T., pp. 279-291, Springer-Verlag, 1982.

Wang, K. C., *On the Disputes About Open Separation*, AIAA Paper No. 83-0292, 1983.

Ward, K. C., and Katz, J., "Development of Flow Structures in the Lee of an Inclined Body of Revolution," *Journal of Aircraft*, Vol. 26, No. 3, pp. 198-206, March, 1989.

Werlé, H., *Étude Expérimentale, au Tunnel Hydrodynamique, de L'écoulement Autour d'une Famille D'ellipsoides aux Faibles Vitesses*, ONERA NT No. 1/1859A 1957.

Werlé, H., "Le Décollement sur des Corps de Révolution à Basse Vitesse," *La Recherche Aéronautique*, No. 90, 1962.

Willmarth, W. W., "Unsteady Force and Pressure Measurements," *Ann. Rev. Fluid Mech.*, Vol. 3, pp. 147-170, 1971.

Willmarth, W. W., "Pressure Fluctuations beneath Turbulent Boundary Layers," *Ann. Rev. Fluid Mech.*, Vol. 7, pp. 311-328, 1975.

Willmarth, W. W. and Roos, F., "Resolution and Structure of the Wall Pressure Field beneath a Turbulent Boundary Layers," *Journal of Fluid Mechanics*, Vol. 22, Part 1, pp. 81-94, 1965.

Yoshihara, H., "Chapter 1. Background and Overview," *Calculations of 3D Separate Turbulent Flows in Boundary Layer Limit*, AGARD-AR-255, May, 1990.

Young,Jr., C. P., and Gloss, B. B., *Cryogenic Wind Tunnel Models*, NASA CP - 2262, May, 1982.

FIGURES

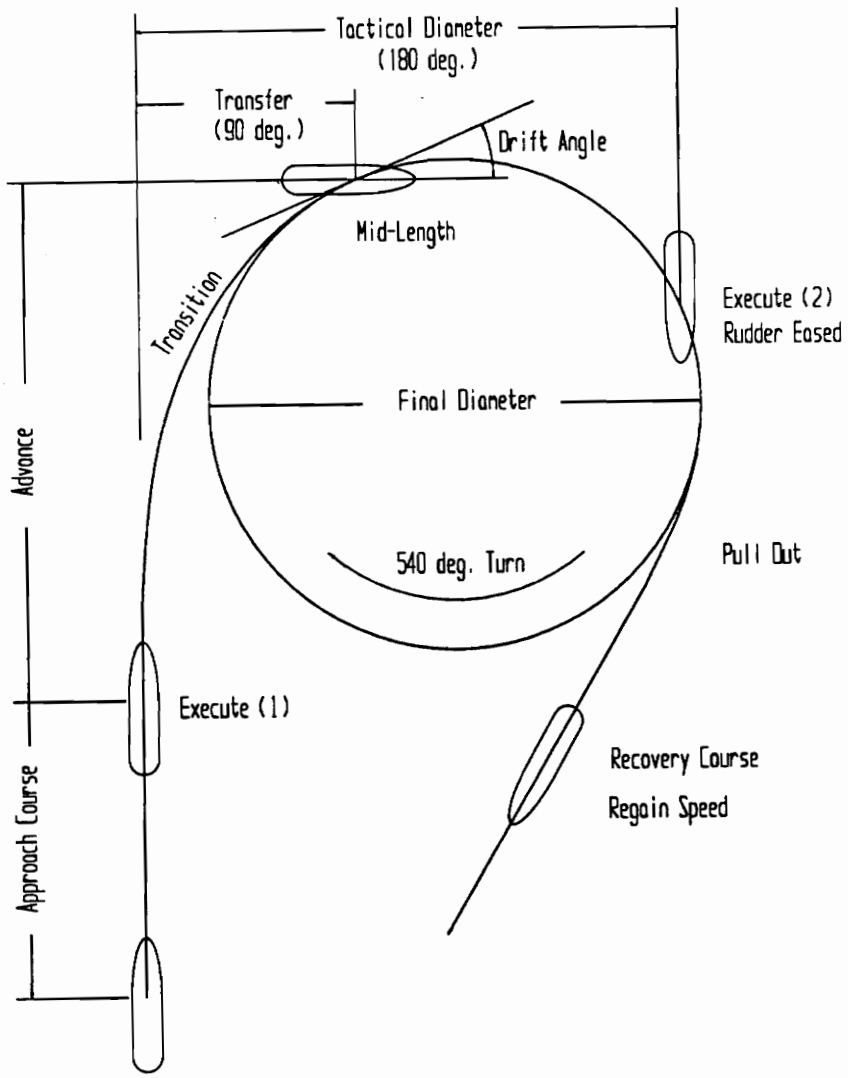

Figure 1. Submarine Turning Maneuver (from Goodman, 1960).

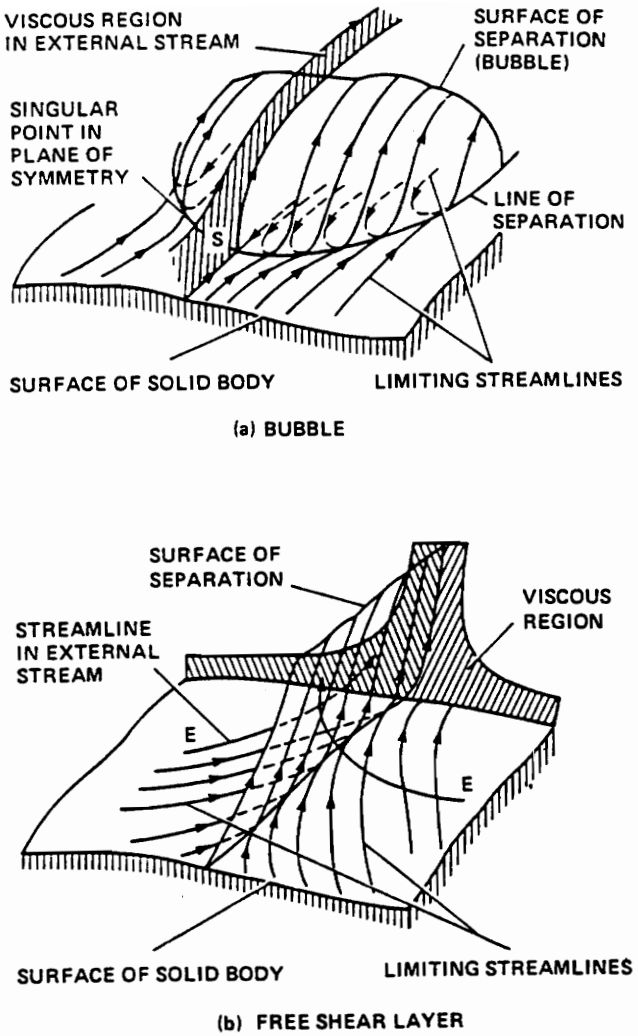

Figure 2. Maskell's Concept of Three Dimensional Flow Separation (after Maskell, 1955).

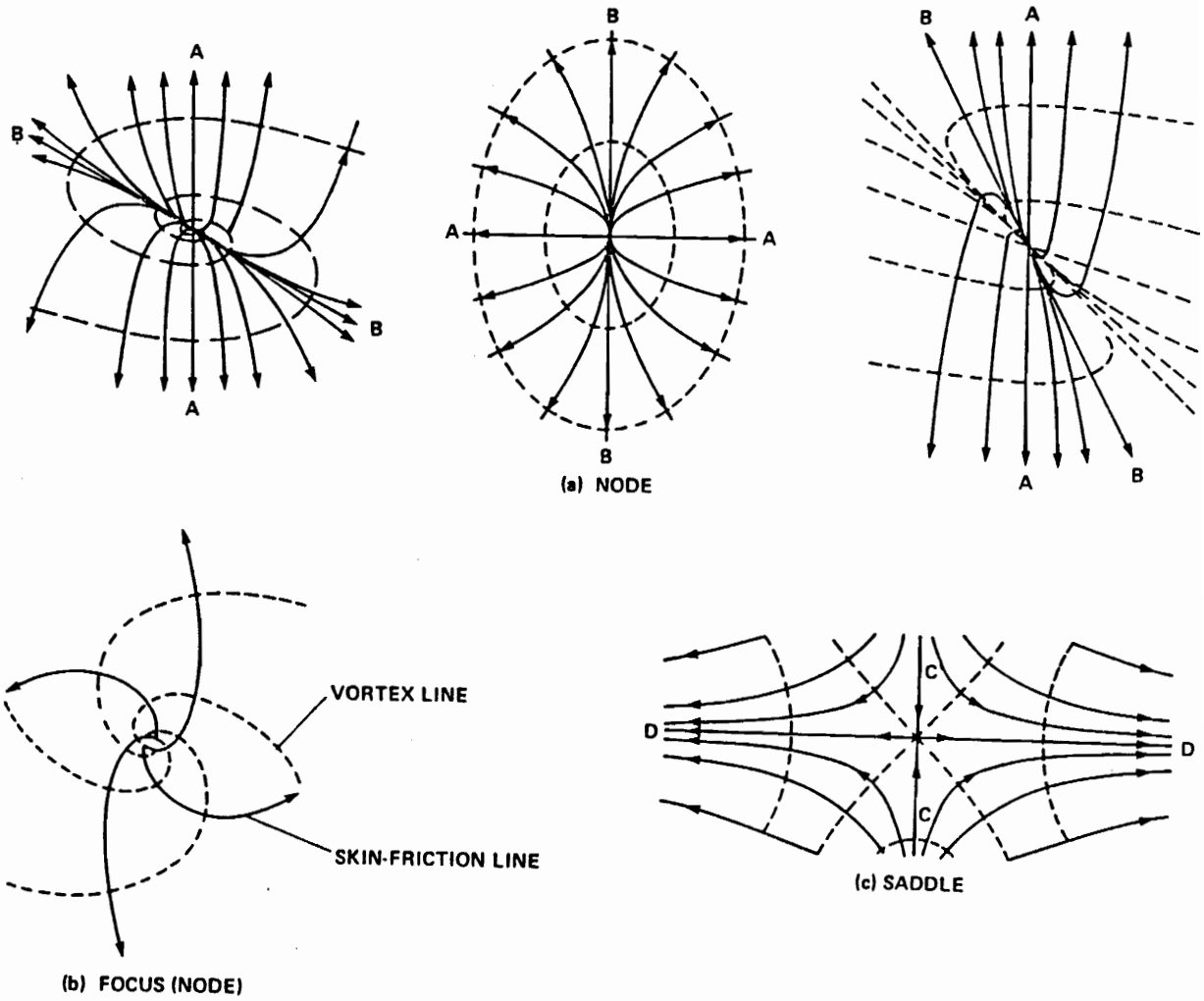

Figure 3. Basic Flow Separation Points (after Peake and Tobak, 1980).

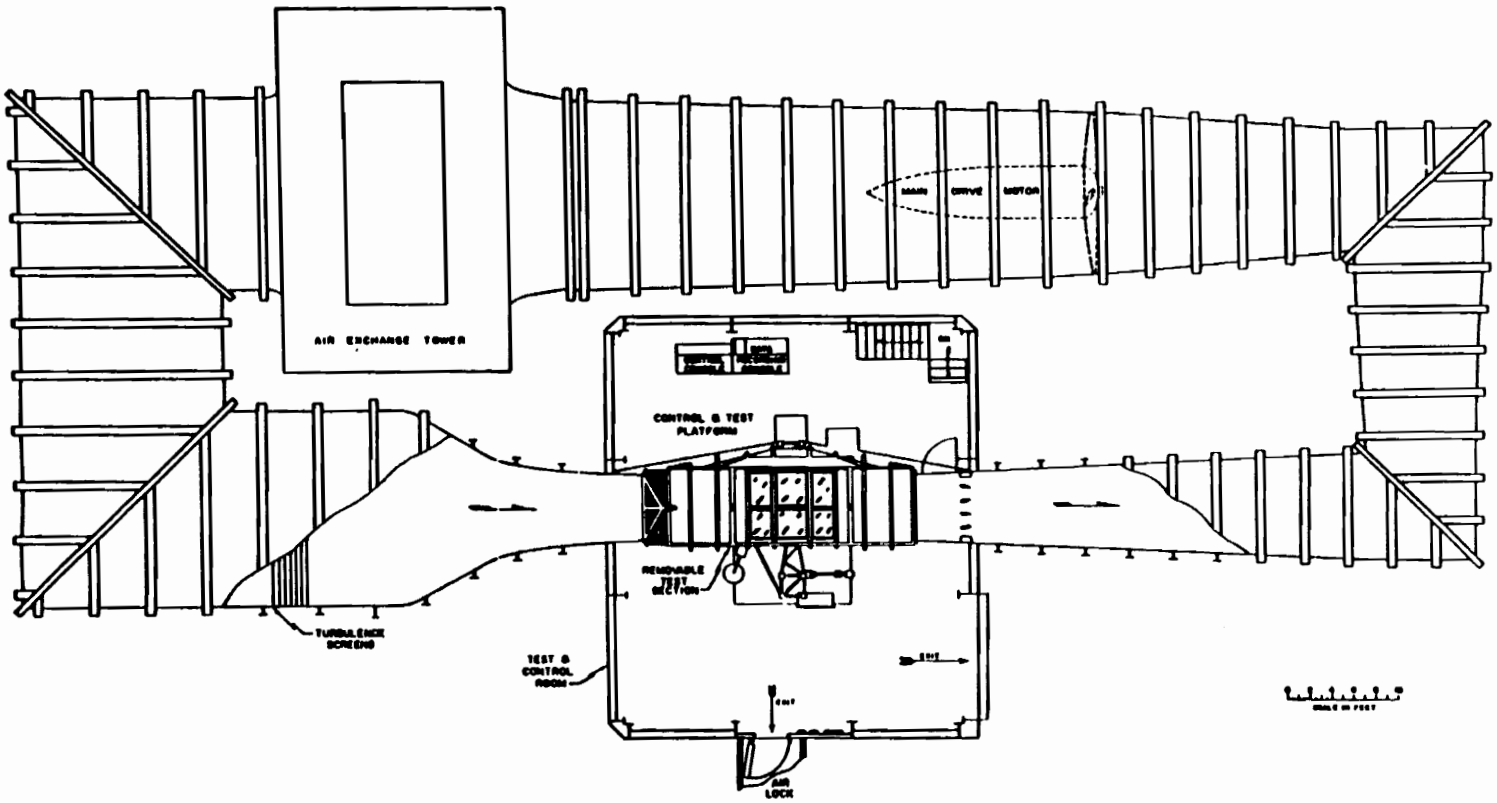

Figure 4. The Virginia Polytechnic Institute and State University Stability Wind Tunnel.

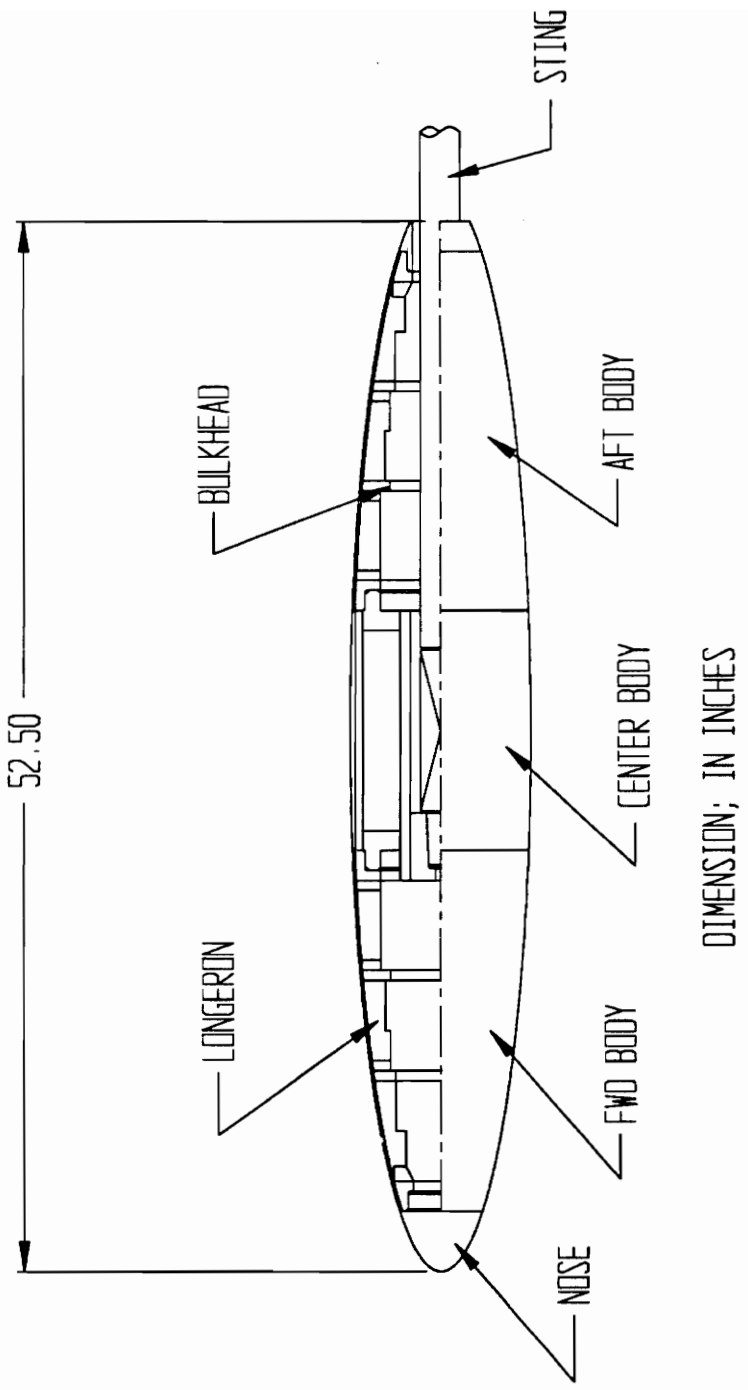

Figure 5. 6 to 1 Prolate Spheroid Model.

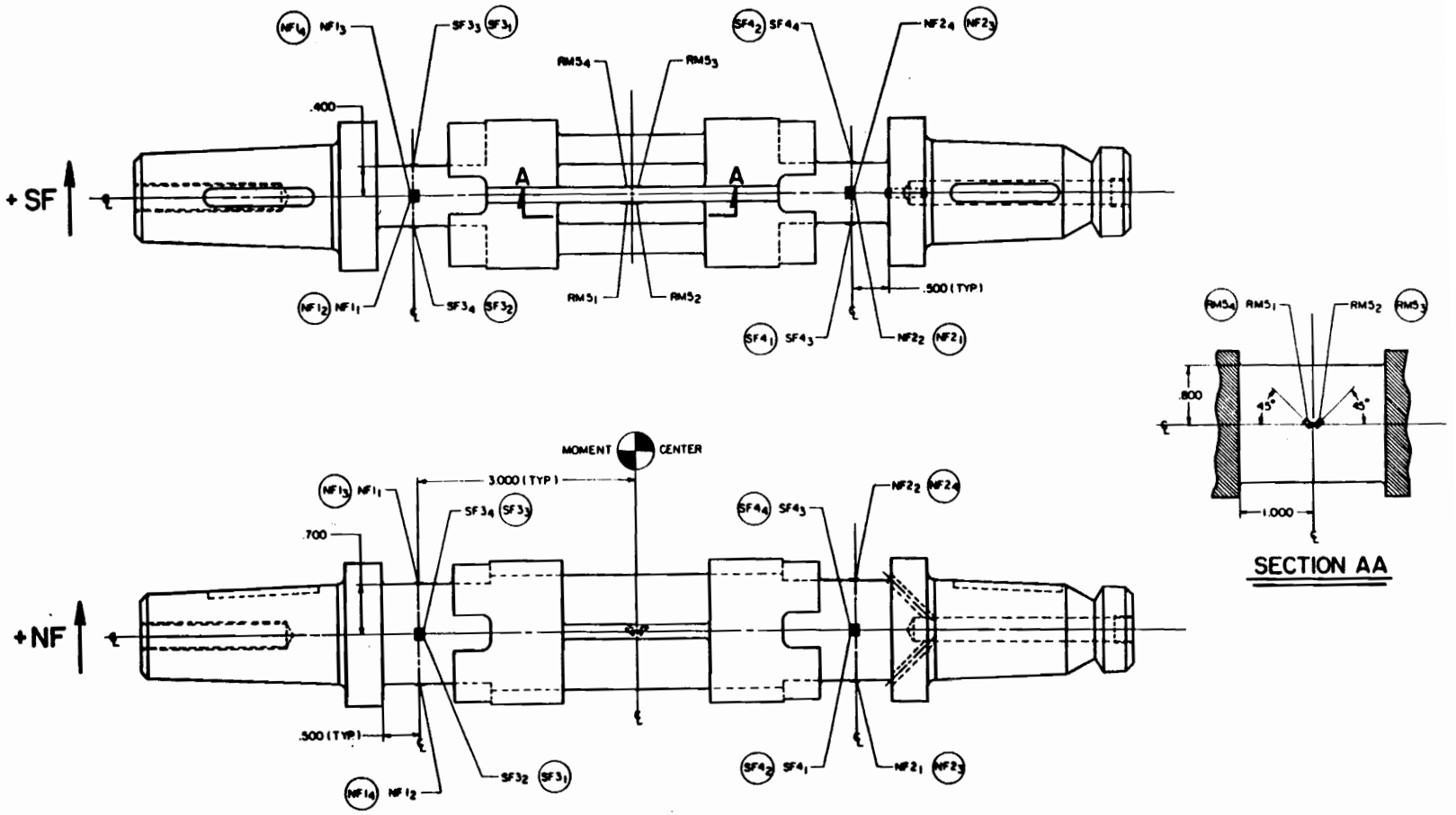

Figure 6. 5-Component Internal Balance.

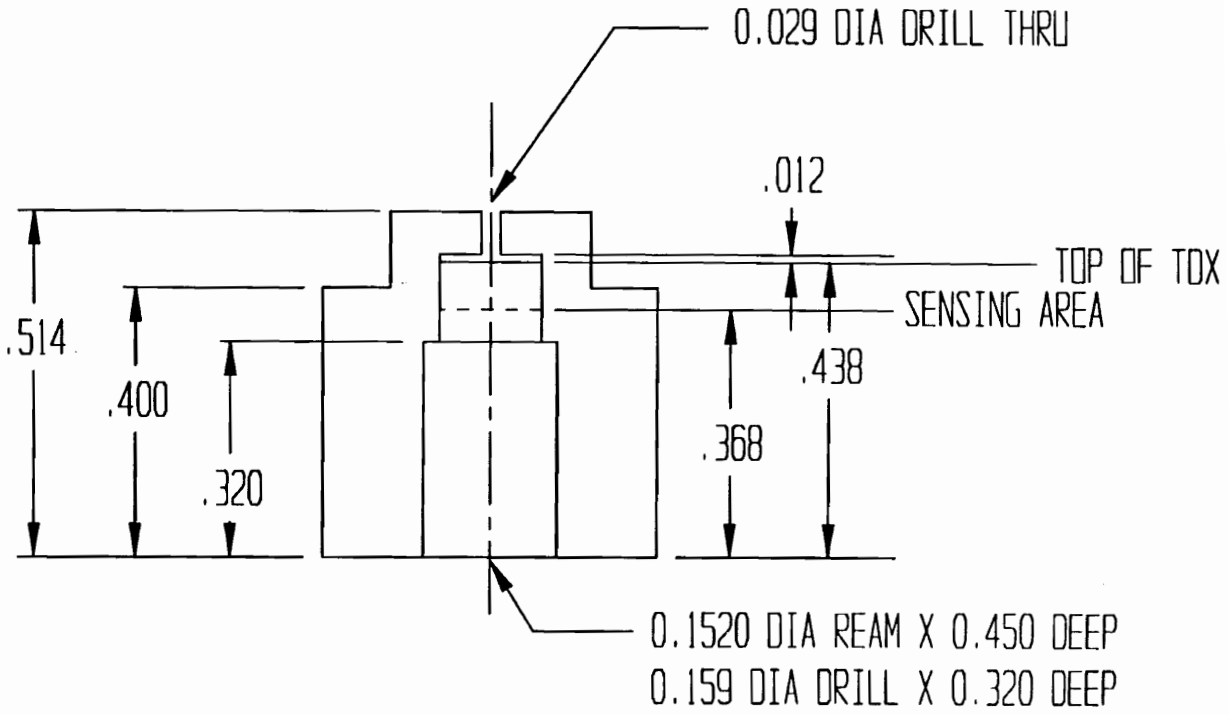

Figure 7. Pin-Hole Adaptor for ENDEVCO 8510B-2 Miniature Pressure Transducer.

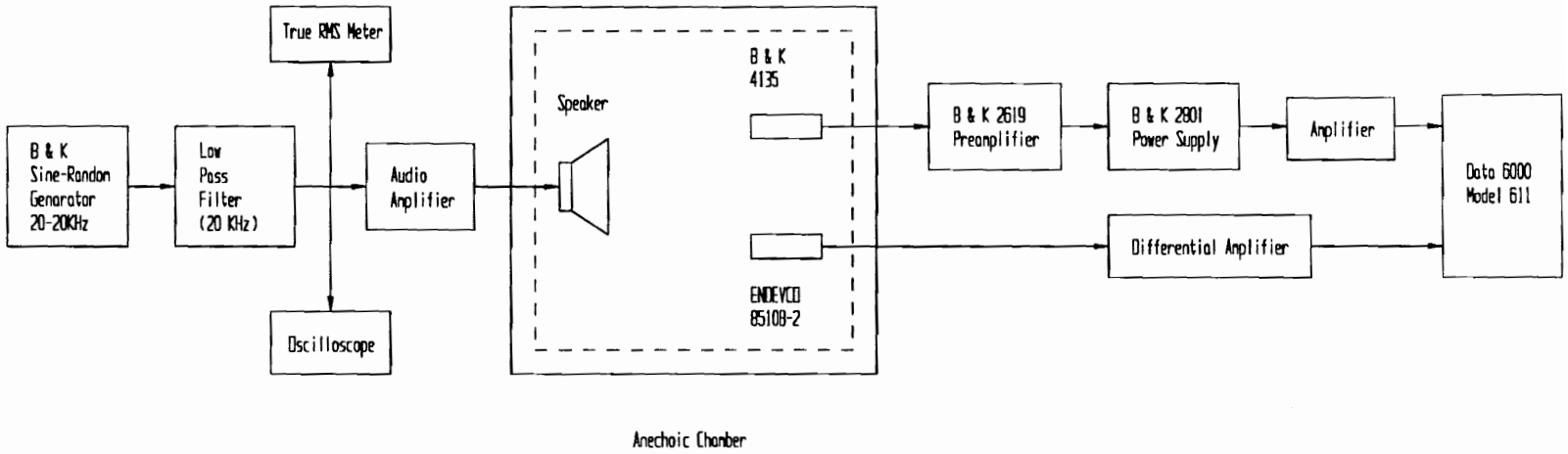

Figure 8. Pressure Transducer Dynamic Calibration Set-up.

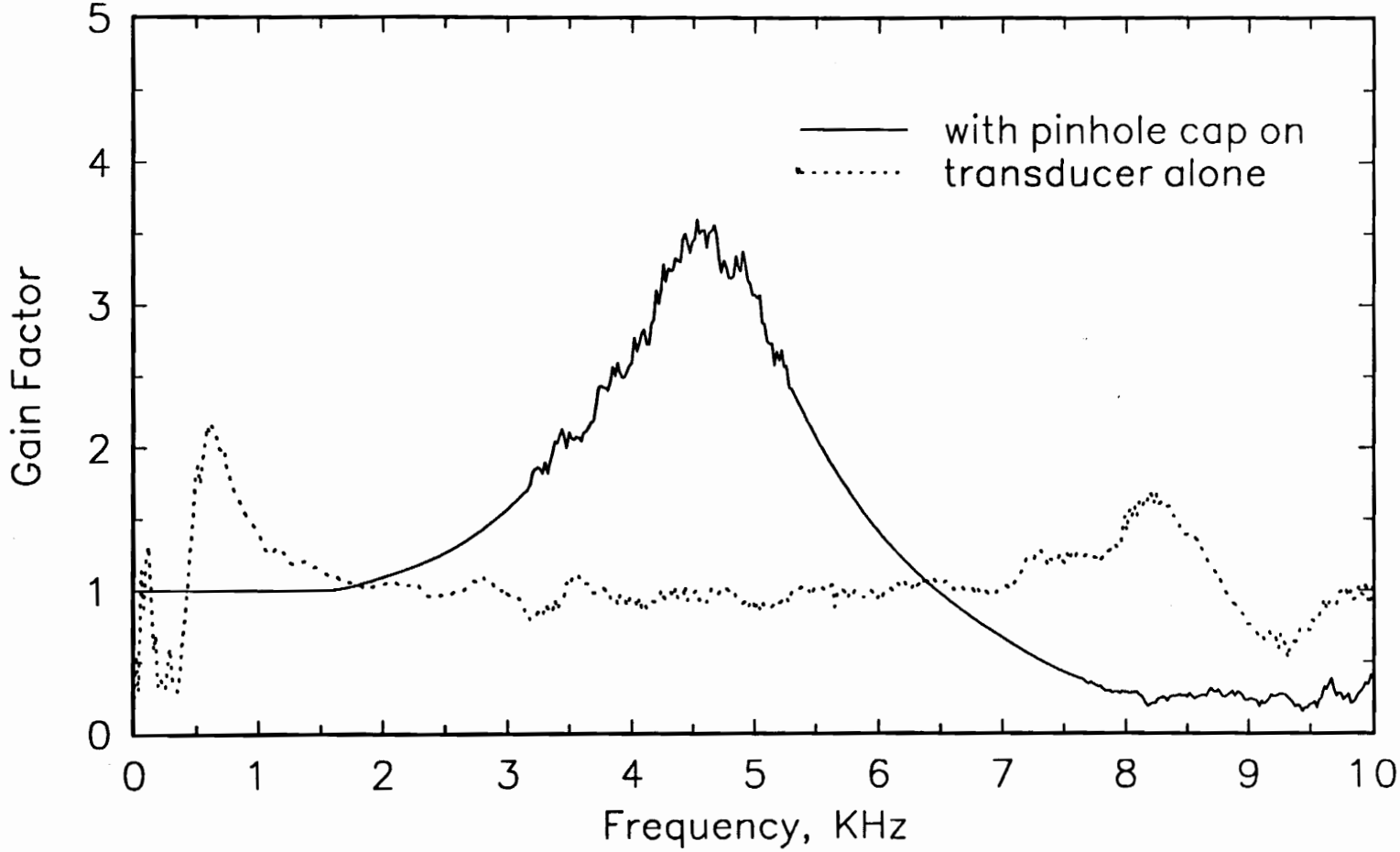

Figure 9. Typical Transducer Transfer Function.

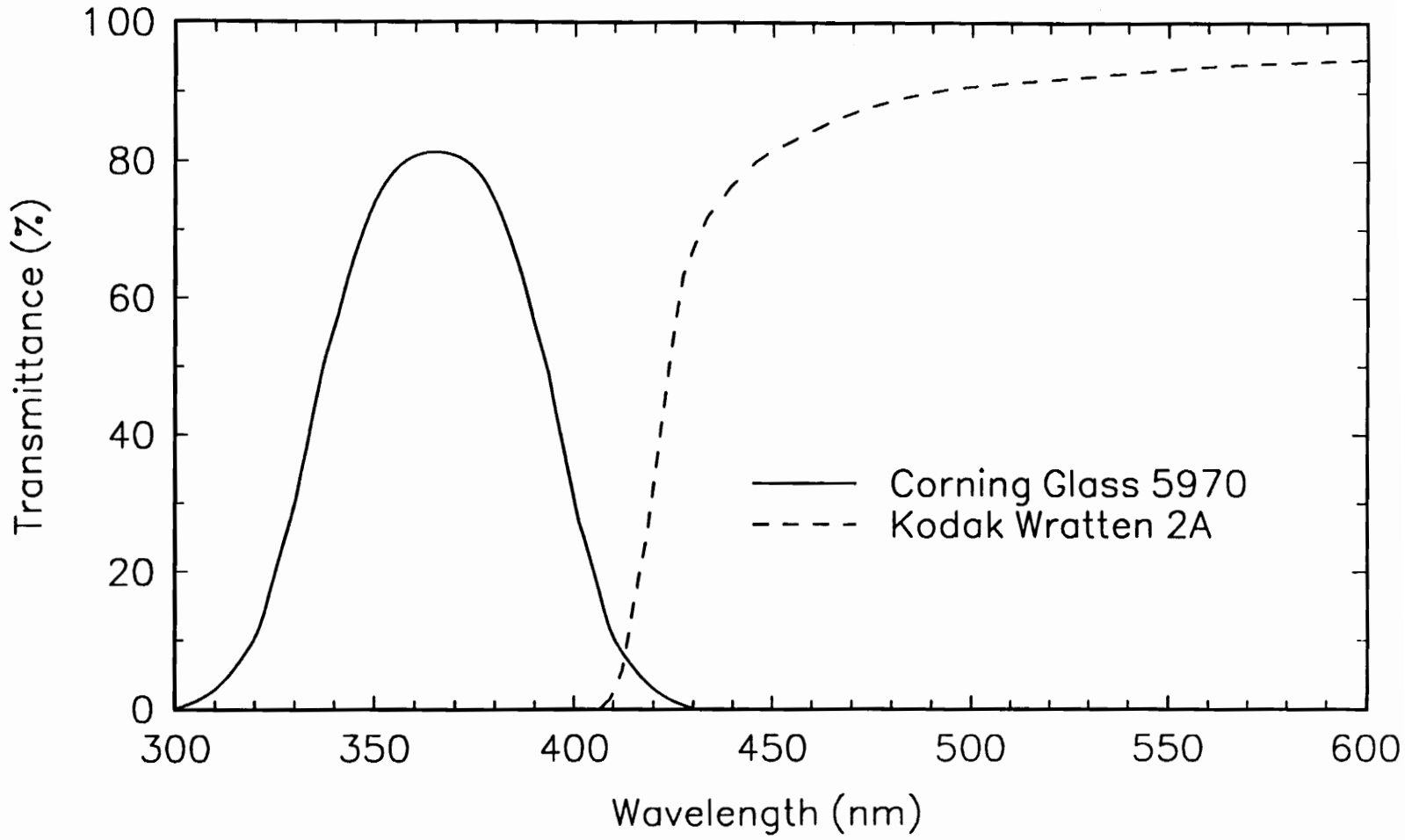

Figure 10. Optical Filter Characteristics.

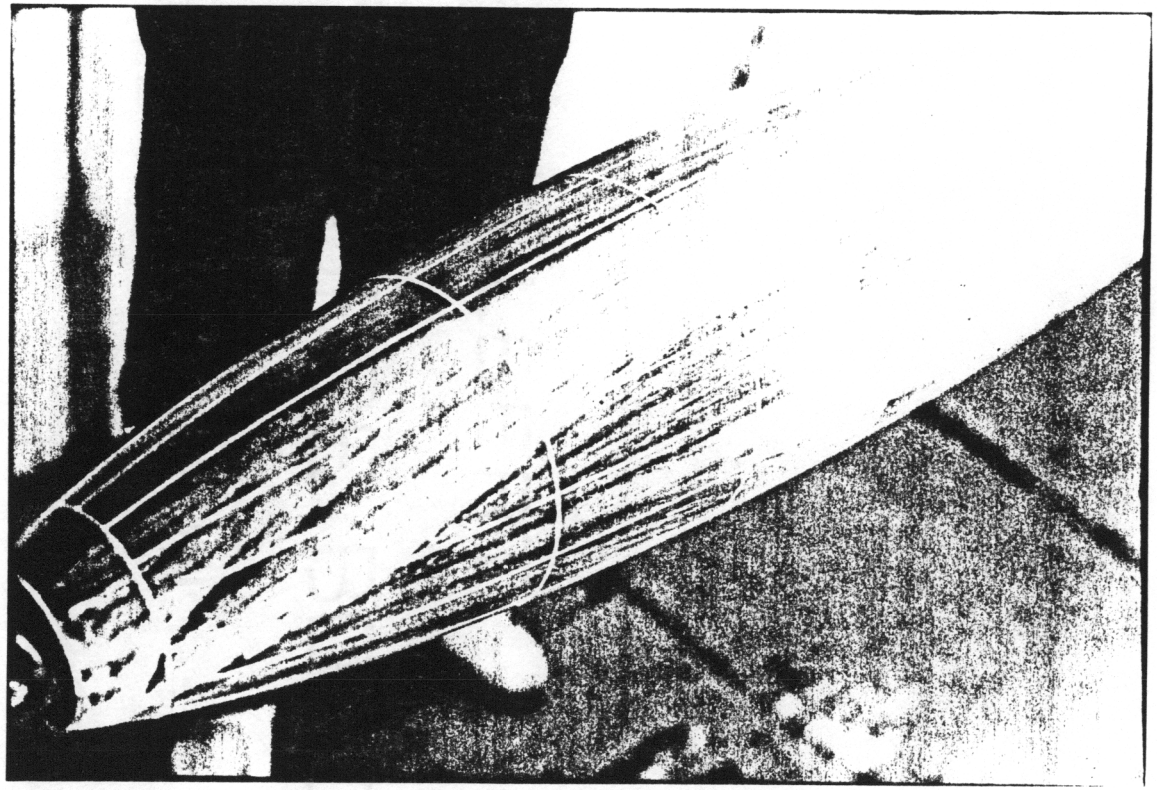

Figure 11. Oil-Flow Pattern at $\alpha = 5$ deg., $Re_L = 4.20 \times 10^6$.

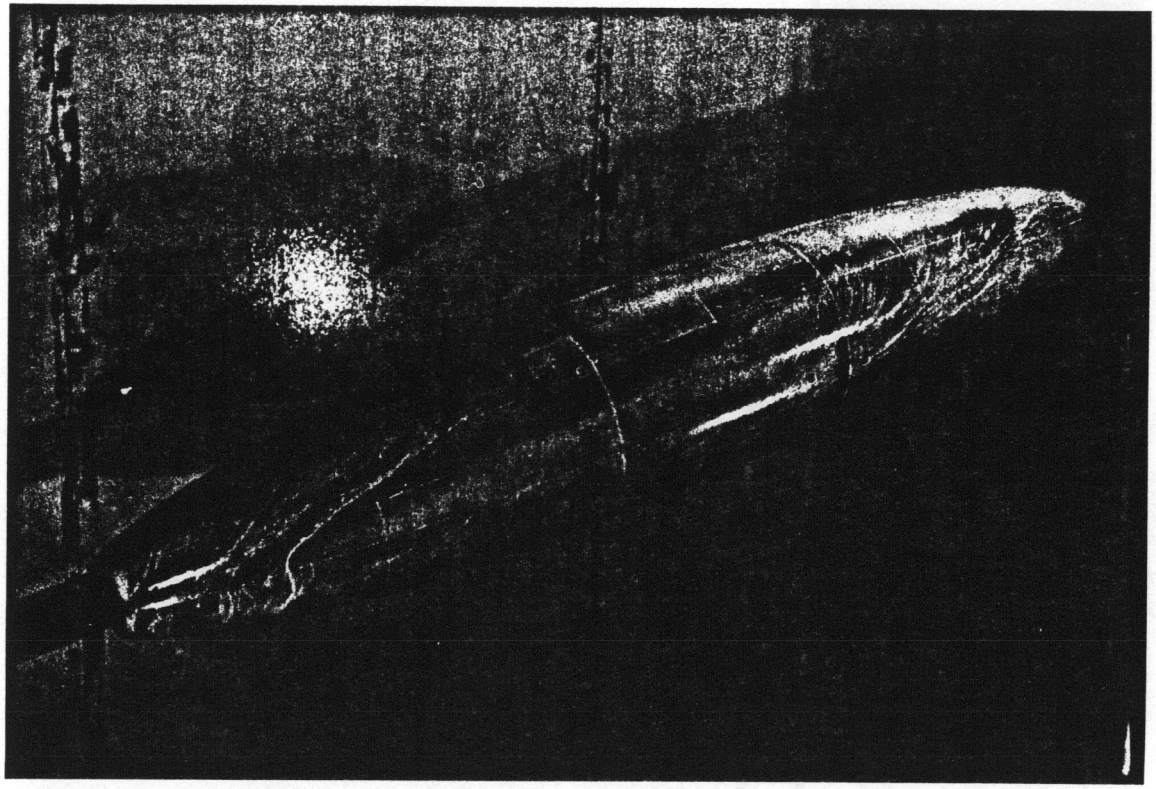

Figure 12. Oil-Flow Pattern at $\alpha = 10$ deg., $Re_L = 2.08 \times 10^6$.

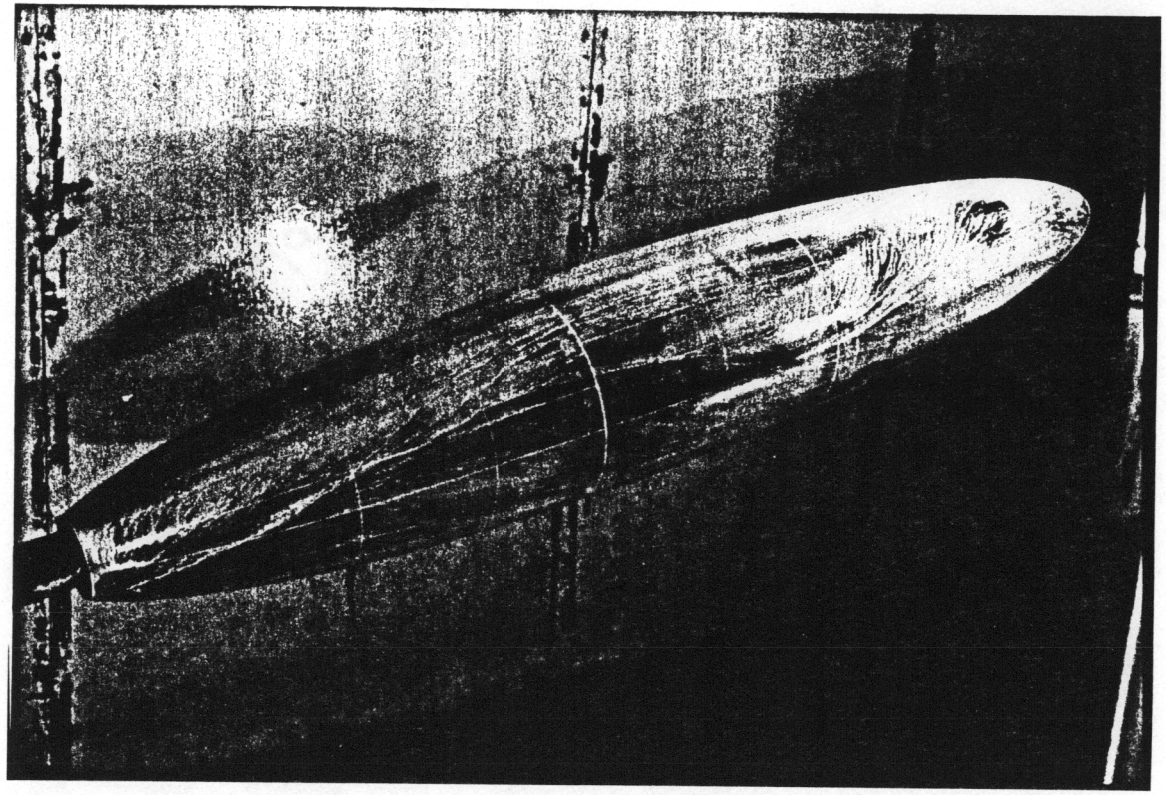

Figure 13. Oil-Flow Pattern at $\alpha = 10$ deg., $Re_L = 2.85 \times 10^6$.

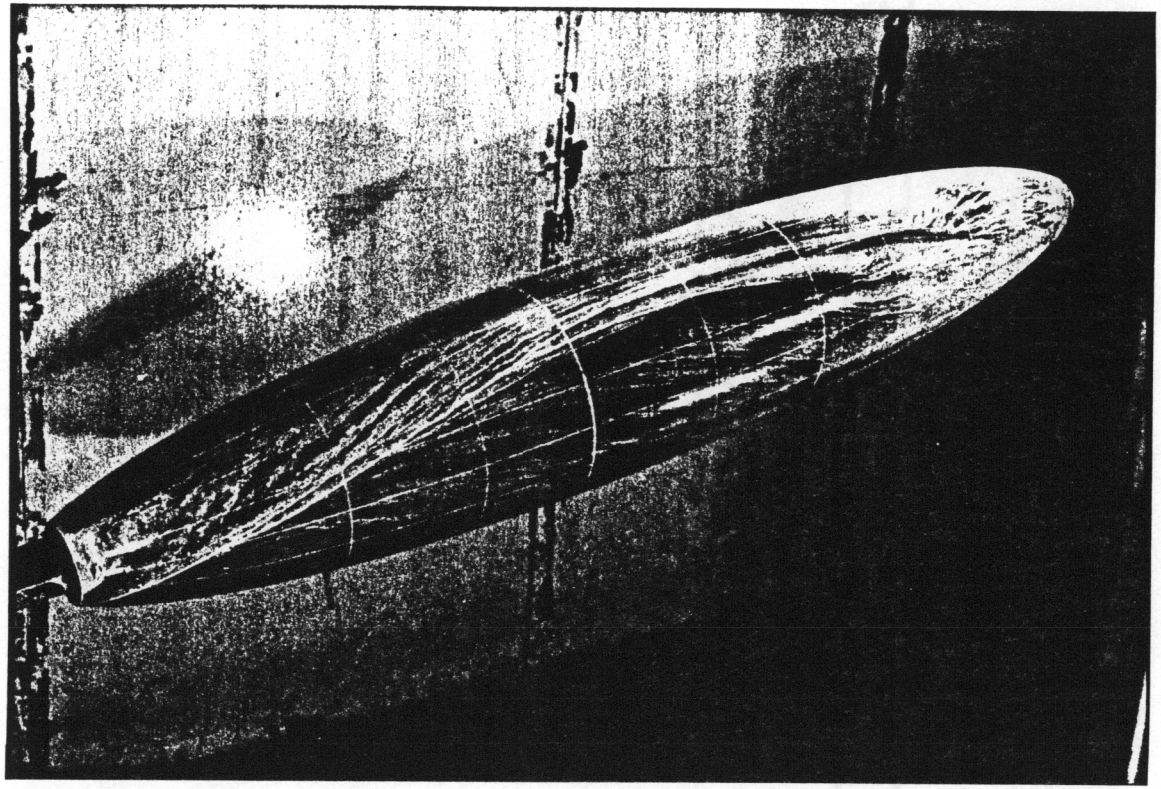

Figure 14. Oil-Flow Pattern at $\alpha = 10$ deg., $Re_L = 3.45 \times 10^6$.

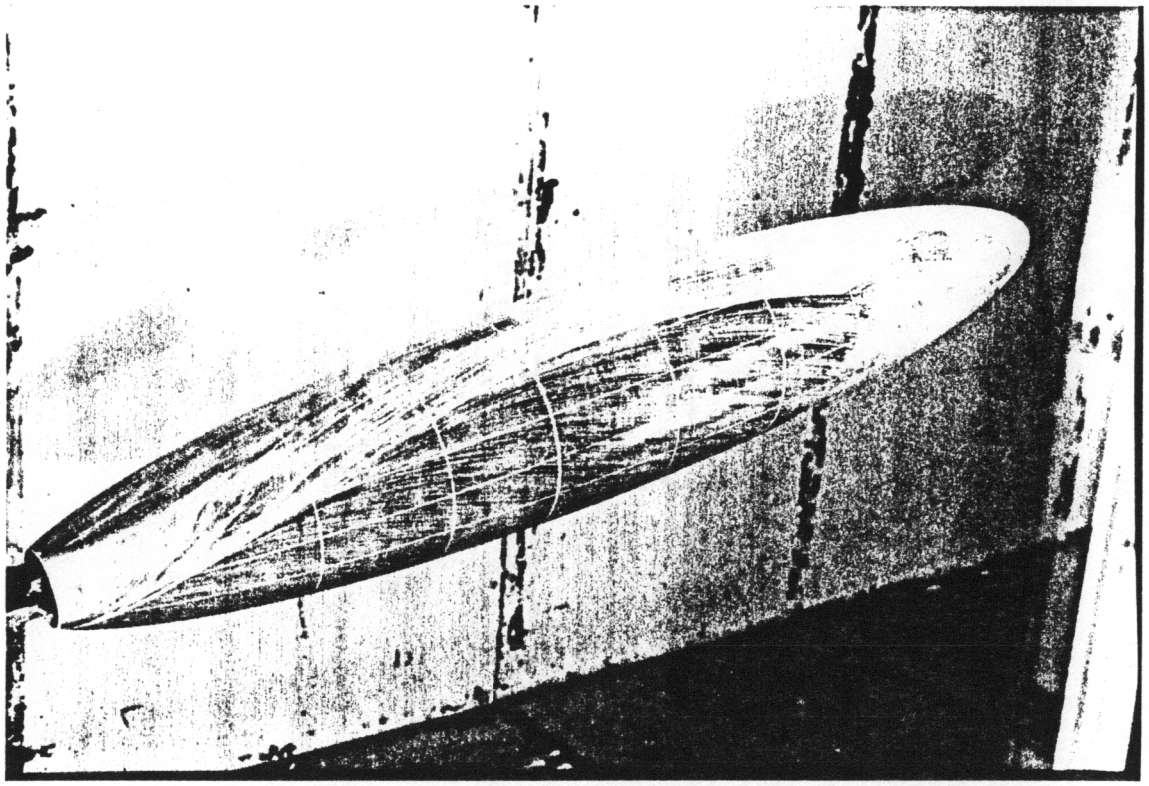

Figure 15. Oil-Flow Pattern at $\alpha = 10$ deg., $Re_L = 4.20 \times 10^6$.

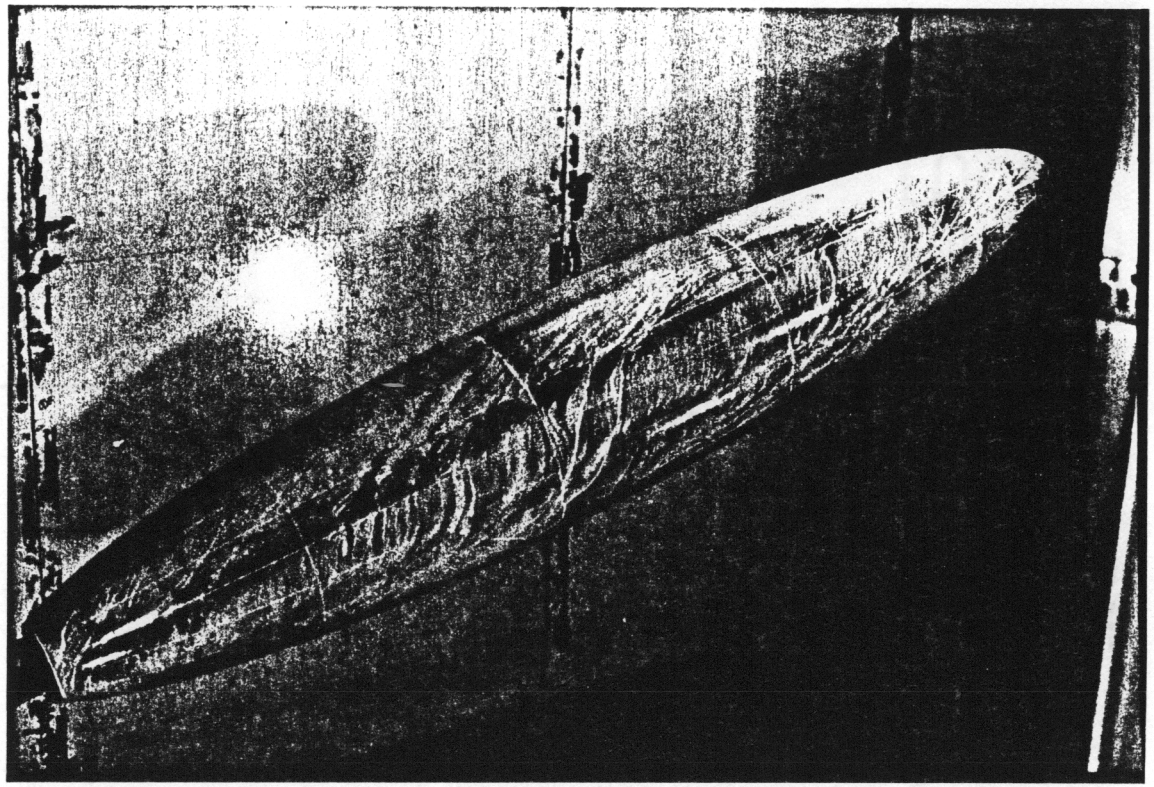

Figure 16. Oil-Flow Pattern at $\alpha = 15$ deg., $Re_L = 1.39 \times 10^6$.

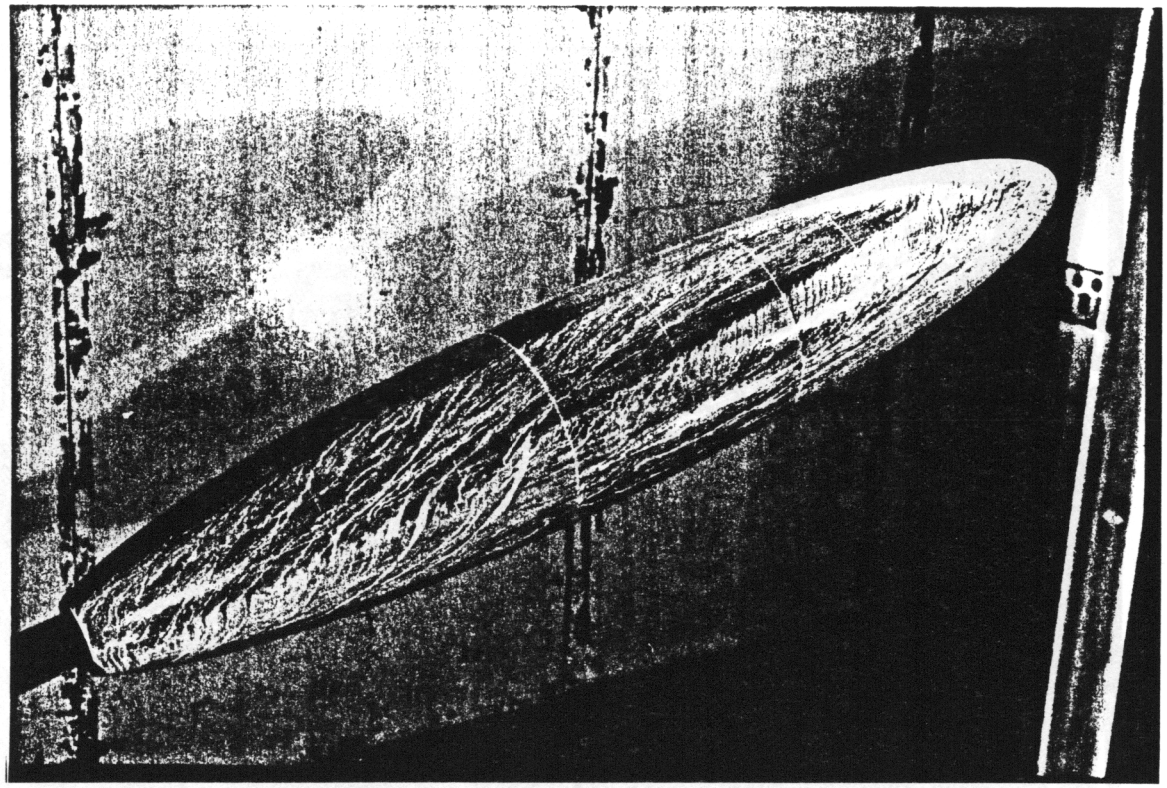

Figure 17. Oil-Flow Pattern at $\alpha = 15$ deg., $Re_L = 2.08 \times 10^6$.

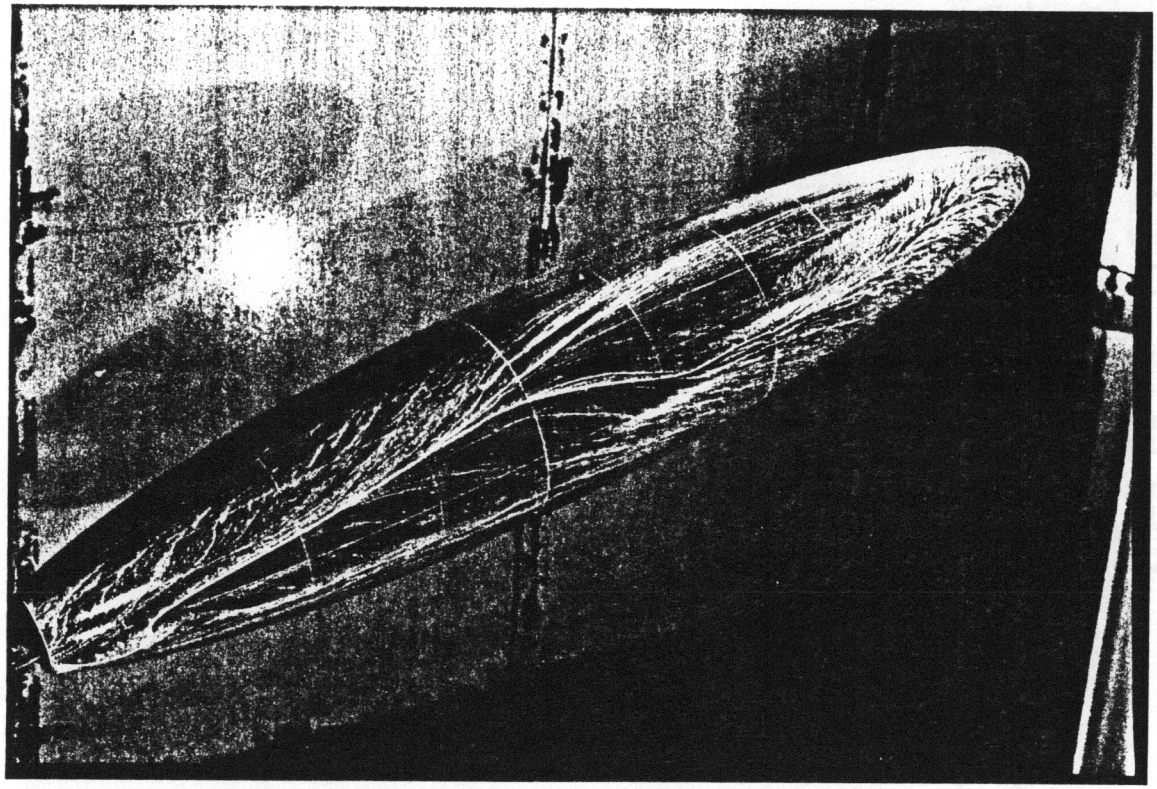

Figure 18. Oil-Flow Pattern at $\alpha = 15$ deg., $Re_L = 2.85 \times 10^6$.

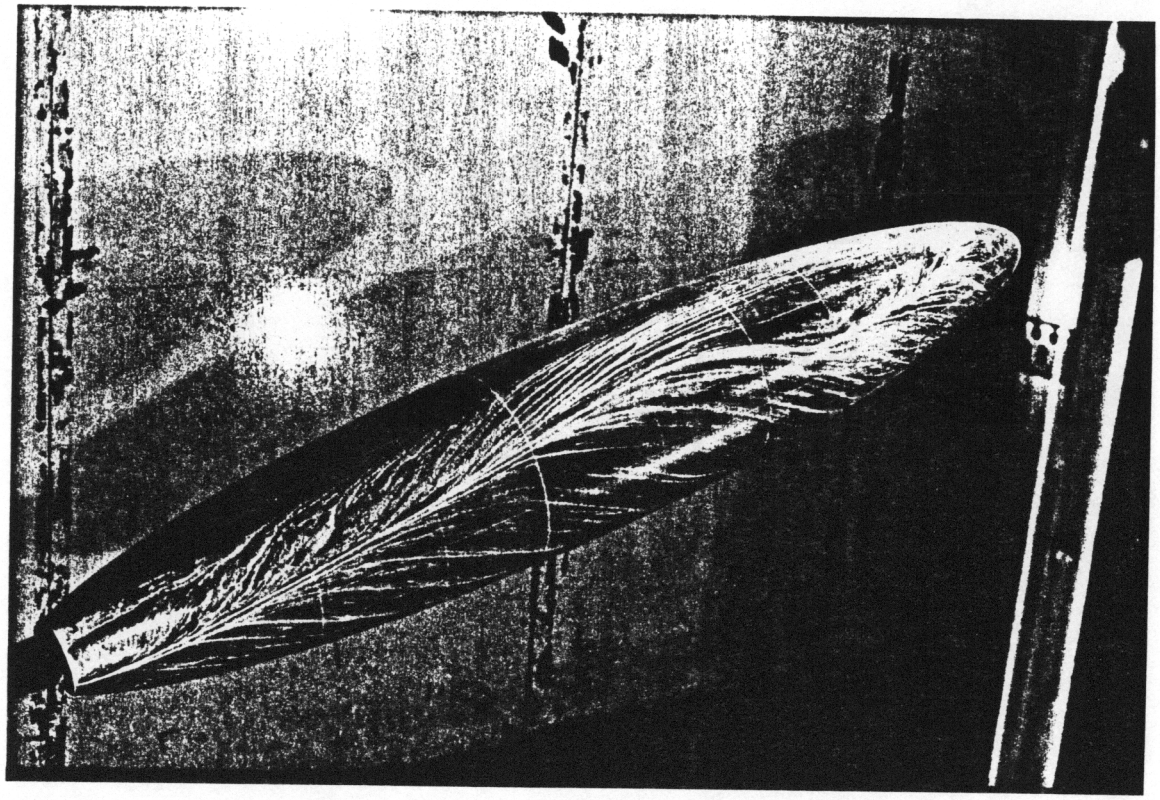

Figure 19. Oil-Flow Pattern at $\alpha = 15$ deg., $Re_L = 3.45 \times 10^6$.

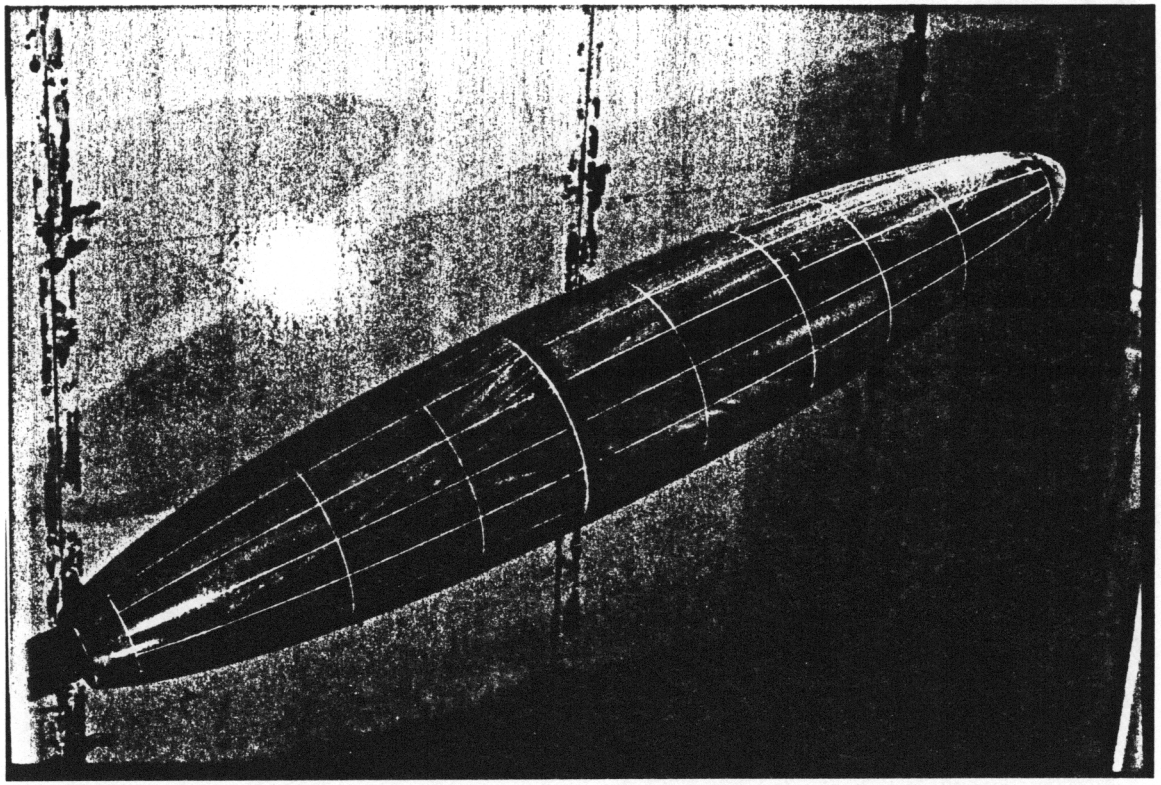

Figure 20. Oil-Flow Pattern at $\alpha = 15$ deg., $Re_L = 4.20 \times 10^6$.

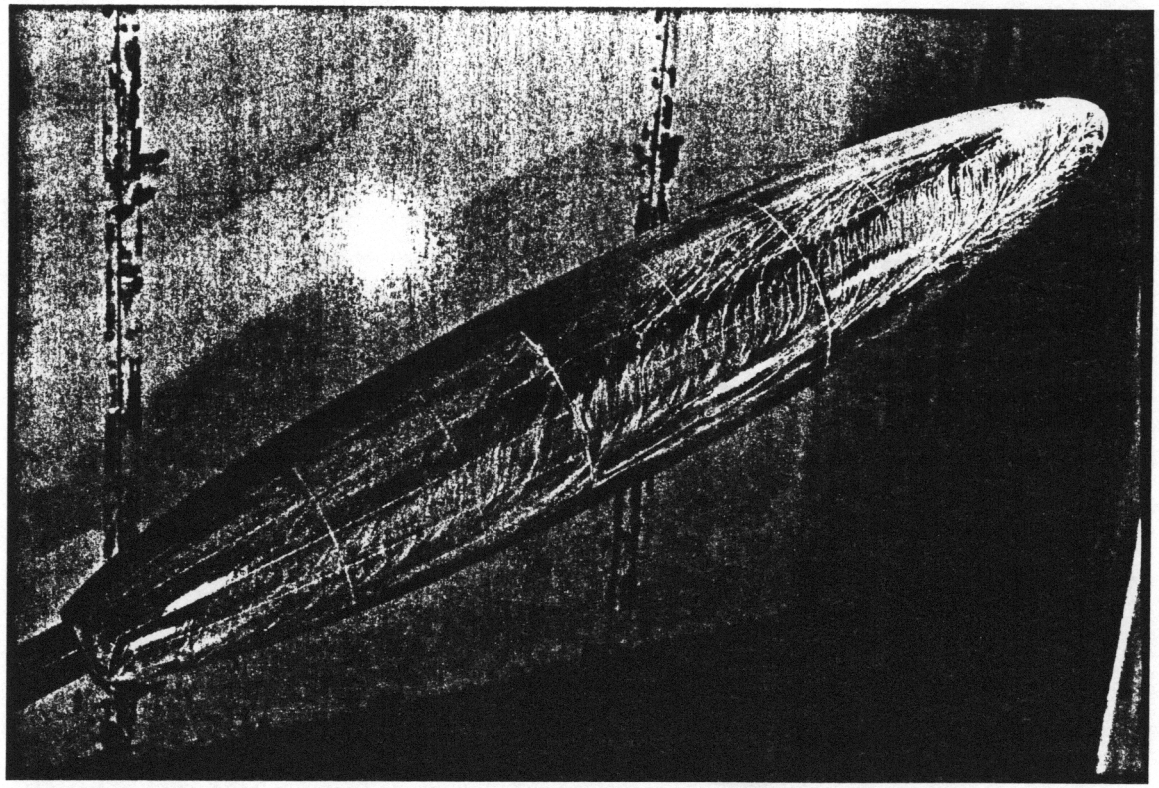

Figure 21. Oil-Flow Pattern at $\alpha = 20$ deg., $Re_L = 1.39 \times 10^6$.

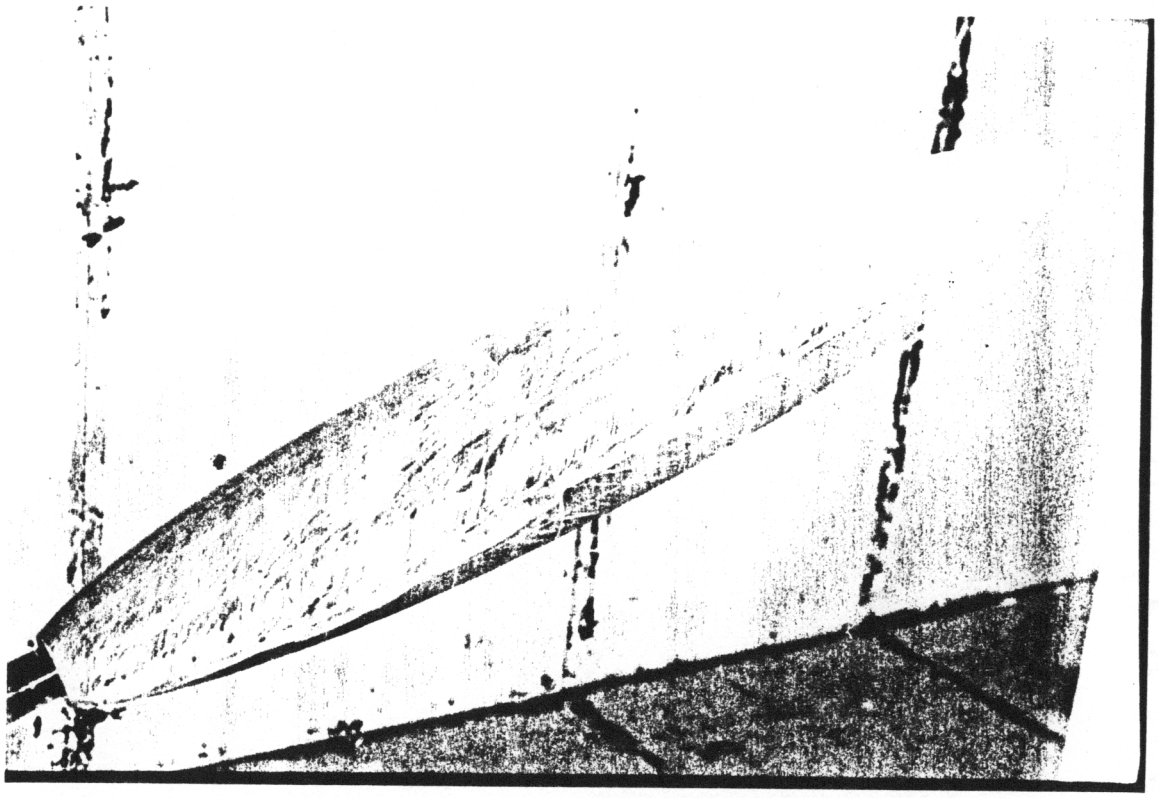

Figure 22. Oil-Flow Pattern at $\alpha = 20$ deg., $Re_L = 2.08 \times 10^6$.

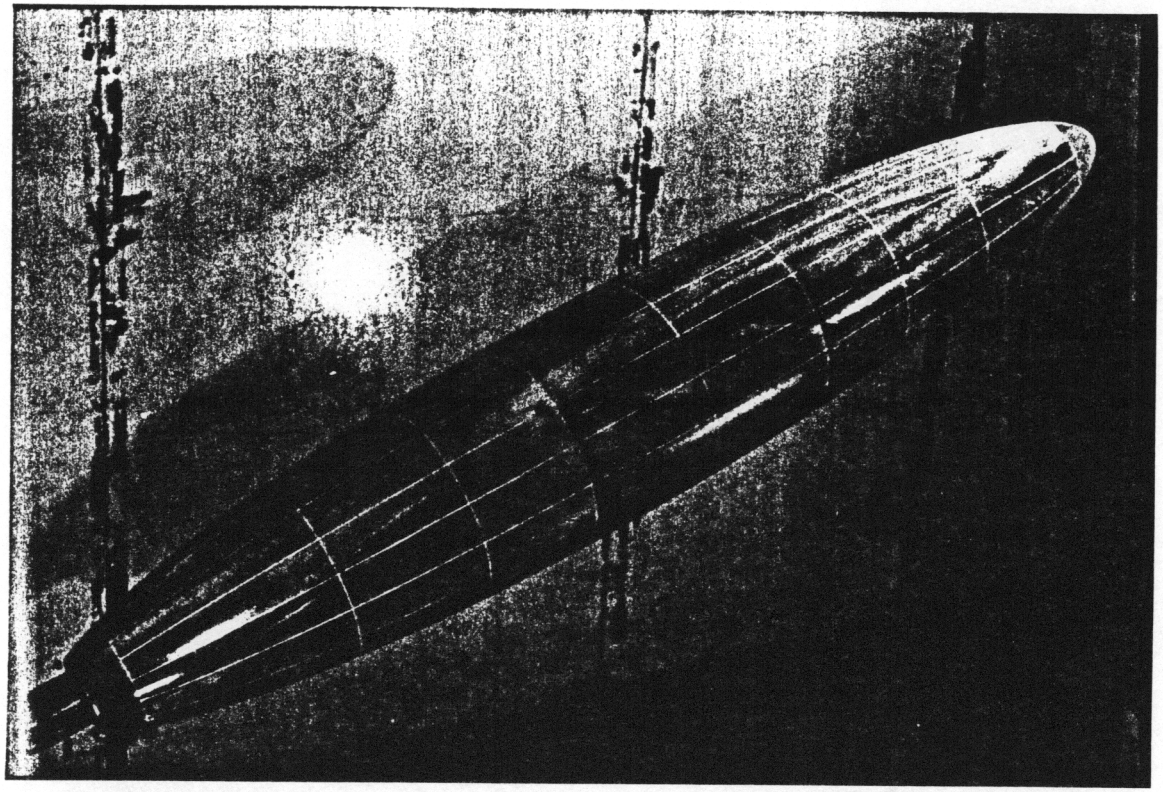

Figure 23. Oil-Flow Pattern at $\alpha = 20$ deg., $Re_L = 2.85 \times 10^6$.

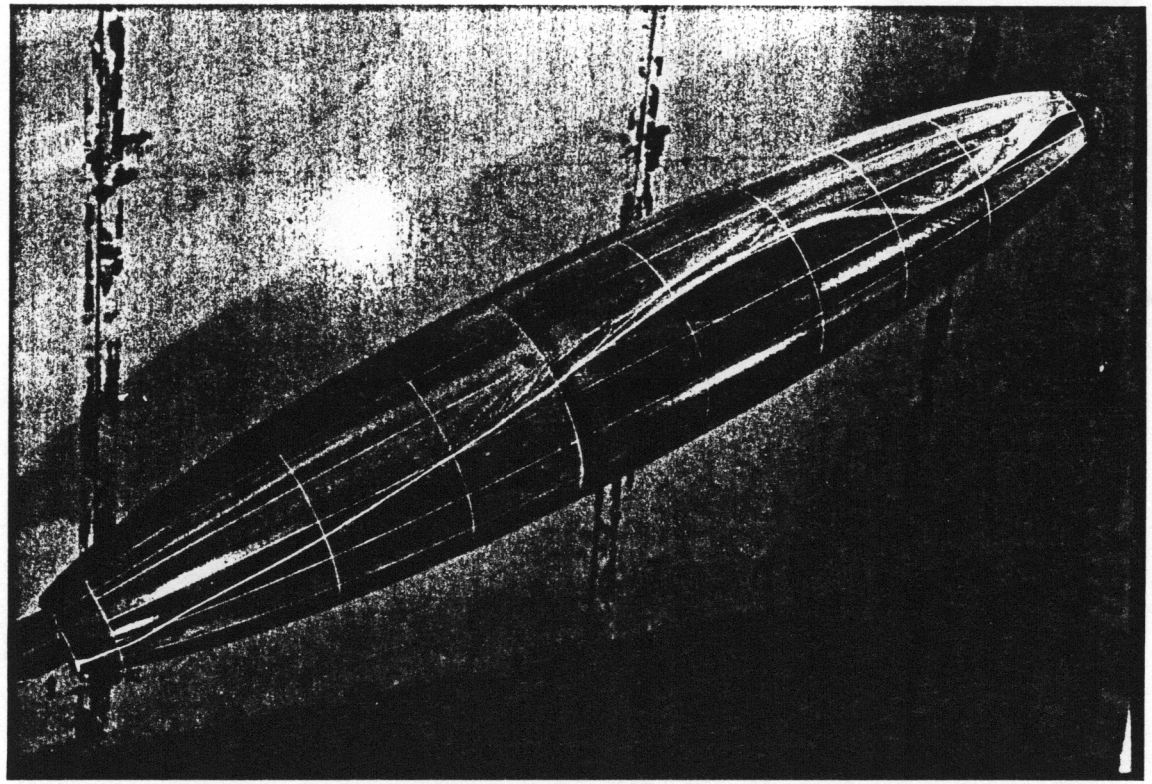

Figure 24. Oil-Flow Pattern at $\alpha = 20$ deg., $Re_L = 3.45 \times 10^6$.

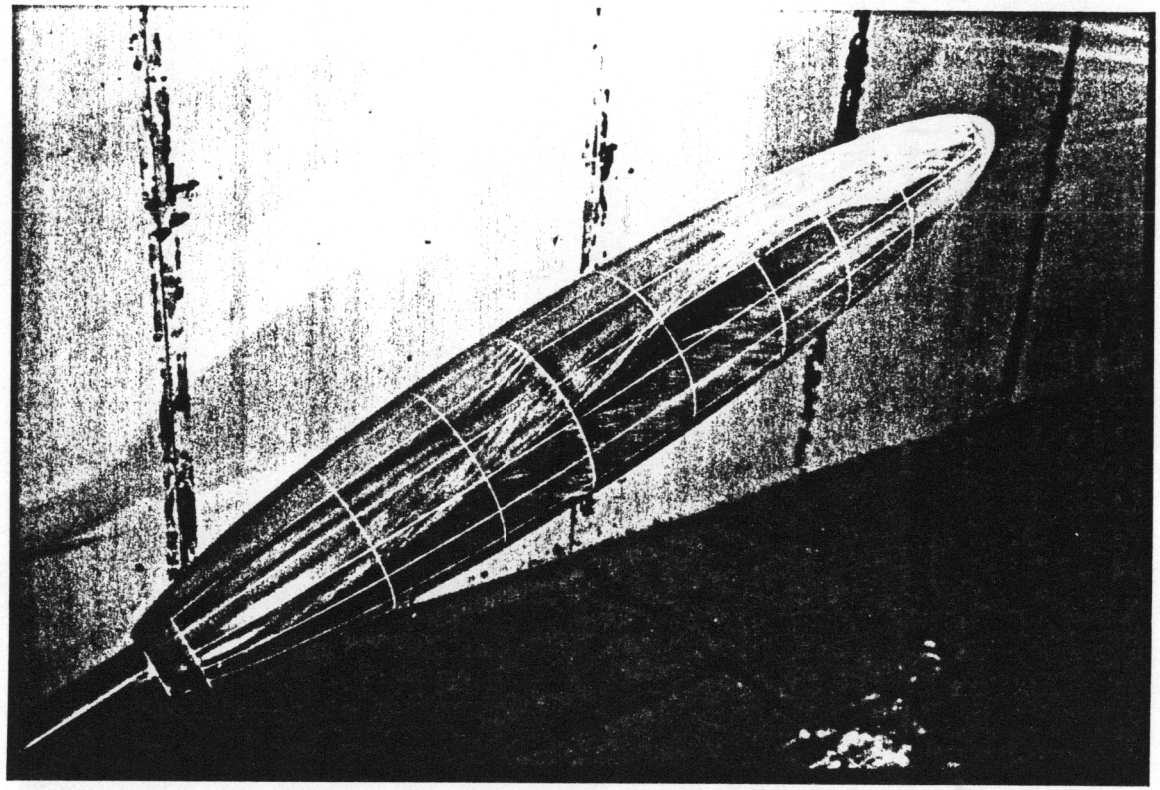

Figure 25. Oil-Flow Pattern at $\alpha = 20$ deg., $Re_L = 4.20 \times 10^6$.

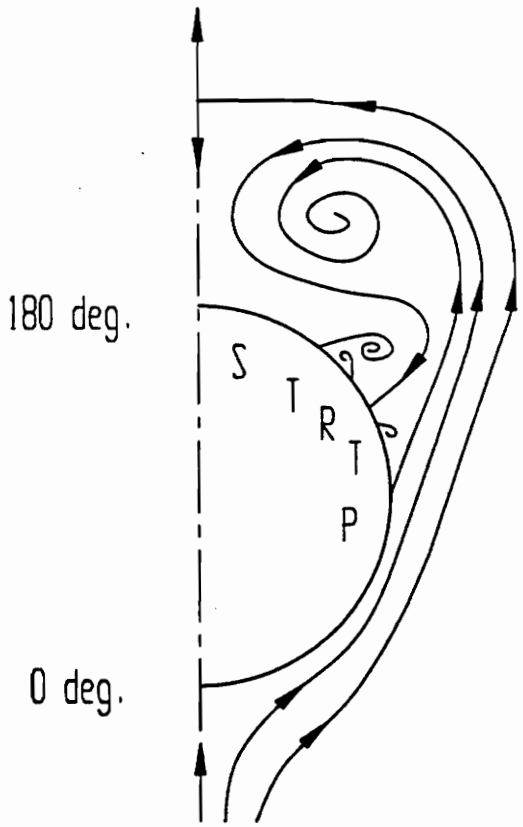

Figure 26. Topological Structure of the After Body Separation.

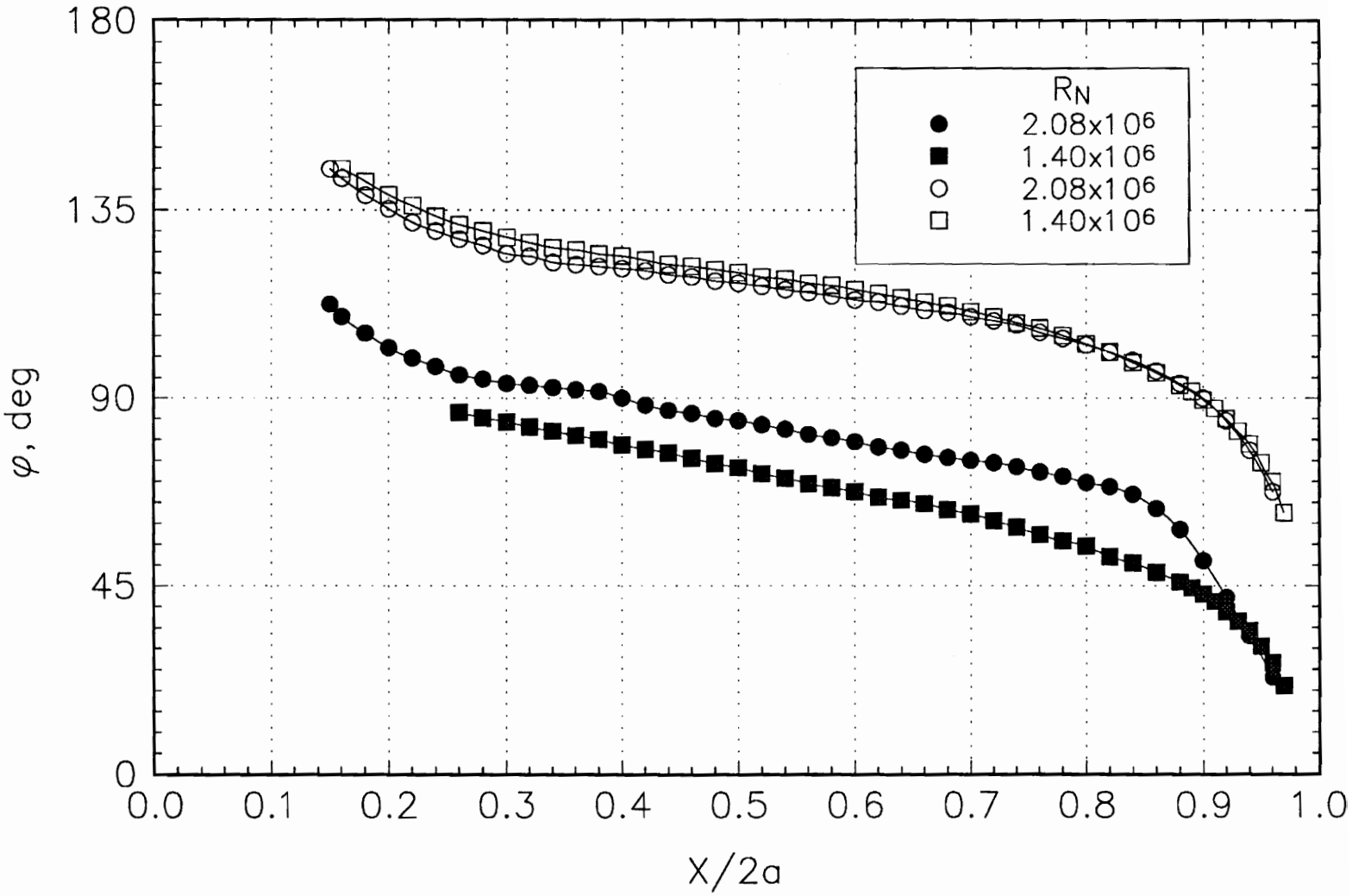

Figure 27. Primary and Secondary Separation Lines at Subcritical Reynolds Numbers , $\alpha = 20$ degrees. Closed Symbols Denote Laminar Separation and Open Symbols Denote Turbulent Separation.

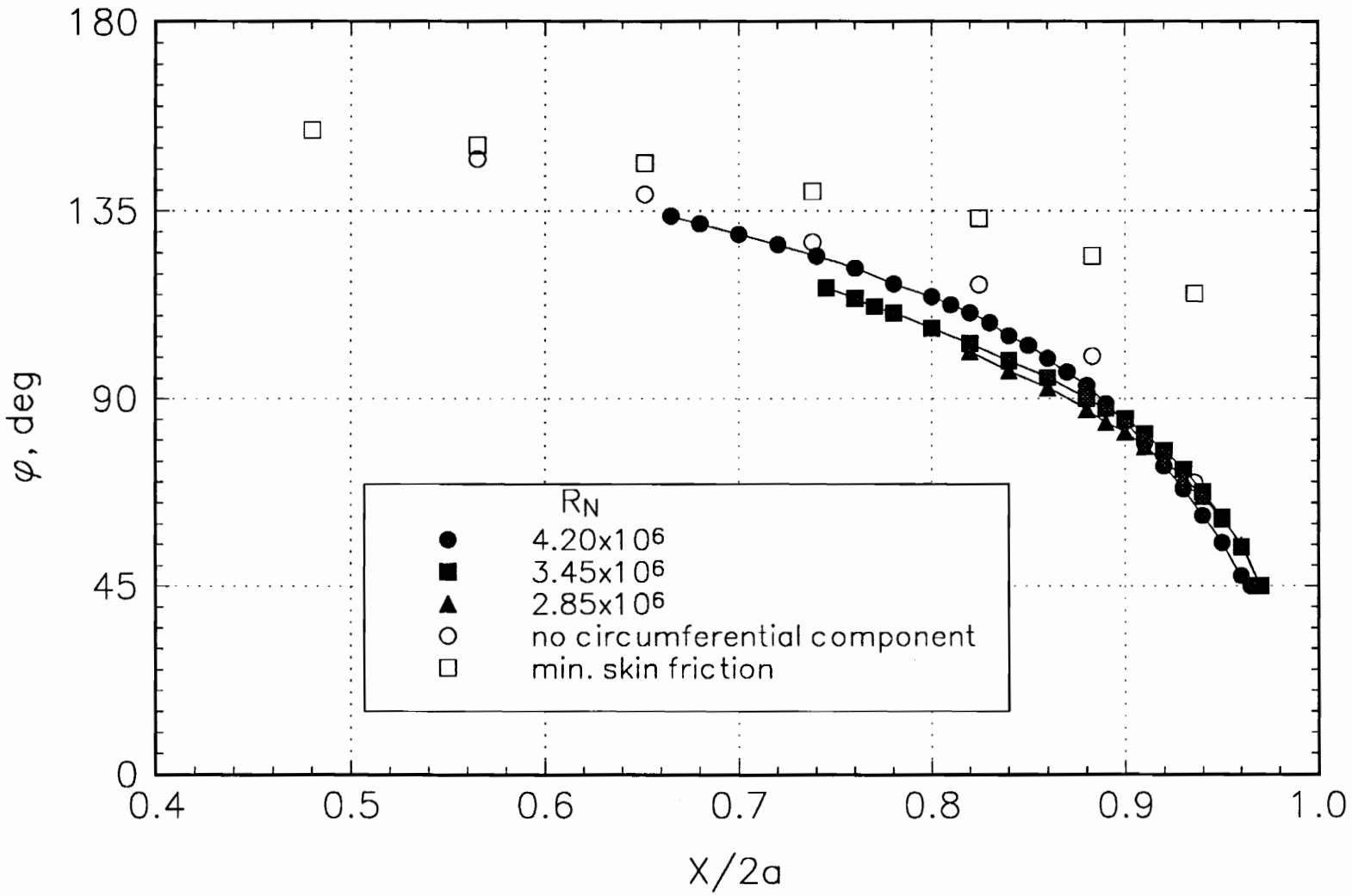

Figure 28. Primary Separation Lines at Different Reynolds Numbers, $\alpha = 10$ degree. Open Symbols are from Skin Friction Measurement of Meier, *et al* (1983).

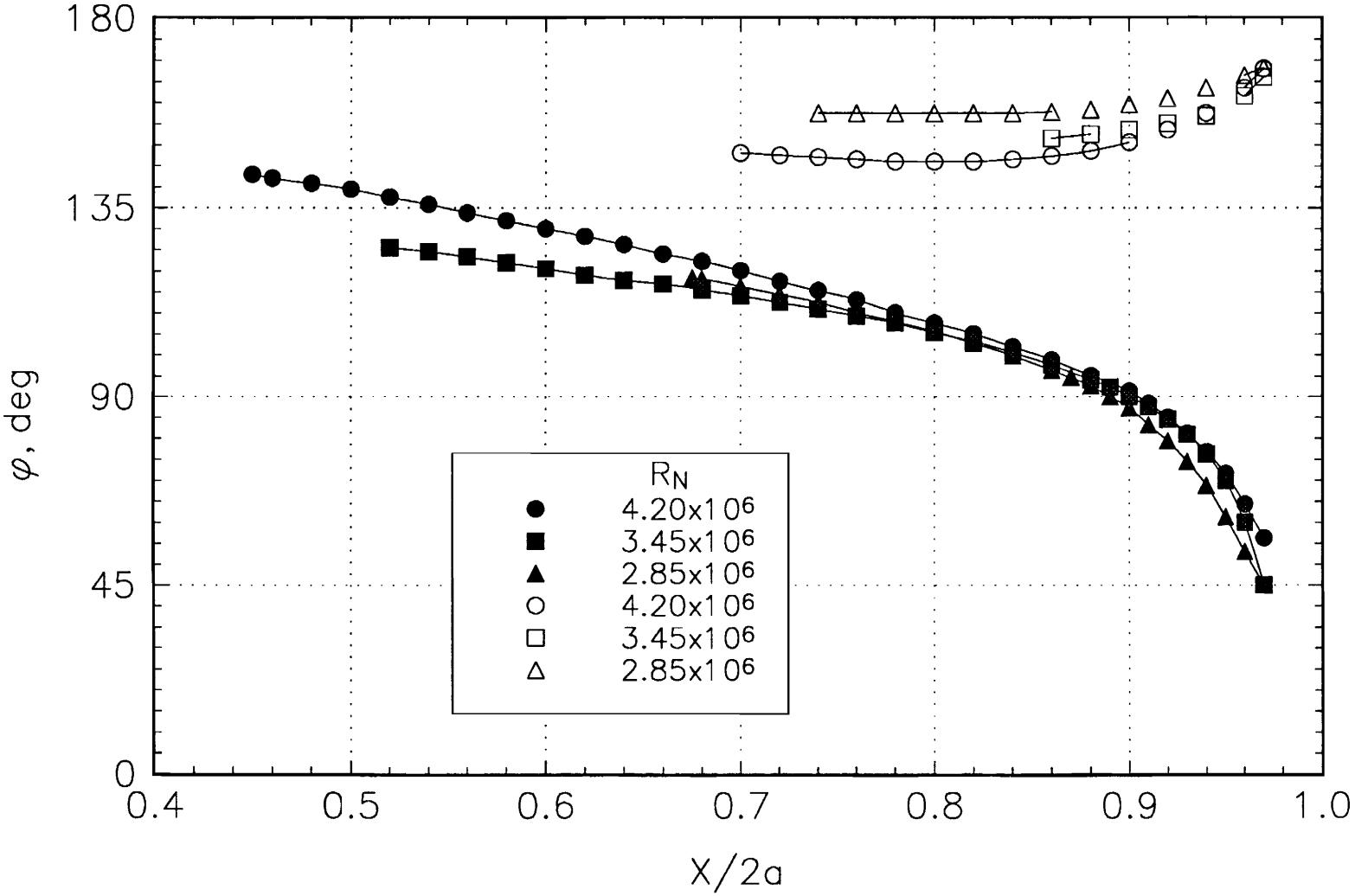

Figure 29. Primary Separation Lines at Different Reynolds Numbers at $\alpha = 15$ degrees. Closed Symbols Denote Primary Separation and Open Symbols Denote Secondary Separation.

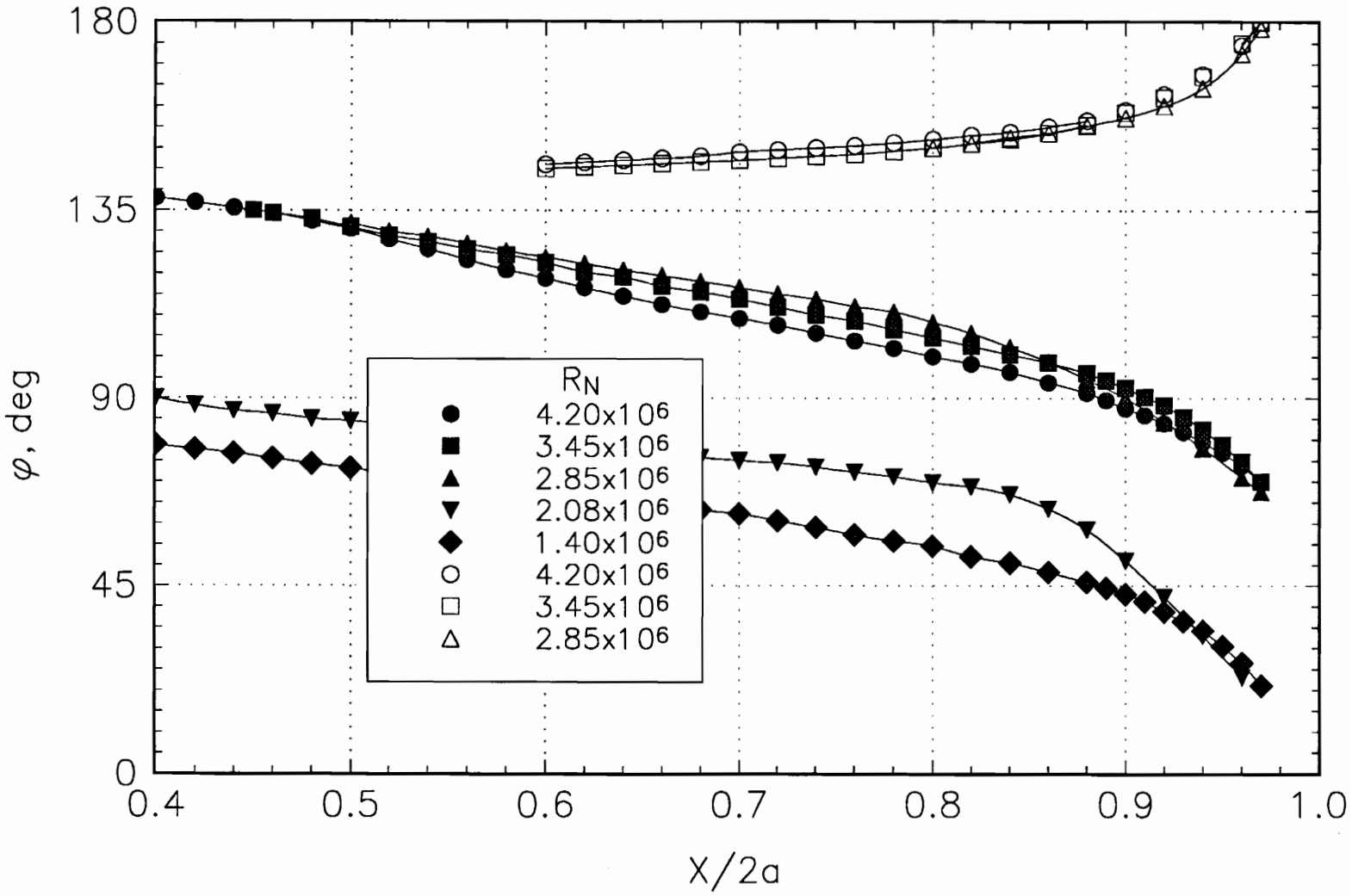

Figure 30. Primary Separation Lines at Different Reynolds Numbers at $\alpha = 20$ degrees. Closed Symbols Denote Primary Separation and Open Symbols Denote Secondary Separation.

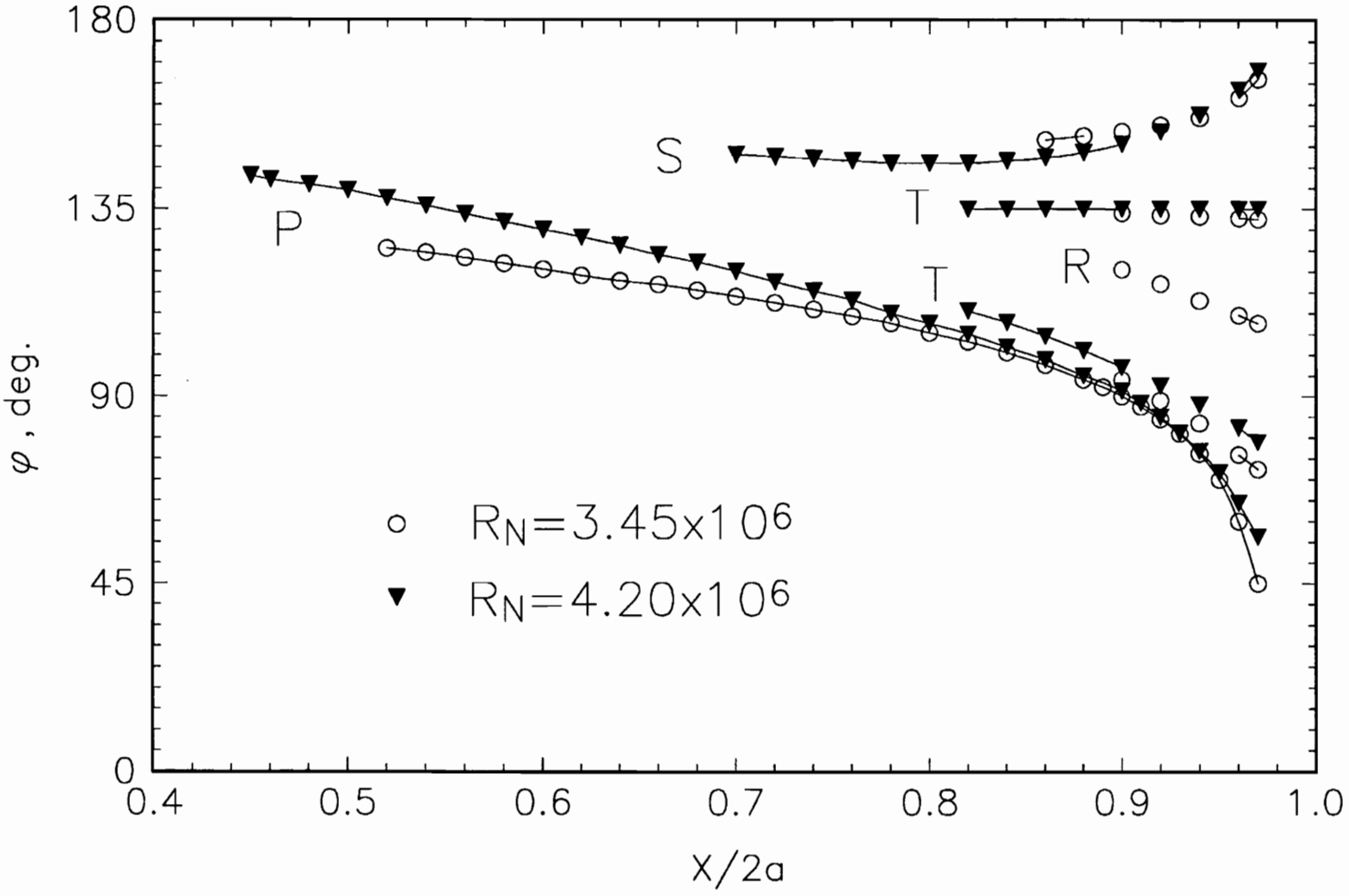

Figure 31. Afterbody Separation Lines at $\alpha = 15$ degrees. P-Primary Separation, S-Secondary Separation, T-Tertiary Separation, R-Reattachment.

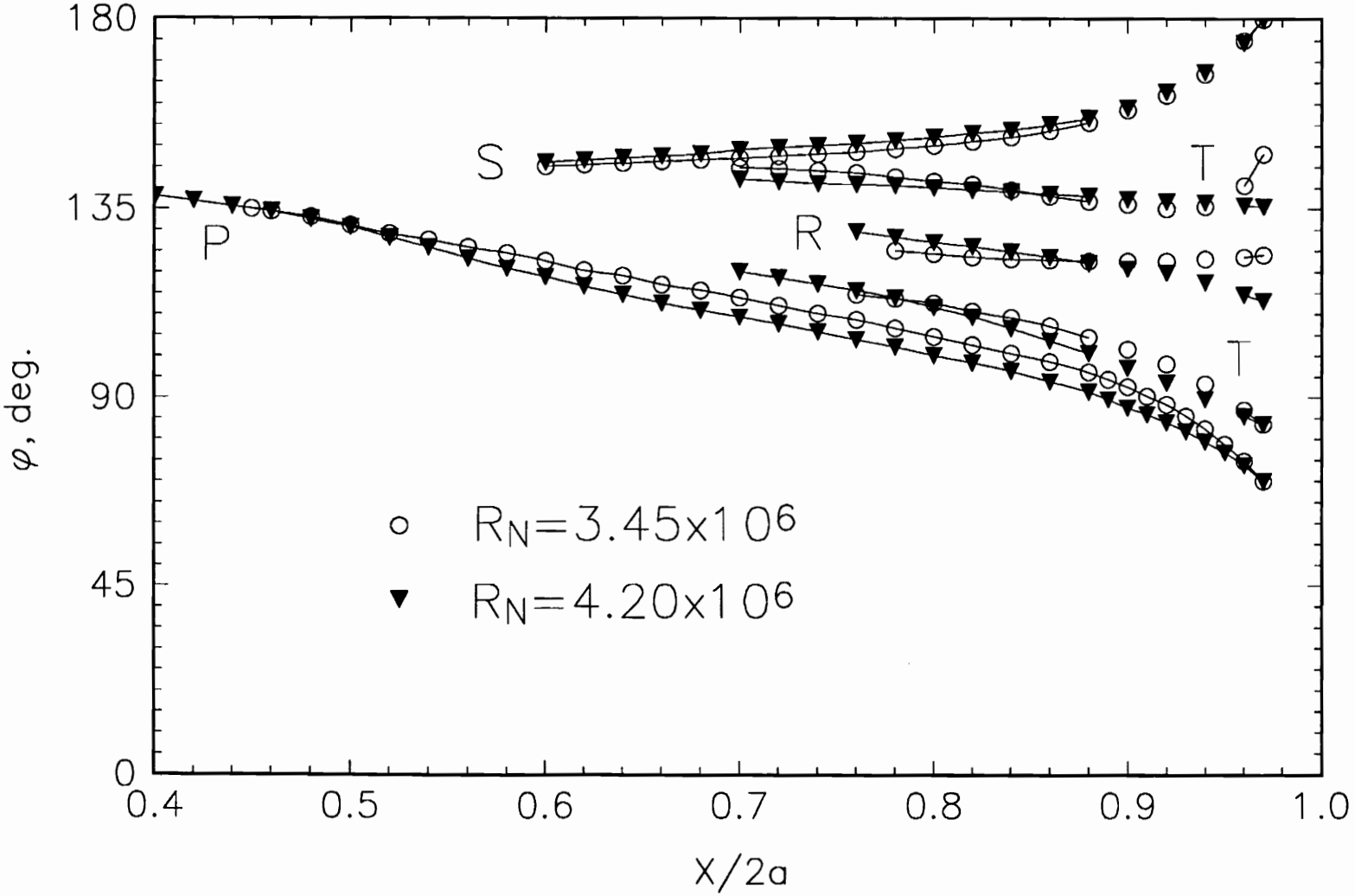

Figure 32. Afterbody Separation Lines at $\alpha = 20$ degrees. P-Primary Separation, S-Secondary Separation, T-tertiary Separation, R-Reattachment.

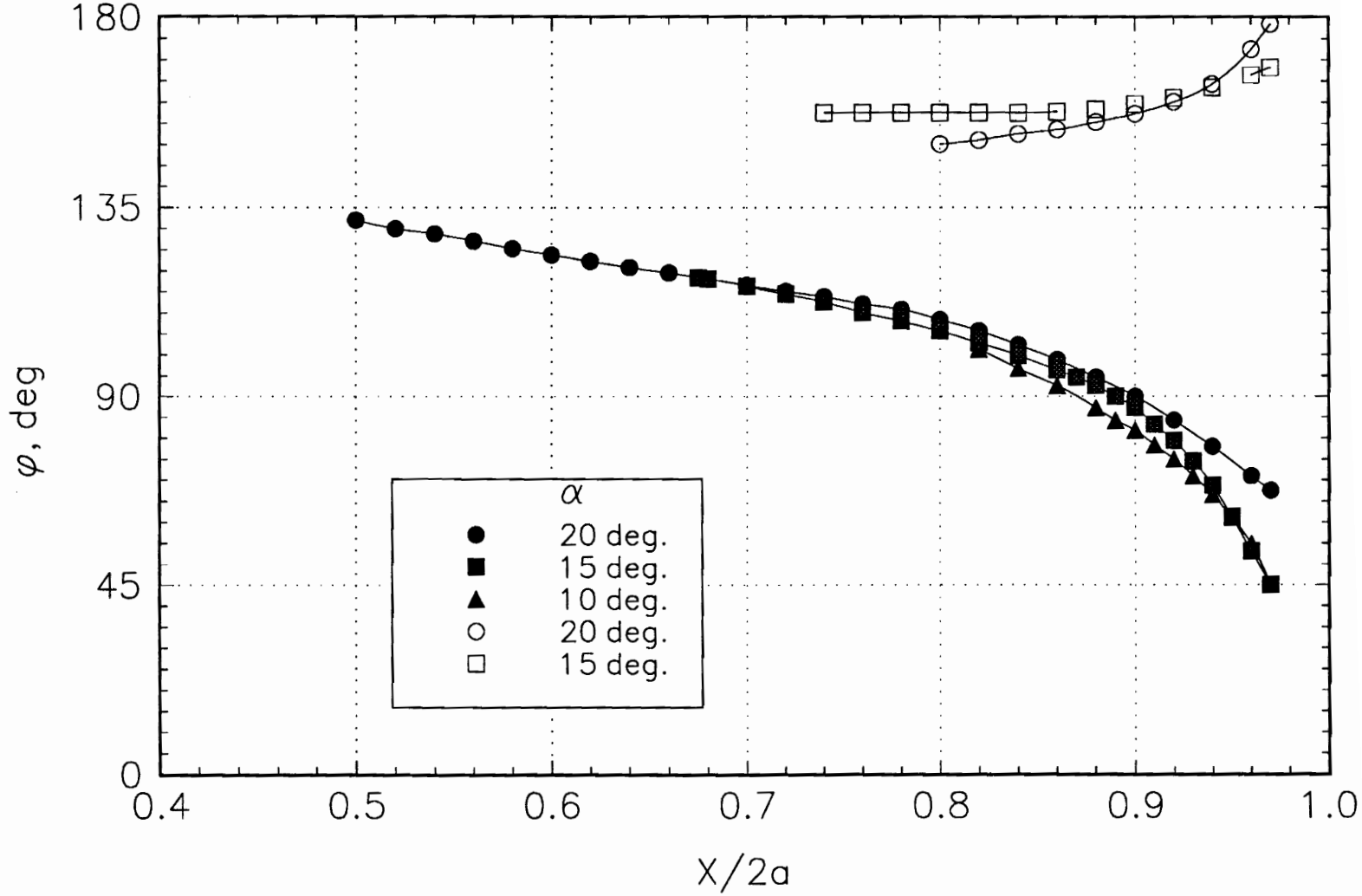

Figure 33. Separation Lines at Different Angles of Attack, $R_N = 2.85 \times 10^6$. Closed Symbols Denote Primary Separation and Open Symbols Denote Secondary Separation.

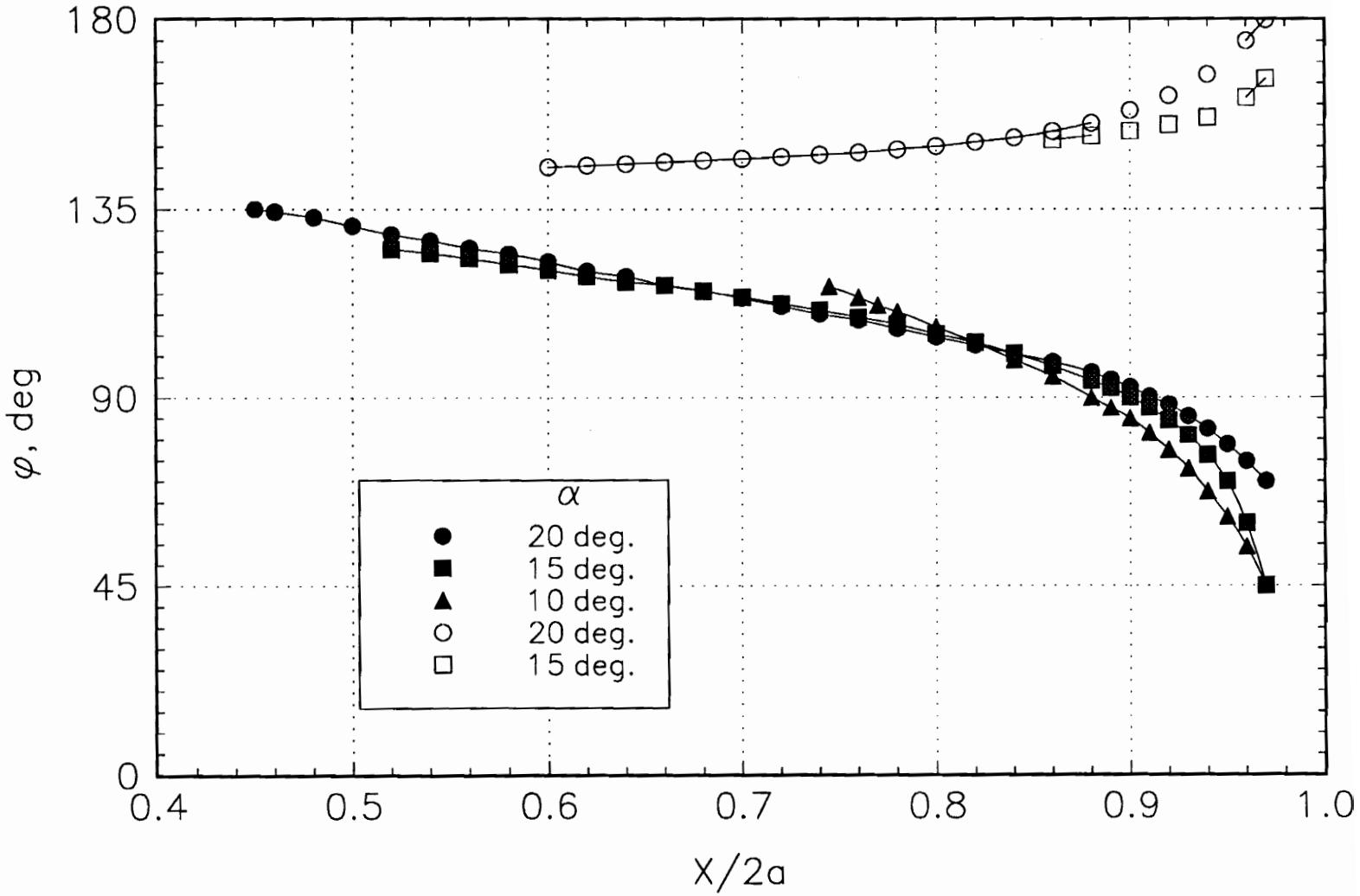

Figure 34. Separation Lines at Different Angles of Attack, $R_N = 3.45 \times 10^6$. Closed Symbols Denote Primary Separation and Open Symbols Denote Secondary Separation.

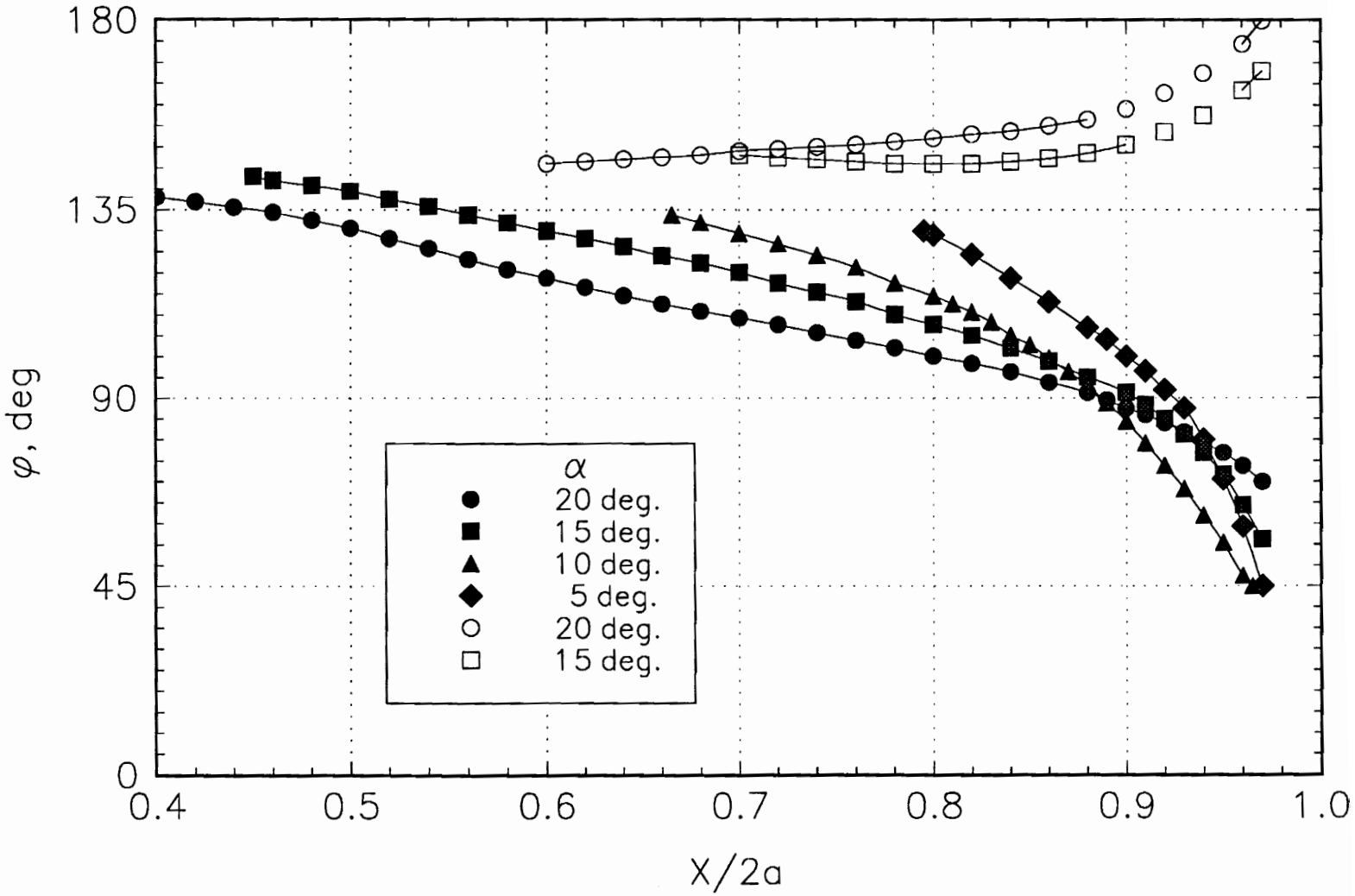

Figure 35. Separation lLnes at Different Angles of Attack, $R_N = 4.20 \times 10^6$. Closed Symbols Denote Primary Separation and Open Symbols Denote Secondary Separation.

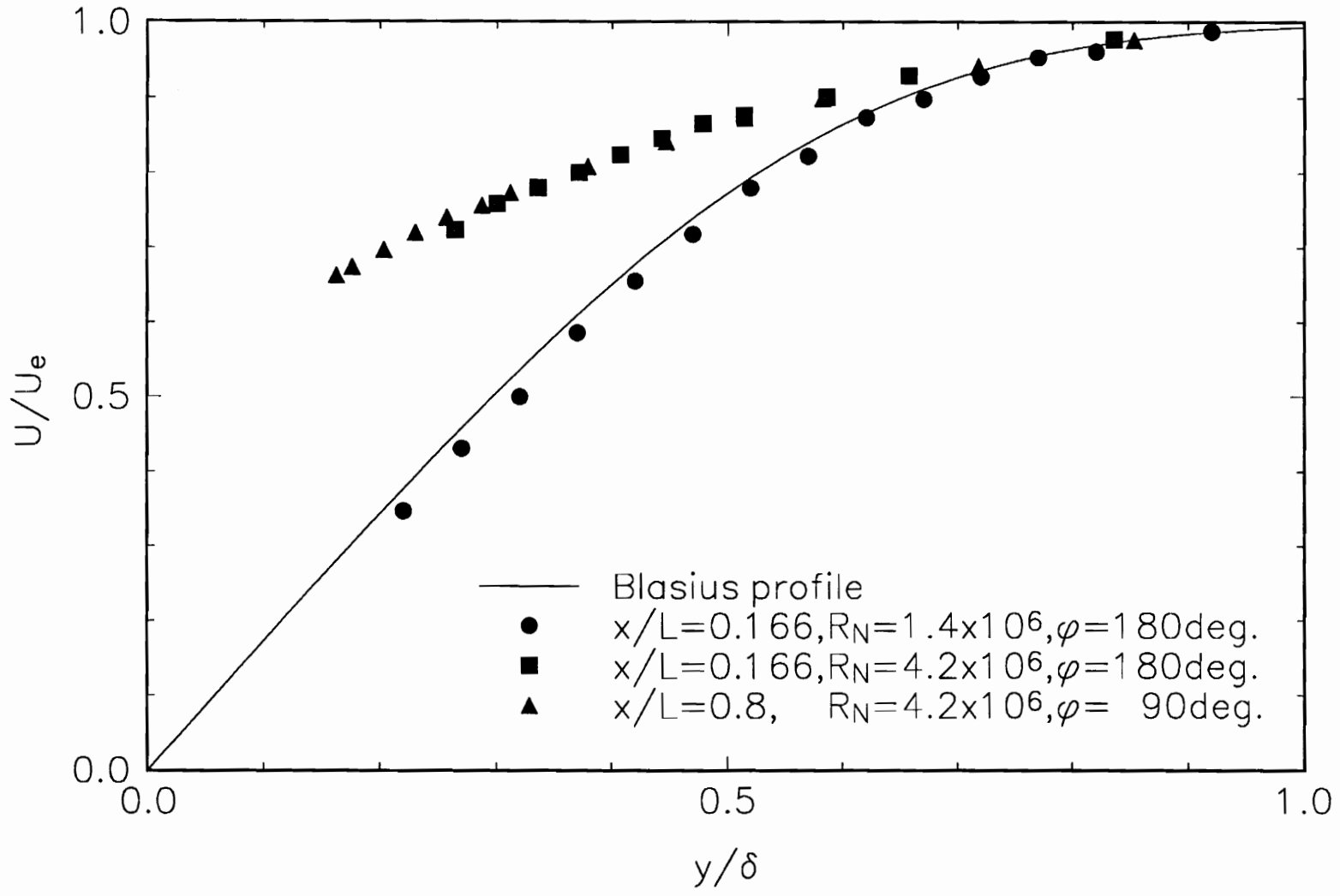

Figure 36. Boundary Layer Profiles Measured with Trip on.

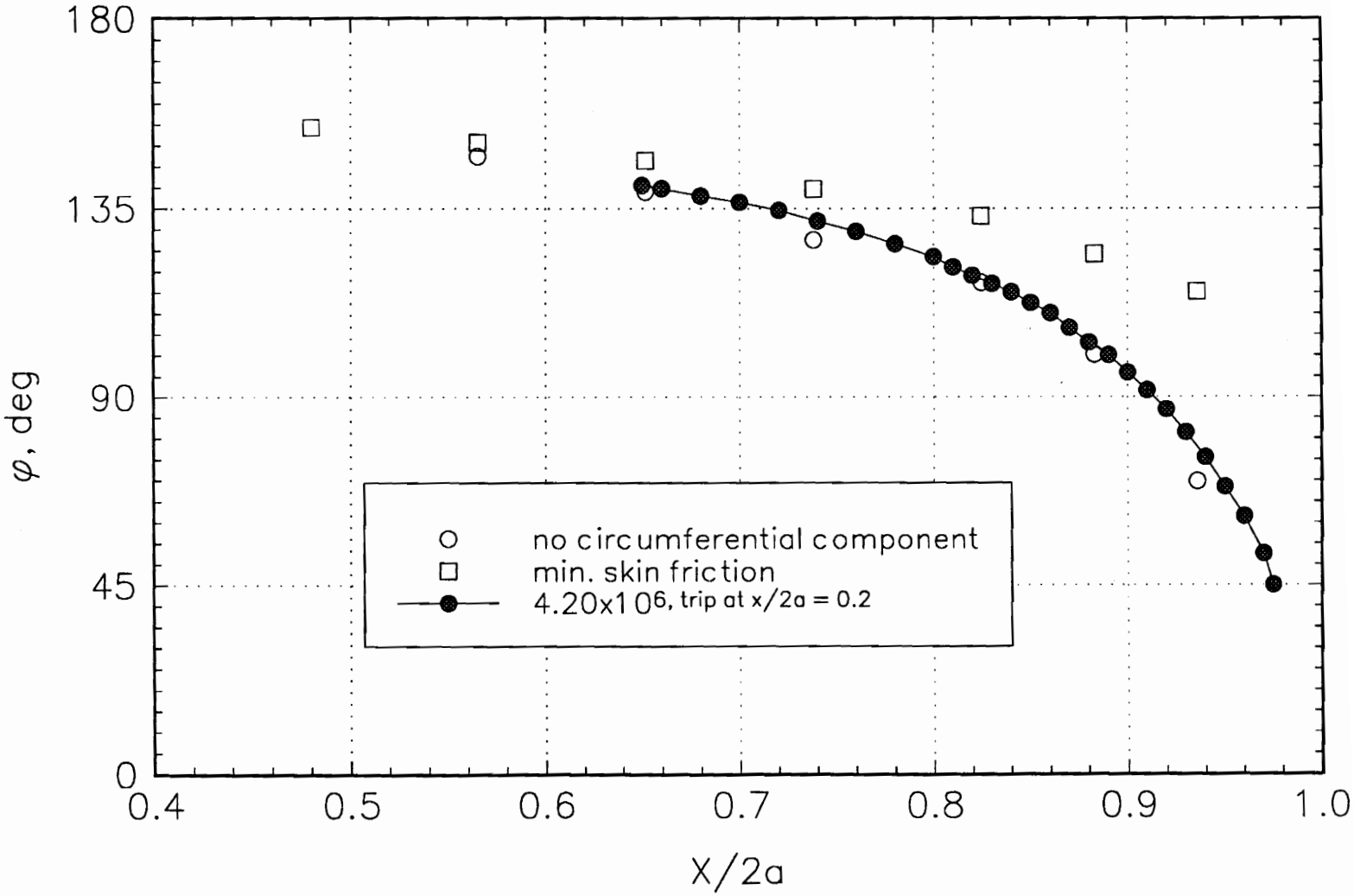

Figure 37. Primary Separation Location Comparison, $\alpha = 10$ degree. Open Symbols are from Kreplin, *et al* (1985), $R_N = 7.7 \times 10^6$.

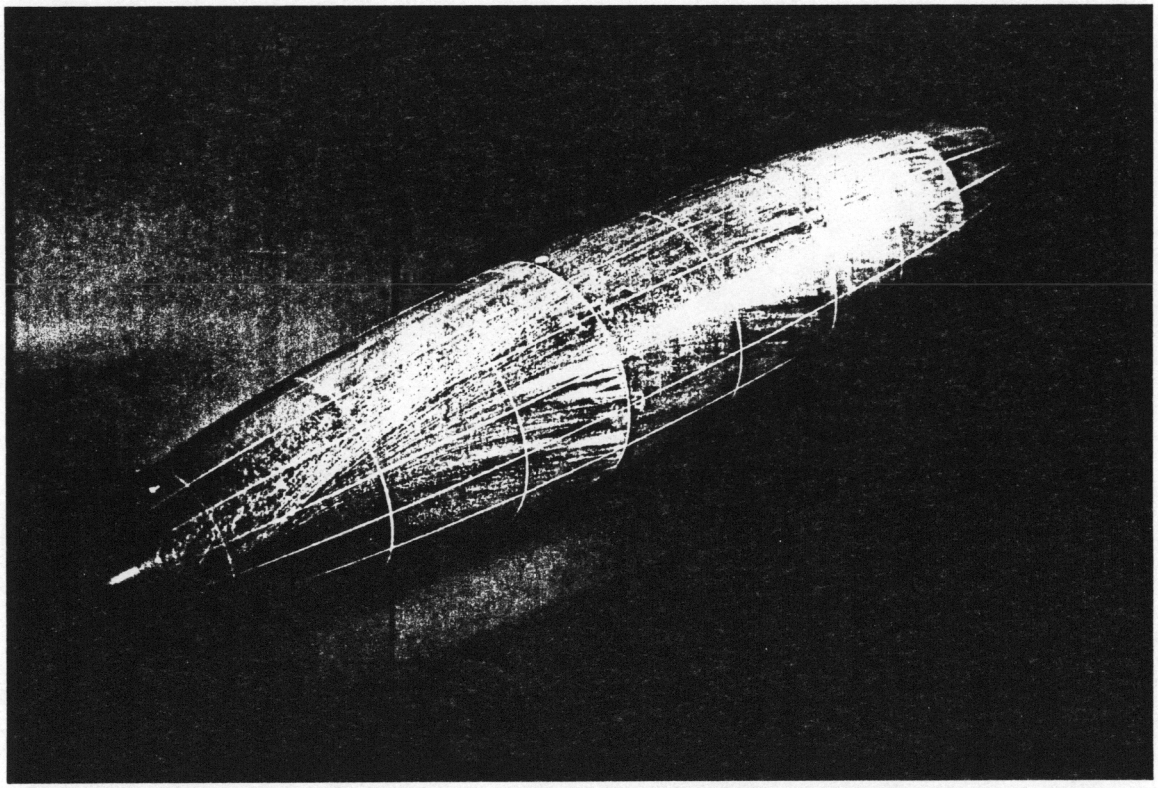

Figure 38. Oil-Flow Pattern at $\alpha = 10$ deg., $Re_L = 4.20 \times 10^6$, Trip at x/2a = 0.2.

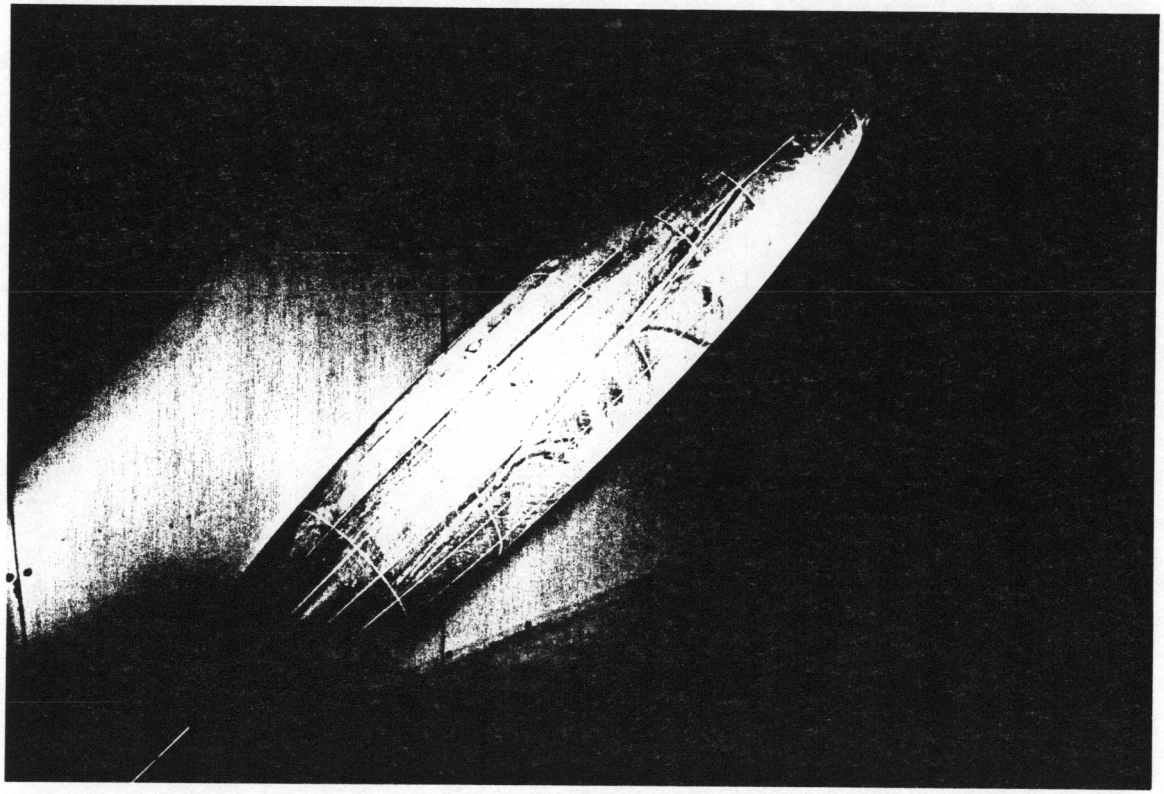

Figure 39. Oil-Flow Pattern at $\alpha = 30$ deg., $Re_L = 4.20 \times 10^6$, Trip at x/2a = 0.2.

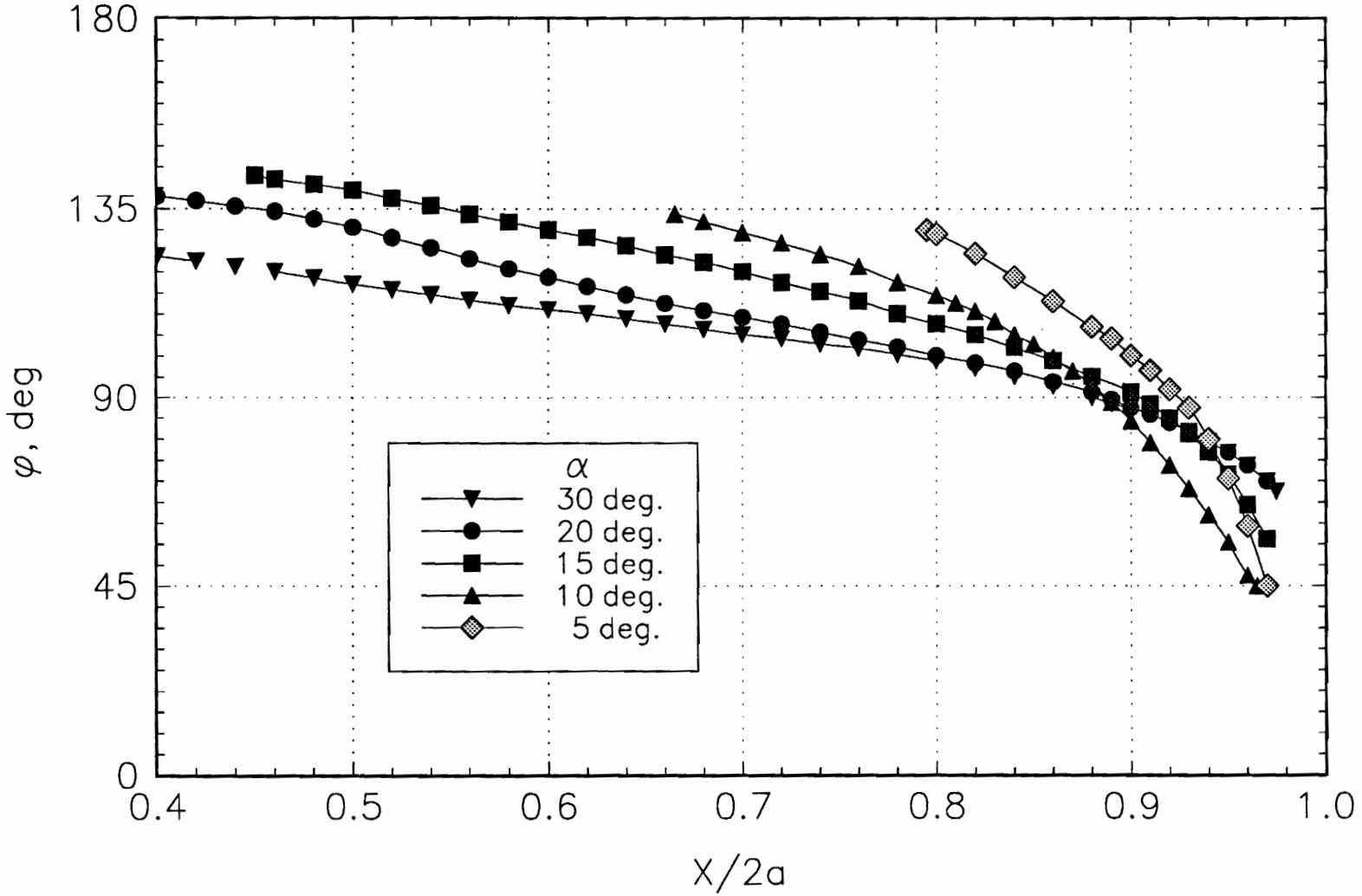

Figure 40. Angle of Attack Effect on the Primary Separation Lines.

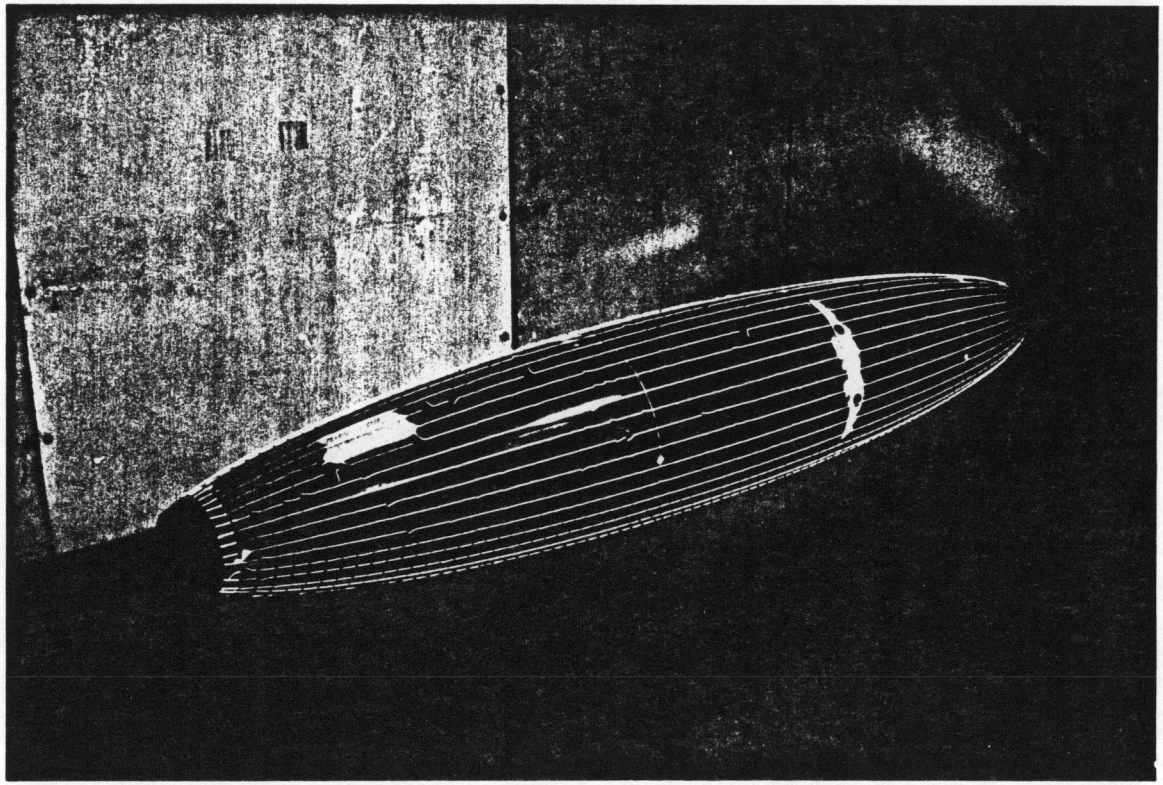

Figure 41. Mini-Tuft Surface Flow Pattern at $\alpha = 0$ deg., $Re_L = 4.20 \times 10^6$.

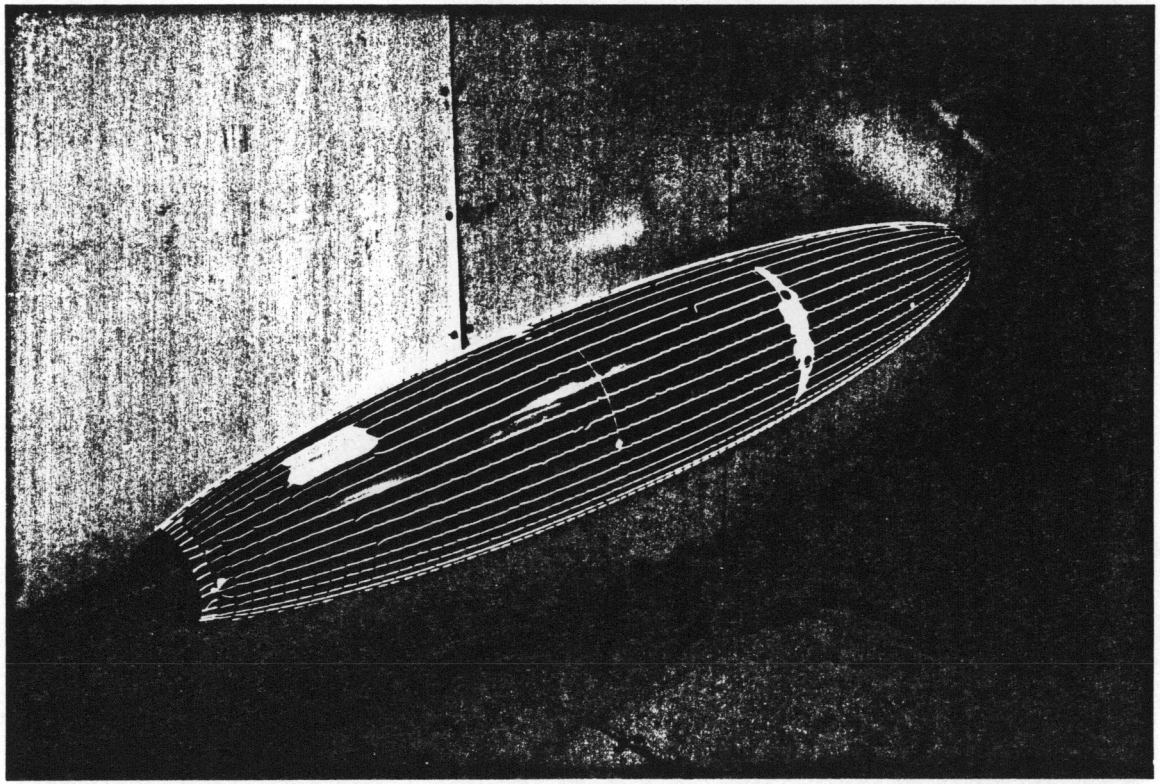

Figure 42. Mini-Tuft Surface Flow Pattern at $\alpha = 5$ deg., $Re_L = 4.20 \times 10^6$.

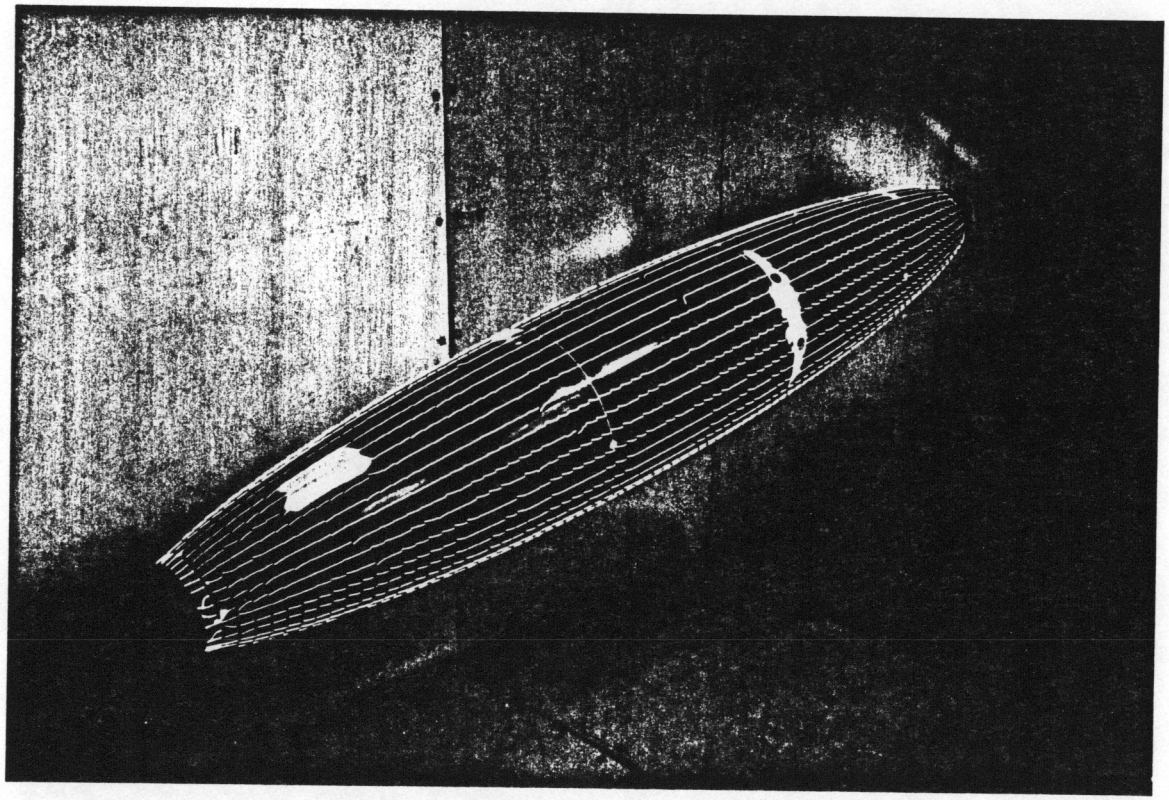

Figure 43. Mini-Tuft Surface Flow Pattern at $\alpha = 10$ deg., $Re_L = 4.20 \times 10^6$.

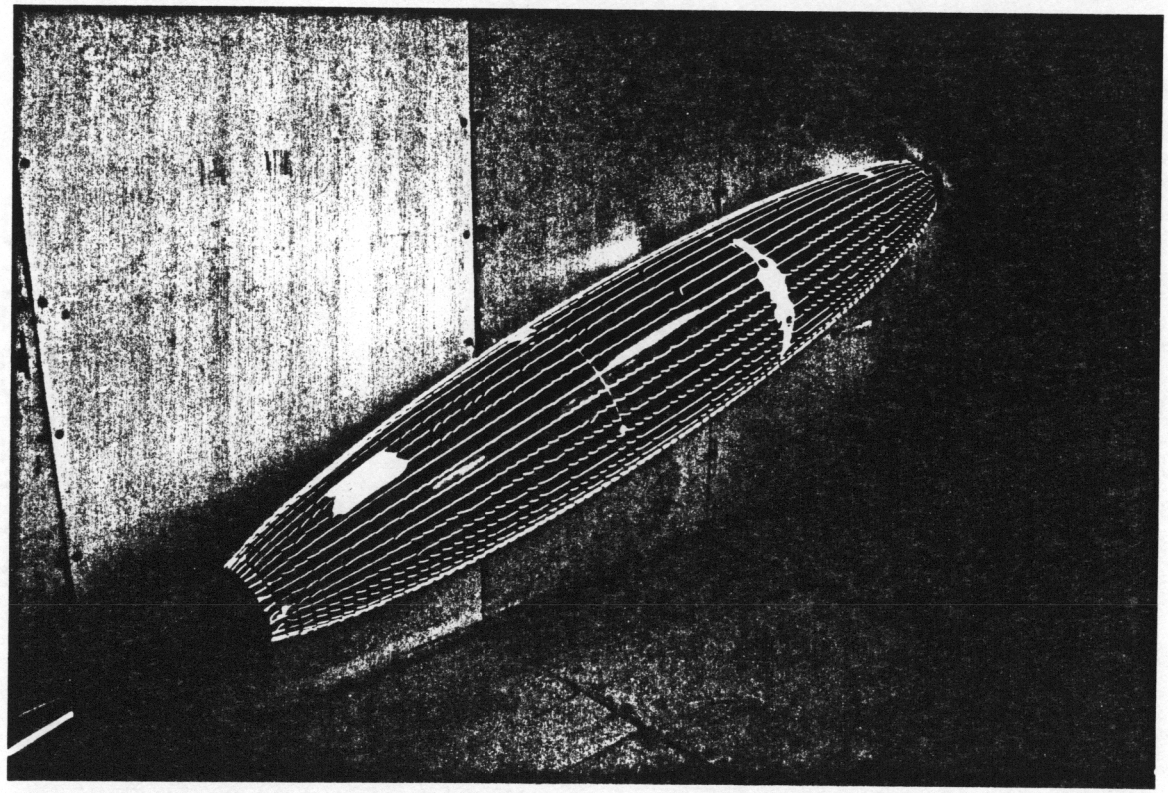

Figure 44. Mini-Tuft Surface Flow Pattern at $\alpha = 15$ deg., $Re_L = 4.20 \times 10^6$.

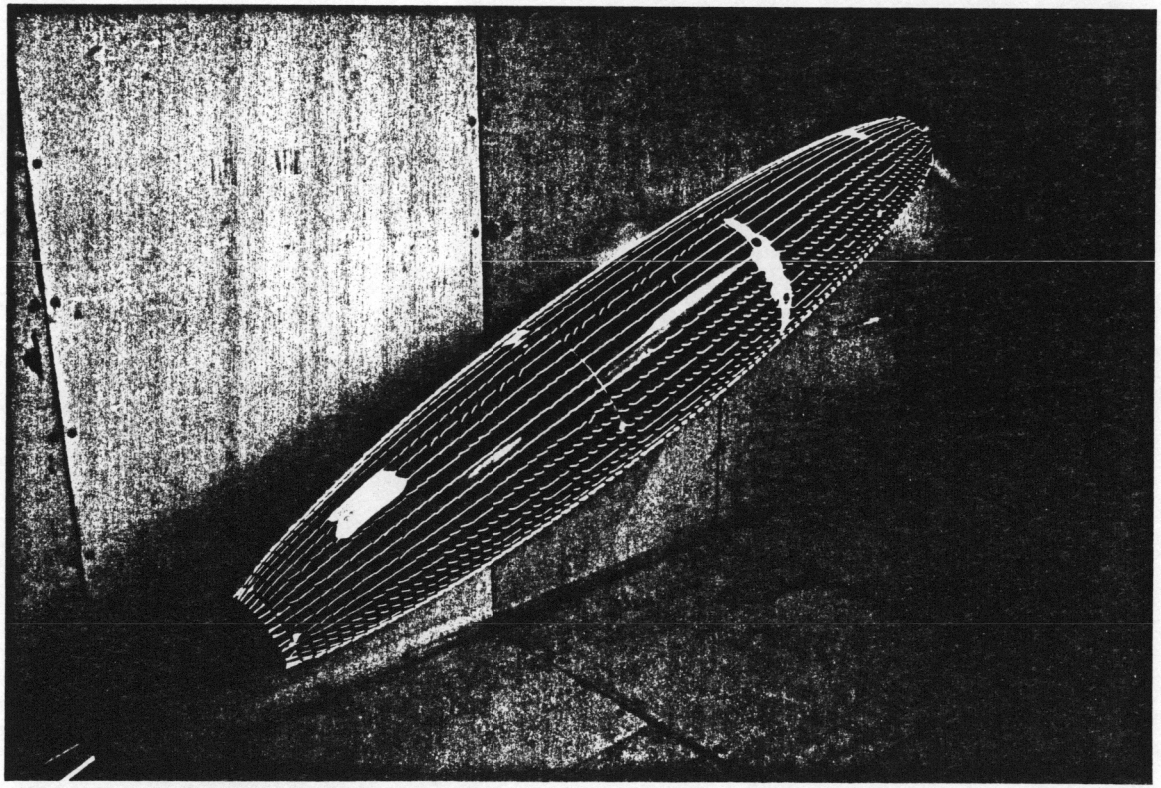

Figure 45. Mini-Tuft Surface Flow Pattern at $\alpha = 20$ deg., $Re_L = 4.20 \times 10^6$.

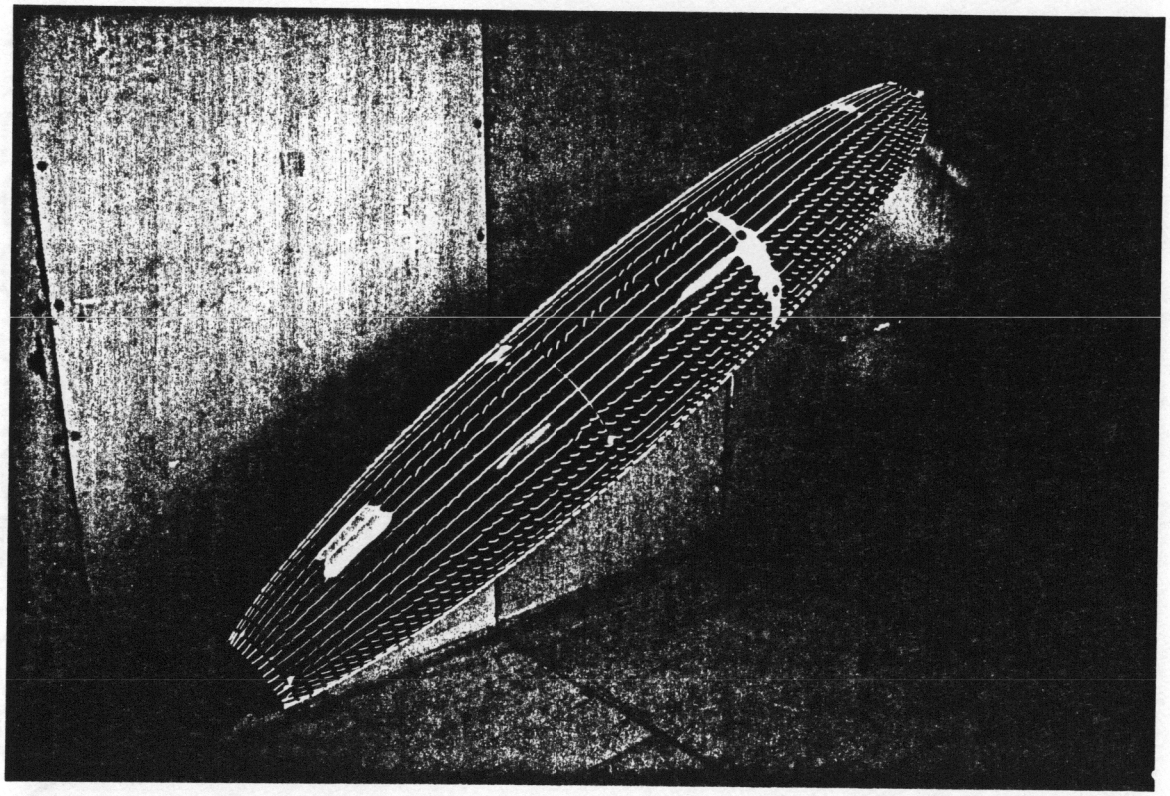

Figure 46. Mini-Tuft Surface Flow Pattern at $\alpha = 25$ deg., $Re_L = 4.20 \times 10^6$.

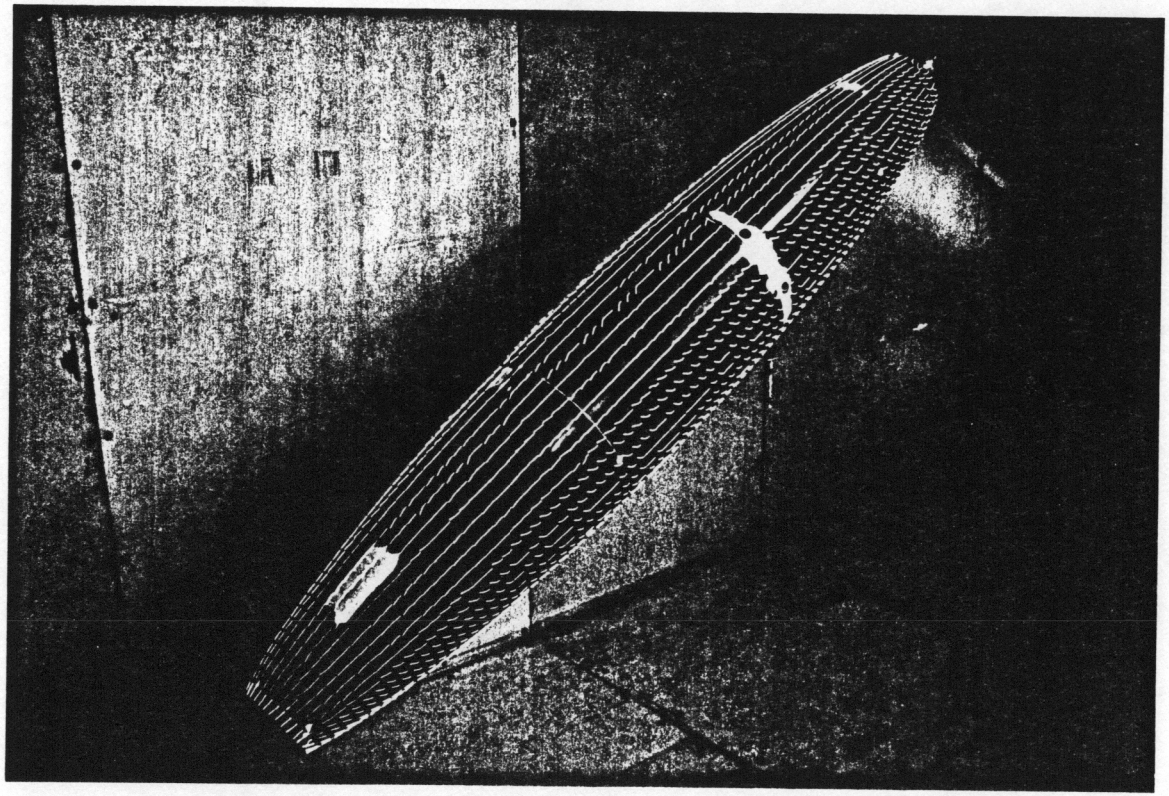

Figure 47. Mini-Tuft Surface Flow Pattern at $\alpha = 30$ deg., $Re_L = 4.20 \times 10^6$.

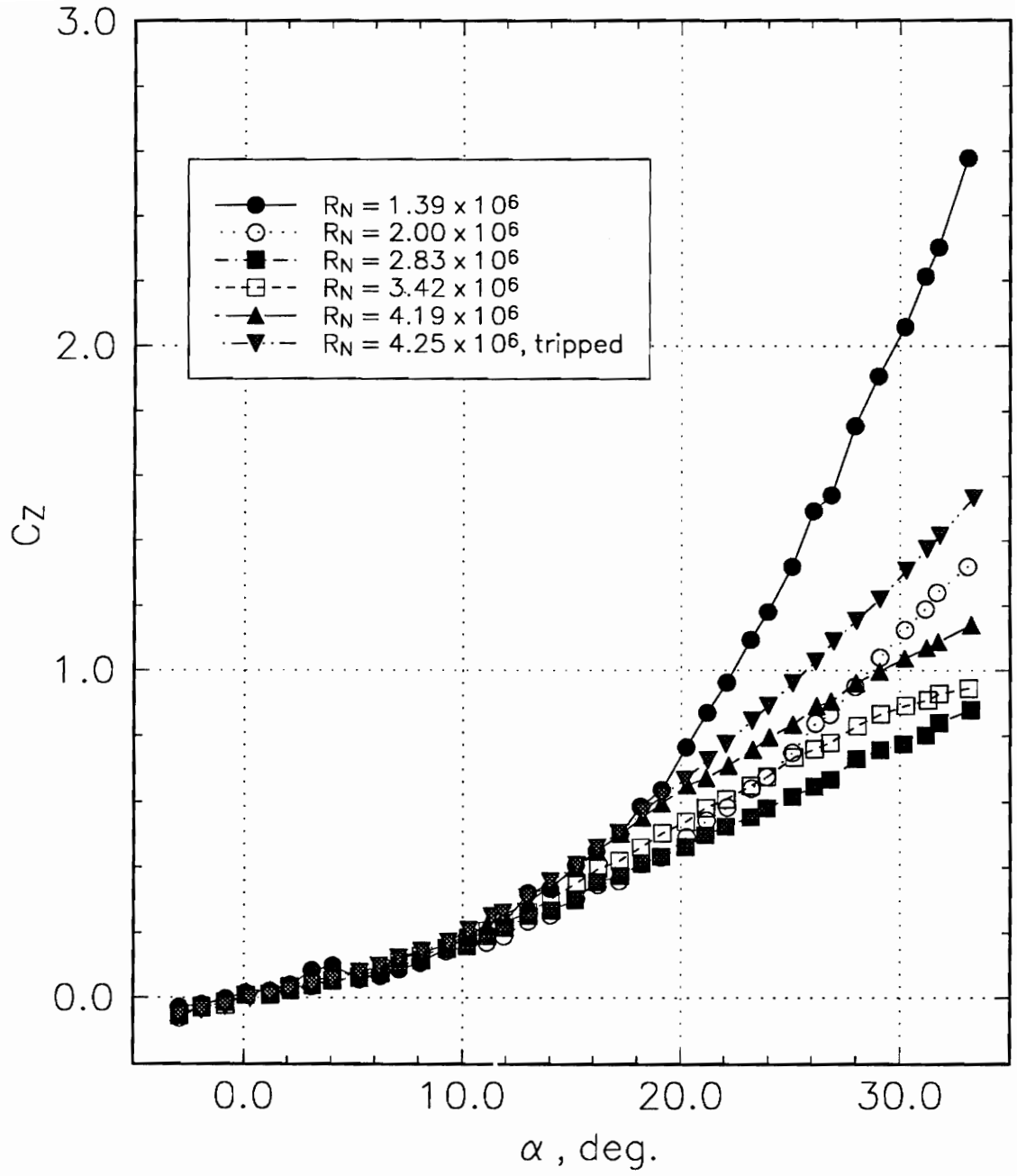

Figure 48. C_Z v.s. Angle of Attack α.

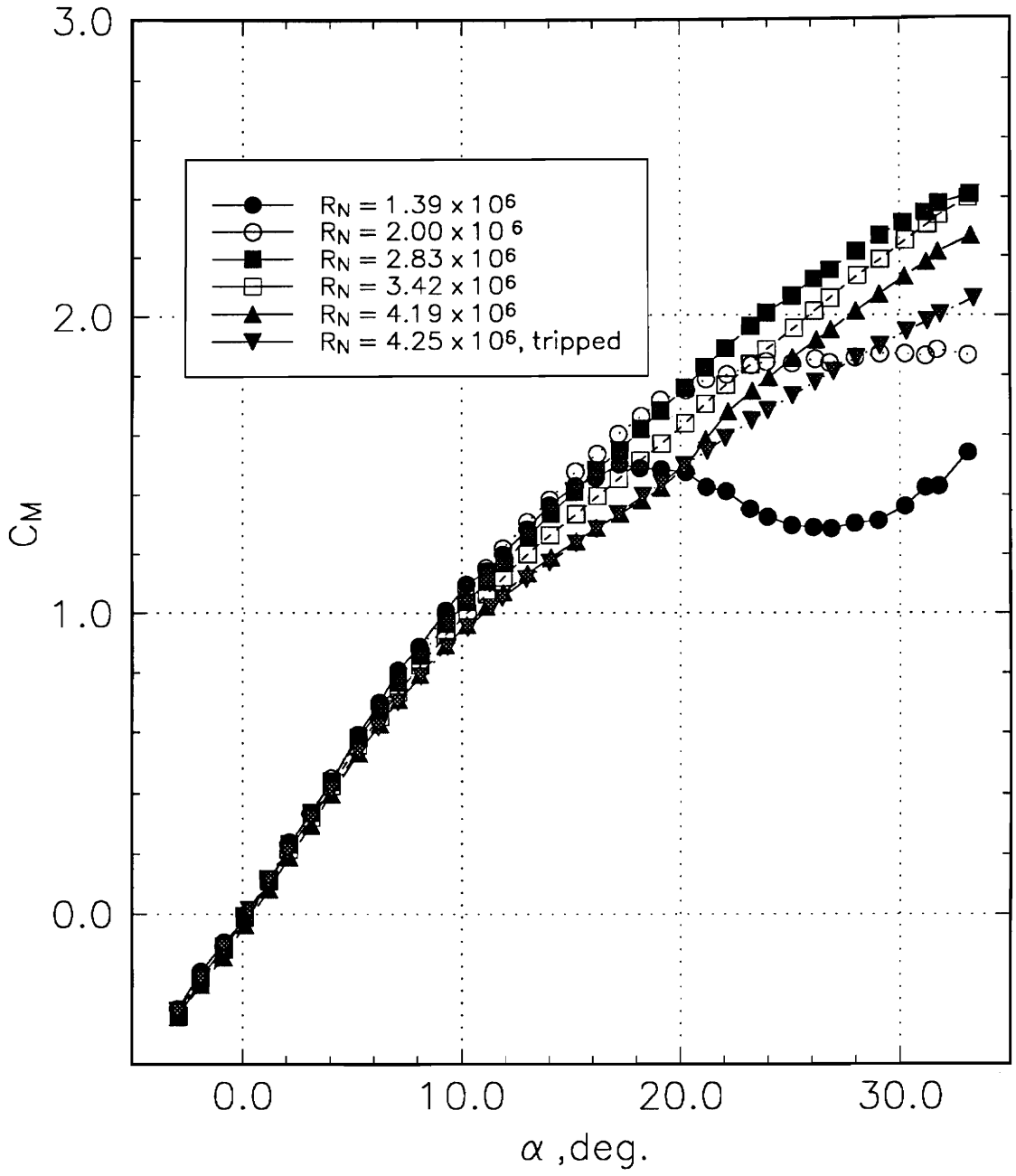

Figure 49. C_M v.s. Angle of Attack α.

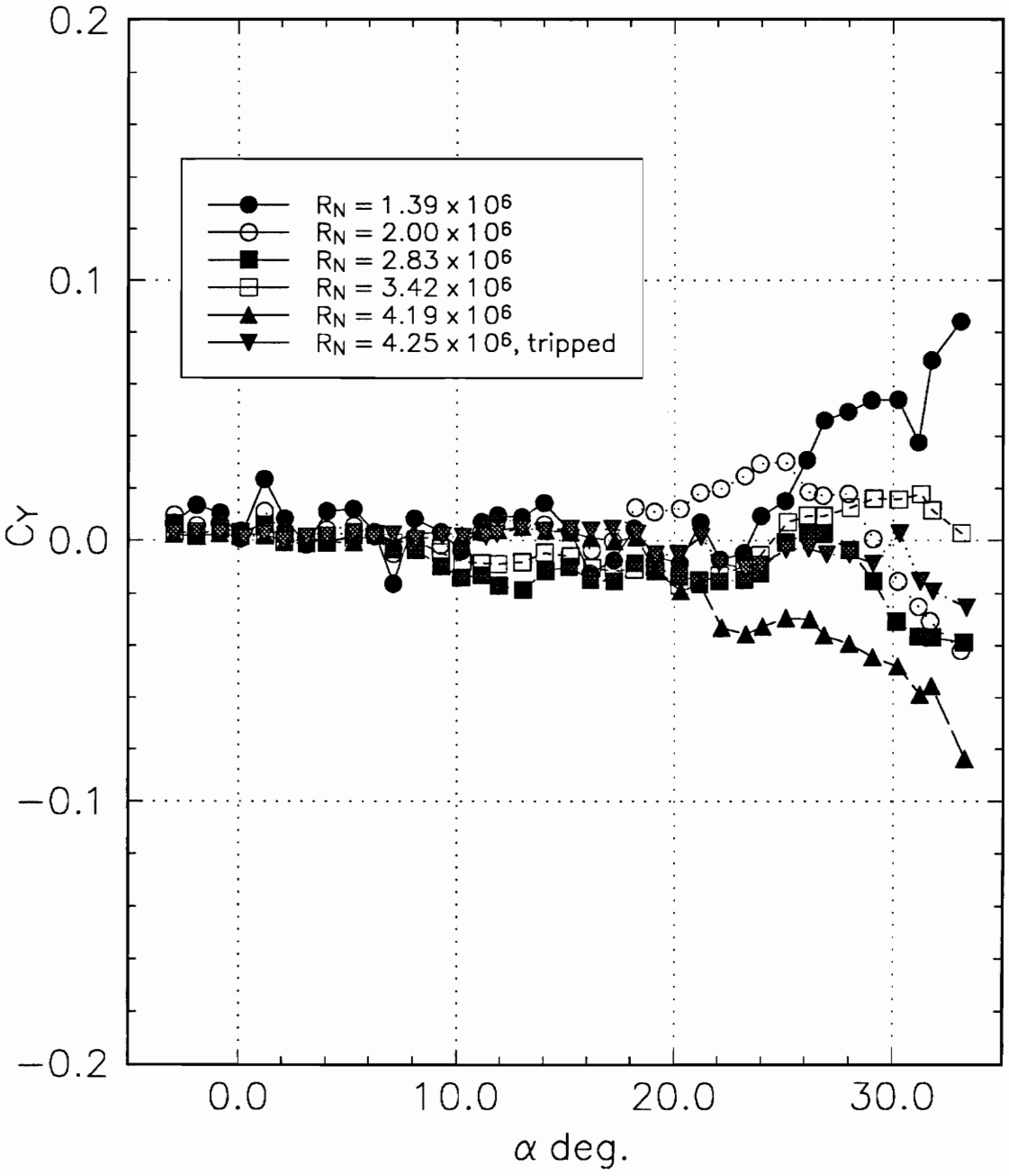

Figure 50. C_Y v.s. Angle of Attack α.

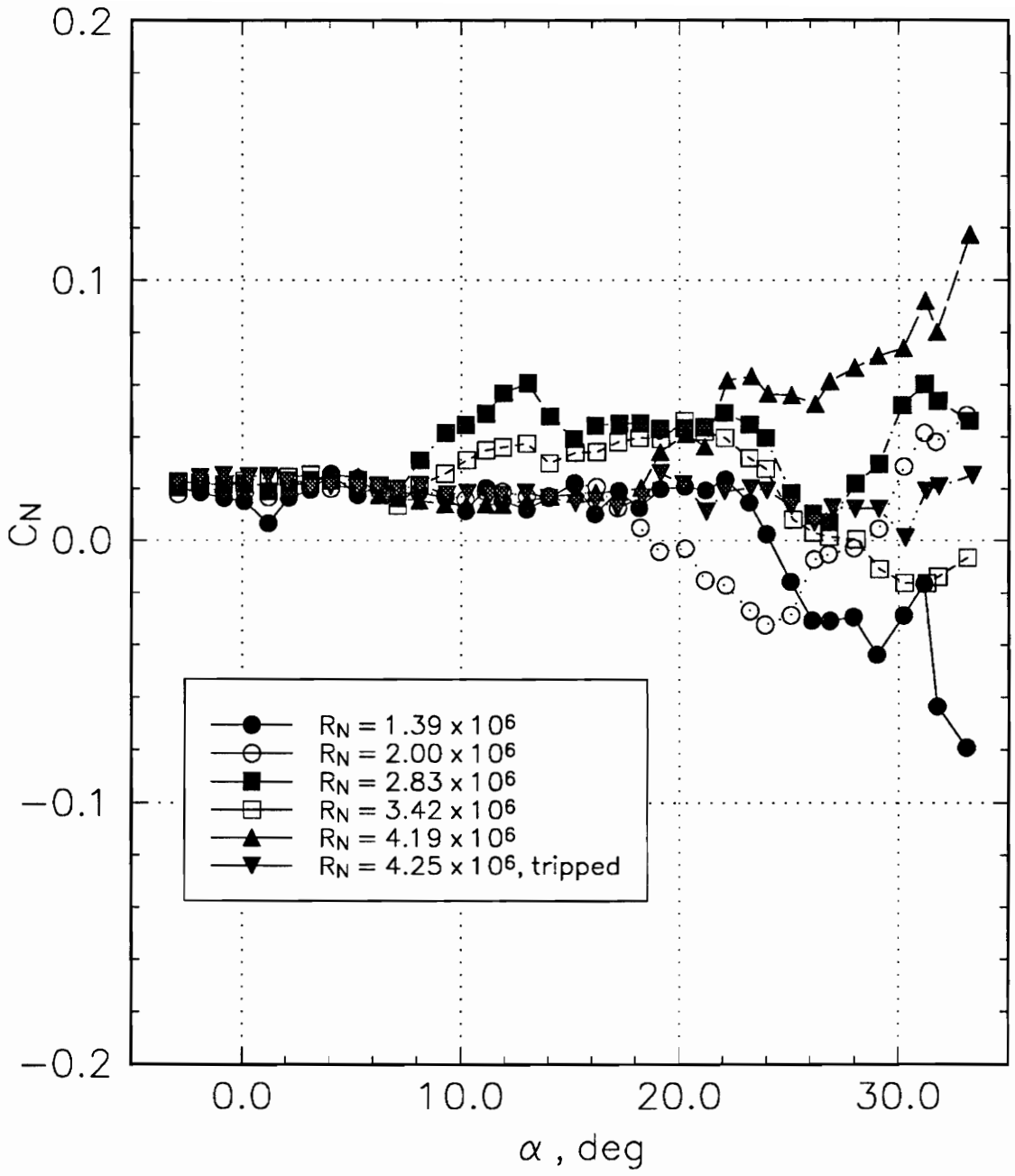

Figure 51. C_N v.s. Angle of Attack α.

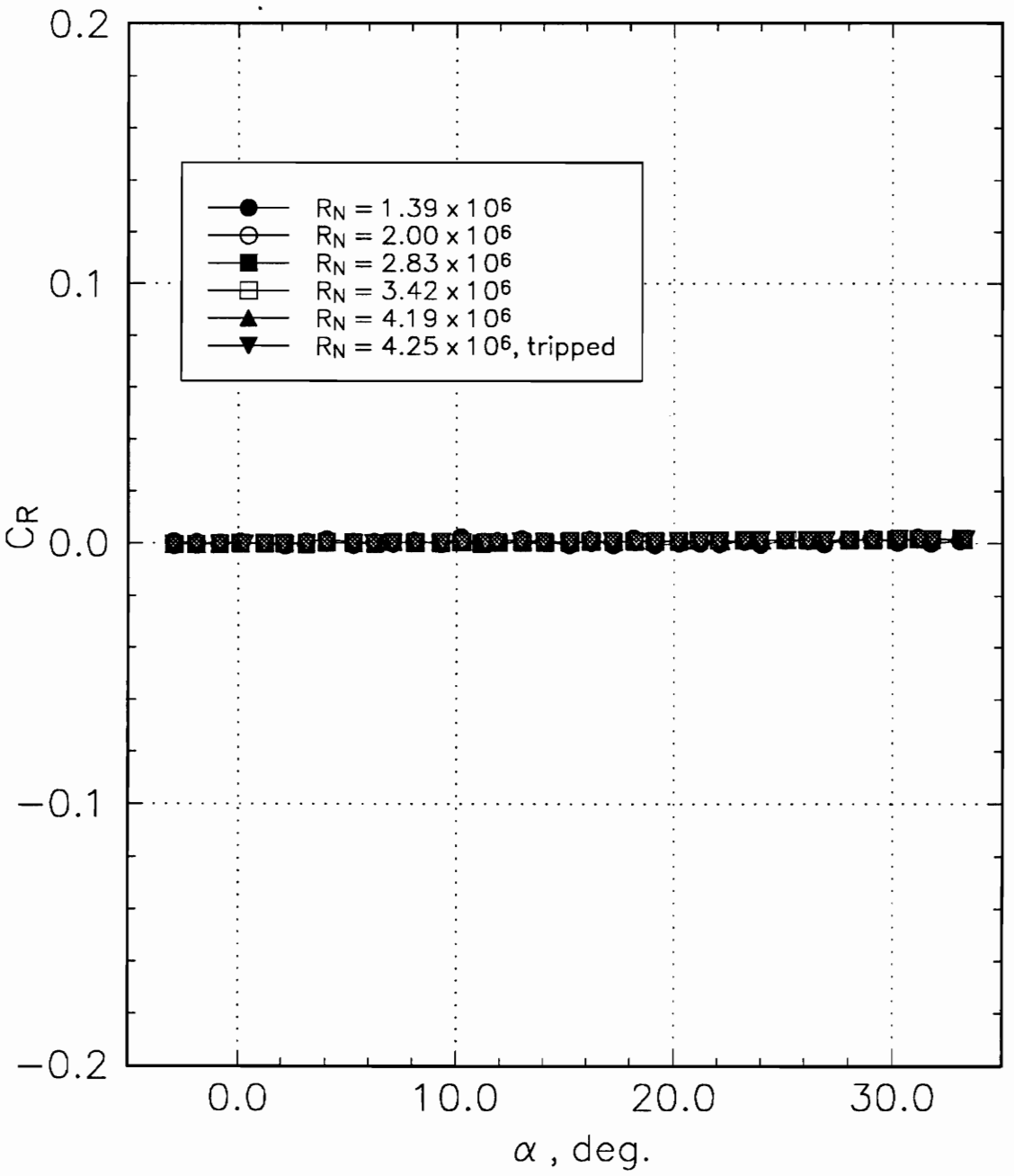

Figure 52. C_R v.s. Angle of Attack α.

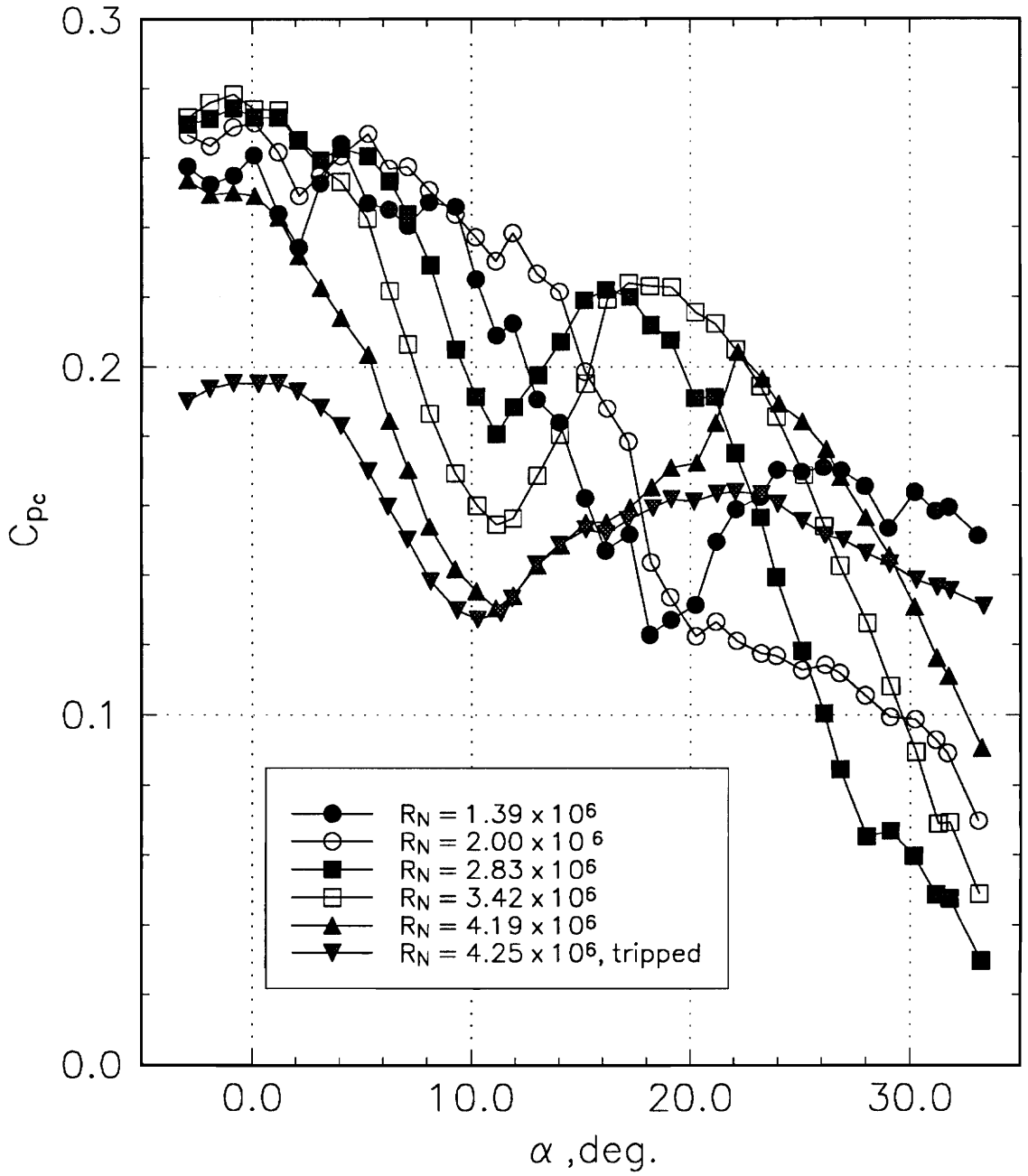

Figure 53. Cavity Pressure Variation v.s. Angle of Attack α.

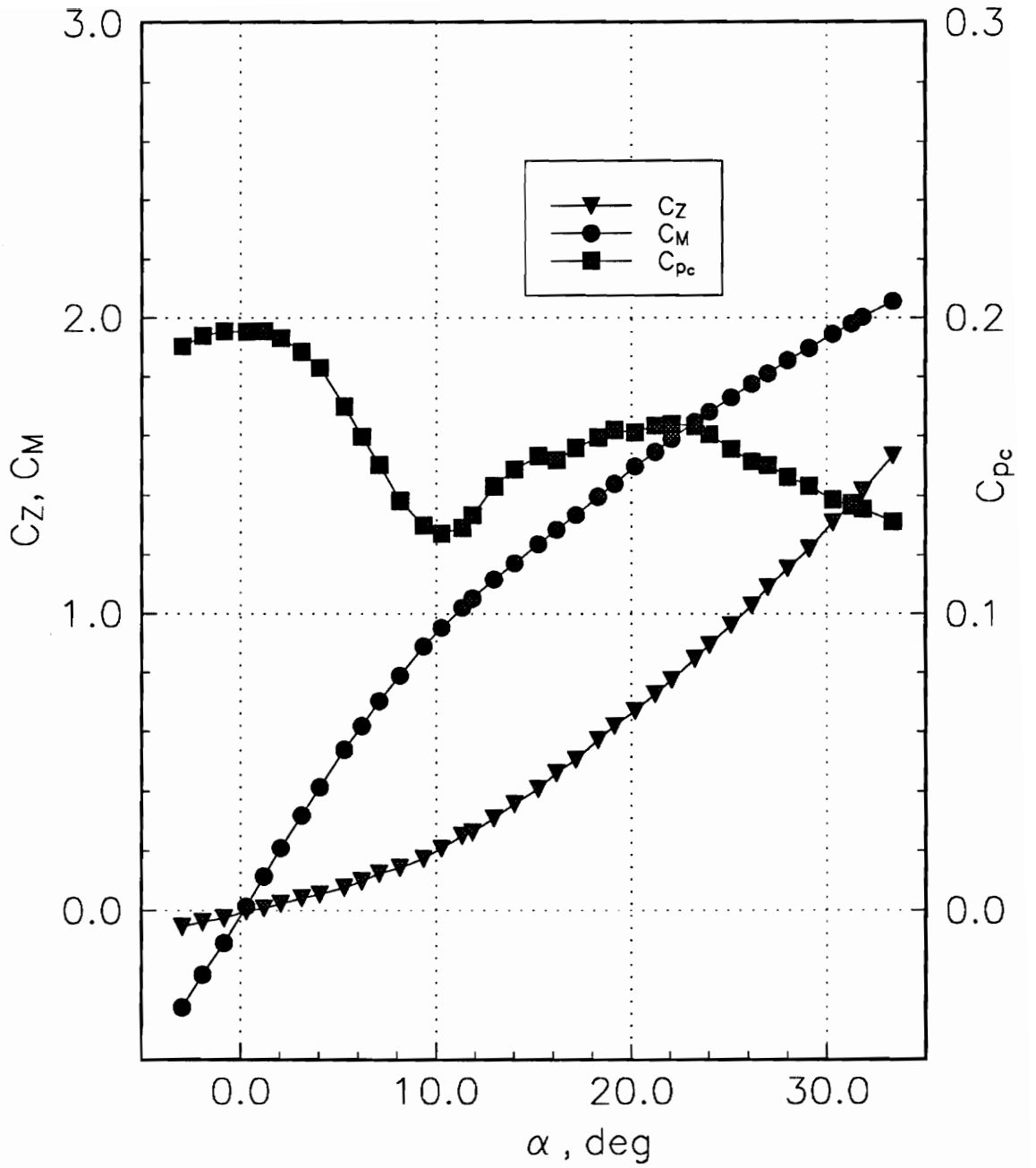

Figure 54. C_Z, C_M, and C_{pc} Variation at $R_N = 4.20 \times 10^6$.

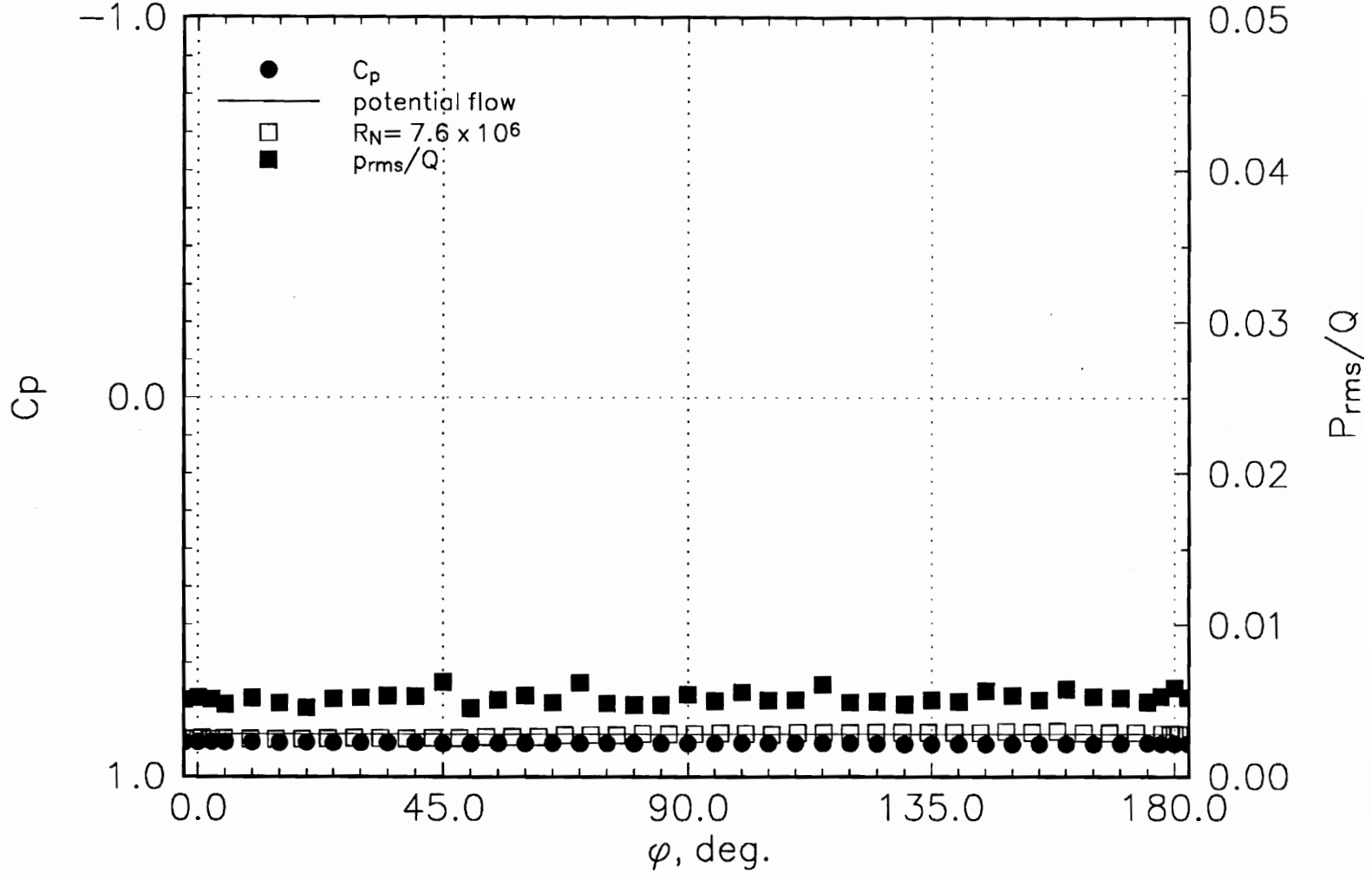

Figure 55. Mean and rms Pressure Distributions at $x/L = 0.0000$, $\alpha = 10$ deg, $Re_L = 4.20 \times 10^6$. $R_N = 7.6 \times 10^6$ Data from Meier *et al.* (1986).

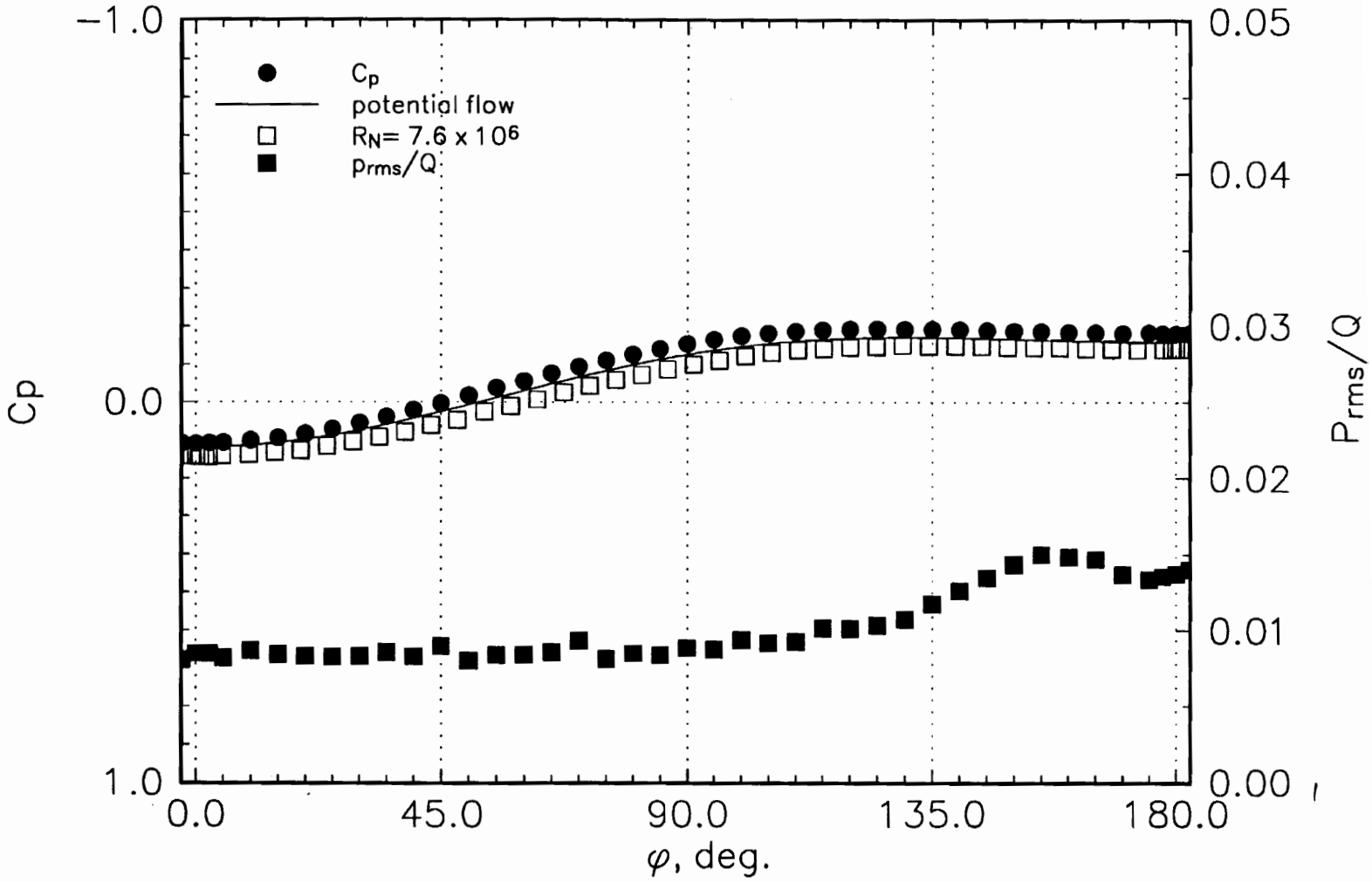

Figure 56. Mean and rms Pressure Distributions at $x/L = 0.1079$, $\alpha = 10$ deg, $Re_L = 4.20 \times 10^6$. $R_N = 7.6 \times 10^6$ Data from Meier *et al.* (1986).

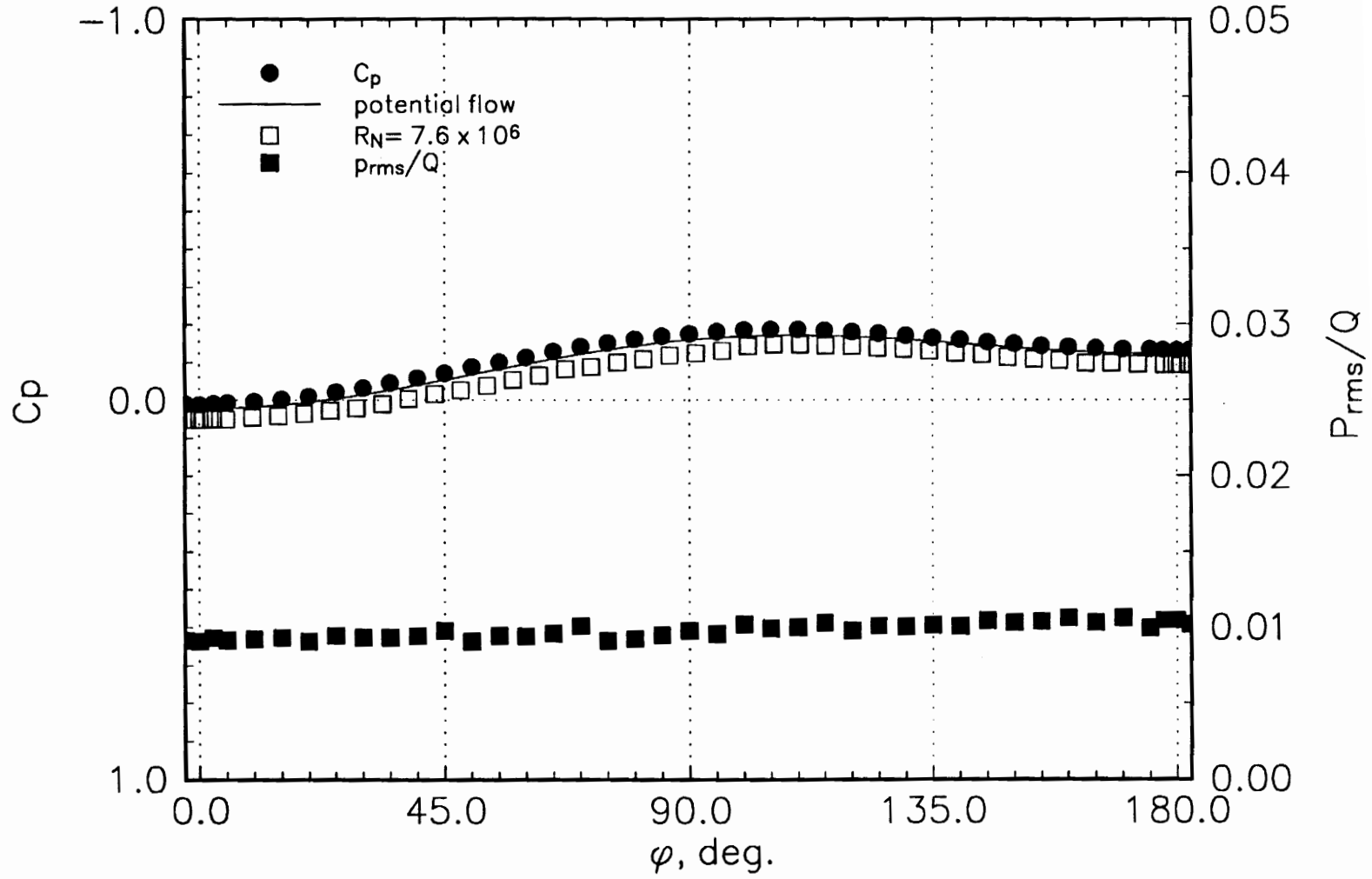

Figure 57. Mean and rms Pressure Distributions at $x/L = 0.2315$, $\alpha = 10$ deg, $Re_L = 4.20 \times 10^6$. $R_N = 7.6 \times 10^6$ Data from Meier *et al.* (1986).

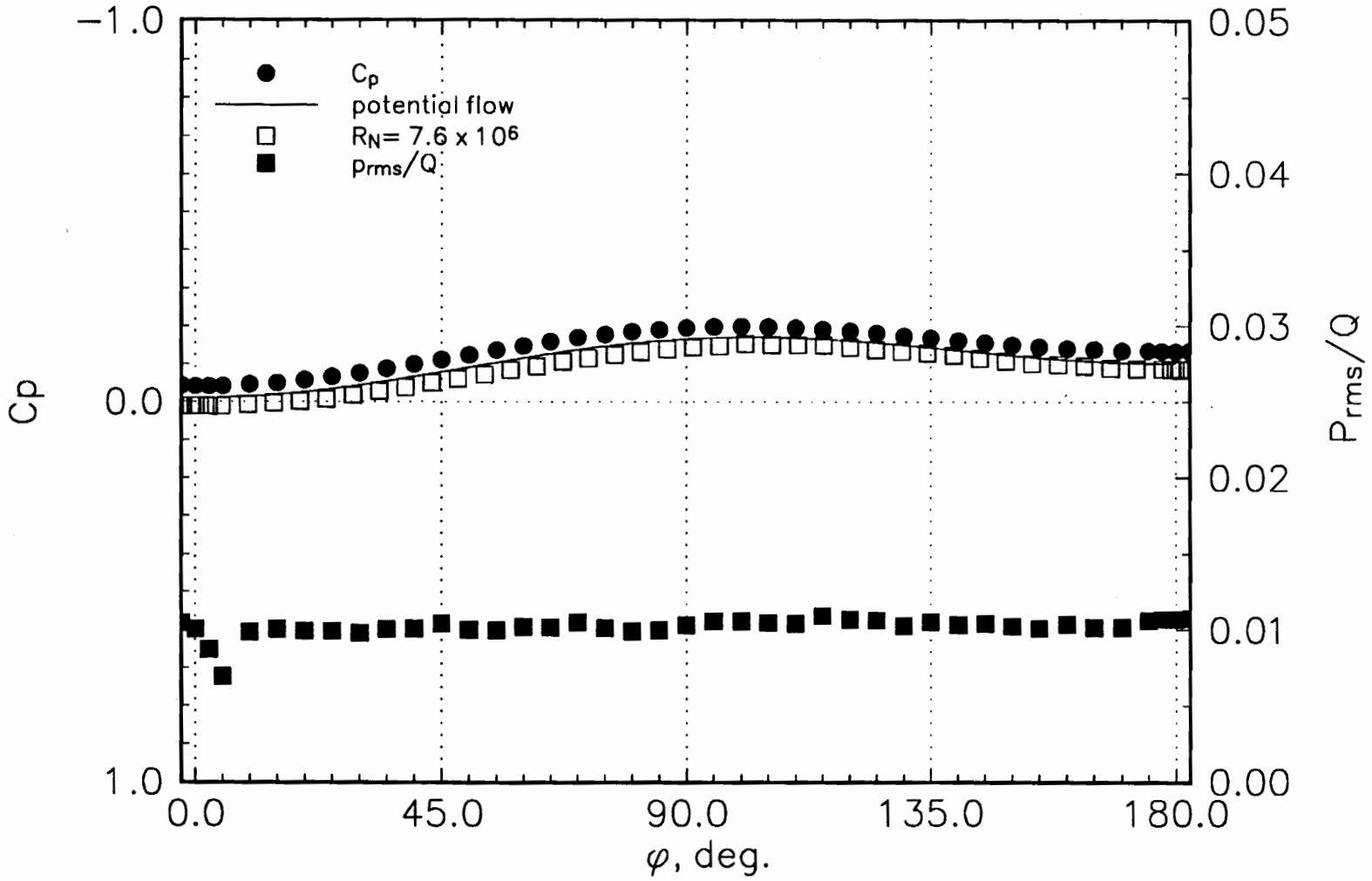

Figure 58. Mean and rms Pressure Distributions at $x/L = 0.3145$, $\alpha = 10$ deg, $Re_L = 4.20 \times 10^6$. $R_N = 7.6 \times 10^6$ Data from Meier *et al.* (1986).

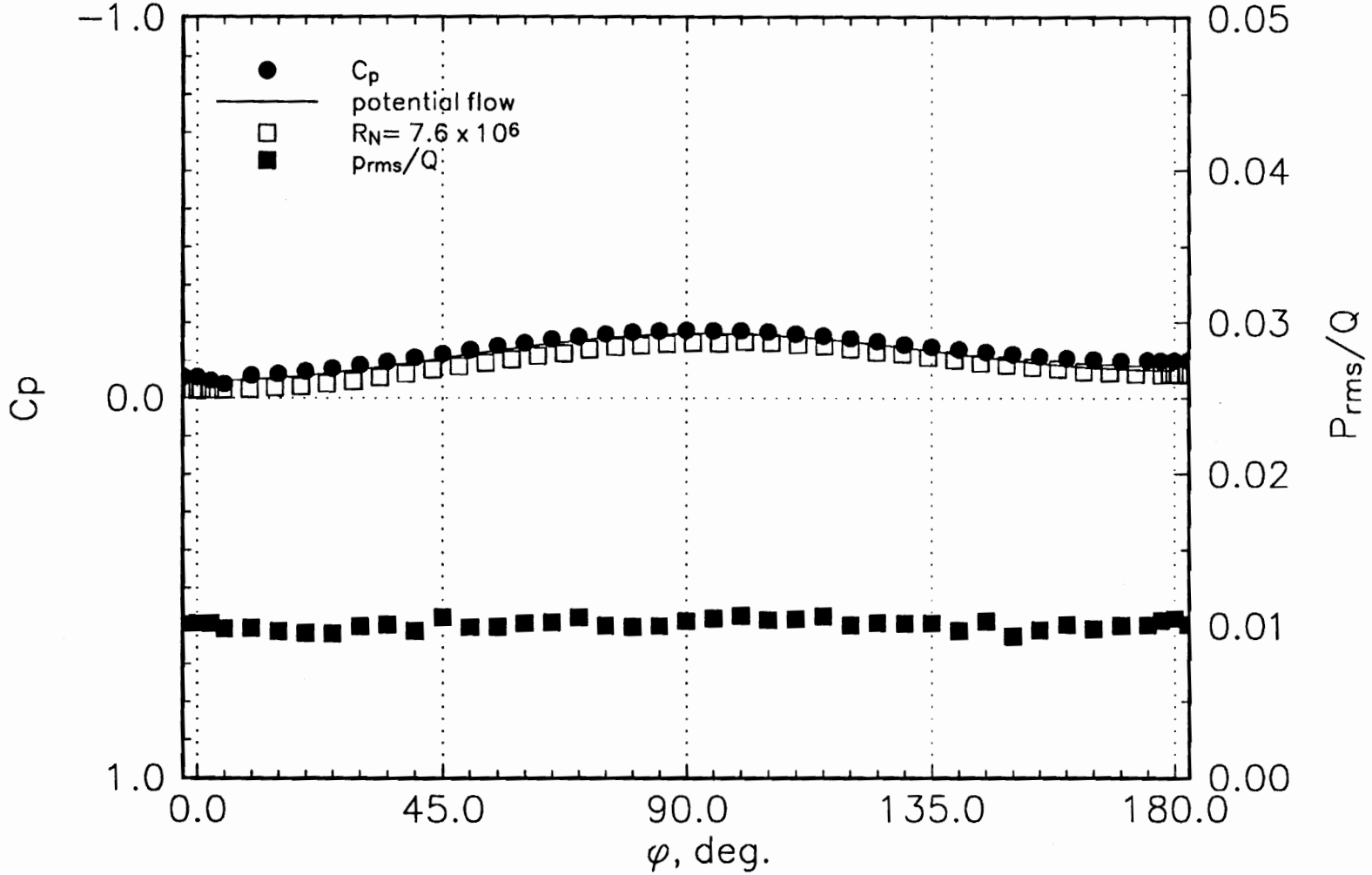

Figure 59. Mean and rms Pressure Distributions at $x/L = 0.4396$, $\alpha = 10$ deg, $Re_L = 4.20 \times 10^6$. $R_N = 7.6 \times 10^6$ Data from Meier *et al.* (1986).

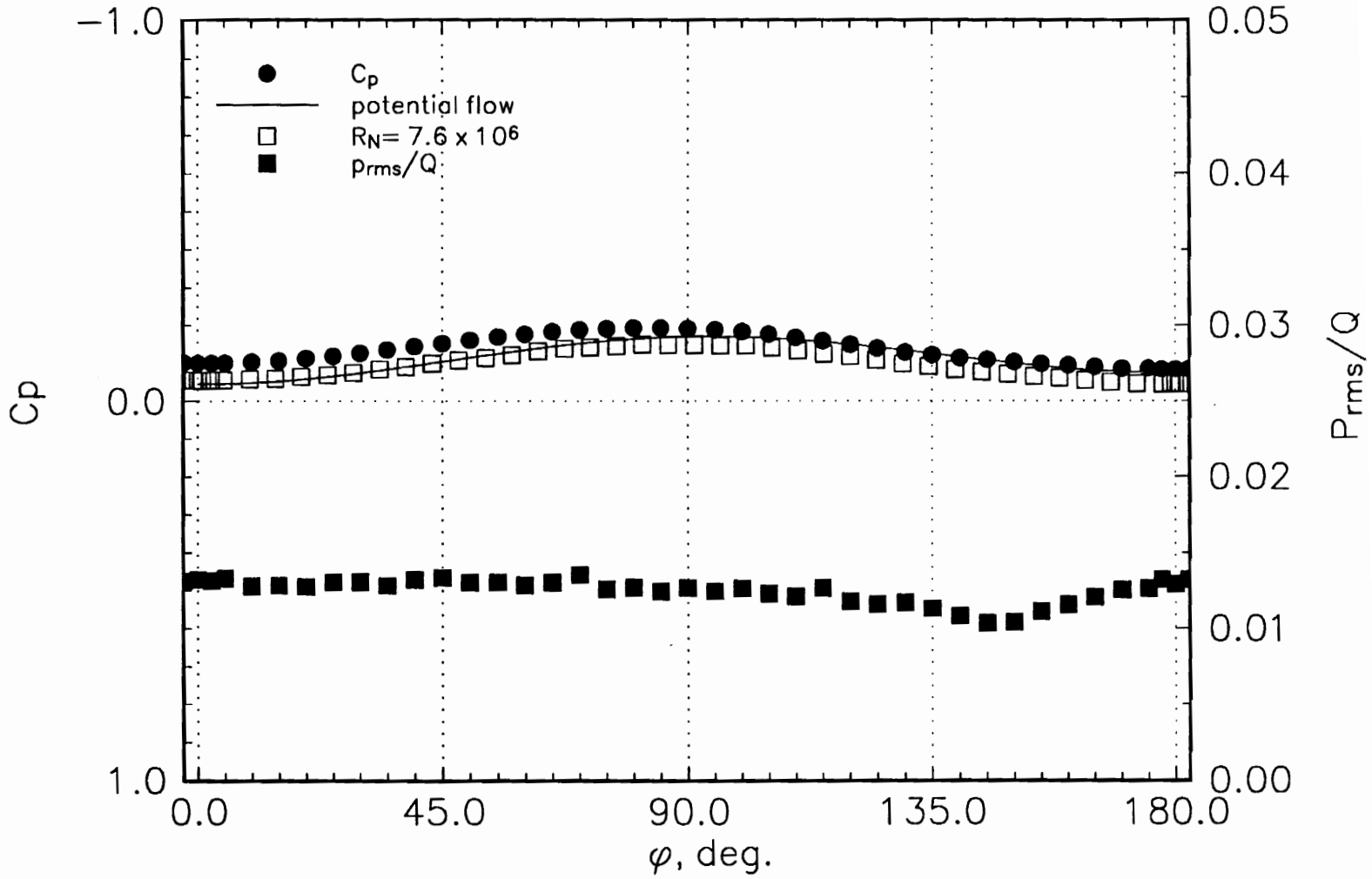

Figure 60. Mean and rms Pressure Distributions at $x/L = 0.5646$, $\alpha = 10$ deg, $Re_L = 4.20 \times 10^6$. $R_N = 7.6 \times 10^6$ Data from Meier *et al.* (1986).

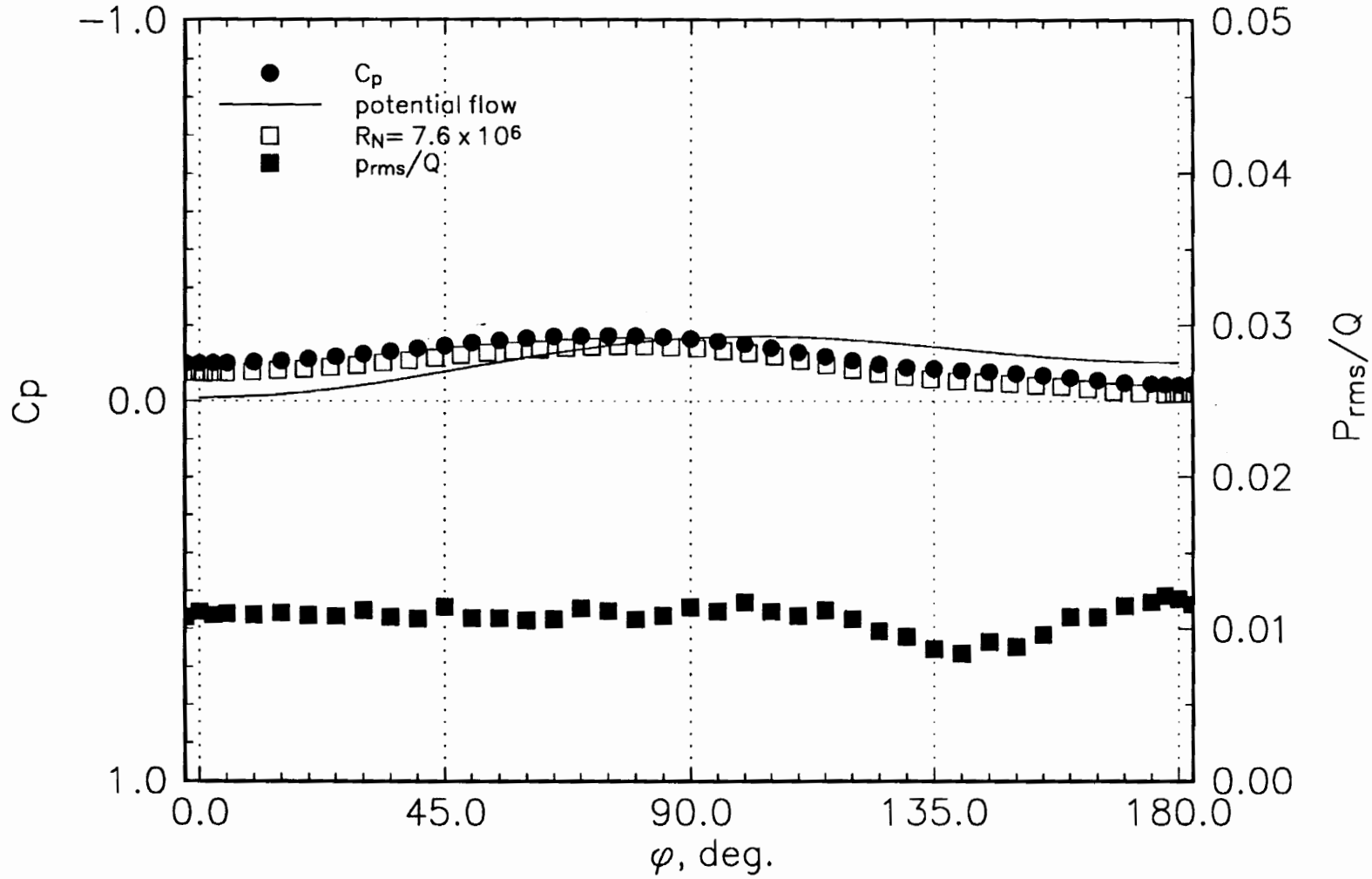

Figure 61. Mean and rms Pressure Distributions at $x/L = 0.6892$, $\alpha = 10$ deg, $Re_L = 4.20 \times 10^6$. $R_N = 7.6 \times 10^6$ Data from Meier *et al.* (1986).

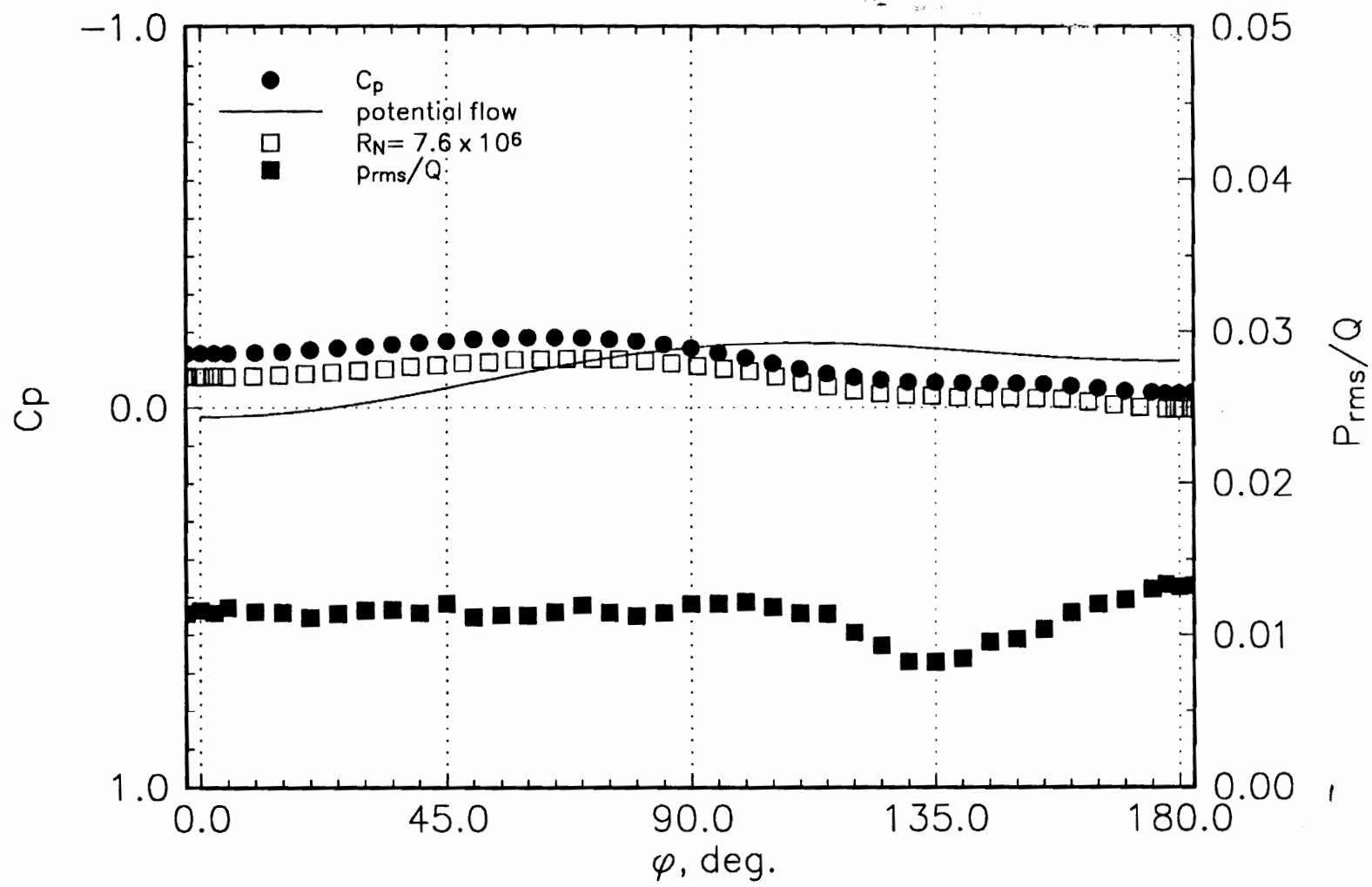

Figure 62. Mean and rms Pressure Distributions at $x/L = 0.7725$, $\alpha = 10$ deg, $Re_L = 4.20 \times 10^6$. $R_N = 7.6 \times 10^6$ Data from Meier *et al.* (1986).

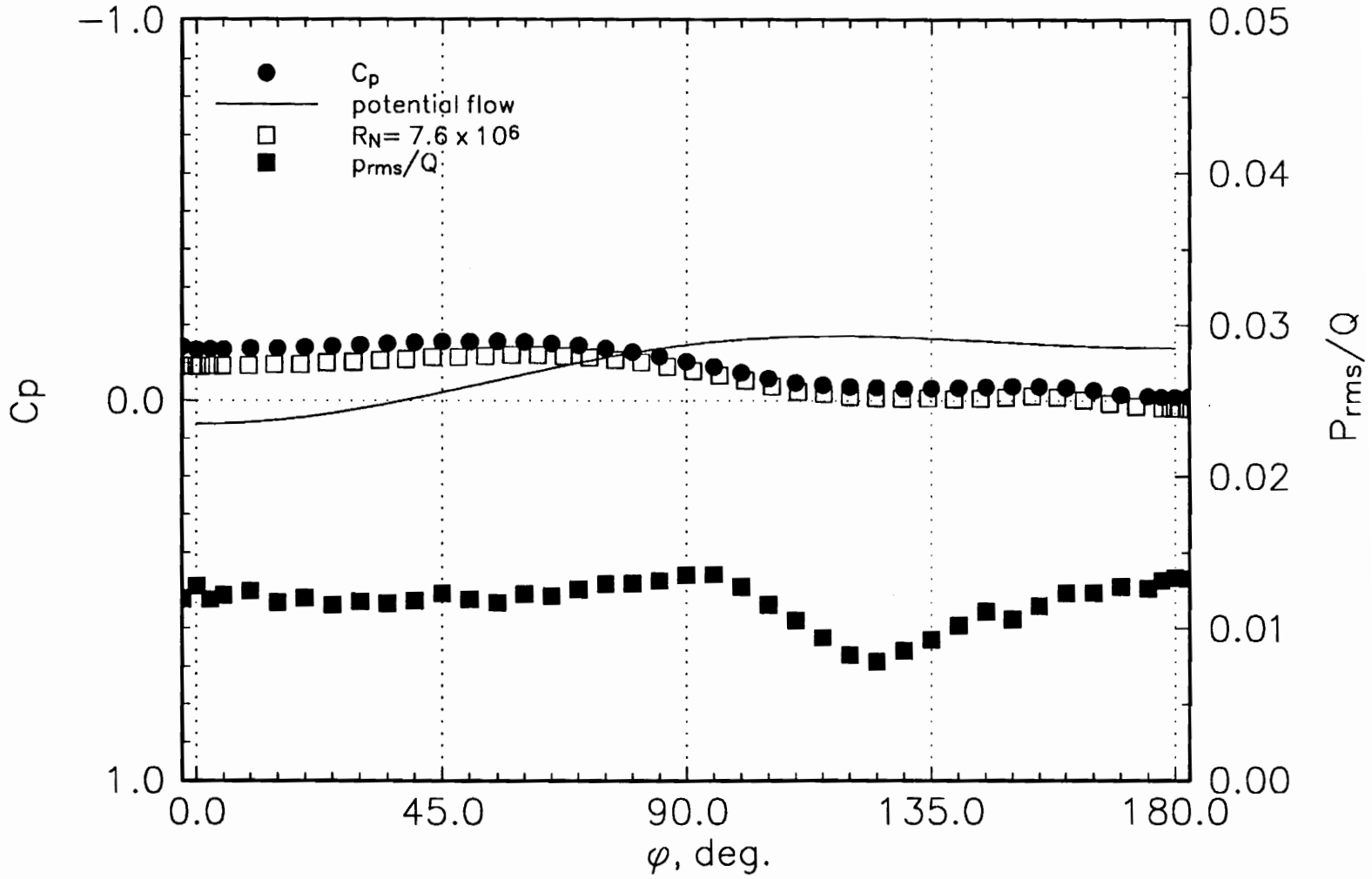

Figure 63. Mean and rms Pressure Distributions at $x/L = 0.8346$, $\alpha = 10$ deg, $Re_L = 4.20 \times 10^6$. $R_N = 7.6 \times 10^6$ Data from Meier *et al.* (1986).

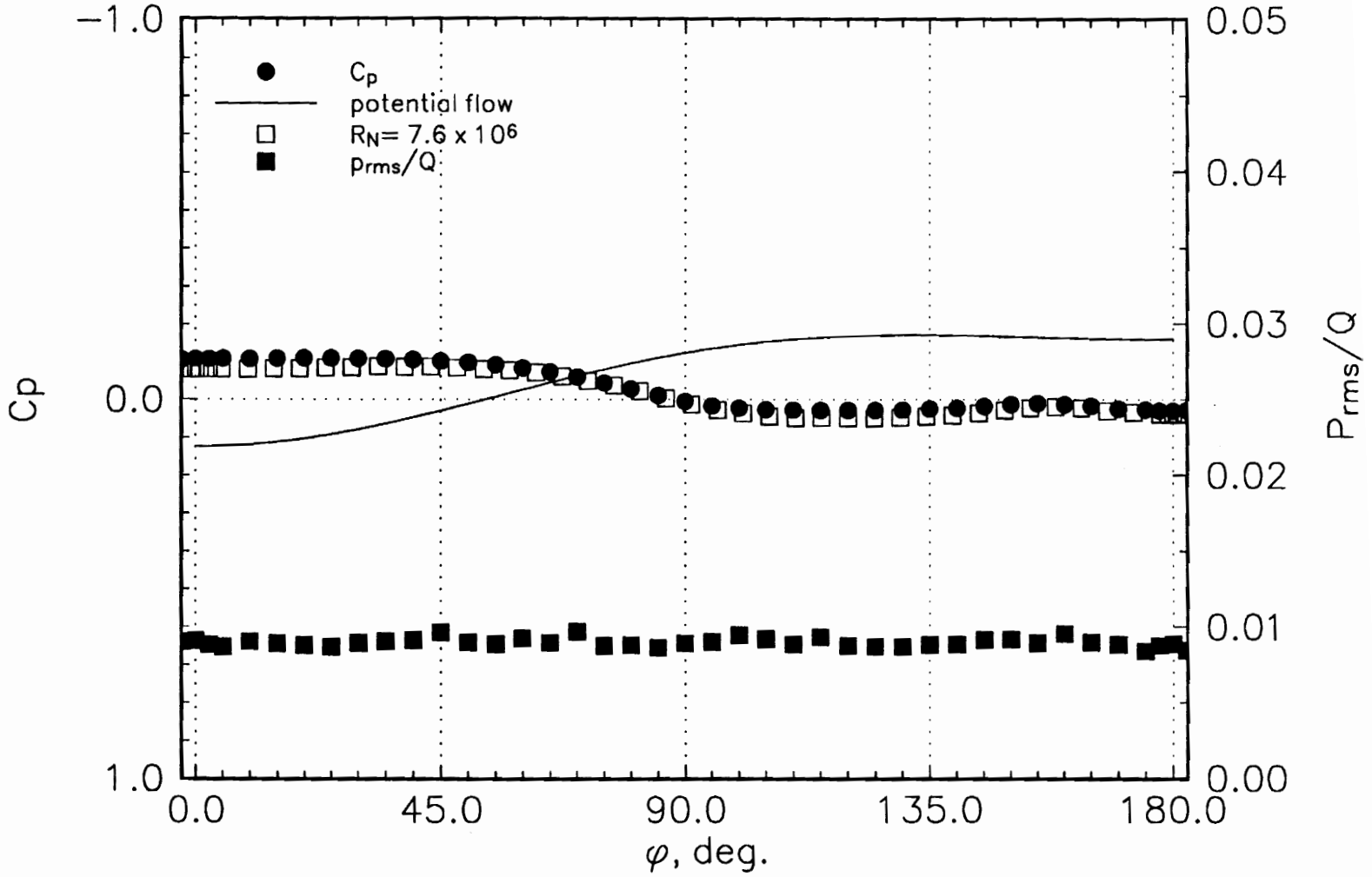

Figure 64. Mean and rms Pressure Distributions at $x/L = 0.8962$, $\alpha = 10$ deg, $Re_L = 4.20 \times 10^6$. $R_N = 7.6 \times 10^6$ Data from Meier *et al.* (1986).

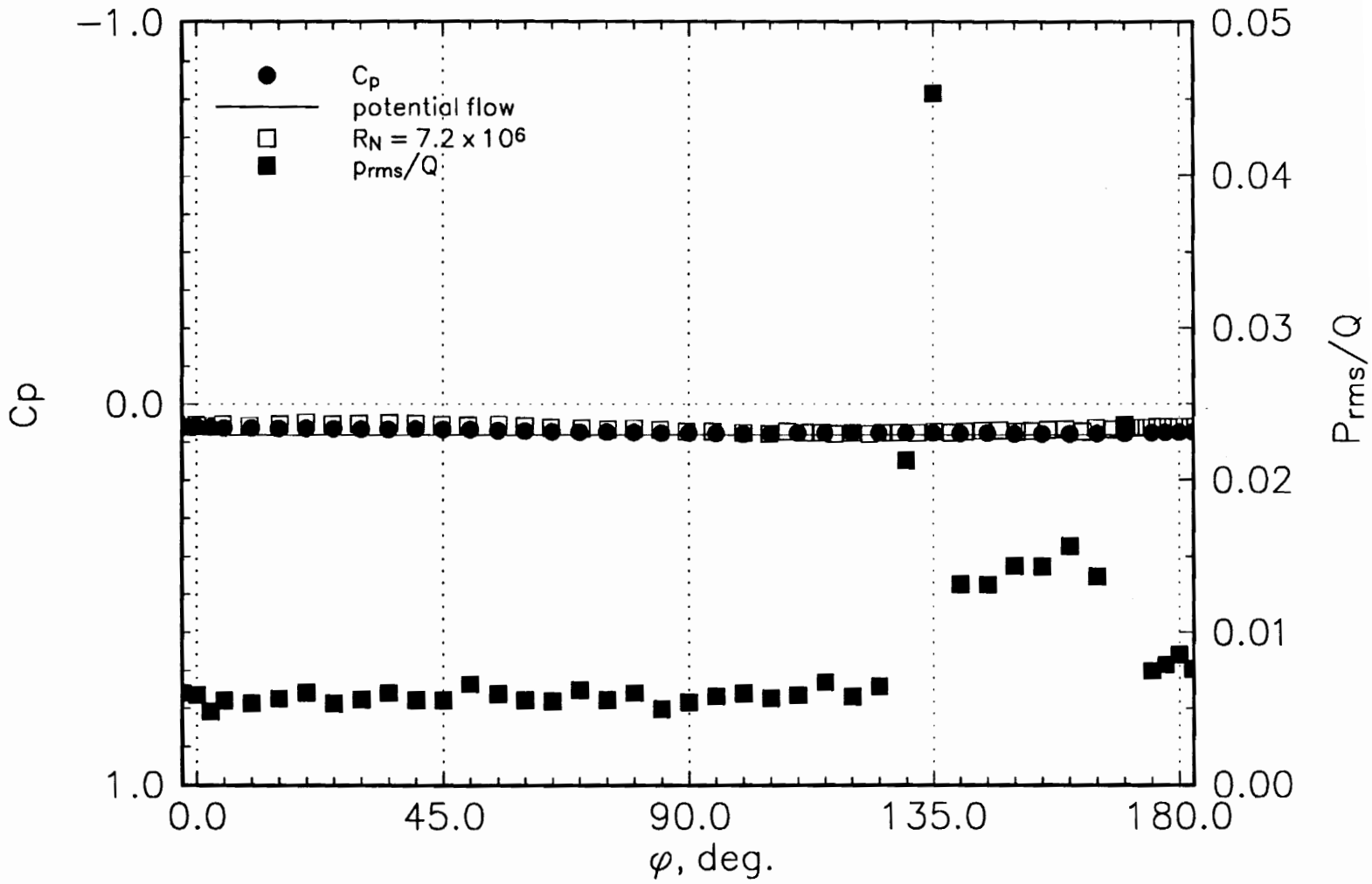

Figure 65. Mean and rms Pressure Distributions at $x/L = 0.0000$, $\alpha = 30$ deg, $Re_L = 4.20 \times 10^6$. $R_N = 7.2 \times 10^6$ Data from Meier *et al.* (Ragab, 1989).

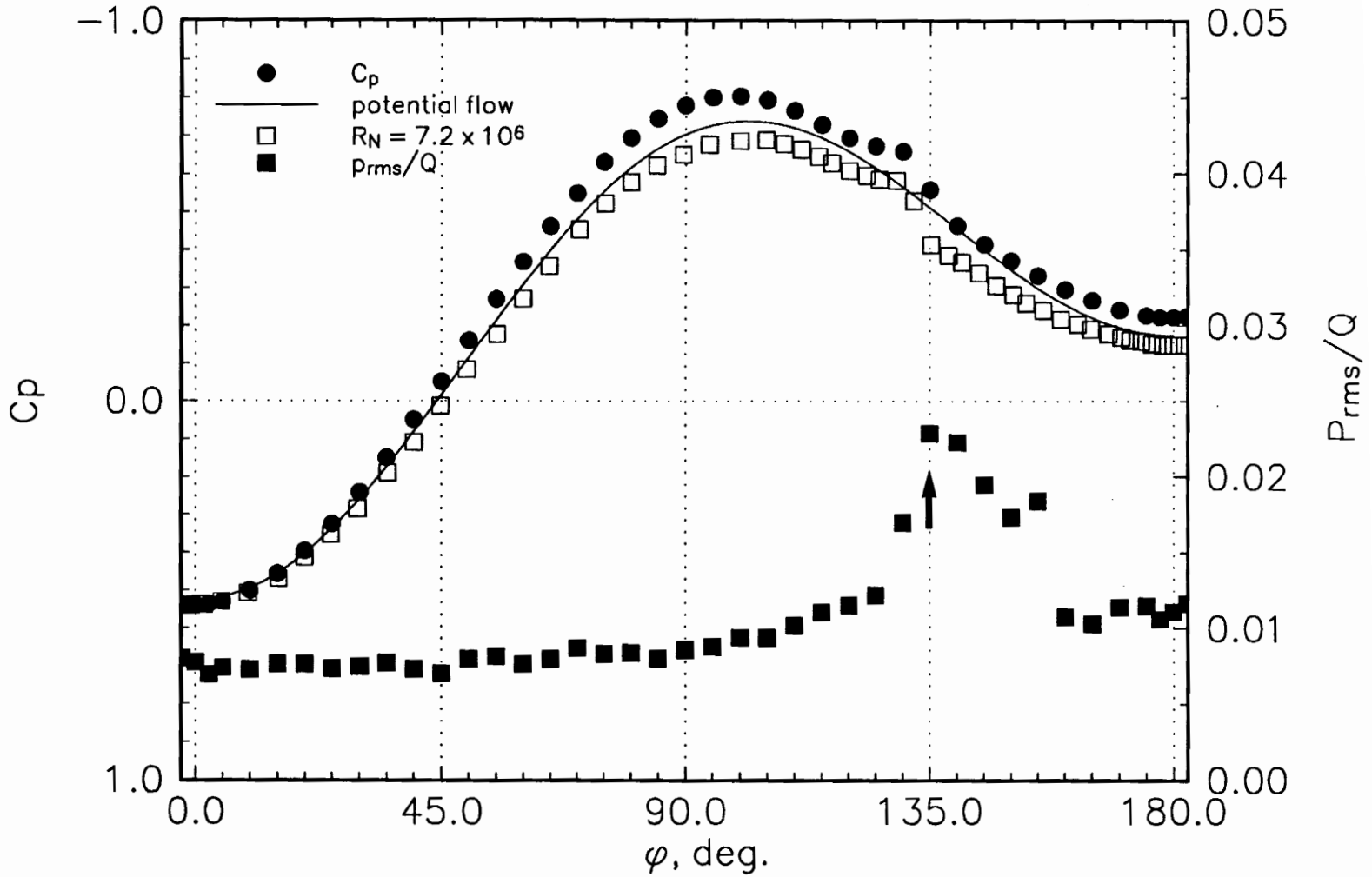

Figure 66. Mean and rms Pressure Distributions at $x/L = 0.1079$, $\alpha = 30$ deg, $Re_L = 4.20 \times 10^6$. $R_N = 7.2 \times 10^6$ Data from Meier *et al.* (Ragab, 1989). The Arrow Denotes Laminar Separation Line.

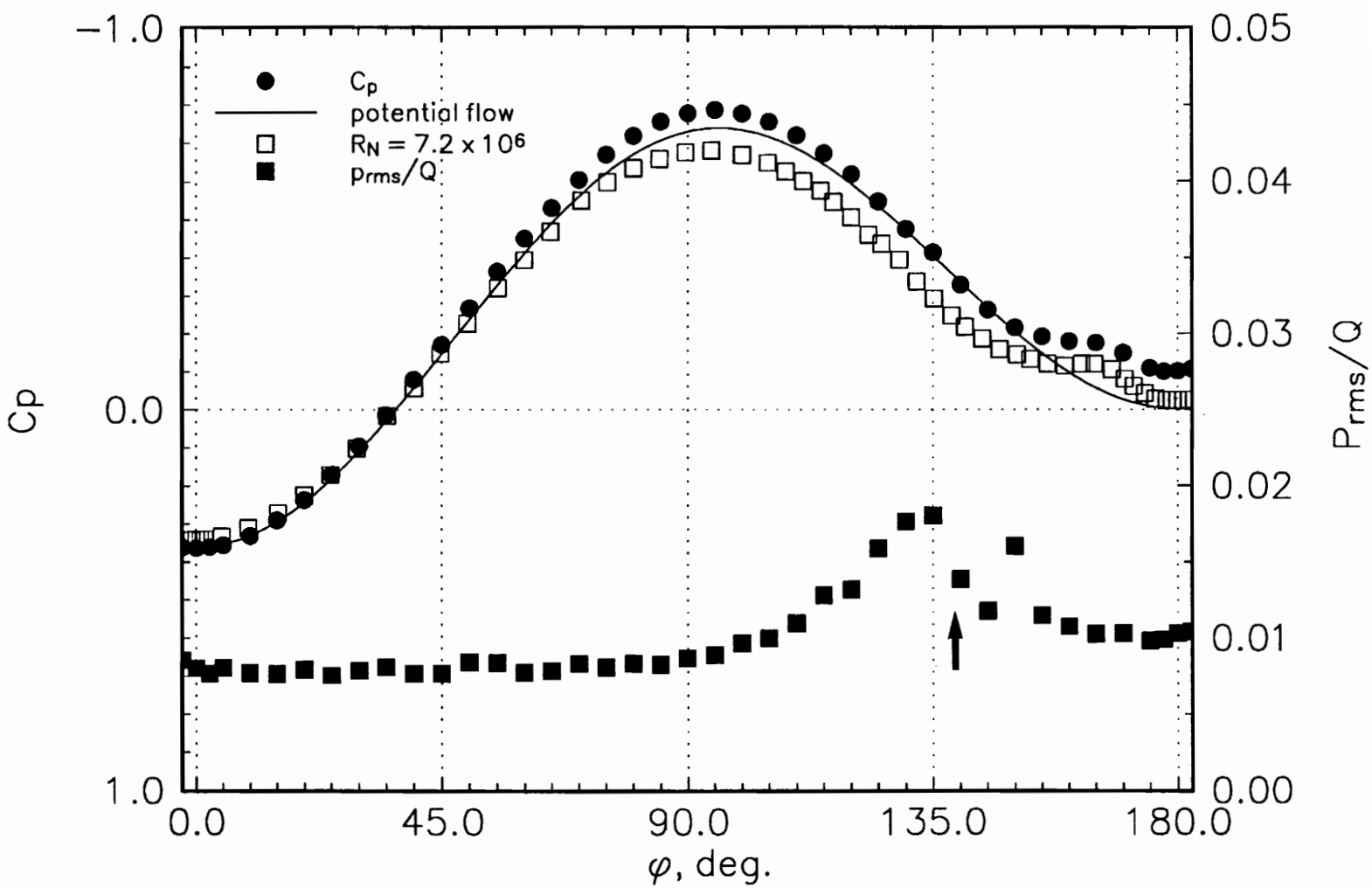

Figure 67. Mean and rms Pressure Distributions at $x/L = 0.2315$, $\alpha = 30$ deg, $Re_L = 4.20 \times 10^6$. $R_N = 7.2 \times 10^6$ Data from Meier *et al.* (Ragab, 1989). The Arrow Denotes Primary Separation Line.

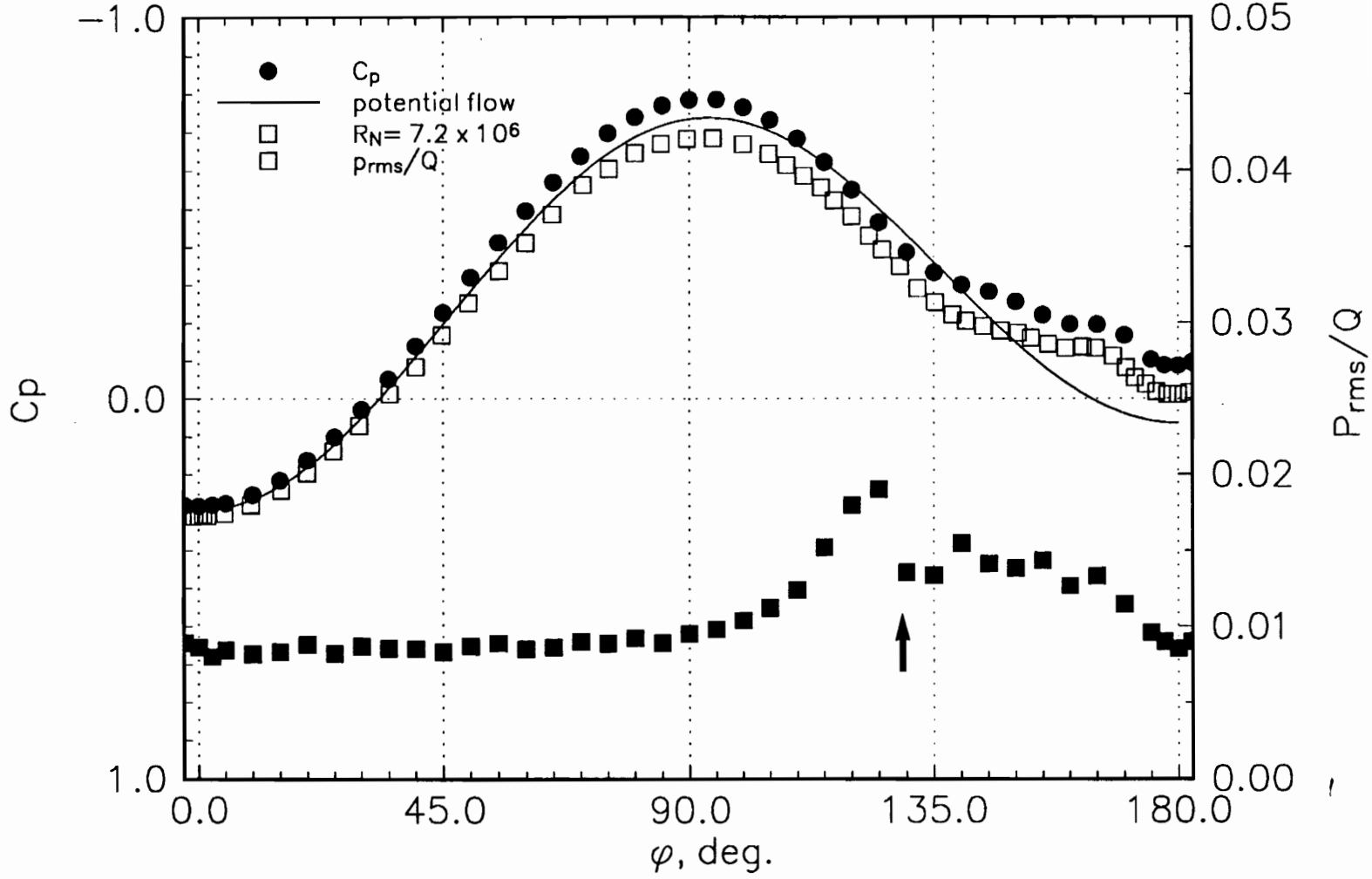

Figure 68. Mean and rms Pressure Distribution at $x/L = 0.3145$, $\alpha = 30$ deg, $Re_L = 4.20 \times 10^6$. $R_N = 7.2 \times 10^6$ Data from Meier *et al.* (Ragab, 1989). The Arrow Denotes Primary Separation Line.

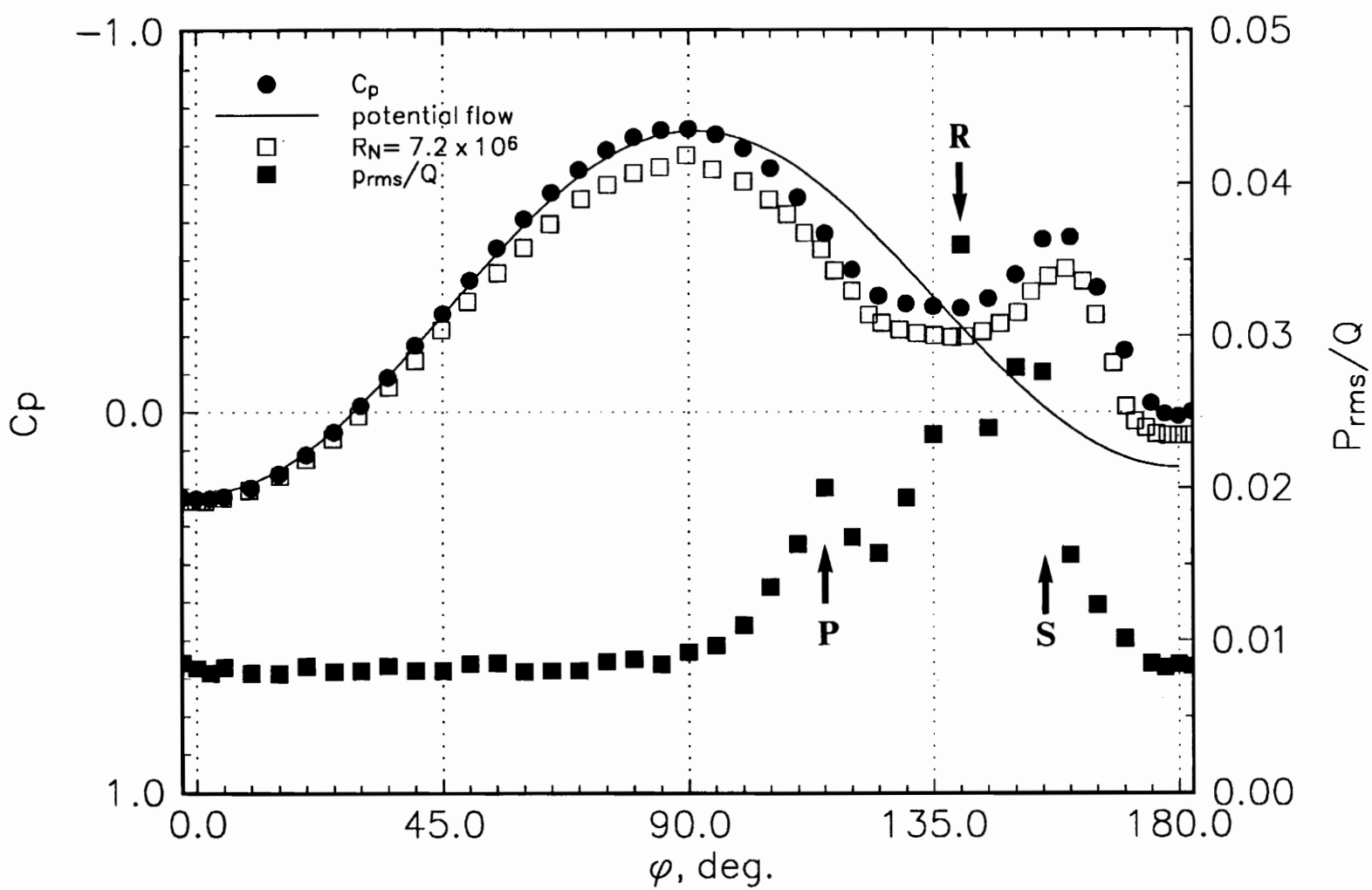

Figure 69. Mean and rms Pressure Distribution at $x/L = 0.4396$, $\alpha = 30$ deg, $Re_L = 4.20 \times 10^6$. $R_N = 7.2 \times 10^6$ Data from Meier *et al.* (Ragab, 1989). The Arrows Denote Primary, Secondary Separation, and Reattachment Lines.

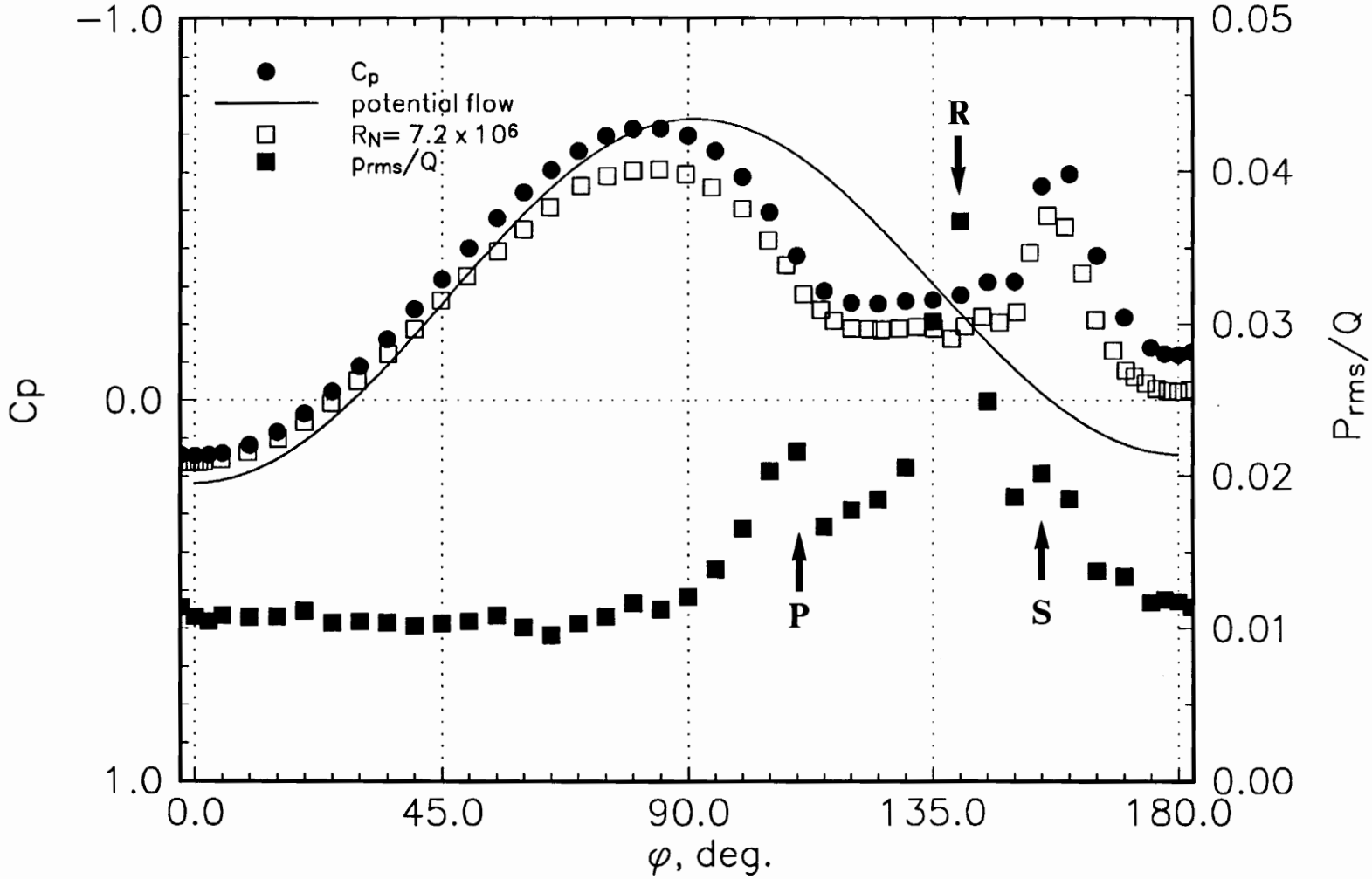

Figure 70. Mean and rms Pressure Distribution at $x/L = 0.5646$, $\alpha = 30$ deg, $Re_L = 4.20 \times 10^6$. $R_N = 7.2 \times 10^6$ Data from Meier *et al.* (Ragab, 1989). The Arrows Denote Primary, Secondary Separation, and Reattachment Lines.

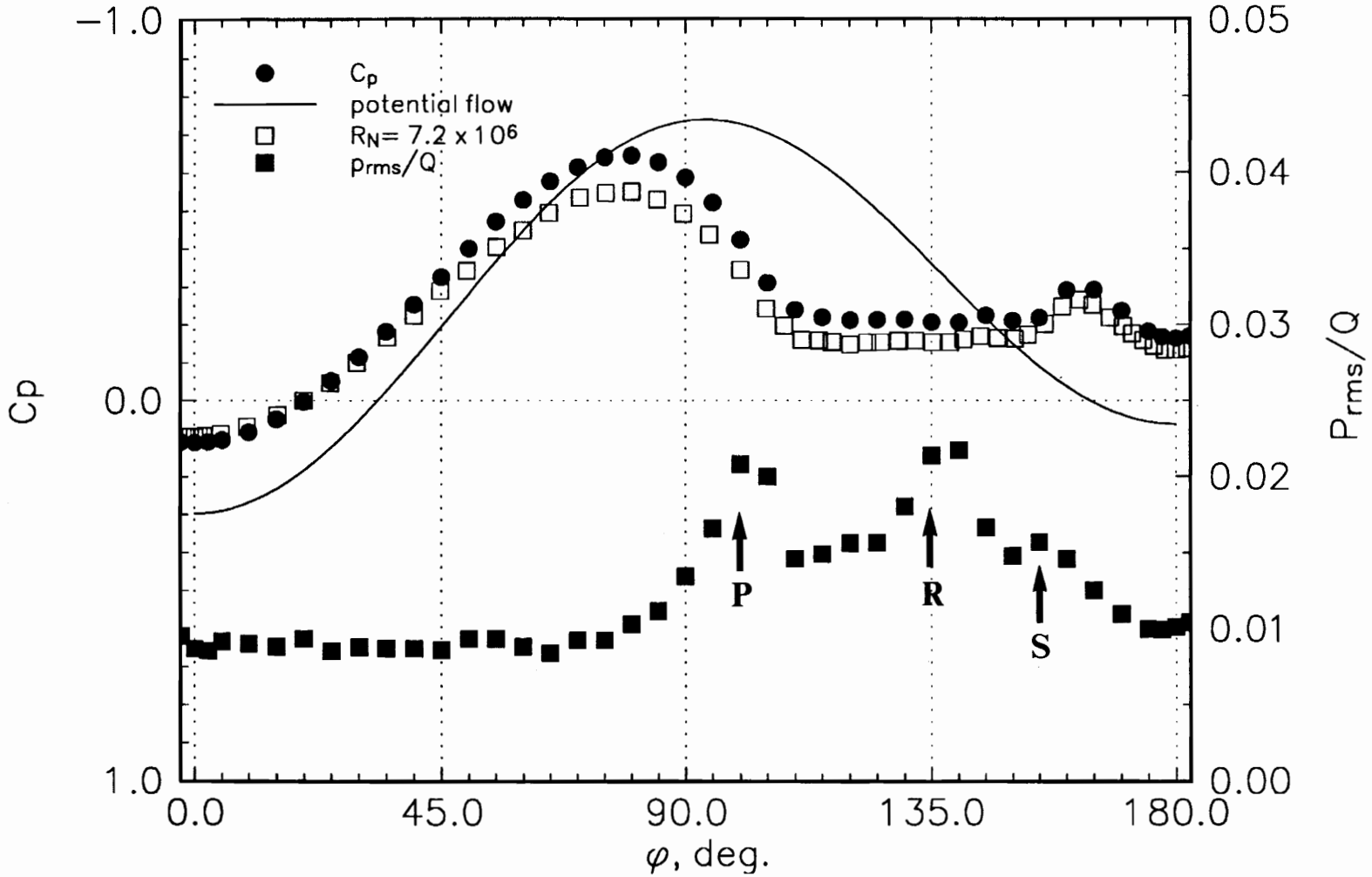

Figure 71. Mean and rms Pressure Distribution at $x/L = 0.6892$, $\alpha = 30$ deg, $Re_L = 4.20 \times 10^6$. $R_N = 7.2 \times 10^6$ Data from Meier *et al.* (Ragab, 1989). The Arrows Denote Primary, Secondary Separation, and Reattachment Lines.

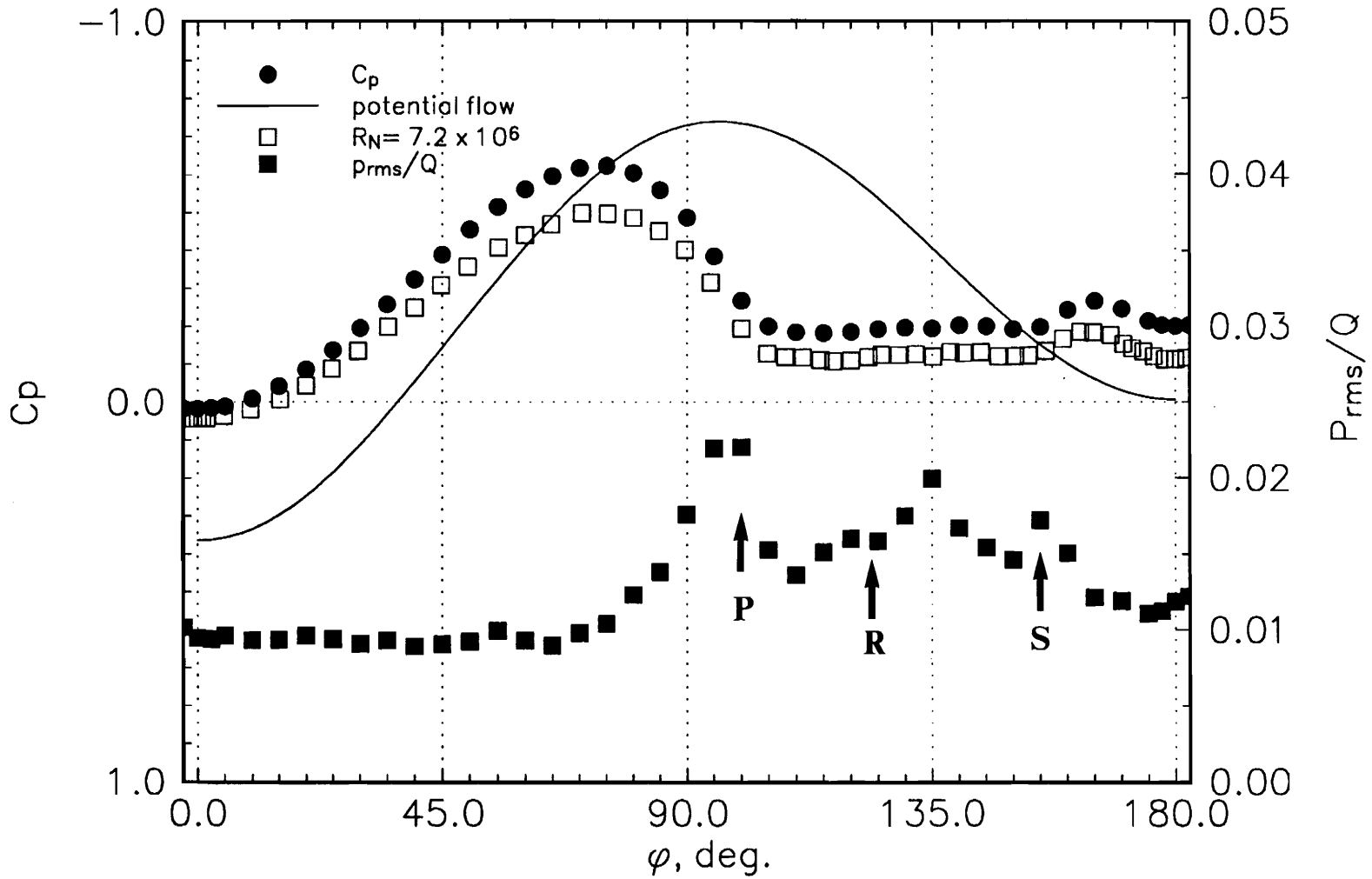

Figure 72. Mean and rms Pressure Distribution at $x/L = 0.7725$, $\alpha = 30$ deg, $Re_L = 4.20 \times 10^6$. $R_N = 7.2 \times 10^6$ Data from Meier *et al.* (Ragab, 1989). The Arrows Denote Primary, Secondary Separation, and Reattachment Lines.

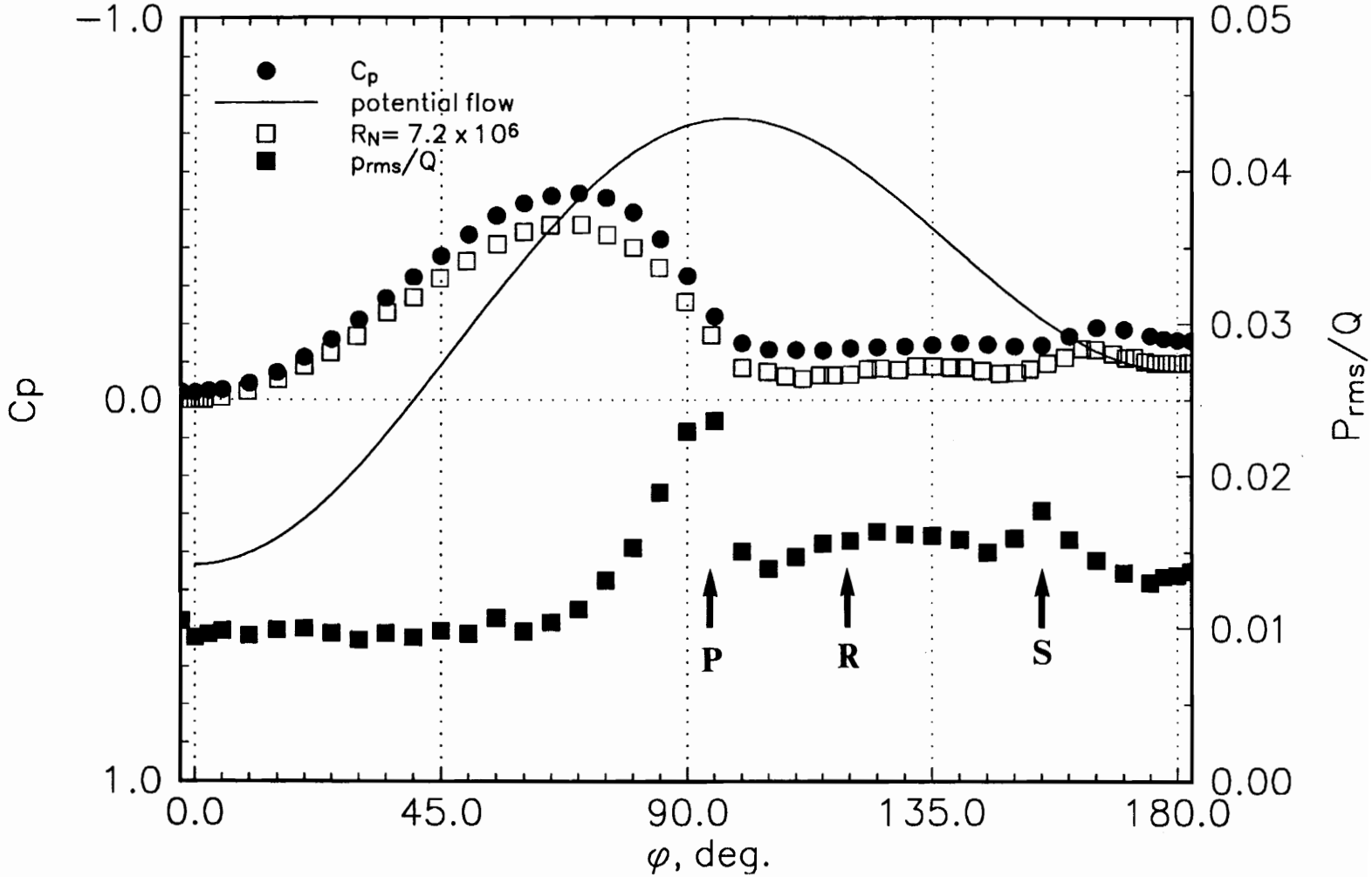

Figure 73. Mean and rms Pressure Distribution at $x/L = 0.8346$, $\alpha = 30$ deg, $Re_L = 4.20 \times 10^6$. $R_N = 7.2 \times 10^6$ Data from Meier *et al.* (Ragab, 1989). The Arrows Denote Primary, Secondary Separation, and Reattachment Lines.

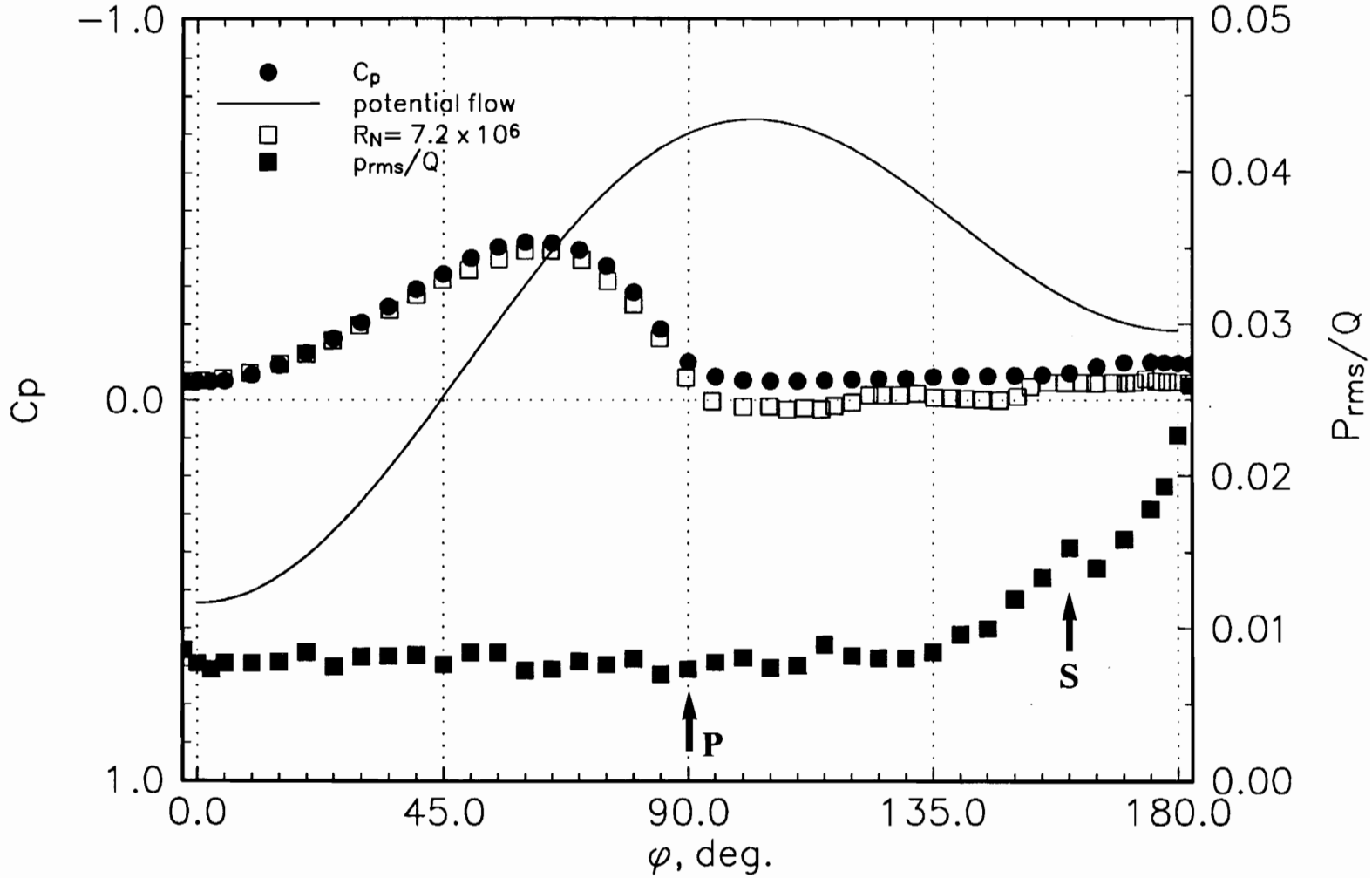

Figure 74. Mean and rms Pressure Distribution at $x/L = 0.8962$, $\alpha = 30$ deg, $Re_L = 4.20 \times 10^6$. $R_N = 7.2 \times 10^6$ Data from Meier *et al.* (Ragab, 1989). The Arrows Denote Primary and Secondary Separation Lines.

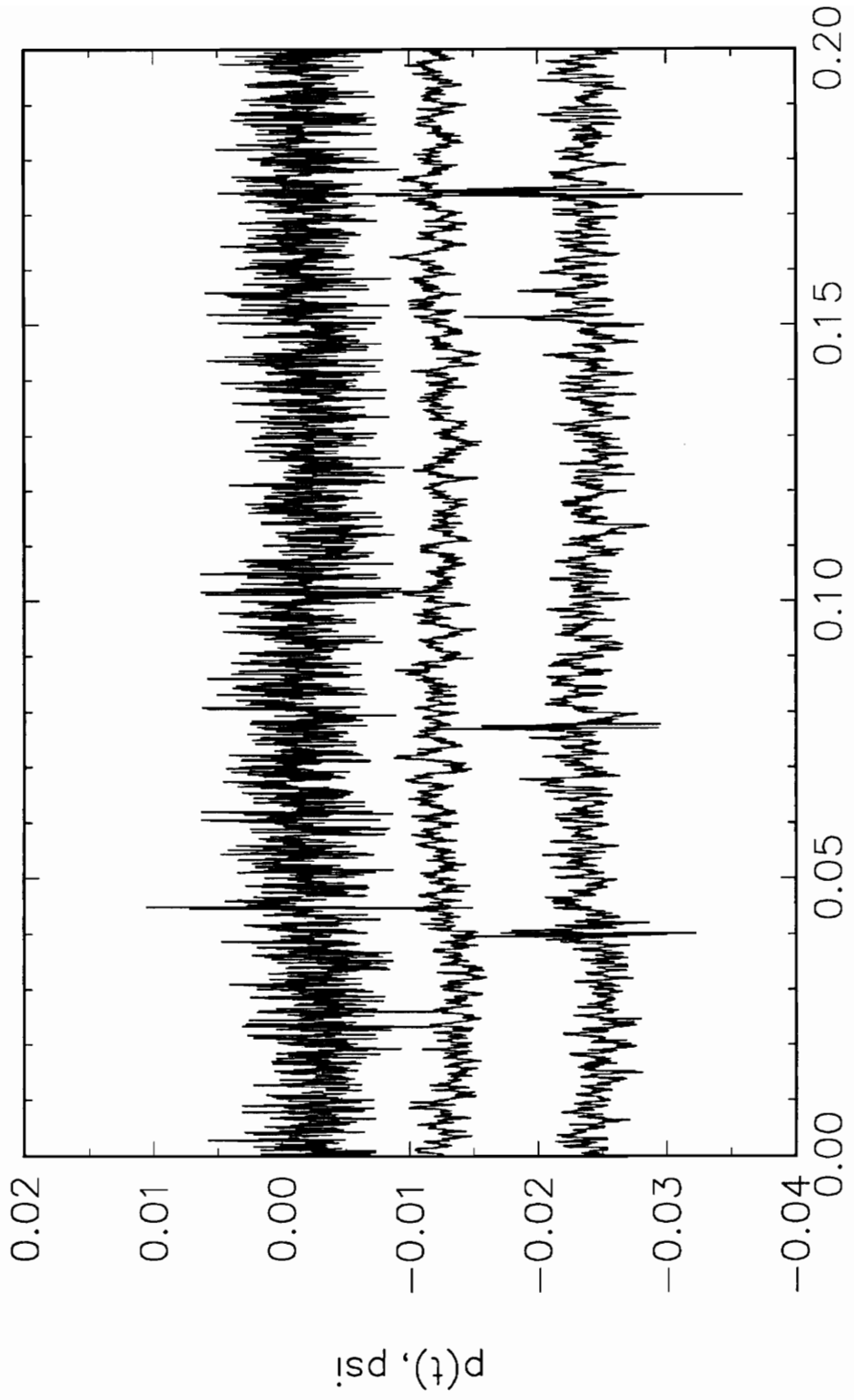

Figure 75. Temporal Signal of Pressure Fluctuation. $\phi = 0.0$ deg., x/L = 0.8962, 0.1079, 0.6892, from top to bottom.

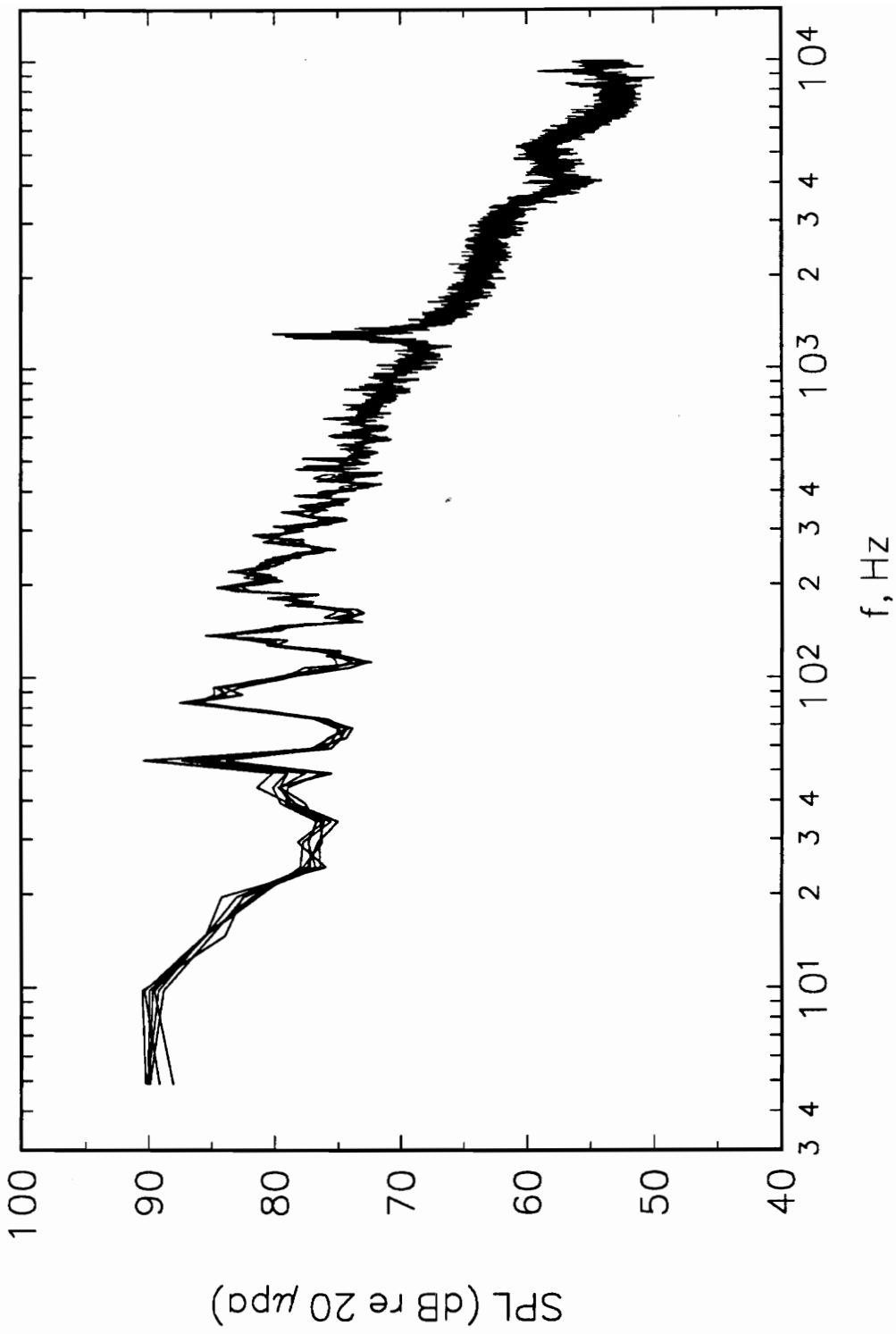

Figure 76. Tunnel Acoustic Noise Signature.

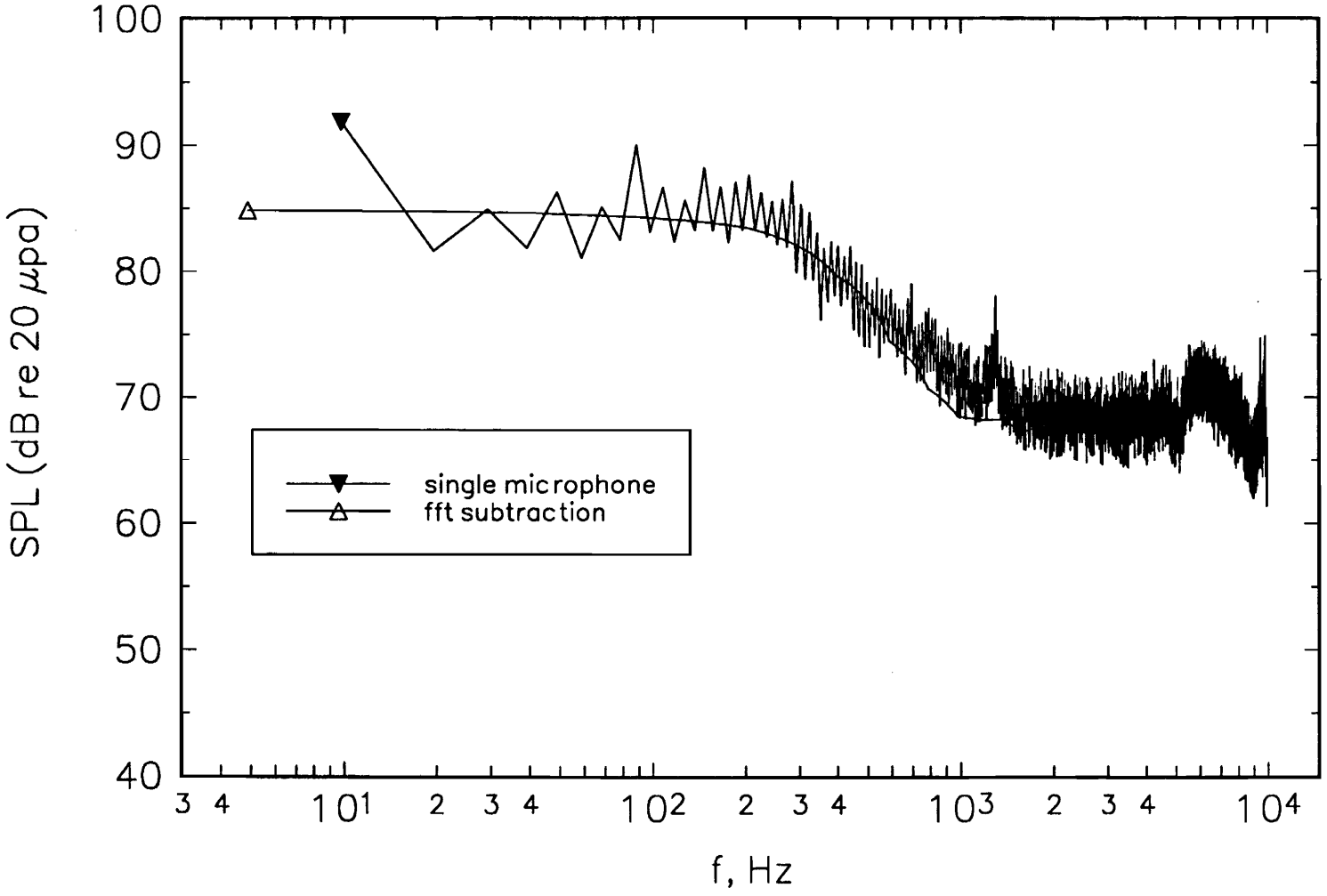

Figure 77. Comparison of the Noise Cancellation Techniques. $\alpha = 30$ deg., x/L = 0.7725, $\phi = 180$ deg.

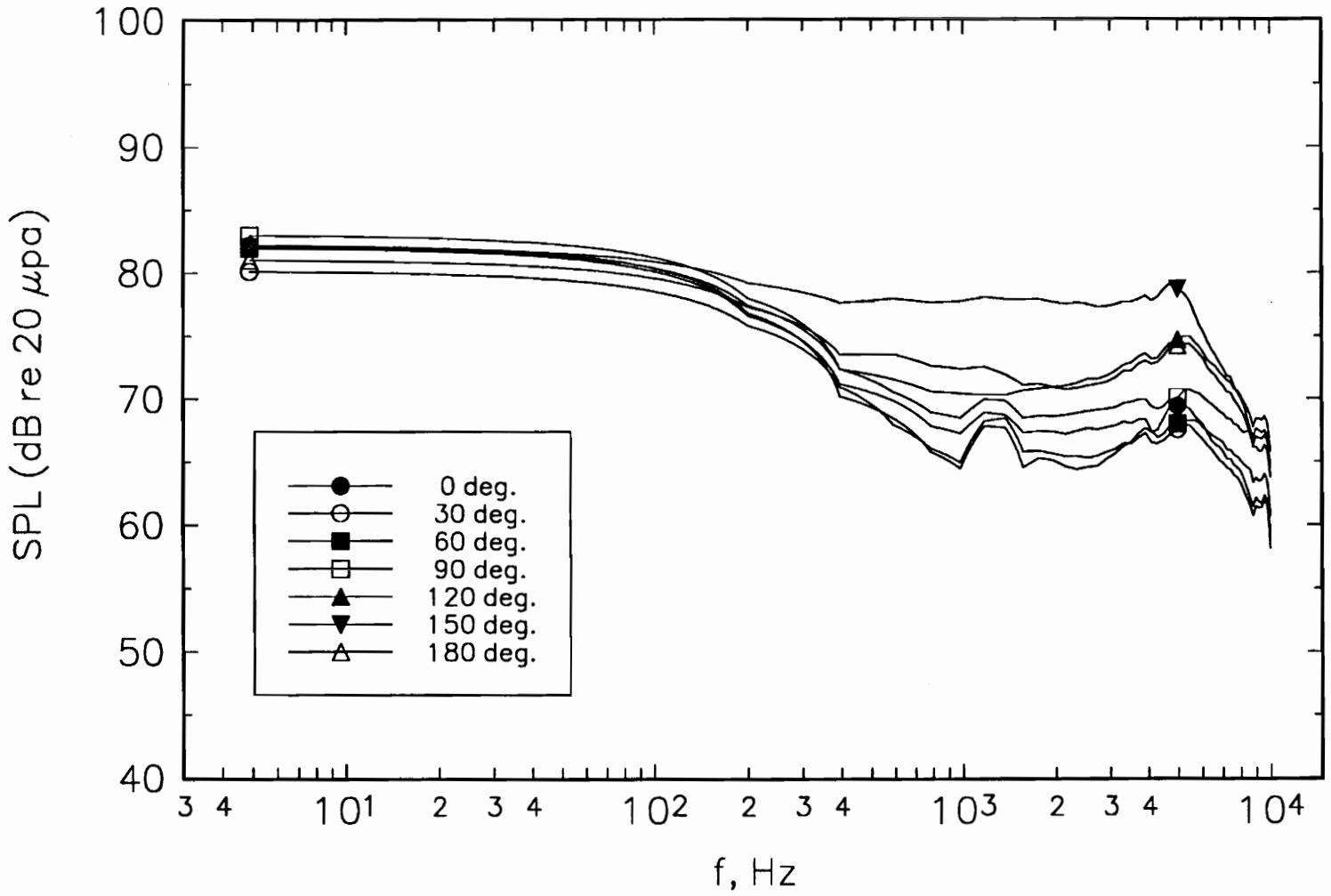

Figure 78. Surface Pressure Spectrum at $x/L = 0.2315$, $\alpha = 30$ deg, $Re_L = 4.20 \times 10^6$; Noise Spectrum Subtraction.

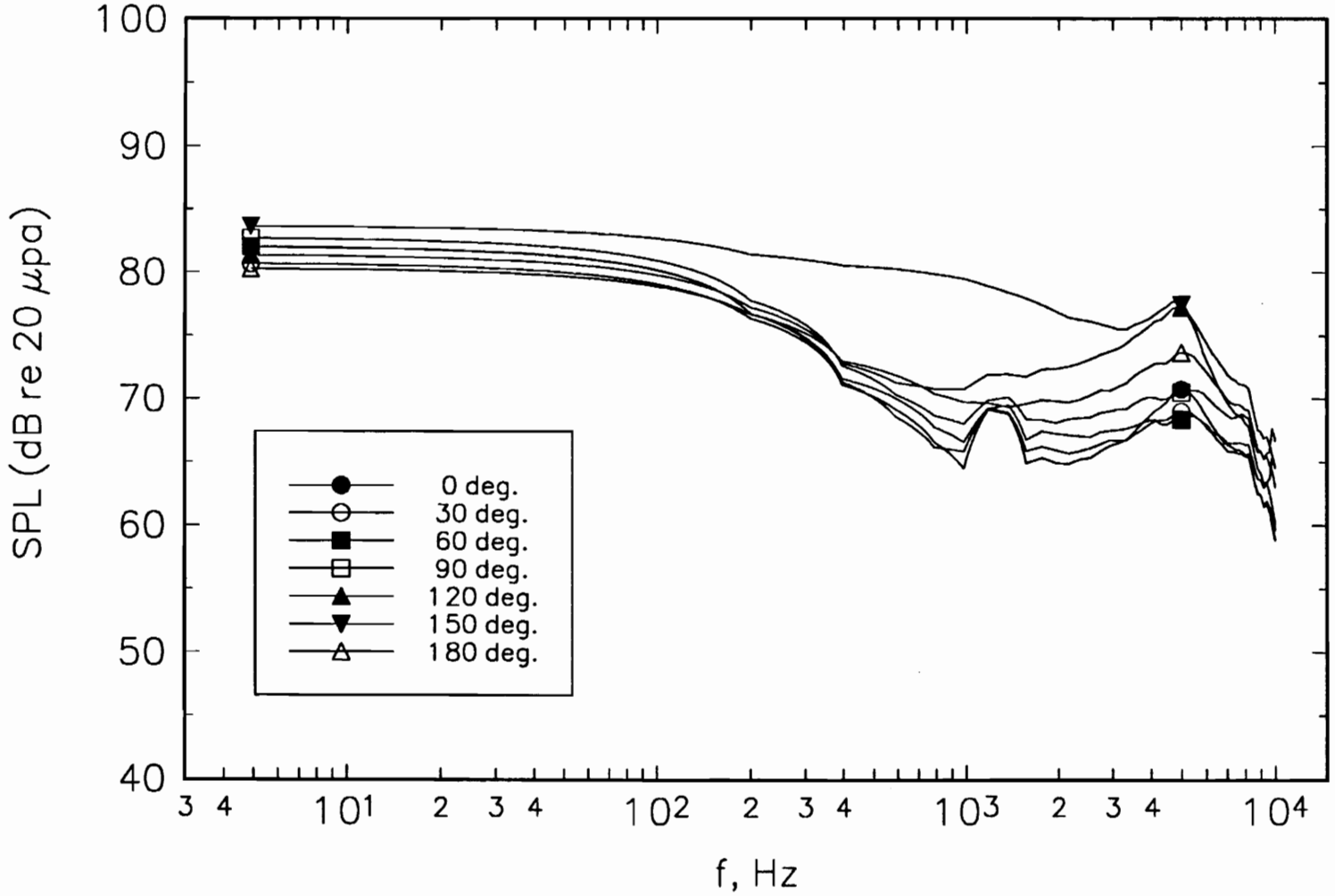

Figure 79. Surface Pressure Spectrum at $x/L = 0.3145$, $\alpha = 30$ deg, $Re_L = 4.20 \times 10^6$; Noise Spectrum Subtraction.

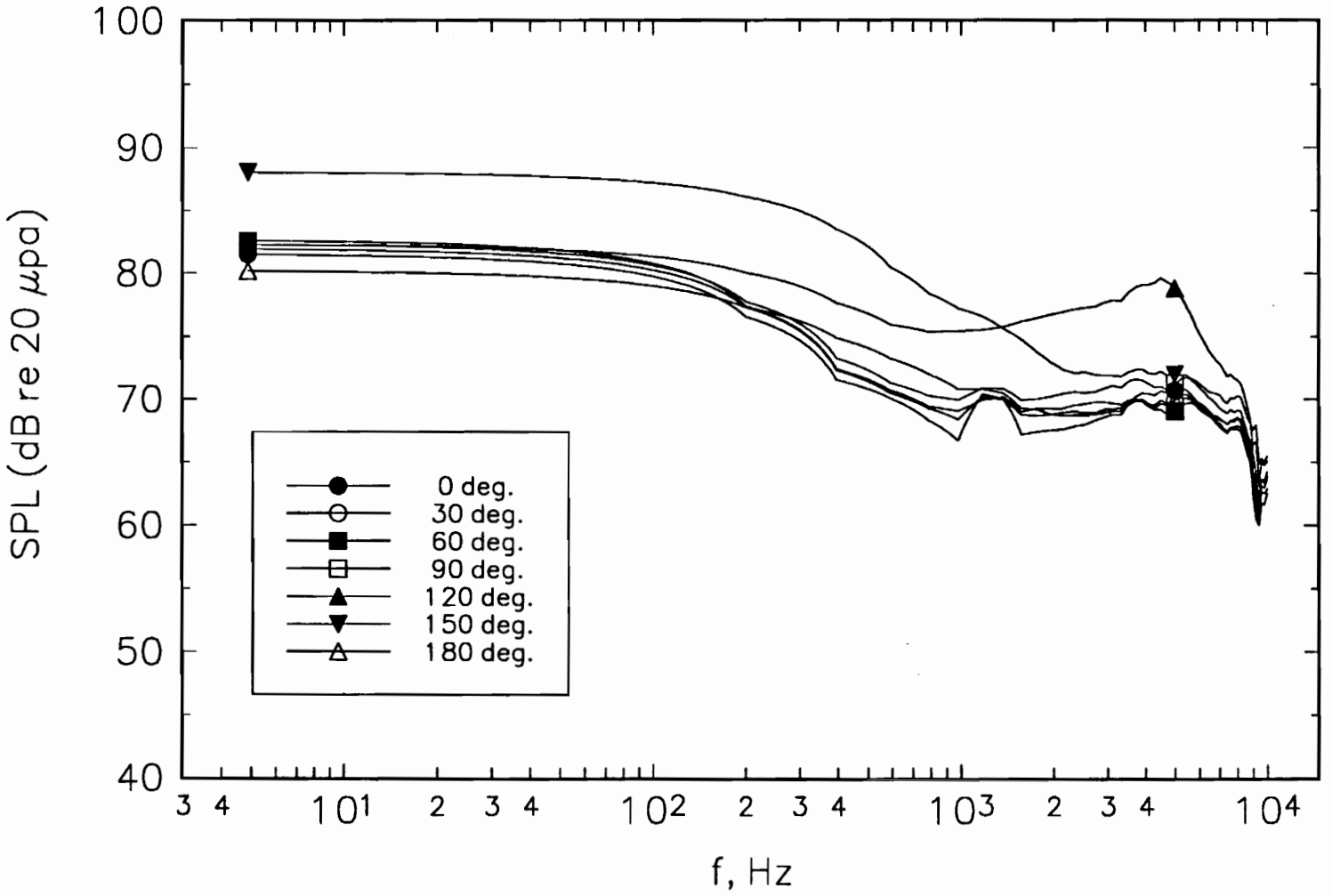

Figure 80. Surface Pressure Spectrum at $x/L = 0.4396$, $\alpha = 30$ deg, $Re_L = 4.20 \times 10^6$; Noise Spectrum Subtraction.

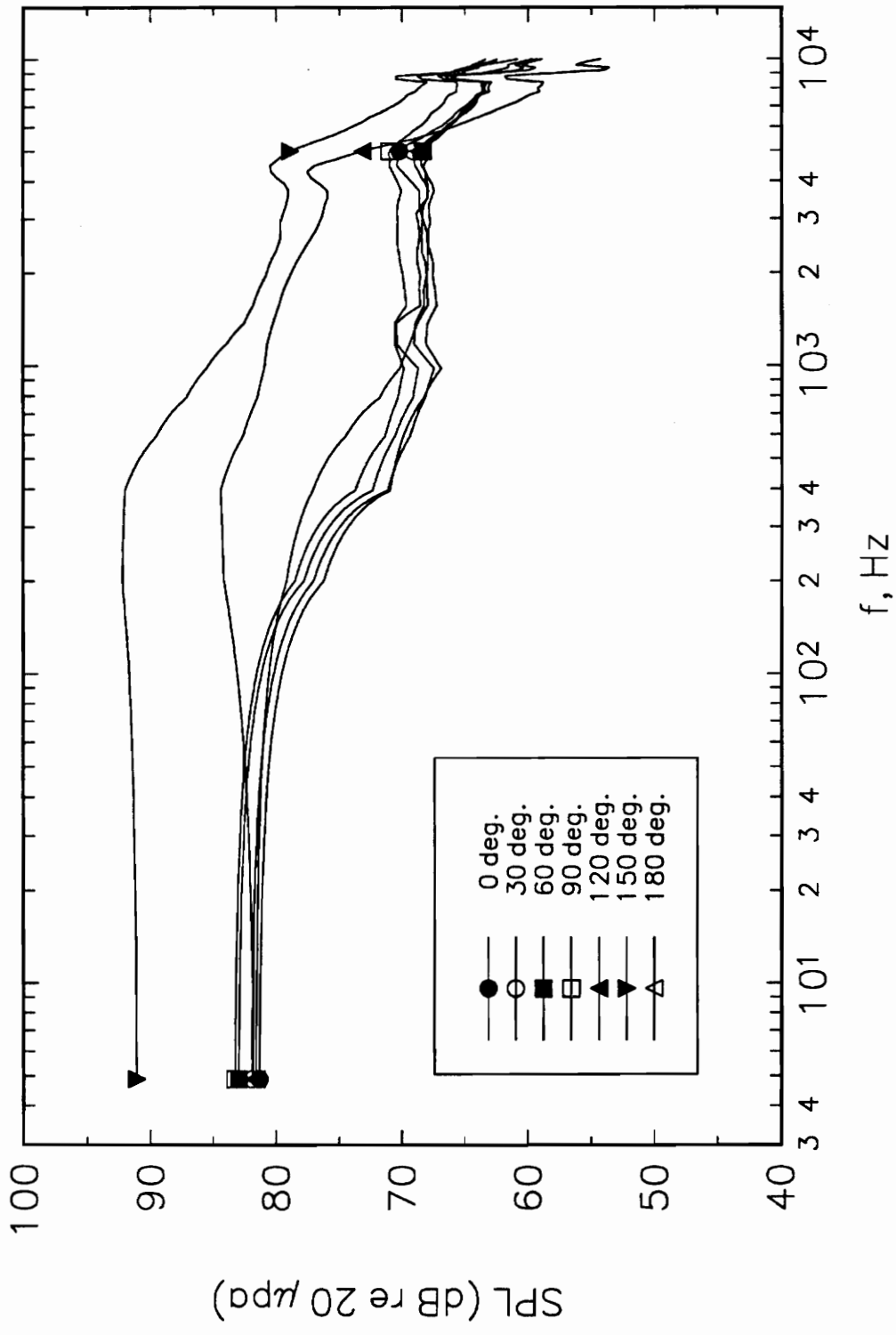

Figure 81. Surface Pressure Spectrum at $x/L = 0.5646$, $\alpha = 30$ deg, $Re_L = 4.20 \times 10^6$; Noise Spectrum Subtraction.

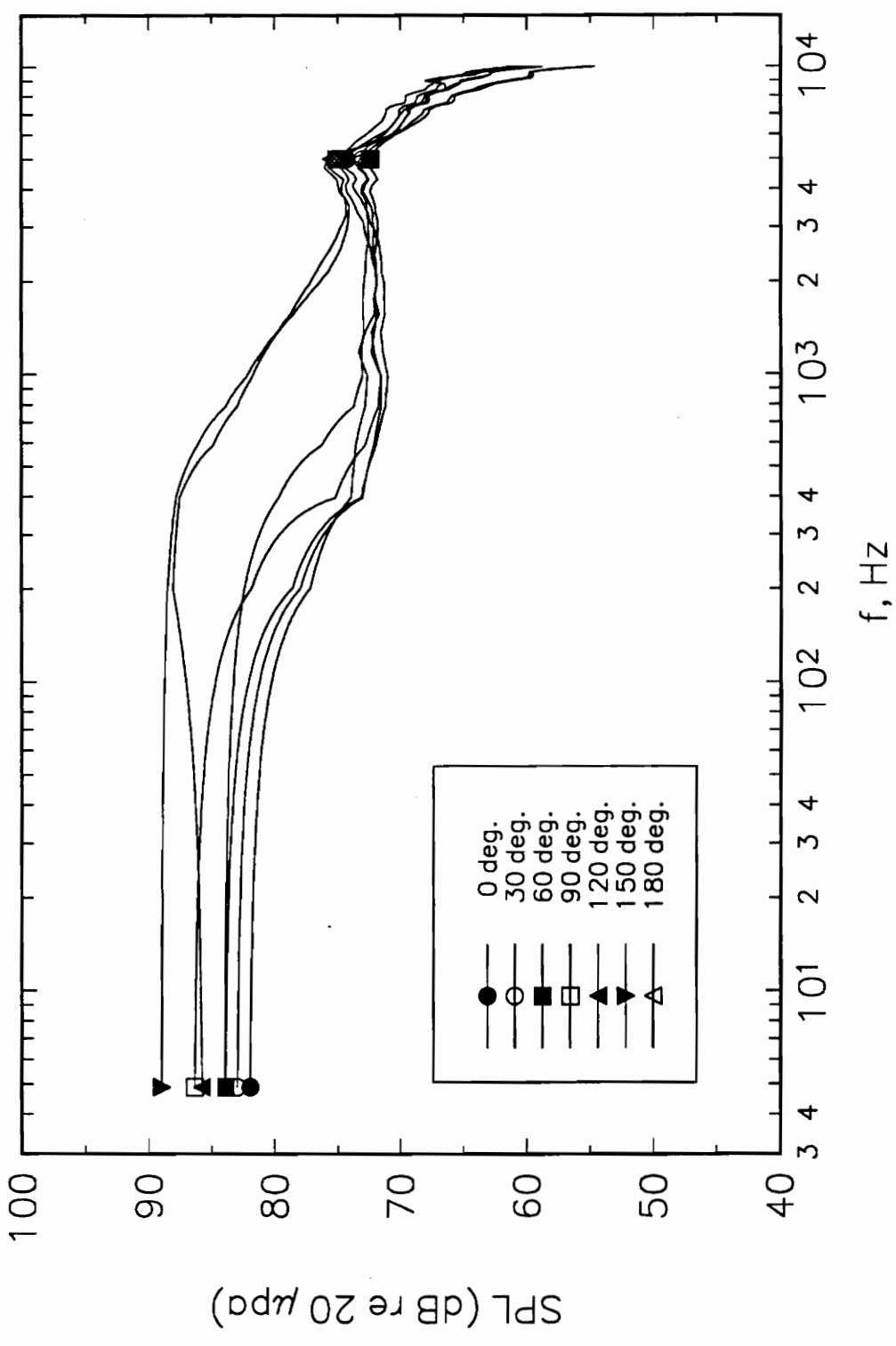

Figure 82. Surface Pressure Spectrum at $x/L = 0.6892$, $\alpha = 30$ deg, $Re_L = 4.20 \times 10^6$; Noise Spectrum Subtraction.

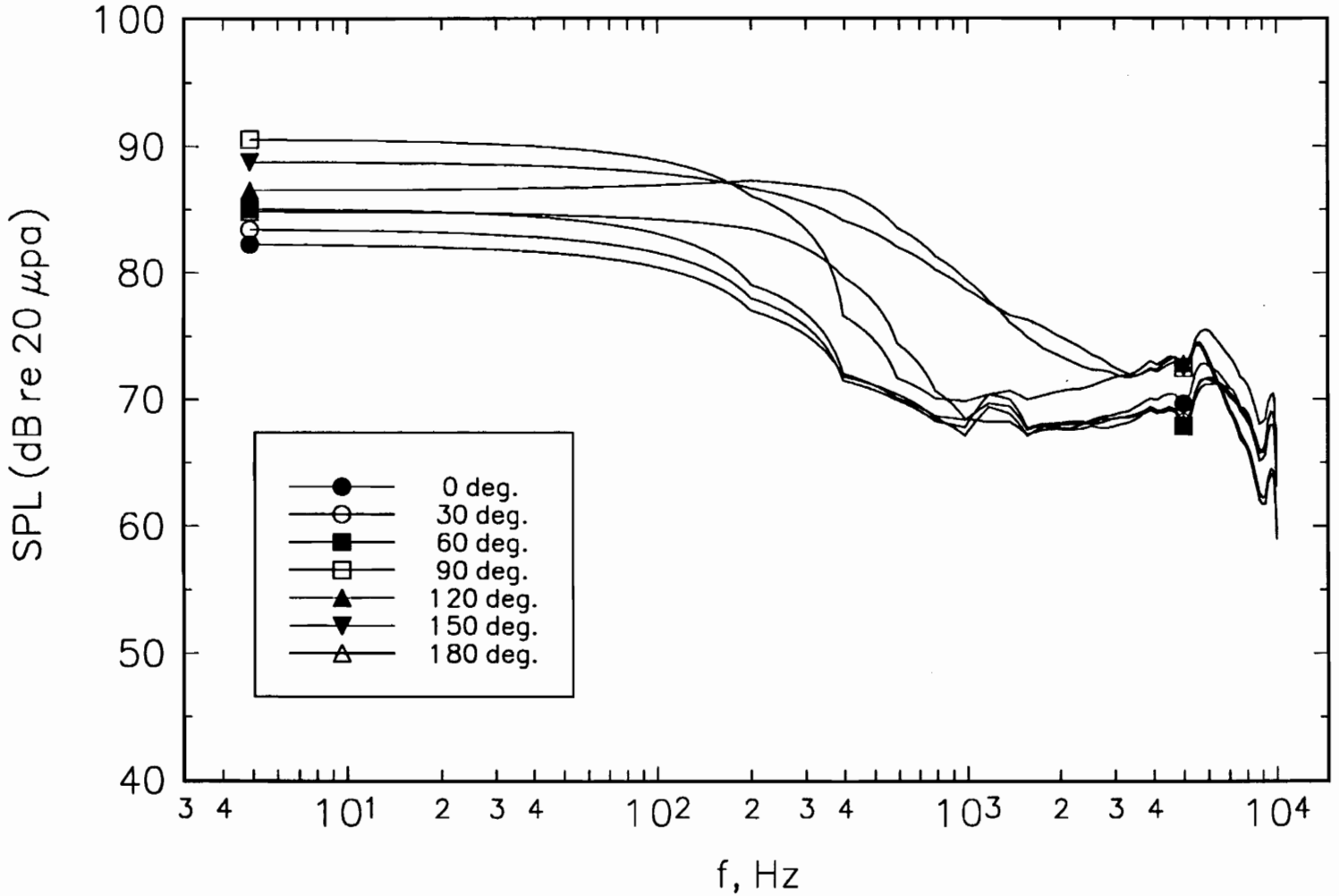

Figure 83. Surface Pressure Spectrum at $x/L = 0.7725$, $\alpha = 30$ deg, $Re_L = 4.20 \times 10^6$; Noise Spectrum Subtraction.

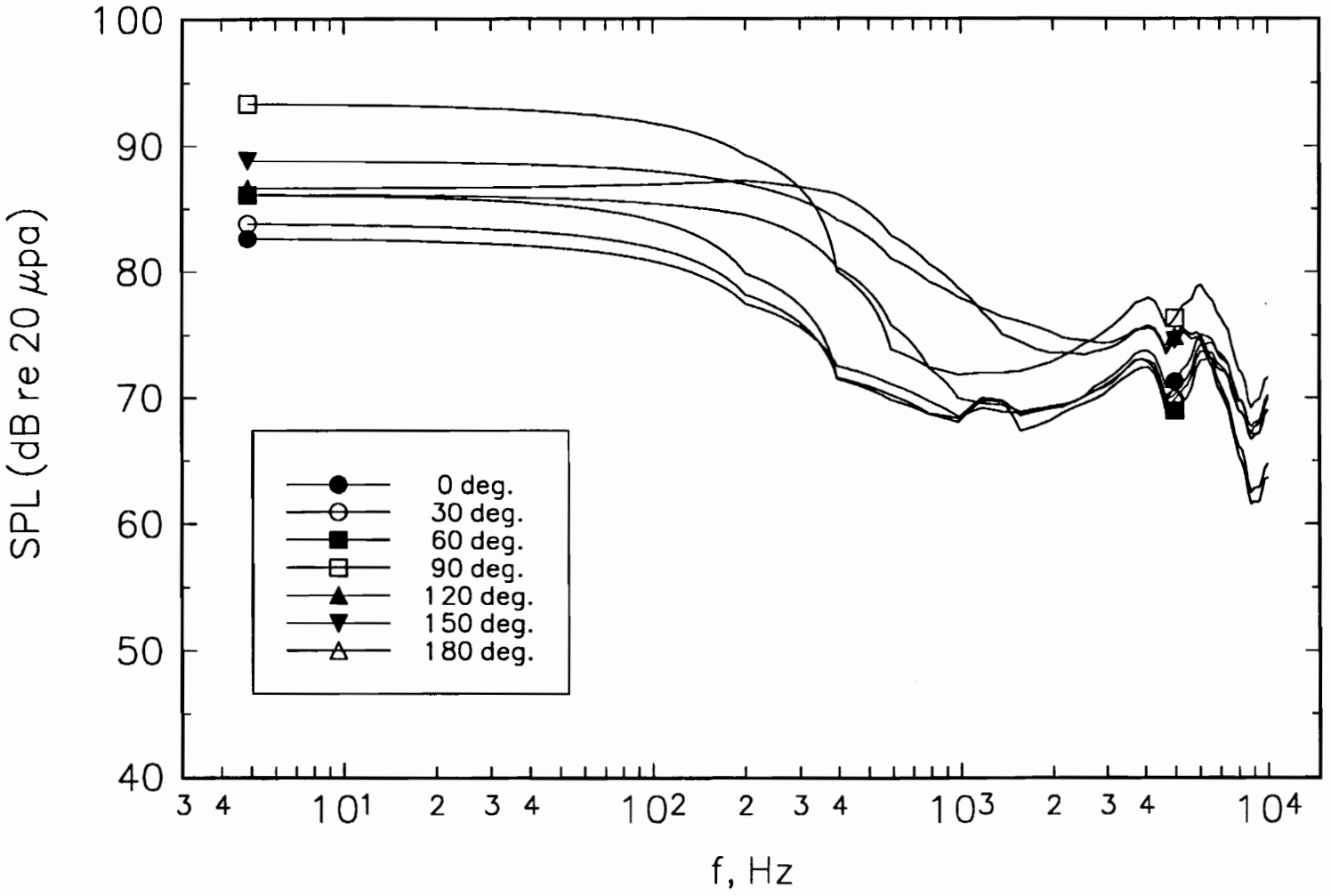

Figure 84. Surface Pressure Spectrum at $x/L = 0.8346$, $\alpha = 30$ deg, $Re_L = 4.20 \times 10^6$; Noise Spectrum Subtraction.

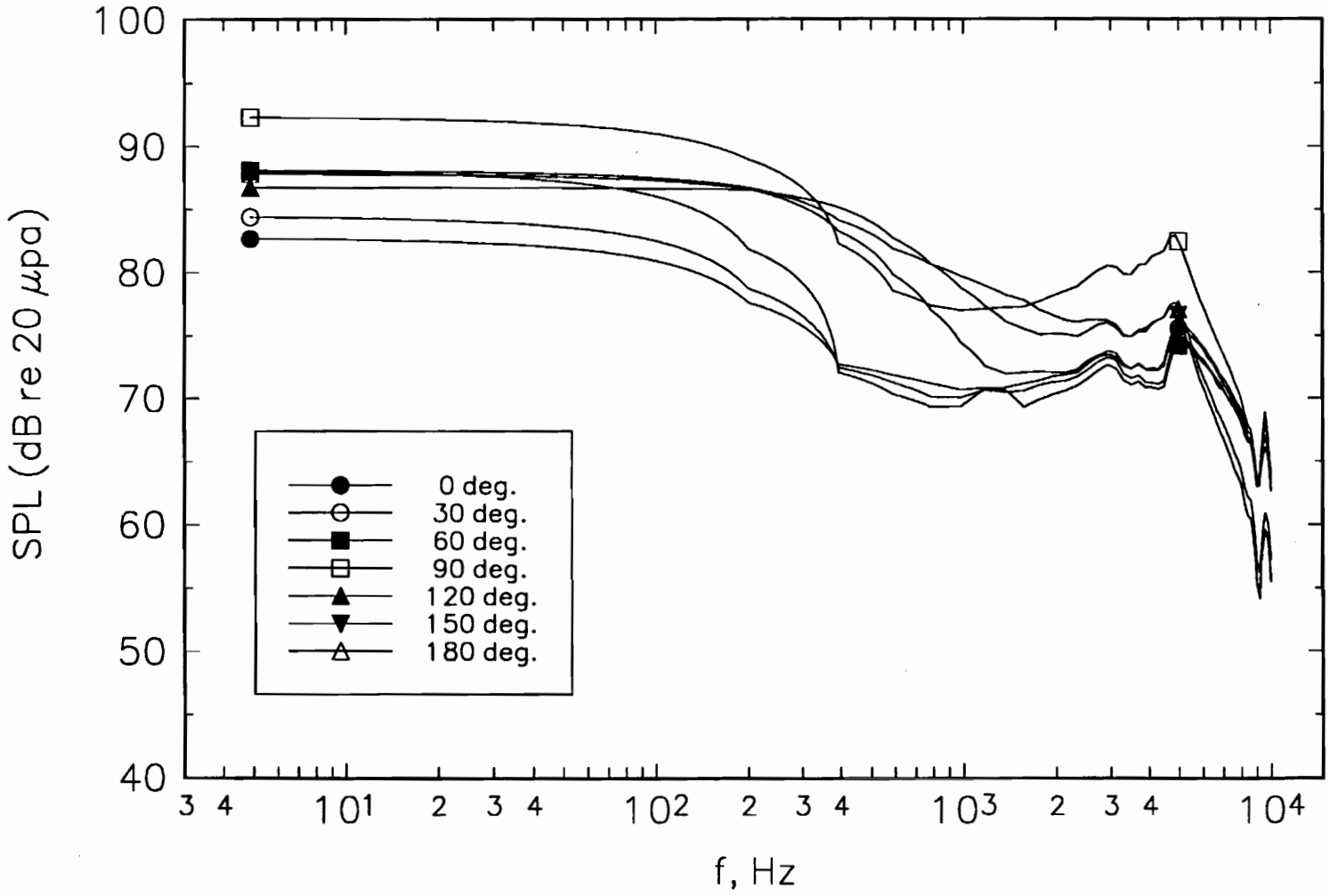

Figure 85. Surface Pressure Spectrum at $x/L = 0.8962$, $\alpha = 30$ deg, $Re_L = 4.20 \times 10^6$; Noise Spectrum Subtraction.

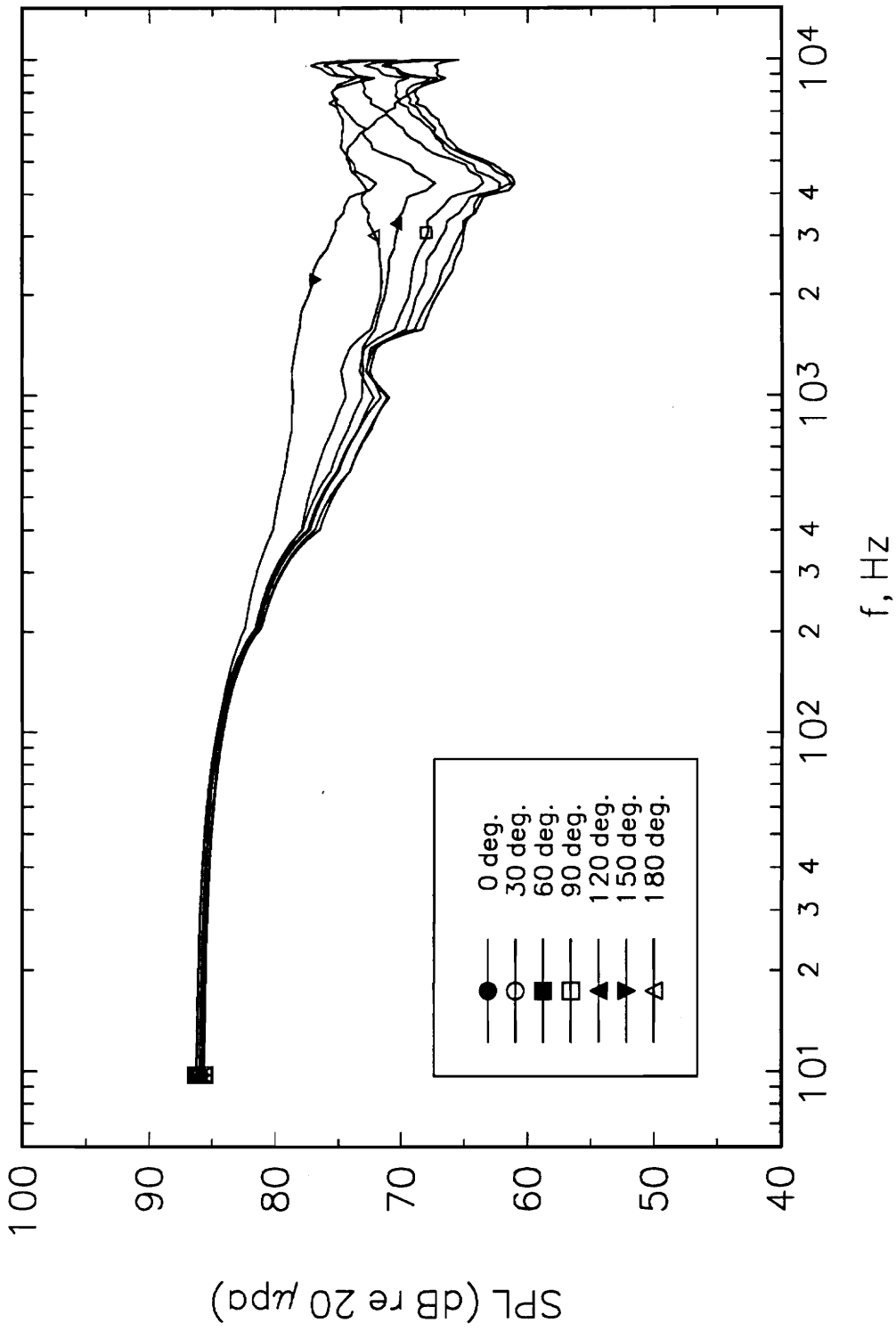

Figure 86. Surface Pressure Spectrum at $x/L = 0.2315$, $\alpha = 30$ deg, $Re_L = 4.20 \times 10^6$; Single Signal with Time Delay.

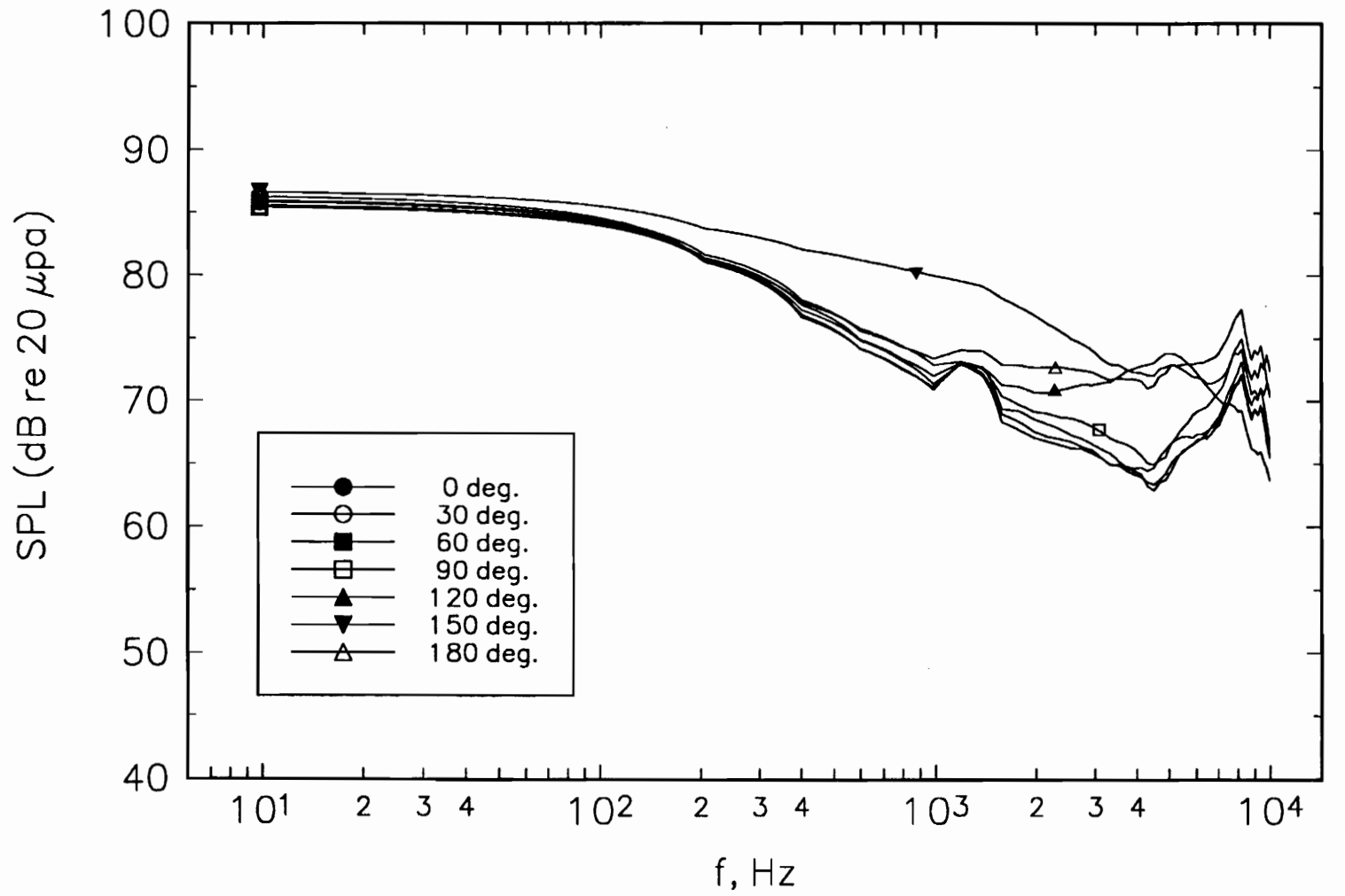

Figure 87. Surface Pressure Spectrum at $x/L = 0.3145$, $\alpha = 30$ deg, $Re_L = 4.20 \times 10^6$; Single Signal with Time Delay.

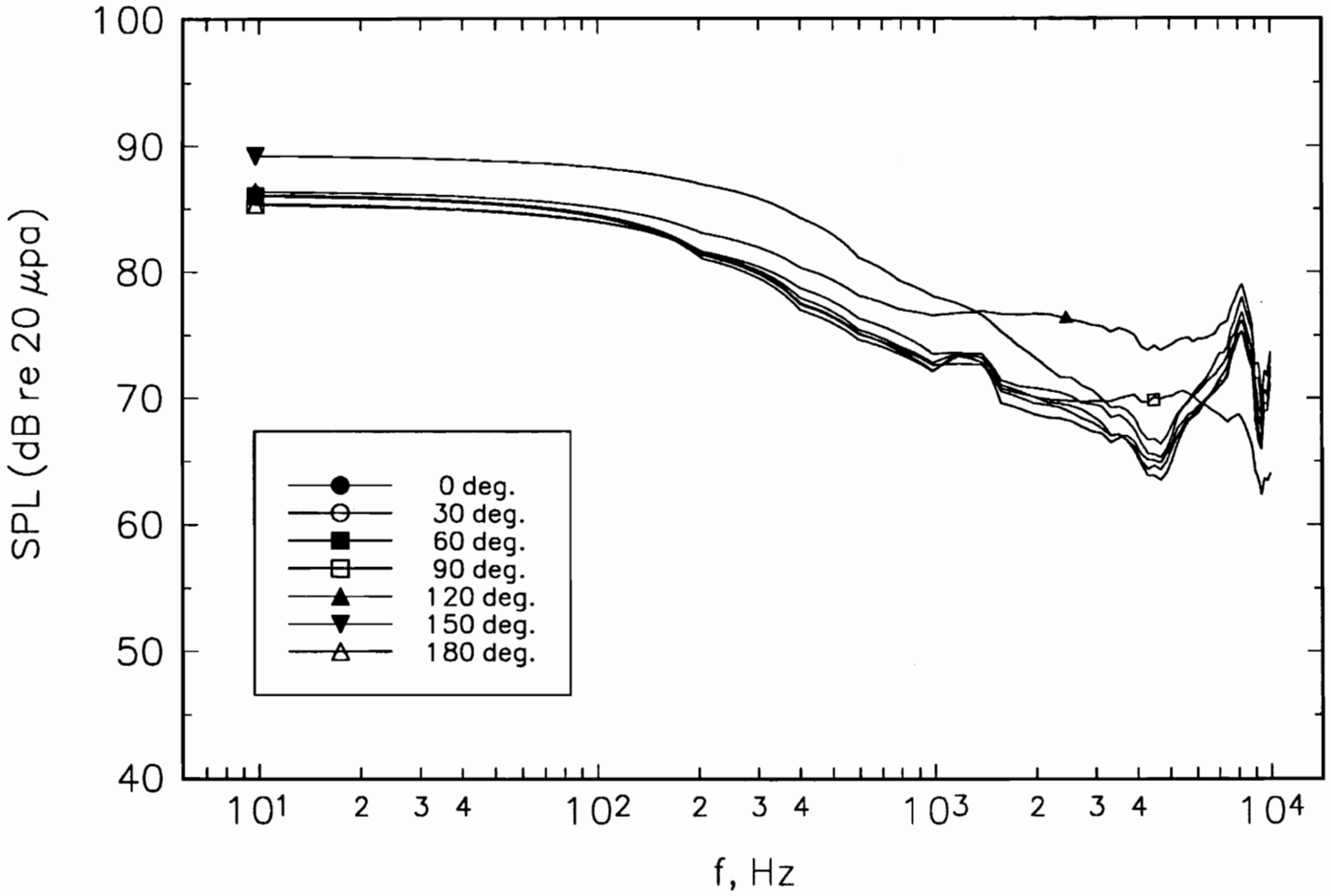

Figure 88. Surface Pressure Spectrum at $x/L = 0.4396$, $\alpha = 30$ deg, $Re_L = 4.20 \times 10^6$; Single Signal with Time Delay.

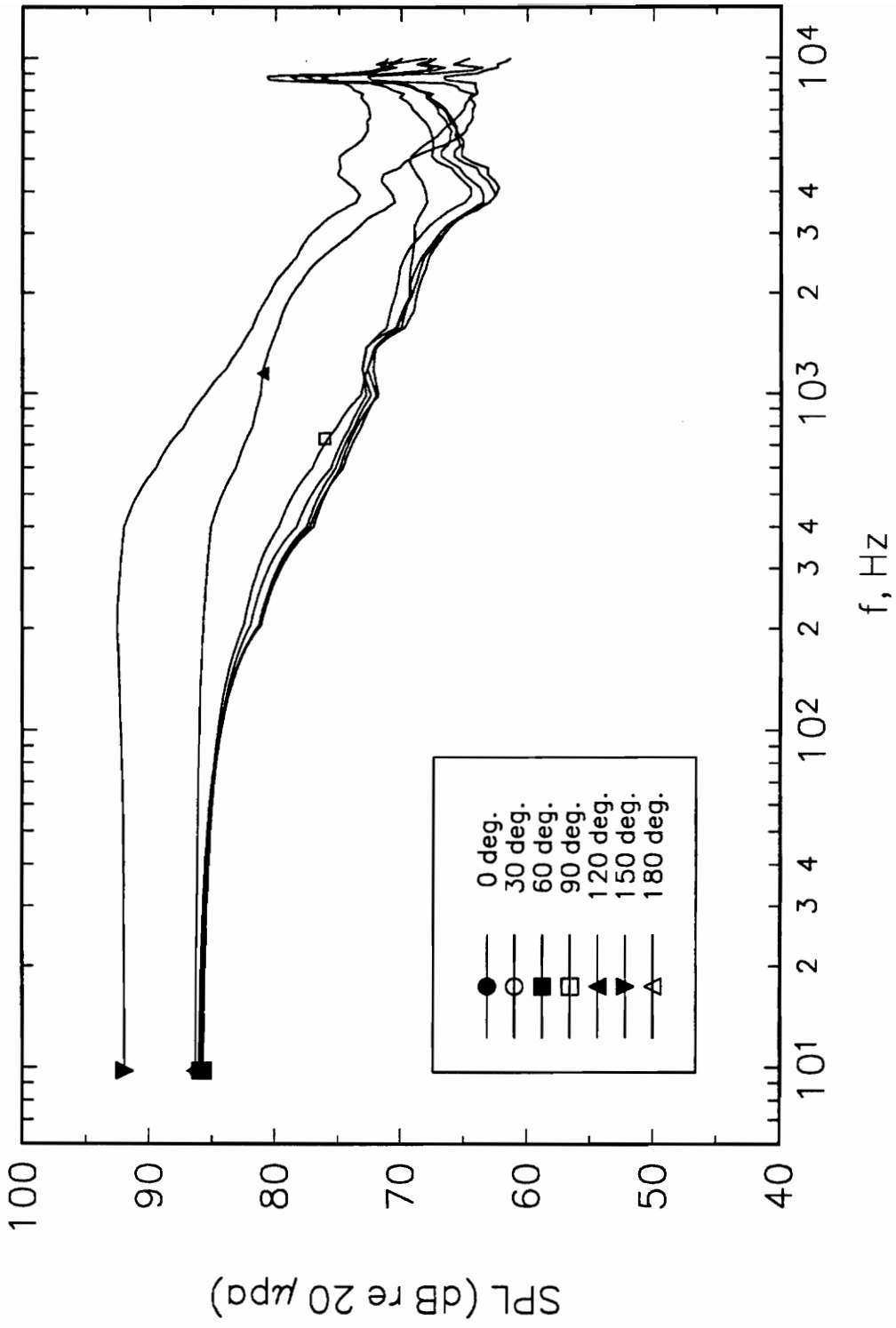

Figure 89. Surface Pressure Spectrum at $x/L = 0.5646$, $\alpha = 30$ deg, $Re_L = 4.20 \times 10^6$; Single Signal with Time Delay.

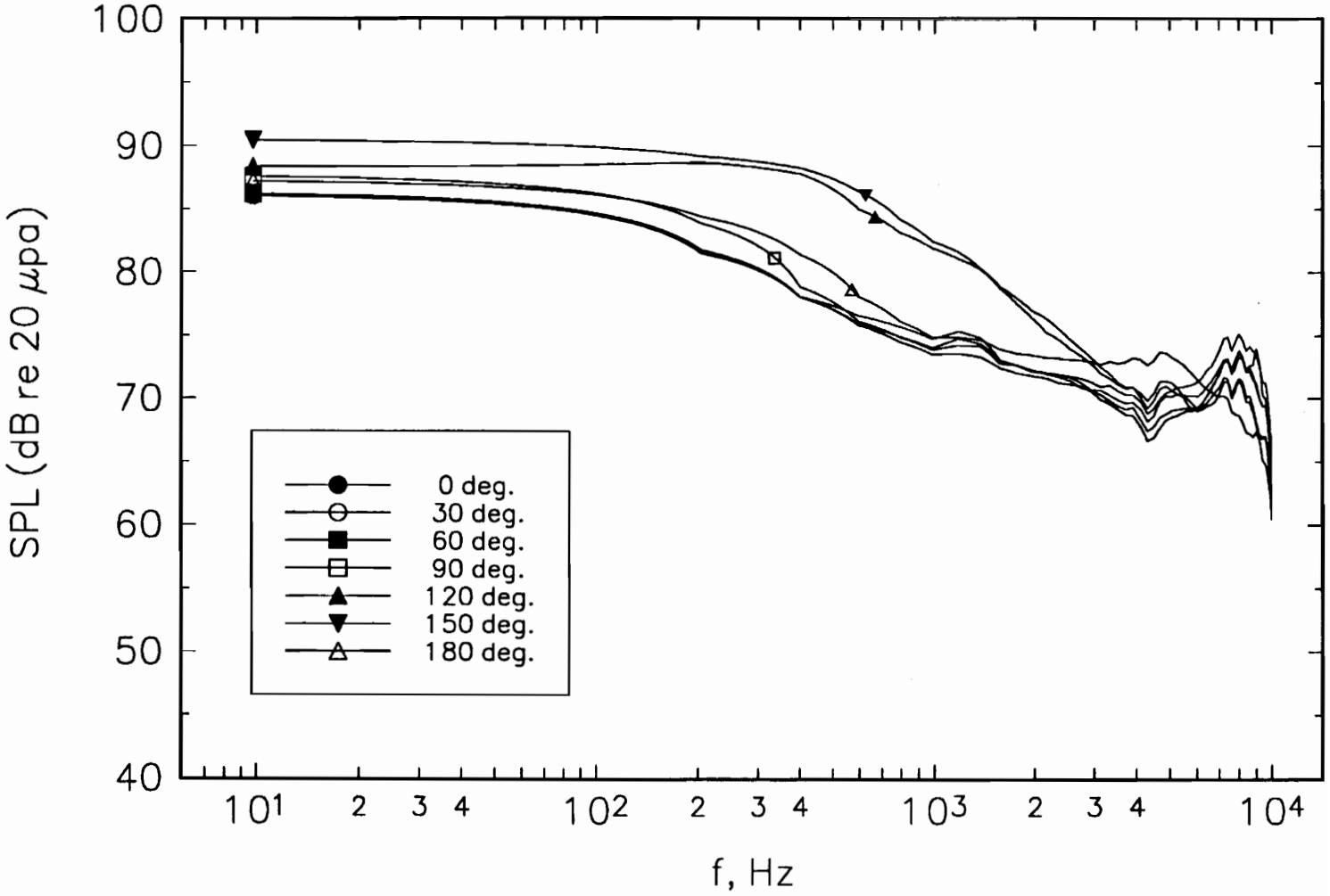

Figure 90. Surface Pressure Spectrum at $x/L = 0.6892$, $\alpha = 30$ deg, $Re_L = 4.20 \times 10^6$; Single Signal with Time Delay.

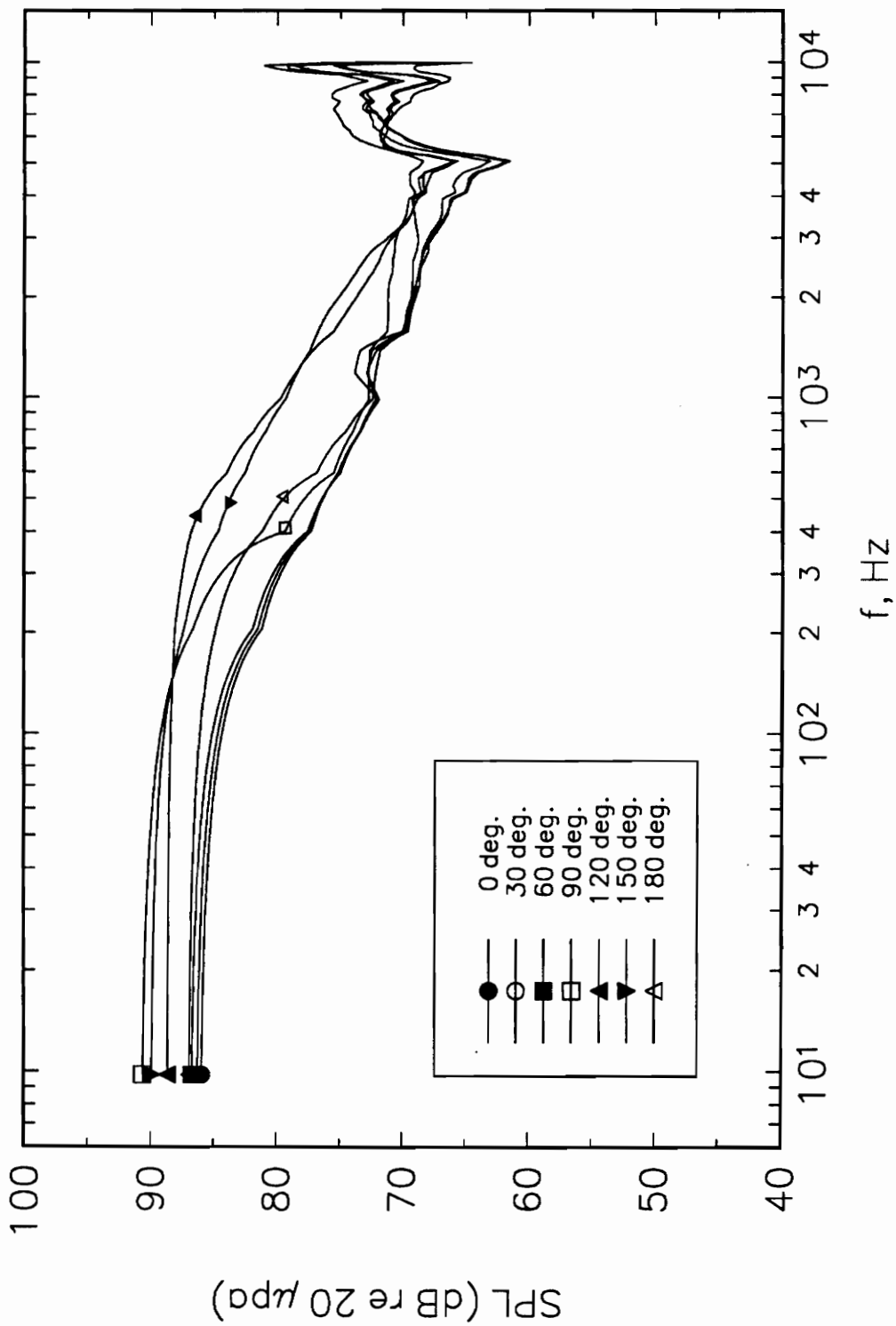

Figure 91. Surface Pressure Spectrum at $x/L = 0.7725$, $\alpha = 30$ deg, $Re_L = 4.20 \times 10^6$; Single Signal with Time Delay.

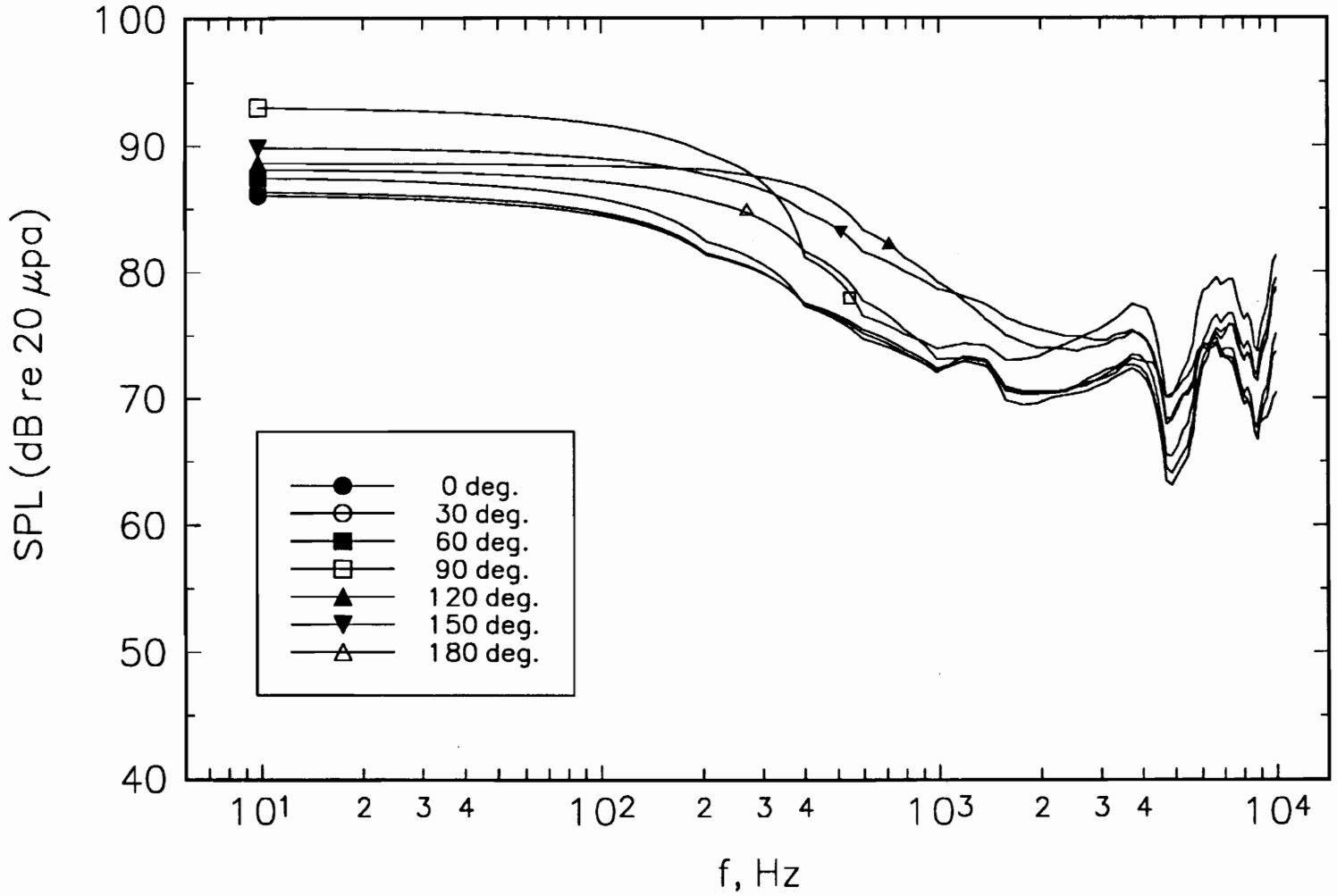

Figure 92. Surface Pressure Spectrum at $x/L = 0.8346$, $\alpha = 30$ deg, $Re_L = 4.20 \times 10^6$; Single Signal with Time Delay.

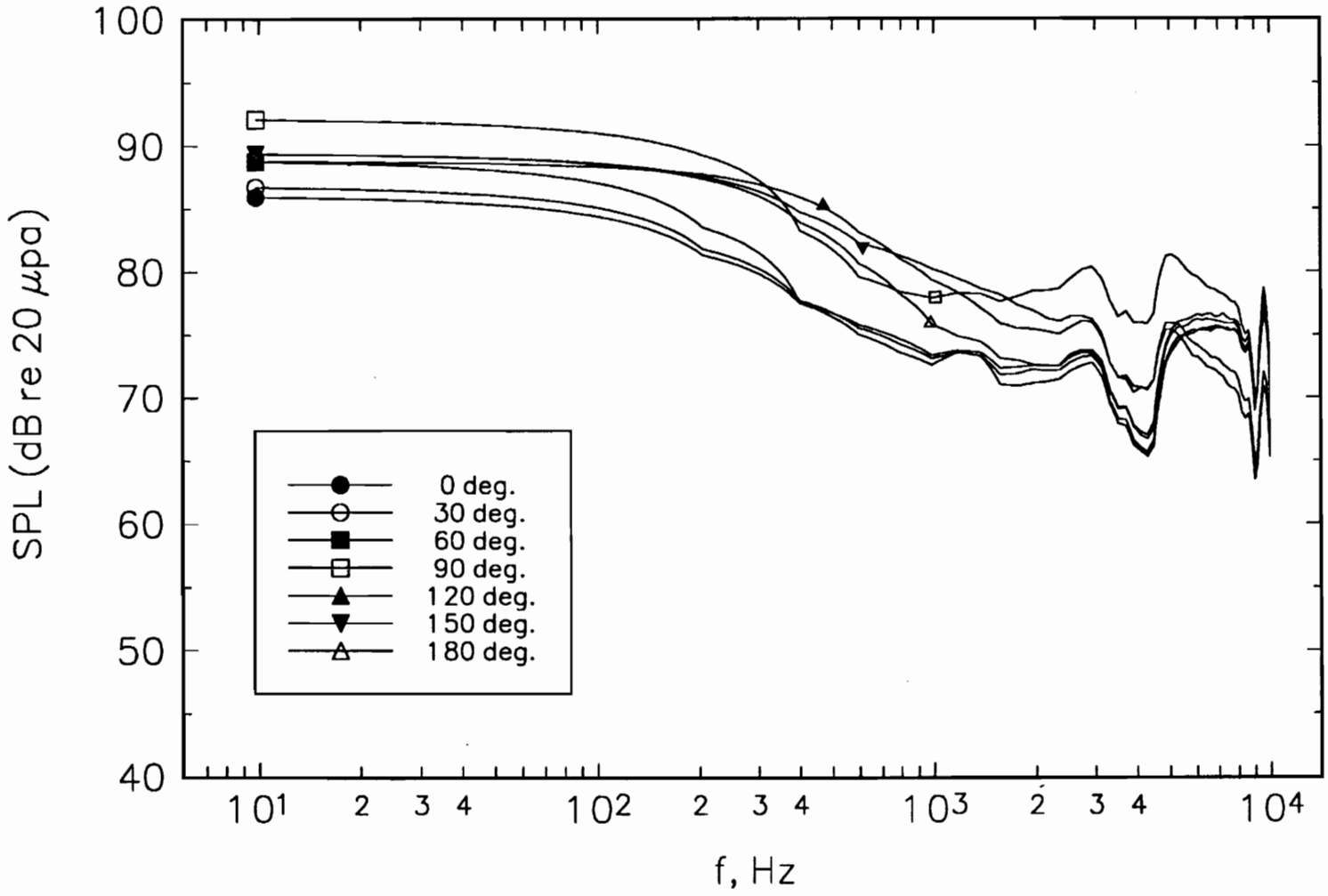

Figure 93. Surface Pressure Spectrum at $x/L = 0.8962$, $\alpha = 30$ deg, $Re_L = 4.20 \times 10^6$; Single Signal with Time Delay.

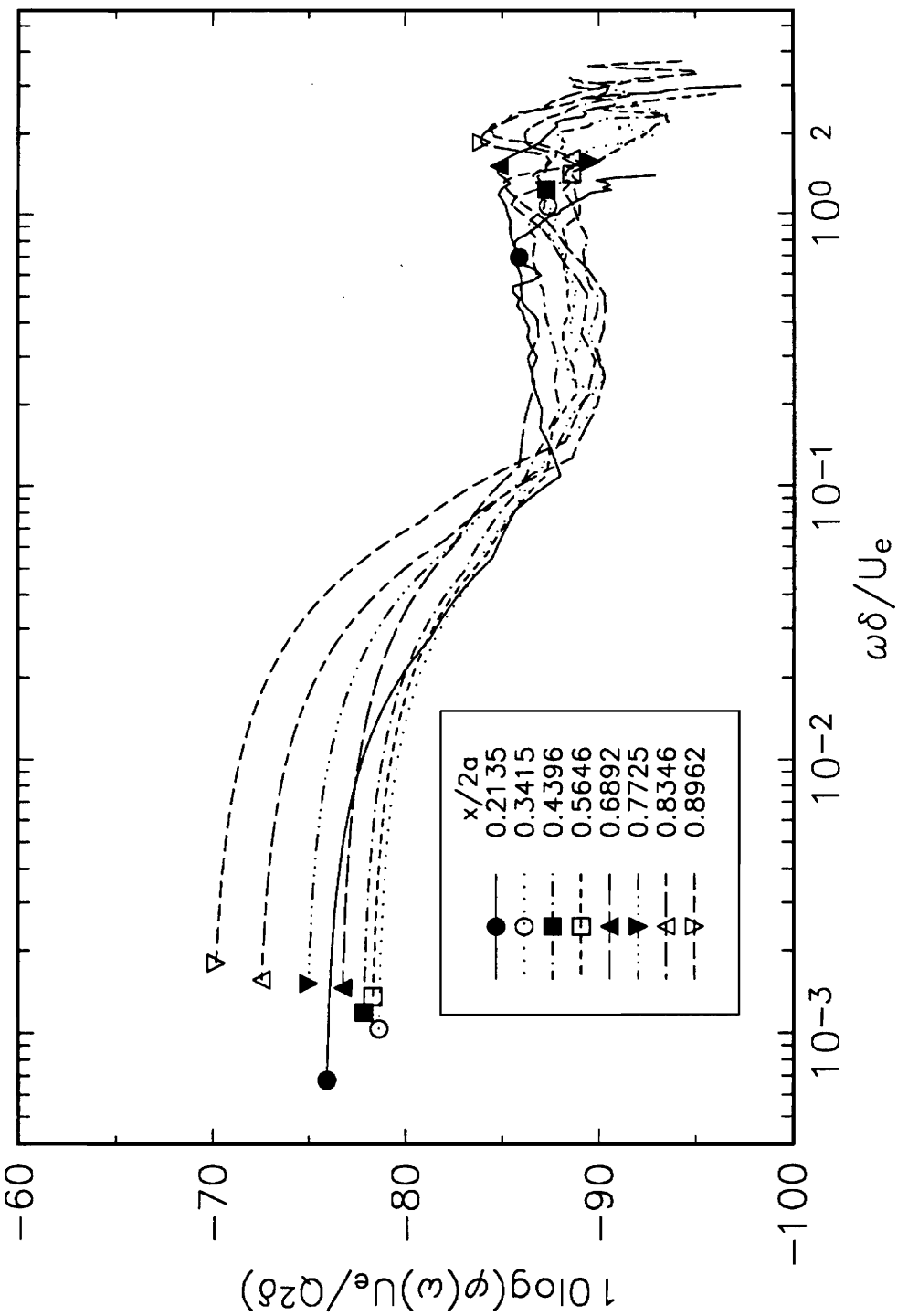

Figure 94. Outer Flow Scaling of Pressure Spectrum at $\phi = 90$ degrees, $\alpha = 30$ deg, $Re_L = 4.20 \times 10^6$; Noise Spectrum Subtraction.

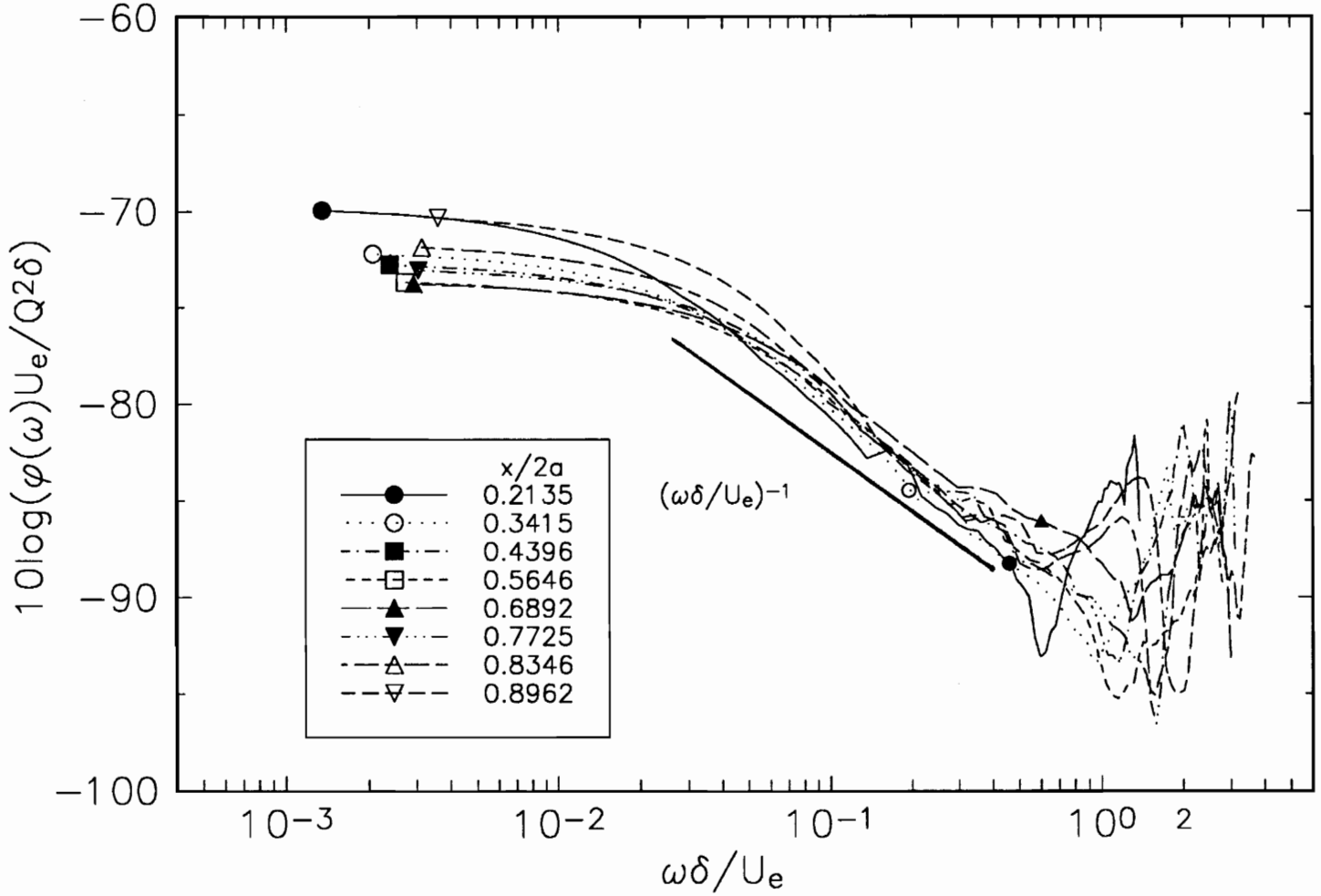

Figure 95. Outer Flow Scaling of Pressure Spectrum at $\phi = 90$ degrees, $\alpha = 30$ deg, $Re_L = 4.20 \times 10^6$; Single Signal with Time Delay.

TABLES

TABLE 1.

Pressure Transducer Location

x (inch)	x/2a	Serial No.
0.000	0.0000	A36N
5.827	0.1079	B38M
12.501	0.2135	B36M
16.983	0.3415	B42M
23.738	0.4396	B08L
30.488	0.5646	B19M
37.217	0.6892	B30M
41.715	0.7725	C13B
45.068	0.8346	B45M
48.395	0.8962	90YM

TABLE 3.

Boundary Layer Characteristics - calculated
$\alpha = 30$ degrees, $\phi = 90$ degrees

x/2a	$\delta \times 10^3$, ft	U_e, ft/sec
0.2135	4.875	221.42
0.3415	7.467	220.92
0.4396	8.550	219.63
0.5646	9.675	217.49
0.6892	10.200	213.88
0.7725	10.392	209.74
0.8346	10.425	204.48
0.8962	11.375	194.26

TABLE 4.

Uncertainties of Measured Data

Temperature	$T \pm 1.0$ %
Velocity	$V \pm 1.3$ %
Static Pressure	$P \pm 1.1$ %
Dynamic Pressure	$Q \pm 2.0$ %
Reynolds Number	$R_N \pm 4.5$ %
Angle of Attack	$\alpha \pm 0.1$ deg.
Roll Angle	$\phi \pm 0.5$ deg.
Normal Force (min.)	NF ± 7.5 %
Pitchinf Moment (min.)	PM ± 15.0 %
Side Force (min.)	SF ± 120 %
Yawing Moment (min.)	YM ± 120 %
Rolling Moment (min.)	RM ± 120 %
C_p	$C_p \pm 3.1$ %
Power spectrum	± 20 %

APPENDIX A.

DYNAMIC PLUNGE-PITCH-ROLL MODEL SUPPORT SYSTEM

Dynamic Plunge-Pitch-Roll Model Support System

When an aerodynamic or submersible vehicle makes rapid changes in orientation relative to its speed, unsteady dynamic flow phenomena occur that are distinctly different from the phenomena that occur at the same orientation and speed with slower changes in orientation or the steady case with the same orientation. The dynamic stall over an airfoil with rapidly varying angle of attack and the dynamic stall on three-dimensional bodies such as maneuvering fighters, missiles, torpedos, and submarines, such as in Figure 1, are examples. While the wings are of the utmost importance aerodynamically, the unsteady flow around the body must play a role in the maneuverability of such bodies. The unsteady aerodynamics of a vehicle is very complex and, although considerable effort is now applied to the development of various analytical and numerical methods of calculation, the most important source of data - at the present time - is experiment (Orlik-Rückemann, 1987). Although dynamic stall has previously been of interest mostly in connection with the helicopter rotor blade oscillations and turbine blades (McCroskey, 1977), it may now prove to be important also for the attainment of sustained dynamic maneuvering in the post-stall flight regime such as e.g. described by Herbst (1985) as "supermaneuverability". For such a purpose, the characteristics of the complete configuration, rather than merely two-dimensional data, will be needed.

In this section, a newly designed and developed Dynamic Plunge-Pitch-Roll(DyPPiR) model support system for the Stability Wind Tunnel of the Virginia

Polytechnic Institute and State University is described. The design objectives of this new apparatus are the generation of a arbitrary motion of sting mounted model, a dynamic stability test using the forced oscillation method, and an aircraft landing simulation. Details of the system are discussed along with hardware problems and their solutions found during the development phase.

A.1 Unsteady Flow Simulation Techniques

Until quite recently an aircraft designer would show only a passing interest on unsteady aerodynamics, concerning probably classical problems such as aeroelasticity and flutter. With the advanced requirements for the modern fighter aircraft, this modest level of investment in unsteady aerodynamics and dynamic characteristics, which enabled many excellent aircraft to be developed, has become clearly inadquate (Orlik-Rückemann, 1981). In this section, some of the typical techniques and apparati will be compared along with their merits and demerits to show the problems involved in the unsteady flow research.

Most of the earlier techniques were developed mainly for the dynamic stability derivatives rather than to study the unsteady flow phenomena. Among the various captive-model techniques used, fairly refined methods have been developed by wind tunnels and model basins for measuring forces and moments due to body rotation. However, the various experimental methods used to determine forces and moments acssociated with variations in linear acceleration, angular velocity, angular acceleration have been successful in only a limited number of cases (Goodman,

1960). The techniques that have been tried in this respect have required the use of facilities such as the rotating arm, free oscillator, forced oscillator, curved-flow and rolling-flows, curved models in a straight flow facility (Gourjienko, 1934, Chang and Purtell, 1986), Planar Motion Mechanism (Goodman, 1960), and Large Amplitude Horizontal Planar Motion Mechanism (Goodman *et al.*, 1987), CAL/Air Force Dynamic simulator (Statler and Hirtreiter, 1963), and MBB Dynamic Stability Rig (1990). Each of these techniques has certain limitations and problems associated with it.

Experiments on turning models using a rotating arm apparatus are difficult and usually lack detailed velocity measurements. Also, the static data obtained should be considered as an indirect procedure since the data must be extrapolated to infinite radius. Measurement about a stationary model in a moving flow, such as in a wind or water tunnel, has distinct advantages, but the curving shear flow required for a turn would be nearly impossible to achieve. However, one approach which has been very successful in two-dimensional potential flow is the transformation of the straight body in a curving flow to an appropriate curved body in a straight flow. In two dimensions, this merely involves a logarithmic transformation. Though not so simple in three-dimensional flow, the method was explored with some success at the Central Aero-Hydrodynamical Institute, Moscow, in 1934 by Gourjienko (1934). The approach was to apply a purely geometrical transformation to physical space based on the concept of maintaining local angle of incidence to the oncoming flow. This is effectively the logarithmic transformation applied to each plane of the body parallel to the plane of motion. The method is not theoretically exact, but the experimental evidence indicates that it is a very

useful approach. Recently, Chang and Purtell (1986) adapted this method and carried out a comparison between computations using a three-dimensional potential flow computer code based on Green's theorem, with doublet distribution coupled with more rigorously founded Kutta condition and experiment on a transformed "banana shaped" body in a steady flow in a wind tunnel and obtained reasonably good agreement. But, this method has several problems such as the accuracy of the curved model constructed with the geometric transformation and the problem of boundary layer which is blown off the body due to the excessive curvature. Due to these problems, it is still to be answered whether this approach is the correct way to simulate the highly interactive viscous-inviscid flow problem occuring during the turning motion or not

A curved-flow technique, originally developed at NASA Langley and now in use at the Virginia Polytechnic Institute and State University (Ko, 1985), is based on the concept of simulating a steady curved-flight condition by using a fixed model and arranging wind tunnel flow in such a way that it is curved in a circular path in the vicinity of the model and that it has a velocity variation normal to the streamlines in direct proportion to the local radius of curvature (Orlik-Rückemann, 1981). This is achieved by using flexible side walls for curving the flow and by employing specially constructed vertical drag screens upstream of the test section for producing the desired velocity gradient across the tunnel flow. These screens vary in mesh size across the wind tunnel, most dense portion of the screens located at the inner radius of the curved test section. The technique allows measuring pure-yawing (due to r only) or pure-pitching (due to q only) derivatives with a fixed model mounted on a static balance. The simulation of the steady curved flight

is not exact, however, and corrections have usually to be made for the buoyancy effect caused by the static-pressure gradient normal to the streamlines which does not exist in curved flight. Furthermore, there are dissimilarities in the behavior of the model boundary layer due to this buoyancy which does not exist in a curved flight.

A two degree-of-freedom apparatus with which known combinations of pitching(or yawing) and vertical(or lateral) oscillations could be obtained was developed at Calspan in the early 1960s (Statler and Hirtreiter, 1966) for use in the 8-foot Transonic Wind Tunnel. The system had the capability to force the model inexorably in any planar sinusoidal motion, including limiting cases of translation and pure rotation. The yawing or lateral oscillations were investigated by rotating the model 90 degrees around the sting. The desired motion was imparted to the model by a mechanical system, consisting of linkages and connecting rods, eccentrically mounted on two high inertia flywheels. The available frequency range was from 3 to 12 Hz and amplitude up to ± 5 degree and ± 0.5 ft and accelerations up to 200 rad/sec^2 or 20 g's could be achieved in the rotational and translational cases, respectively. Models could be installed at non-zero angles of attack, using bent stings, subject to load limitations. This apparatus has not been used for some time now and it is not known whether it can still be considered operational. It seems certain that at least the electronic part of it, including the instrumentation used for data analysis, may need updating (Orlik-Rückemann, 1981). Furthermore, since this apparatus was designed mainly for oscillation mode, it lacks linear translational and large angle rotational motion capabilities such as large amplitude plunging and large angle pitch-up.

To study the problems associated with the dynamic behavior of the submarine and other submerged bodies, such as stability, performance, and handling characteristics, a unique apparatus called the Planar-Motion-Mechanism System was developed at the David Taylor Model Basin (Goodman, 1960). This system was designed for the oscillation mode of operation due to the requirement for the dynamic stability derivative measurement and improved to the Large Amplitude Horizontal Planar Motion Mechanism in 1970s. The oscillation frequency ranges from 0.01 Hz to 0.20 Hz with an amplitute of ± 3 ft and ± 30 degrees for swaying/heaving motion and yaw/pitch motion, respectively. The facility is about 25-feet wide, 13-feet deep, and 420 feet long and can be operated at controlled speed up to 20 ft/sec to move the model through the water (Goodman *et al.*, 1987). This system has advantages over conventional wind tunnel testing techniques on some areas such as; low turbulence environment, higher Reynolds number due to lower kinematic viscosity, high dynamic pressure resulting in large forces and moments, and and accordingly better resolution. This system is an excellent one compared to the state of the art of the ground simulation technique. But, it has a severe problem for instrumentation, especially for flow field measurements because of its test medium, and it requires a longer turn-around time to achieve the same initial condition because of the model wake generated during the previous run.

Due to the limitations of existing methodology, it is impossible to fully assess analytically the ground effect transients for aircraft in relation to performance, stability and control, and handing qualities. Ground effect testing was carried out using static model in a close proximity to a ground board in a wind tunnel or using an actual aircraft passing through a prescribed flight path close to the ground

(Chang and Muirhead, 1987). In order to identify the proper experimental approach in terms of facility, testing techniques, and cost, a detailed feasibility study for conducting transient model tests of STOL aircraft simulating takeoff, approach, and landing was made (Crowder, *et al.*, 1975). To cope with the increasing interest in aircraft approach and landing simulation, DNW (Deutsch-Niederlandischer Windkanal) developed a sting-mount model support for this special use. ONERA also developed a new rig for analytical study, permitting the determination of the steady and unsteady forces and corresponding dimensionless coefficients in various flight conditions (Christophe, 1980). This new rig of ONERA is aimed for the measurement of the ground effect, side wind on the runway during aircraft landing, and atmospheric gust, as well as large angle of attack excursion. It has a single mast system connected to the center of the model with all the moving parts inside, giving an unfavorable interference on the rear part of the model.

Motivated by the need to design rapidly maneuvering torpedos and submarines, some of the early work considered the hydrodynamic forces acting on a body of revolution undergoing a periodic change of incidence. Szebehley and Niederer (1953) were perhaps the first to conduct an experiment to find the effect of frequency and amplitude of oscillations on the forces acting on a prolate spheroid, which had a 7 to 1 fineness ratio. Another important contribution was made by Sevik (1963), who measured the instantaneous pressure at various locations on a 8 to 1 prolate spheroid oscillating at a constant amplitude. With the requirement of extreme flight agility to accomplish large and rapid heading change of tactical missile missions, Smith (1974), Smith and Nunn (1976) estabilished a baseline aerodynamic

data on a 15 to 1 fineness ratio ogive-cylinder body which is undergoing a rapid pitch-up motion at varying constant pitch rate.

Although, the supermaneuverability is rather a new concept of fighter aircraft flight dynamics which is drawing a great interest (Mabey, 1988), the idea and concept to increase the lift of the wing by rapidly changing the angle of attack was sought in the late 1940's and early 1950's at NACA. Inspired by the discrepencies between the wind tunnel data and flight test data, Davis and Sweberg (1948) tested a full scale aircraft in the Langley full scale tunnel. Their major concern was the maximum lift coefficient which is important for the landing performance. Later, with the increasing significance of the rate of change of angle of attack among the parameters affecting the maximum wing loads and therefore the maneuverability of high-speed aircraft and missiles, Harper and Flanigan (1950) tested a small model in a wind tunnel at Mach numbers up to 0.8 with a pitching rate up to 20 radians per second. They found that the maximum lift coefficient increased linearly with the pitching velocity up to a limiting value which is decreasing with the Mach number and the increment was largest, about 100 percent, at lower Mach numbers. From the flight test, Gadeberg (1951) found that the Mach number and Reynolds numbers effects were of sufficient importance to produce more than twofold variation in the increament of maximum lift coefficient and, above Mach number about 0.3, Reynolds number had less effect on the rate of change of maximum lift coefficient with rate of change of angle of attack than at lower Mach numbers. After a careful examination of the currently available data, Mabey (1988) revealed the same conclusion in his review on the possibility of dynamic lift.

For a better understanding of such unsteady dynamic flow phenomena, wind tunnel experiments of dynamically moving models are needed. Gallaway and Osborn (1985) point out that dynamic model mount apparati need to be developed to aid fluid dynamicist, vehicle dynamicist, and control engineer in understanding the unsteady fluid dynamics and the time dependent forces and moments and stability derivatives on a rapidly reorienting vehicles.

A.2 Design Requirements

The design objective of the VPI & SU DyPPiR model support system is to simulate unsteady flow phenomena occuring over 3-dimensional bodies. A fighter during a pull-up maneuver and a submarine undergoing a turning maneuver are such examples. An extensive survey of the performance and capability of the existing facilities (Christophe, 1980; Seidel, 1982; Statler *et al.*, 1966; Goodman, 1960; Goodman, 1987) and the expected test requirements (Smith and Nunn, 1976; Lang and Francis, 1985; Chang and Muirhead, 1987; Mabey, 1988; Jumper *et al.*, 1987) revealed that it is also important to have a linear motion capability in the vertical plane as well as rotational motion capabilities. Three-dimensional model support interference considerations showed a sting type support to be the best. These requirements resulted in a single apparatus as shown in Figure A.1. Other design goals are to simulate aircraft landing motion, as in the case of the ONERA (Christophe, 1980) and the DNW (Seidel, 1982) facilities, and to extract dynamic stability derivatives using the oscillation mode of the DyPPiR.

The VPI & SU DyPPiR is designed to meet the following requirements.

- Linear as well as oscillatory motion capabilities in the vertical plane of the tunnel.
- Sting - Strut type model support.
- 3-degree-of-freedom motion.

  Plunge.

  Pitch.

  Roll.
- Maximum pitch rate of 8 rad (458 deg.)/sec.
- Pitching oscillation frequency up to 7 Hz at an amplitude of ± 5 degrees. Larger amplitude motions up to ± 37.5 degrees are possible at lower frequencies.
- Plunging oscillation frequency up to 7 Hz at an amplitude of ± 6 inches. Larger amplitude motions up to ± 2.5 ft are possible at lower frequencies.
- Roll oscillation frequencies up to 5 Hz at an amplitude of ± 22.5 degrees. Larger amplitude motions up to ± 135 degrees are possible at lower frequencies.
- Typical model length of 5 ft.
- Model loads at 5 ft from the pitch center.

  Normal force 500 lbs.

  Pitching moment 750 in-lbs.

  Side force 400 lbs.

  Yawing moment 600 in-lbs.

  Rolling moment 750 in - lbs.

  Axial force 500 lbs.

Figure A.2, A.3, and A.4 show performance and physical limitations on the Plunge, Pitch, and Roll motions. Plunging performance is based on a 600 lb moving weight of the pod assembly , pitching and roll motions are for the moments of inertia of 20 $slug - ft^2$ and 1 $slug - ft^2$,respectively.

A.3 Hydraulic System

High pressure (3000 psig) hydraulic power was selected as the power source due to its compact size and the linear motion capability requirement of the system. Main problems faced during the VPI & SU DyPPiR design phase were the high speed vertical actuator development and high flow rate required by the vertical actuator. A specially designed hydraulic servoactuator with the following specifications has been developed to meet the requirement.

- Available stroke should be 60 inches.
- Maximum piston speed should be over 30 ft/sec.
- Maximum flow rate of 800 GPM.
- Cushions at both ends of the actuator to accept at least 60 g shock load to prevent the catastrophic failure of the actuator.
- Effective stroke should be at least 3 ft at 30 ft/sec piston speed with 600 lbs moving weight in the middle of the available stroke.
- Readily available control electronics.

The control of the hydraulic fluid flow rate of 800 GPM in a short period of time is critical to maintain the required performance of the whole system. To

meet this requirement, three high response, high flow rate servovalves are used in parallel to power the vertical actuator. An integral manifold for mounting the servovalves and connecting supply and return hydraulic lines is mounted onto the side of the actuator as shown in Figure A.5. The integral servovalve minimizes fluid compliance of the cylinder lines which gives the highest drive resonant frequency.

To achieve a smooth and jitter-free oscillatory and rotary motion, rotary actuators are used as the pitch and the roll actuators. A low weight double vane rotary actuator with a torque of 58,000 in-lb, ± 50 degree rotational angle, was specially developed as the pitch actuator, shown in Figure A.6. A single vane rotary actuator which has a torque of 5,800 in-lb and roll angle range from -5 degree to +275 degree is mounted in front of the pitch actuator through two coupling brackets so that rolling motion of the model is possible at any angle of attack. The sting is mounted on to the axis of the roll actuator through a taper joint.

Design of a hydraulic power system to meet the unusually high flow rate requirement was another problem. After an optimization study of the size of the accumulator and pump capacity required, a high constant flow rate open type hydraulic circuit as shown in Figure A.7 was selected to minimize the required volume of the accumulator bank and the space occupied by them. Three sets of a 250 HP motor and a 140 GPM pump combination are used with a 400 Gallon reservoir and four 15 Gallon bladder type accumulators precharged with 2000 psig nitrogen are included in the circuit. The total displacement volume of the accumulator bank is approximately 5 Gallons. The main purposes of the accumulator bank are as follows:

- Accomodate peak loads in the hydraulic circiuit.

- Absorb system shock.
- Maintain the system supply pressure while the actuators are operating.
- Provide a gradual shutdown of the DyPPiR if the pumps should fail.

The hydraulic oil is recirculated through a heat exchanger mounted to the hydraulic oil reservoir and chilled water from a cooling tower keeps the hydraulic oil at an acceptibly low temperature of 80 deg. F. The entire high pressure pipings were evaluated through the hydro-static testing at 4500 psi and X-ray test were also performed on several required locations according to the ANSI/ASME standard code.

A.4 Support Structure

The support structure for the strut is just as important because of the dynamics of the pod assembly and vibration isolation from the existing tunnel structure and surrounding buildings. A massive concrete foundation with two vertical piers, partly buried under the ground, was poured and isolated from the base of the tunnel and buildings. The 70,000 lb-weight foundation is heavily reinforced with 10 inch I-beams and reinforcing bars for the maximum fatigue life and all the steel structures are mounted on top of this foundation. The 15,000 lb-weight steel structure shown in Figure A.8 permits less than 0.1 inches of deflection and motion of the strut. Structural dynamic simulations of this structure and foundation performed on the CAEDS program have shown the resonant frequencies above 29 Hz, well

above the DyPPiR operating frequencies. The model for the analysis is shown in Figure A.9.

The high speed motion of the vertical plunge actuator required a special bearing which has a high rolling load and yet small in size. This may cause a large flow blockage by a bulky design of the strut on which all the moving parts are riding. Normal bushing type linear bearings can be used without binding up to 12 to 16 ft/sec of speed which is only a half of the speed required. Special arrangement of 8 roller bearings on V-mounting block riding on 4 roundways was chosen to achieve the structural integrity and the maximum speed in excess of 30 ft/sec.

A.5 Control System Design and Analysis

Because of the rather high frequency and arbitrary motion required, a full digital control scheme was considered at the beginning. Full digital control allows "locked-in solid" operation of the actuators but requires a fast CPU to update the required command parameters through sampling, calculation, comparison, and feedback to generate a smooth motion. Performance requirements and budget status led to a trade-off and resulted in a microcomputer based, pre-loop processing, digital command/analog feedback control system.

A servoactuator control schematic diagram designed around a microcomputer is the position control system as shown in Figures A.10 to A.12 for vertical axis, pitch axis, and roll axis, respectively. Position feedback forms the major loop. The calculated natural frequency of the load/actuator combination is approximately 30

Hz. The specified control frequency of 7 Hz is considered to be high when compared to the system natural frequency. Additional feedback signals of velocity and pressure are required for position control at higher frequencies. Feedback of actuator pressure difference in the form of a dynamic pressure feedback in a minor loop acts to increase the system damping (Geyer, 1958; Edwards, 1972). Load pressure tends to become large near resonance and feedback of this quantity reduces the gain which reduces the resonant peak, thus providing damping. Velocity feedback in a minor loop effectively adds stiffness to the load and thus increases the load resonant frequency. By utilizing the appropriate amount of velocity and pressure feedback a higher loop gain can be achived, providing better position control. Detailed control system set-up and analysis is as follows.

A.5.1 System Modeling

Models representing the physical control system components were created and analyzed. The models include not only the electrical components such as analog controllers and transducers but also mechanical components such as servovalves, hydraulic actuators, and load masses. The mechanical components also include friction and leakage at the actuators as well as their system of load, mass, and damping. The hydraulic properties of the servovalves and actuators are also represented. Typical analysis was performed on the vertical axis and its result was projected onto the pitch and the roll axes system.

A.5.2 Load-mass system

The total weight of the moving part of the system is approximately 660 lbs and it is composed of as follows;

$$\text{Sting and pod assembly} \approx 546 \quad \text{lbs}$$

$$\text{Actuator rod and piston} \approx 55 \quad \text{lbs}$$

$$\text{Model} \approx 59 \quad \text{lbs}$$

$$\text{Total} \approx 660 \quad \text{lbs}$$

Detailed weight break-down is presented in Table A.1. Maximum load frequency f_L fo the actuator can be calculated by following simple relation

$$f_L = \frac{1}{2\pi}\left[\frac{K_0}{M_T}\right]^{\frac{1}{2}}$$

$$\approx 41(\text{Hz})$$

where, $K_0 = \dfrac{4\beta A^2}{V_T}$

V_T = total trapped volume of oil

β = bulk fluid modulus of oil (psi)

M_T = total weight = 660 (lbs)

For the roundway bearing on a V-block configuration, the friction is

$$F_B = 0.007 \times \text{load}$$

and the maximum load $\approx 4000 \times 4 = 16000$ lbs. Thus the total friction force becomes

$$F_B = 16000 \times 0.007 = 112 \quad \text{(lbs)}$$

at 30 ft/sec actuator speed. The friction coefficient becomes

$$B = \frac{112}{(30 \times 12)} = 0.3 \quad \text{lb/(in/sec)}$$

A.5.3 Hydraulic system

The hydraulic cylinder and fluid compressiblity can be modeled as

$$\frac{P \quad (\text{psi})}{Q \quad (\text{cis})} = \frac{4\beta}{V_T}\frac{1}{s}$$

For Mobil DTE-24 petroleum based hydraulic oil at room temperature, the bulk fluid modulus β can be assumed as $\beta = 250,000$ psi. The total fluid compressed inside the actuator was estimated, as an average of the piston end and rod end, to be $V_T = 425.7in^3$. The hydraulic cylinder converts the hydraulic fluid flow into force or torque.

$$\frac{F \quad (\text{lb})}{P \quad (\text{psi})} = A$$

where, A = piston area. The piston area was $7.1in^2$ as an average of the piston end and rod end.

In any hydraulic system, there exist a leakage. The cylinder was estimated to have about 3% of leakage at 3000 psi supply pressure.

$$K_L = \frac{(0.03)(Q)(\text{cis})}{\text{Available pressure}(=3000 \text{ psi})} = 0.03 \quad (\text{cis/psi})$$

where, Q = Average fluid flow rate = $\dot{z}A$

A = piston area

$\dot{z}$ = actuator speed

Additionaly, there is a back-velocity fluid flow Q_A which is the fluid flow behind the forcing piston. The back-velocity loop subtract the flow rate Q_A from the available flow rate Q_T and it is proportional to the piston speed as shown in the schematic diagram.

A.5.4 Servo-loop gain

To drive the actuator with suitable dynamic response, three high flow rate, high response servovalves were used in parallel. The servovalve can be modeled with a small signal, second-order transfer function (Thayer, 1965).

$$G_1(s) = \frac{K_s(\omega_n)^2}{s^2 + 2\zeta\omega_n + {\omega_n}^2}$$

where, K_s = spool flow gain (cis/in)

ζ = damping coefficient (0.45)

ω_n = frequency of servovalve (450 rad/sec)

The servovalve has an LVDT on the power spool to form an internal closed loop position feedback. The inner loop gain of the servovalve is defined as

$$K_{il} = \frac{K_A K_{pv} K_D K_x}{A_s}$$

where, K_{il} = inner loop gain, (sec^{-1})

K_A = servoamp gain, (mA/Vdc)

K_{pv} = pilot valve gain = 0.83355 (cis/mA)

K_D = demodulator gain = 4.3 (Vdc/Vrms)

K_x = LVDT gain = 6.74 (Vrms/in)

A_s = Power spool end area = 1.107 (in^2)

With 3000 psi pilot supply and for the maximum recommended inner loop gain of $700 sec^{-1}$, the amplifier gain becomes

$$K_A = \frac{700 \times 1.107}{(0.83355) \times 4.3 \times 6.74} = 32.0783 \quad \text{(mA/Vdc)}$$

Taking 90 % for the stable operation, the servo amplifier gain becomes

$$K_A = 28 \quad (\text{mA/Vdc})$$

The outer loop gain is defined as

$$K_{val} = \frac{K_s}{K_D K_x}$$

where, K_{val} = overall valve gain, (cis/Vdc)

K_s = power spool flow gain

$= 15.0169 \times 10^3 (\text{cis/in})$ at 3000 psi

K_D = demodulator gain

K_x = LVDT gain

For the spool length of ± 0.13 in and ± 40 mA nominal input on the coil, the servovalve flow gain K_Q becomes

$$K_Q = \frac{1952.197 \quad \text{cis}}{40 \quad \text{mA}} = 48.8 \quad \left(\frac{\text{cis}}{\text{mA}}\right)$$

A.5.5 Transfer function

After simplifying the transfer function of the servovalve to a second-order system, the closed loop transfer function of the system, shown in Figure A.10, can be expressed as

$$\frac{z}{e} = \left(\frac{1}{K_z}\right)\left(\frac{1}{1+G_z(s)}\right)$$

$$\begin{aligned} G_z(s) = \left(\frac{s}{K_V}\right)\Bigg\{\left[\left(\frac{s}{\omega_n}\right)^2 + \frac{2\zeta}{\omega_n}s + 1\right] \\ \times \left[\left(1+\frac{BK_L}{A^2}\right) + \left(\frac{B}{K_T} + \frac{MK_L}{A^2}\right)s + \left(\frac{M}{K_T}\right)s^2\right] \\ + \left(\frac{K_V}{K_z}\right)\left[K_{\dot{z}} + \left(\frac{M}{A}\right)\left(s+\frac{B}{M}\right)K_p\right]\Bigg\} \end{aligned}$$

$$K_V = \left(\frac{3K_1K_2K_QK_z}{A}\right)$$

$$K_T = \left(\frac{4\beta}{V_T}\right)A^2$$

The dynamic lags inherent in the servoamplifier can be held to a negligible value in the frequency regime under consideration. Amplifiers with low output impedence using current feedback are used to drive the inductive load of the valve torque motor. With current feedback, the amplifier dynamics are negligible. So, for the summing amplifier

$$K_1 = 1$$

$$G_1(s) = 1$$

In order to stabilize the system, the velocity feedback was applied for damping and load force feedback was applied for a desired load damping without the loss of static stiffness (Geyer, 1972). The feedback gains for the best performance were

found to be

$$K_z = \left(\frac{1}{3}\right)\left(\frac{\mathrm{V}}{\mathrm{in}}\right)$$
$$K_{\dot{z}} = 0.0001418\left(\frac{\mathrm{V}}{\mathrm{in/sec}}\right)$$
$$K_p = 0.000085\left(\frac{\mathrm{V}}{\mathrm{psi}}\right)$$

Similar analysis can be made on the pitch and roll axes. The transfer function for the pitch axis is

$$\frac{\theta}{e} = \left(\frac{1}{K_\theta}\right)\left(\frac{1}{1+G_\theta(s)}\right)$$
$$G_\theta(s) = \left(\frac{s}{K_V}\right)\left\{\left[\left(\frac{s}{\omega_n}\right)^2 + \frac{2\zeta}{\omega_n}s + 1\right]\right.$$
$$\times \left[\left(1 + \frac{BK_L}{{D_M}^2}\right) + \left(\frac{B}{K_T} + \frac{JK_L}{{D_M}^2}\right)s + \left(\frac{J}{K_T}\right)s^2\right]$$
$$\left. + \left(\frac{K_V}{K_\theta}\right)\left[K_{\dot{\theta}} + \left(\frac{J}{D_M}\right)\left(s + \frac{B}{J}\right)K_p\right]\right\}$$

And for the roll axis

$$\frac{\phi}{e} = \left(\frac{1}{K_\phi}\right)\left(\frac{1}{1+G_\phi(s)}\right)$$
$$G_\phi(s) = \left(\frac{s}{K_V}\right)\left\{\left[\left(\frac{s}{\omega_n}\right)^2 + \frac{2\zeta}{\omega_n}s + 1\right]\right.$$
$$\times \left[\left(1 + \frac{BK_L}{{D_M}^2}\right) + \left(\frac{B}{K_T} + \frac{JK_L}{{D_M}^2}\right)s + \left(\frac{J}{K_T}\right)s^2\right]$$
$$\left. + \left(\frac{K_V}{K_\phi}\right)\left[K_{\dot{\phi}} + \left(\frac{J}{D_M}\right)\left(s + \frac{B}{J}\right)K_p\right]\right\}$$

For the pitch axis control, the pressure feedback is not applied in order to keep the flat frequency response range wide. The feed back gains applied are

$$K_\theta = 10\left(\frac{\text{V}}{\text{rad}}\right)$$
$$K_{\dot{\theta}} = 0.100\left(\frac{\text{V}}{\text{rad/sec}}\right)$$
$$K_p = 2.75 \times 10^{-5}\left(\frac{\text{V}}{\text{psi}}\right)$$

For the roll axis control, only the position feedback is applied. The feed back gains applied are

$$K_\phi = 4.1\left(\frac{\text{V}}{\text{rad}}\right)$$
$$K_{\dot{\phi}} = 0.000368\left(\frac{\text{V}}{\text{rad/sec}}\right)$$
$$K_p = 1.98 \times 10^{-3}\left(\frac{\text{V}}{\text{psi}}\right)$$

All the physical values used for pitch and roll axes are tabulated in Table A.2. The Bode plots and step responses of each axis system are shown in Figures A.13 to A.18.

For the best performance of the pitch axis system, special care was necessary. Depending on the location and weight of the model to be tested, the mass moment of inertia of the pitch axis system changes. And this change has to be accounted for in the system feedback gain adjustment for the stable operation of the system. For the simplicity of the adjustment, fixed gain of the pressure feedback was chosen. The velocity feedback gain only was able to compensate the change of the mass moment of inertia of the pitch axis and this was successfully demonstrated. Detailed variation of the velocity feedback is presented in Figure A.19 in terms of the pitch axis mass moment of inertia J. The step response of the actual plunge actuator is also shown in Figure A.20 for a 6 inch command input. The piston achieved $\approx 19 ft/sec$ linear speed and the flow rate was about 450 GPM.

A.6 Sting Deflection Correction

For the calculation and correction of the sting deflection, first-order linear system is assumed throughout the analysis. The DyPPiR can be modeled as shown in Figure A.21. It is composed of Pitch actuator (A), Roll actuator and actuator brackets (B), Sting (C), and Model (D). Pitch actuator and roll actuator are assumed to be rigid and the vertical translation motion was given at the pitch actuator. This system can be described by the following system of equations.

$$\mathbf{R}_A = R\mathbf{n}_2$$

$$\mathbf{R}_B = R\mathbf{n}_2 + \xi\mathbf{a}_1$$

$$\mathbf{R}_C = R\mathbf{n}_2 + (r+x)\mathbf{a}_1 + u\mathbf{a}_2$$

$$\mathbf{R}_D = R\mathbf{n}_2 + (r+l)\mathbf{a}_1 + u_l\mathbf{a}_2 + \eta\mathbf{b}_1$$

$$\mathbf{a}_1 = \cos\theta\mathbf{n}_1 + \sin\theta\mathbf{n}_2$$

$$\mathbf{a}_2 = -\sin\theta\mathbf{n}_1 + \cos\theta\mathbf{n}_2$$

$$\mathbf{b}_1 = \cos(\theta+\beta)\mathbf{n}_1 + \sin(\theta+\beta)\mathbf{n}_2$$

where, R = translation from the origin

θ = rotation of the roll actuator B

r = arm length of the actuator B

l = length of the sting including balance

u = bending displacement

u_l = bending displacement at $x = l$

β = elasticslope at $x = l$

l_m = distance of center of rotation from $x = l$

The total kinetic energy of the system is expressed as

$$T = \frac{1}{2}\int_{m_A} \dot{\mathbf{R}}_A\dot{\mathbf{R}}_A dm_A + \frac{1}{2}\int_{m_B} \dot{\mathbf{R}}_B\dot{\mathbf{R}}_B dm_B + \frac{1}{2}\int_{m_C} \dot{\mathbf{R}}_C\dot{\mathbf{R}}_C dm_C + \frac{1}{2}\int_{m_D} \dot{\mathbf{R}}_D\dot{\mathbf{R}}_D dm_D$$

Introducing

$$u = \phi\mathbf{q}$$

and define

$$M_C = \int \phi^T \phi dm_C$$

$$\bar{\phi} = \int \phi dm_C$$

$$\tilde{\phi} = \int x \phi dm_C$$

$$\beta = \phi_l{}' \mathbf{q}$$

The total kinetic energy T becomes

$$\begin{aligned} T = & \frac{1}{2} m_t \dot{R}^2 + \frac{1}{2} I_t \dot{\theta}^2 + S_t \dot{R} \dot{\theta} \cos\theta \\ & + \frac{1}{2} \dot{\mathbf{q}}^T M_t \dot{\mathbf{q}} + \frac{1}{2} \dot{\theta}^2 \mathbf{q}^T M_r \mathbf{q} + \dot{R} \cos\theta \bar{\phi}_t \dot{\mathbf{q}} \\ & - \dot{R} \dot{\theta} \sin\theta \bar{\phi}_t \mathbf{q} + \dot{\theta} \tilde{\phi}_t \dot{\mathbf{q}} - \dot{R} \sin\theta \dot{\mathbf{q}}^T (S_D \phi_l{}'^T \phi_l{}') \mathbf{q} \end{aligned}$$

where, ϕ is admissible function and $\mathbf{q}$ is the generalized coordinates. The potential energy V and the stiffness matrix K can be expressed as

$$V = \frac{1}{2} \mathbf{q}^T K \mathbf{q}$$

$$K = \int_0^l EI(x) \phi''^T \phi'' dx$$

The force equation becomes

$$M_t\ddot{\mathbf{q}} + \bar{\phi_t}^T\ddot{R}\cos\theta + \tilde{\phi_t}^T\ddot{\theta} - \ddot{R}\sin\theta(S_D{\phi_l}'^T\phi_l')\mathbf{q}$$

$$- \dot{R}\dot{\theta}\cos\theta(S_D{\phi_l}'^T\phi_l')\mathbf{q} - \dot{\theta}^2M_r\mathbf{q} + K\mathbf{q} = \mathbf{Q}$$

And the moment equation becomes

$$I_t\ddot{\theta} + S_t\ddot{R}\cos\theta + \ddot{\theta}\mathbf{q}^TM_r\mathbf{q} + 2\dot{\theta}\dot{\mathbf{q}}^TM_r\mathbf{q}$$

$$- \dot{R}\sin\theta\bar{\phi_t}\dot{\mathbf{q}} + \tilde{\phi_t}\ddot{\mathbf{q}} + \dot{R}\dot{\theta}\cos\theta\dot{\mathbf{q}}^T(S_D{\phi_l}'^T\phi_l')\mathbf{q} = \mathbf{M}$$

where, $\mathbf{Q}$ = generalized force

$\mathbf{M}$ = generalized moment

And, $m_t = m_A + m_B + m_C + m_D$

$$I_t = I_B + I_C + m_Cr^2 + 2S_Cr + I_D + m_D(r+l)^2 + 2S_D(r+l)$$

$$S_t = S_B + S_C + m_Cr + S_D + m_D(r+l)$$

$$M_t = M_C + m_D\phi_l^T\phi_l + I_D{\phi_l}'^T\phi_l' + 2S_D{\phi_l}'^T\phi_l'$$

$$M_r = M_C + m_D\phi_l^T\phi_l$$

$$\bar{\phi_t} = \bar{\phi} + m_D\phi_l + S_D\phi_l'$$

$$\tilde{\phi_t} = \tilde{\phi} + r\bar{\phi} + (S_D + m_D(r+l))\phi_l + S_D(r+l)\phi_l'$$

m_t = total mass

$$I_t = \int x^2dm$$

$$S_t = \int xdm$$

The displacements of the model due to sting deflection can be expressed as

$$e_m = R + (r + l + l_m \cos\beta)\sin\theta + (u_l + l_m \sin\beta)\cos\theta$$

$$\theta_m = \theta + \beta$$

If we define the vertical position R and pitch angle θ as

$$R = R_0 + R_1$$

$$\theta = \theta_0 + \theta_1$$

and assume small displacement u.

Then,

$$\theta_0 = \theta_m \tag{A.1}$$

$$\theta_1 = -\left.\frac{\partial u}{\partial x}\right|_{x=l} \tag{A.2}$$

$$R_0 = e_m - (r + l + l_m \sim \theta_m) \tag{A.3}$$

$$R_1 = -(r + l+)\cos\theta_m\theta_1 - u_l \cos\theta_m \tag{A.4}$$

$$\left.\frac{\partial u}{\partial x}\right|_{x=l} = \left.\frac{\partial \phi}{\partial x}\right|_{x=l} \mathbf{q} = \phi'_l \mathbf{q}, \text{ and}$$

$$u\big|_{x=l} = \phi(l)\mathbf{q} = \phi_l b f q$$

$$M_t \ddot{\mathbf{q}} + K_t \mathbf{q} = \mathbf{Q}_t \tag{A.5}$$

$$K_t = K - \ddot{\theta}_m^2 M_r$$

$$- \left[\ddot{e}_m \sin\theta_m + (r + l + l_m)\dot{\theta}_m^2 \sin\theta_m - (r + l + l_m)\ddot{\theta}_m \cos\theta_m \sin\theta_m\right.$$

$$\left. + \dot{e}_m \dot{\theta}_m \cos\theta_m - (r + l + l_m)\dot{\theta}_m^2 \cos^2\theta_m\right](S_D {\phi'_l}^T \phi'_l)$$

$$Q_t = -\bar{\phi_t}^T(\ddot{e}_m + (r + l + l_m)\dot{\theta}_m^2 \sin\theta_m - (r + l + l_m)\ddot{\theta}_m \cos\theta_m)\cos\theta_m$$

$$- \tilde{\phi_t}^T \ddot{\theta}_m$$

Define e_m and θ_m and the velocity and acceleration are calculated using central differencing scheme for equations (A.1) and (A.3) Solve equation (A.5) to get $\mathbf{q}(t)$. Calculate θ_1 and R_1 from equations (A.2) and (A.4). Then the final motion is described as

$$R = R_0 + R_1$$

$$\theta = \theta_0 + \theta_1$$

A.7 Unsteady Motion Trajectory Shaping

In order to generate the transient motions, first, the capability of the DyPPiR has to be considered. Since any moving system has a finite mass, the trajectory is divided into 4 segments as shown in Figure A.22. They are acceleration phase(1), ramp motion phase(2), decelaration phase(3), and pause phase(4). Maximum accelaration and deceleration allowable was used so that wider ramp motion range can be obtained. Maximum angle of attack for pitch was limited to 45 degrees. The trajectory design procedure was as follows.

- Calculate the weight and position of each moving part.
- Calculate the mass moment of inertia through pitch axis.
- Calculate the maximum possible pitch acceleration and take 90 % as allowable acceleration.
- Calculate acceleration time t_1 and θ_1.
- Calculate maximum acceleration of the vertical actuator $\ddot{z}$ and take 90% as maximum allowable acceleratrion. Calculate $\dot{z}$ and $v = r\dot{\theta}$. $\dot{z}$ and v should be $\leq$ 30 ft/sec.
- Consider other geometrical constraints and find proper z_{off}.

The weight of the moving parts were found to be 660 lbs, including the 6 to 1 prolate spheroid model, which is 59 lbs. The weight distribution forward of the pitch axis is as shown in Table A.1. The mass moment of inertia of the system can

be calculated as

$$J_{total} = J_0 + \frac{1}{g}\sum_{i=1}^{n} w_i {r_i}^2$$

where, J_0 = pitch actuator vane assembly

w_i = weight of the ith component

r_i = distance from the pitch actuator center

The maximum pitch acceleration can be obtained

$$\ddot{\theta}_{max} = \frac{T_{max}}{J_{total}}$$

$$\approx 85 \quad rad/sec^2$$

Consider only 90 % for safe operation and we get

$$\ddot{\theta} = (0.9) \times (\ddot{\theta}_{max})$$

Using this angular acceleration, calculate the acceleration time t_1 and acceleration angle θ_1 to achieve the given constant pitch rate. Since the center of rotation should remain at the initial z-location while the body is pitching, there exist a relation

$$z = -r\sin\theta(t)$$

Calculate $\ddot{z}_{max}$ using given moving weight and available actuator force assuming 90 % efficiency. Using this vertical speed achievable in time t_1. Also, calculate pod vertical speed to compensate the pitching motion of the model

$$v = r\dot{\theta}$$

Compare $\dot{z}$, v, and $\dot{z}_{max} = 30$ ft/sec. The relation should be

$$v = r\dot{\theta} < 30 ft/sec < \dot{z}(t_1)$$

Find a proper $\ddot{\theta}$ and z to compensate the model pitching motion.

TABLE A.1

Moving Parts Weight Summary

item	Weight (lbs)
pitch actuator assembly	90.1
roll actuator assembly	41.5
sting	27.0
actuator bracket no. 1	40.8
actuator bracket no. 2	41.0
actuator bracket bolts	0.7
roll actuator fairing	6.8
vertical actuator coupling	9.8
roll resolver	1.0
pitch resolver	1.0
pod sideplate no.1	93.0
pod sideplate no.2	93.0
front bearing mounting block	50.0
rear bearing mounting block	50.0
actuator rod and piston	55.0
Total	600.7

TABLE A.2

Pitch and Roll Axes Characteristic Constants

item	pitch axis	roll axis	unit
D_M	20.26	2.15	in^3/rad
V_T	35.36	10.53	in^3
T	57740	5820	$in-lb$
J	600.00	4.00	$in-lb-sec^2$
B	206.20	18.77	$in-lb-sec/rad$
K_T	11.608×10^6	440.619×10^3	psi/rad
K_V	98.39	11.13	sec^{-1}
τ	0.0025	0.0025	
K_Q	14.238	1.67	$in^3/sec/mA$
K_L	0.0056	0.000668	$in^3/sec/psi$
K_A	14.00	3.50	mA/Vdc
K_θ, K_ϕ	10.00	4.10	V/rad
$K_{\dot{\theta}}, K_{\dot{\phi}}$	0.06	0.00	$V/(rad/sec)$
K_p	0.00	0.00	mA/psi

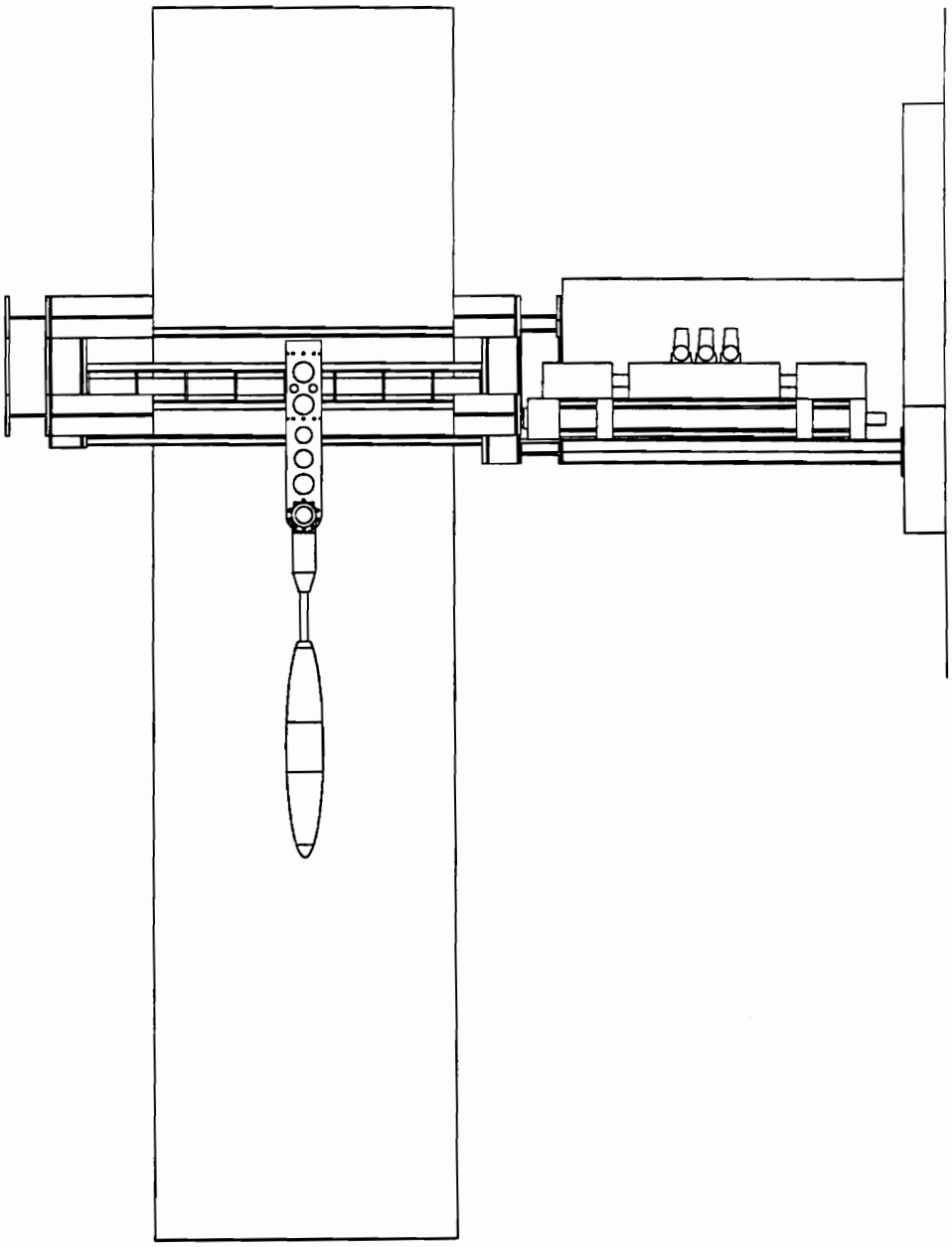

Figure A.1. DyPPiR Side View.

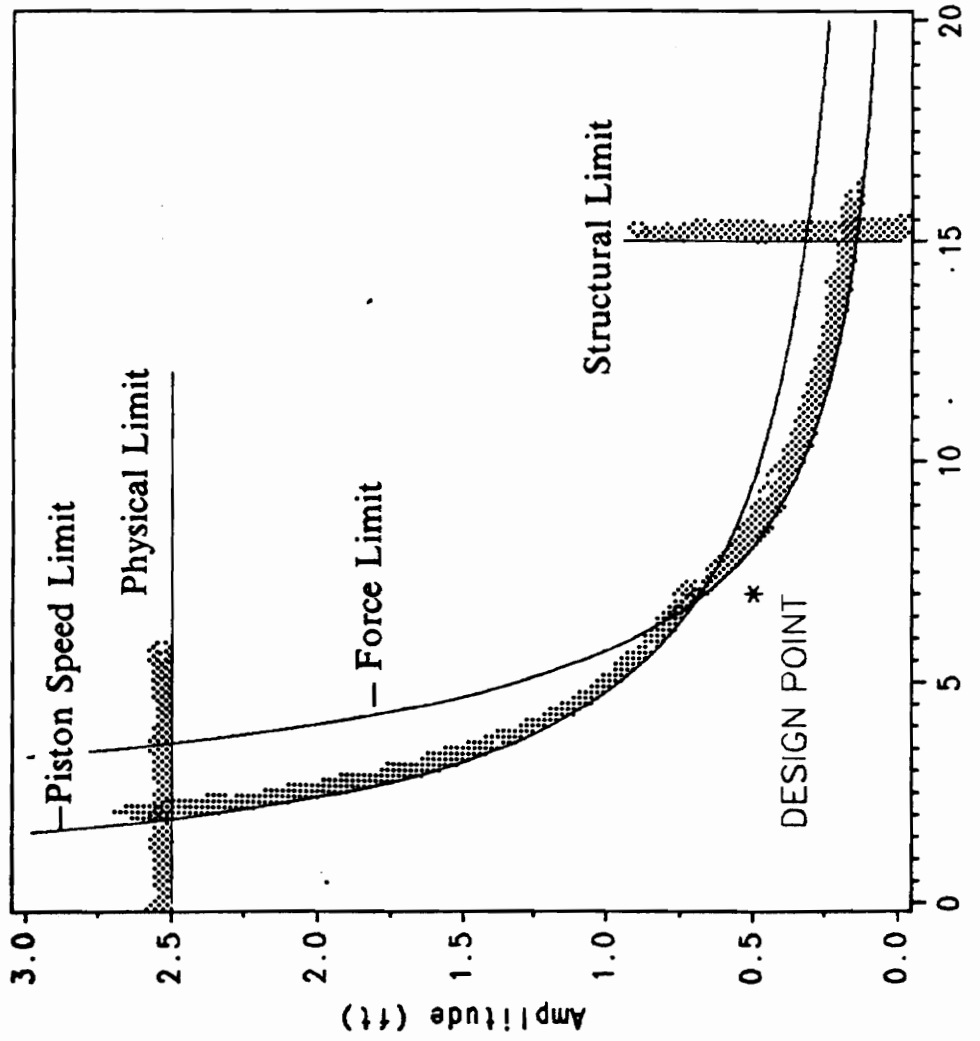

Figure A.2. Vertical Axis Performance Specification.

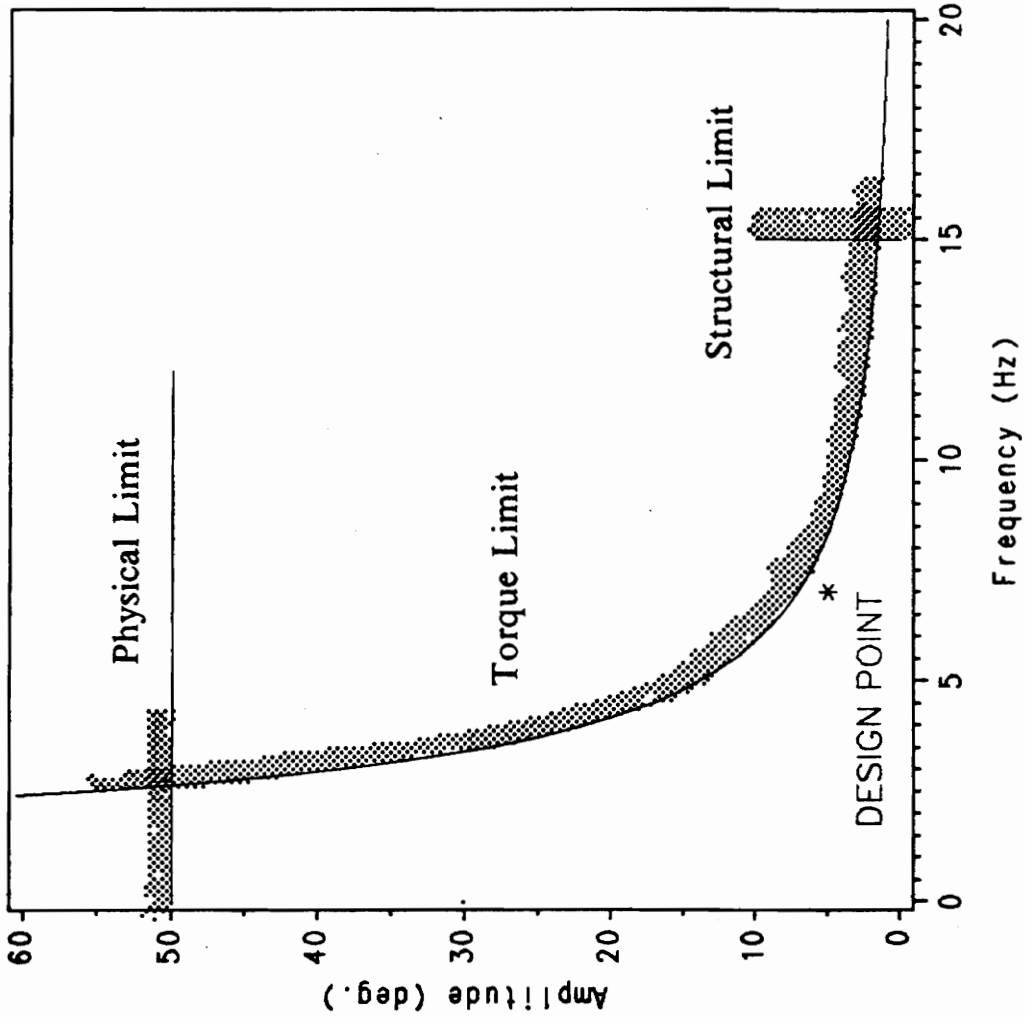

Figure A.3. Pitch Axis Performance Specification.

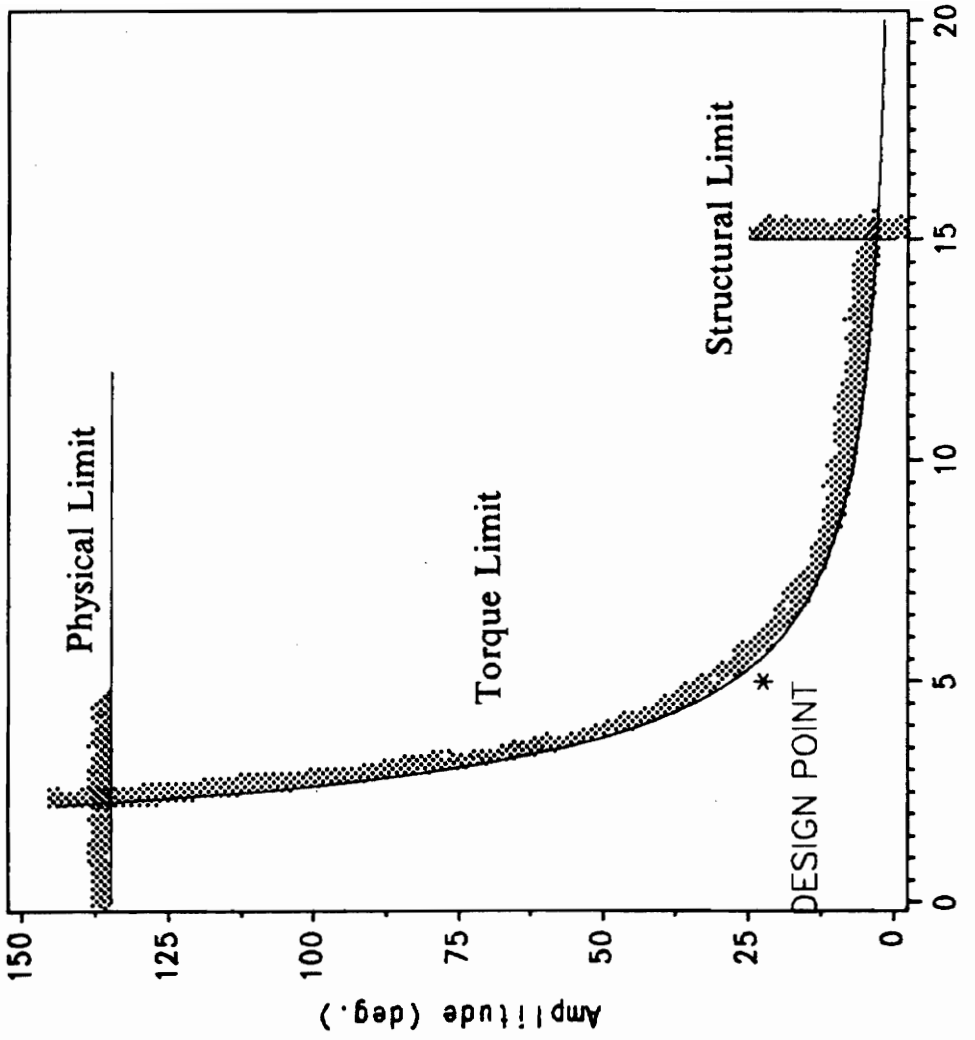

Figure A.4. Roll Axis Performance Specification.

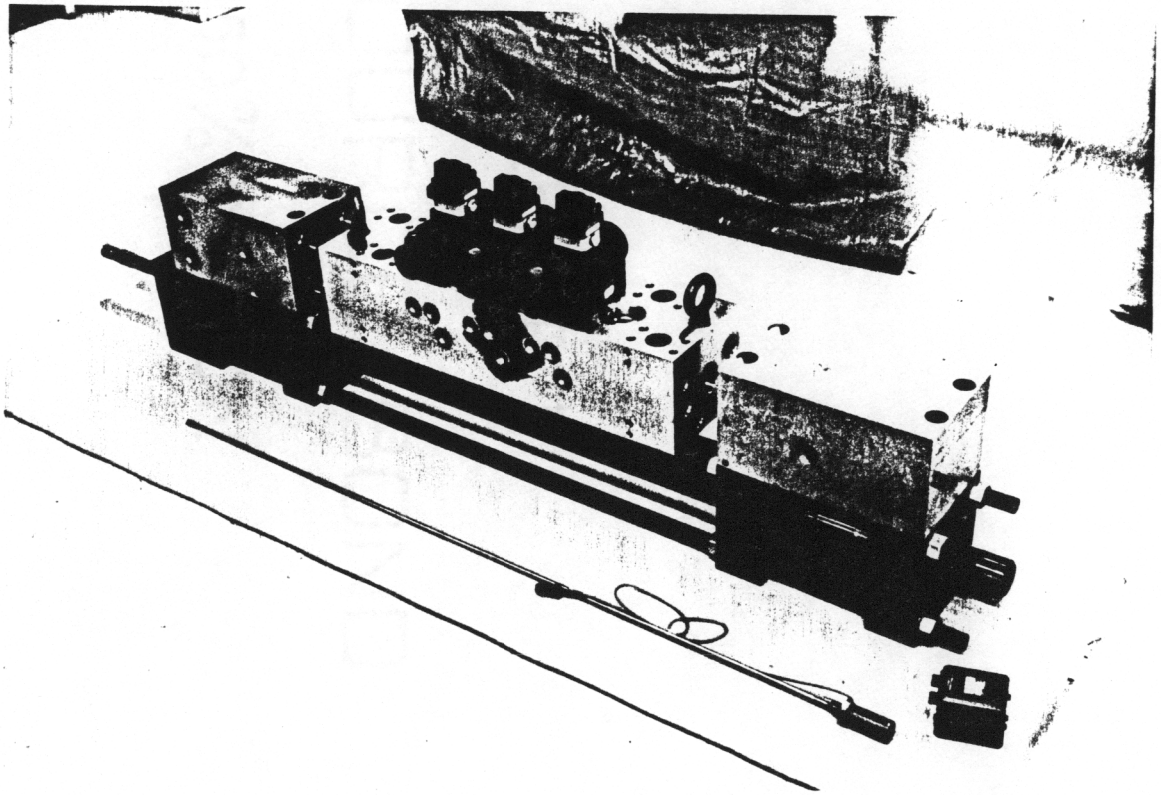

Figure A.5. Vertical Actuator with Integral Manifold.

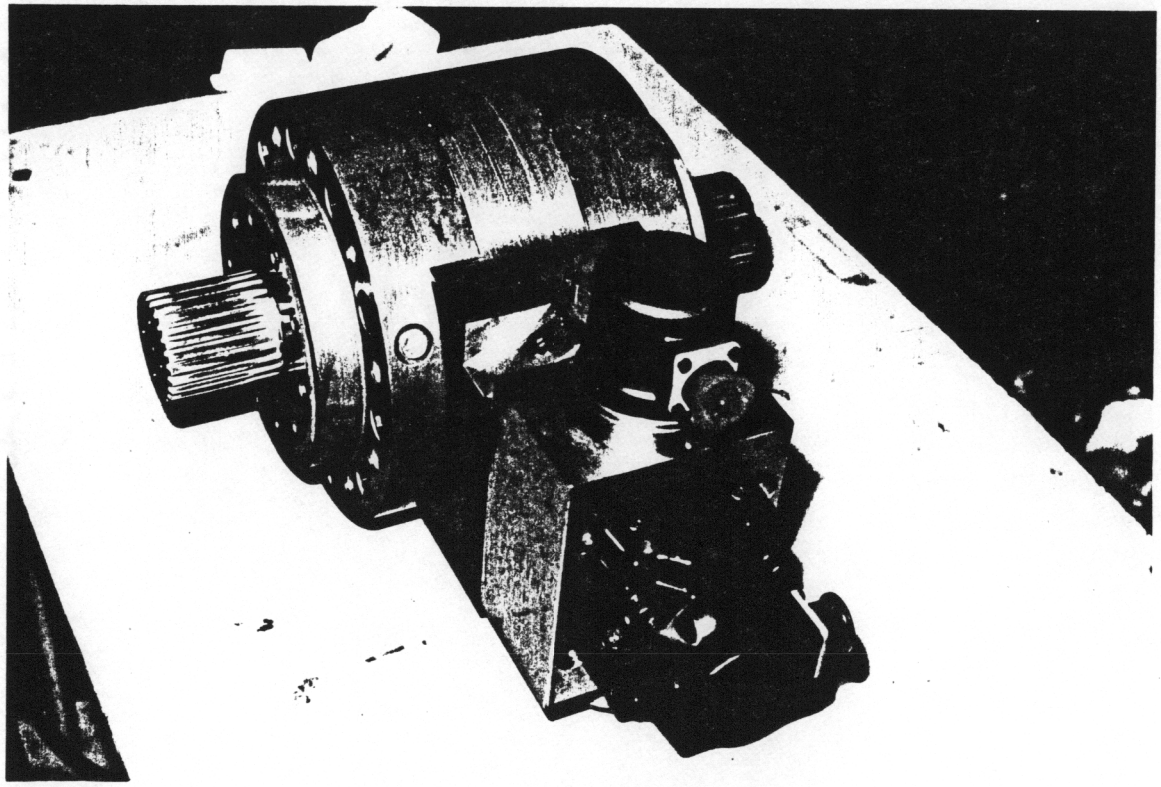

Figure A.6. Pitch Actuator with Servovalve Mounted.

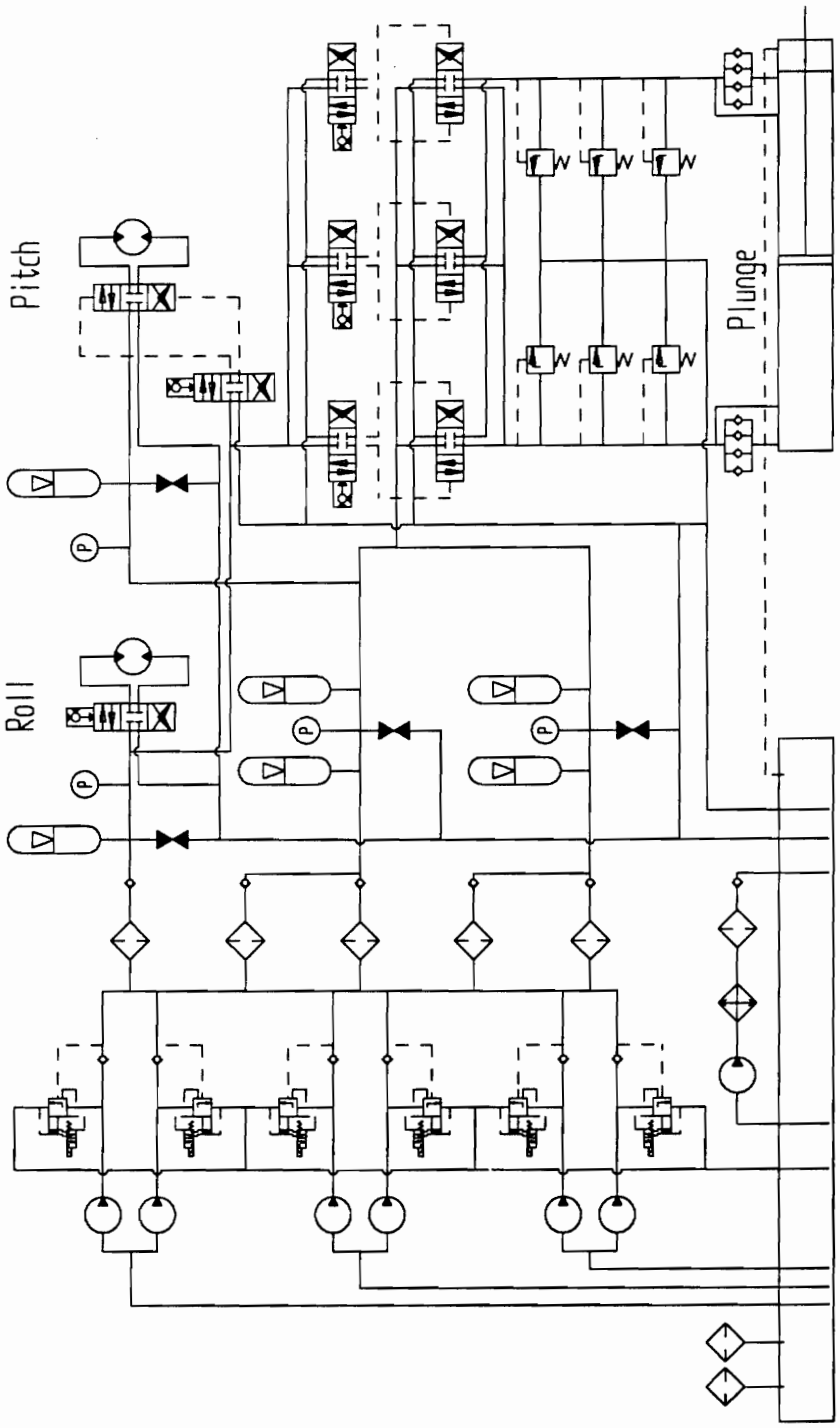

Figure A.7. Hydraulic Power System Diagram.

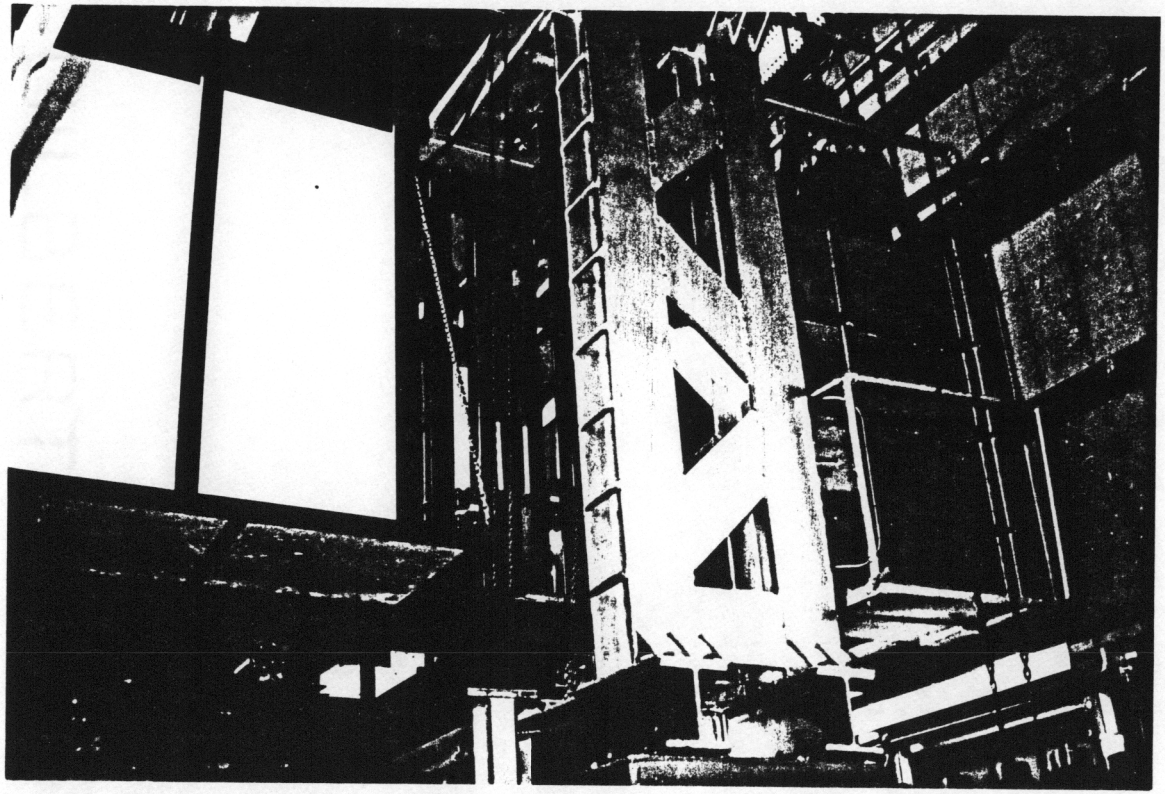

Figure A.8. Steel Support Structure.

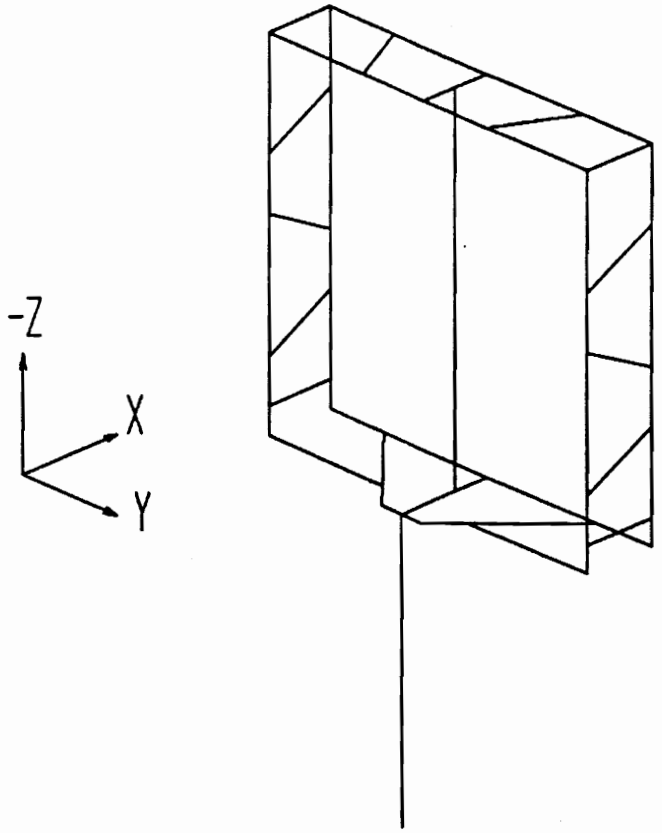

Figure A.9. Structure Model for Modal Analysis.

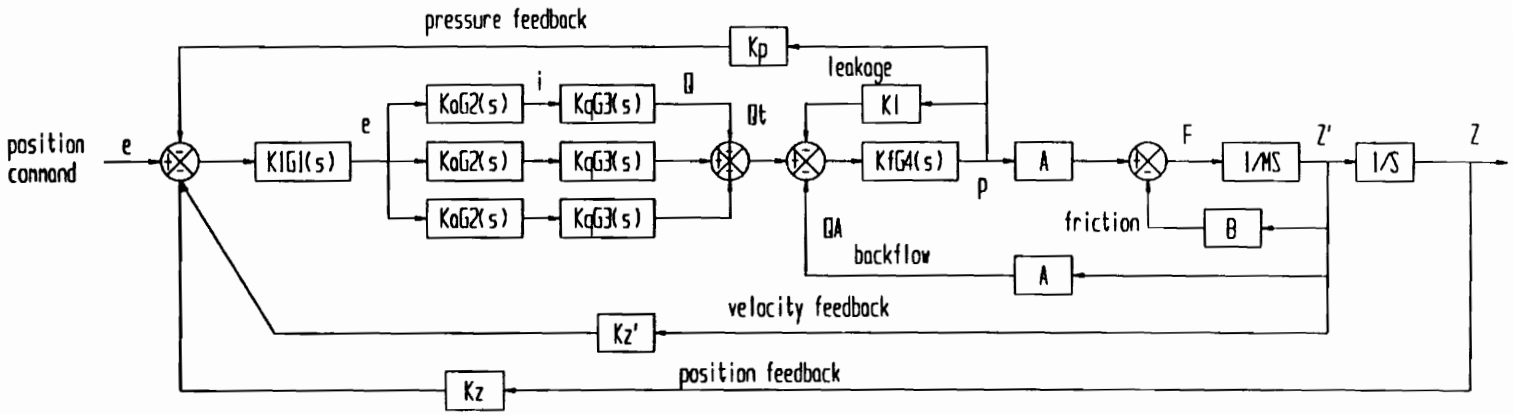

Figure A.10. Vertical Axis Control Loop Diagram.

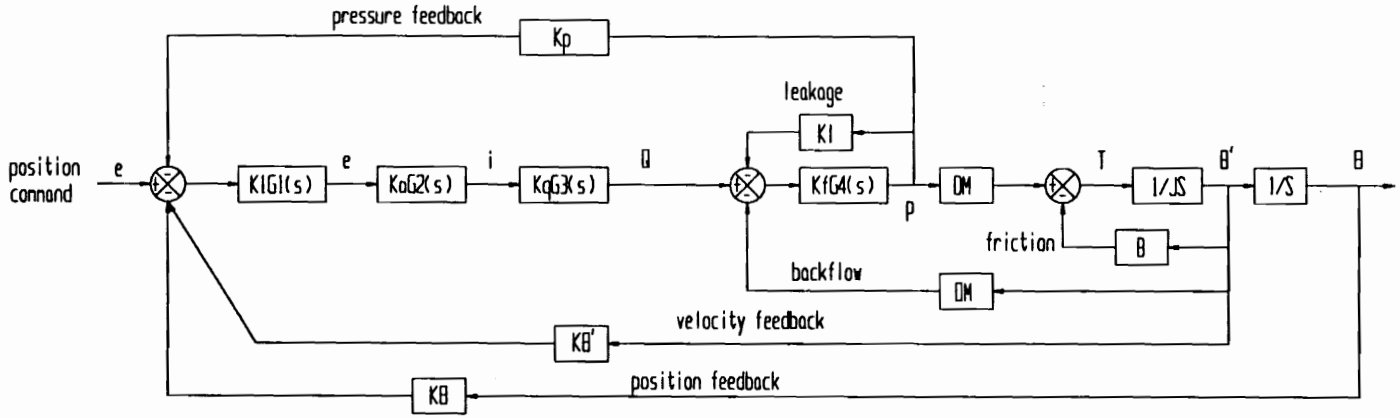

Figure A.11. Pitch Axis Control Loop Diagram.

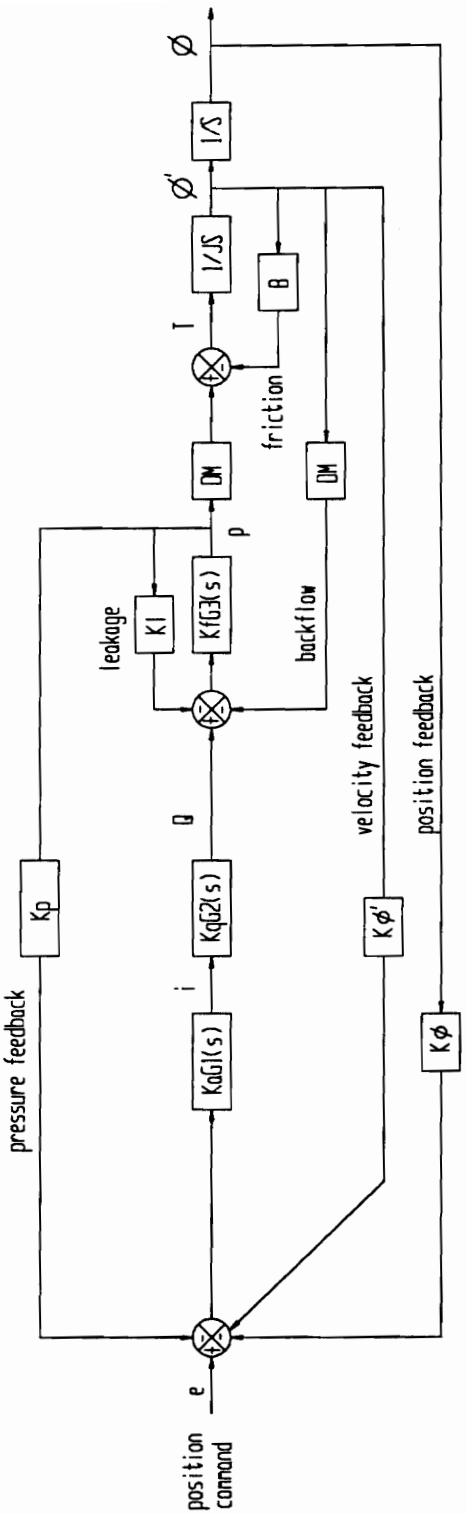

Figure A.12. Roll Axis Control Loop Diagram.

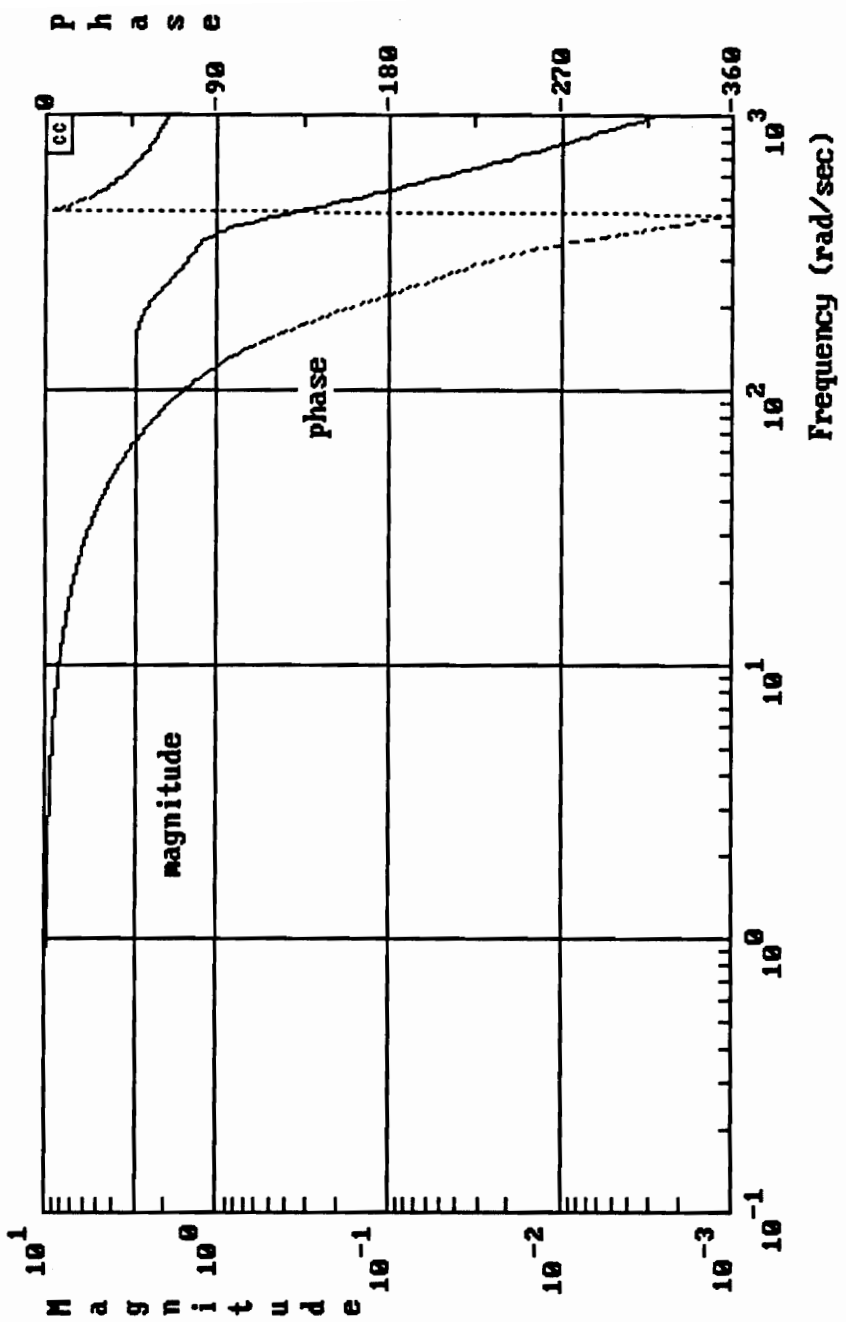

Figure A.13. Vertical Axis System Bode Plot

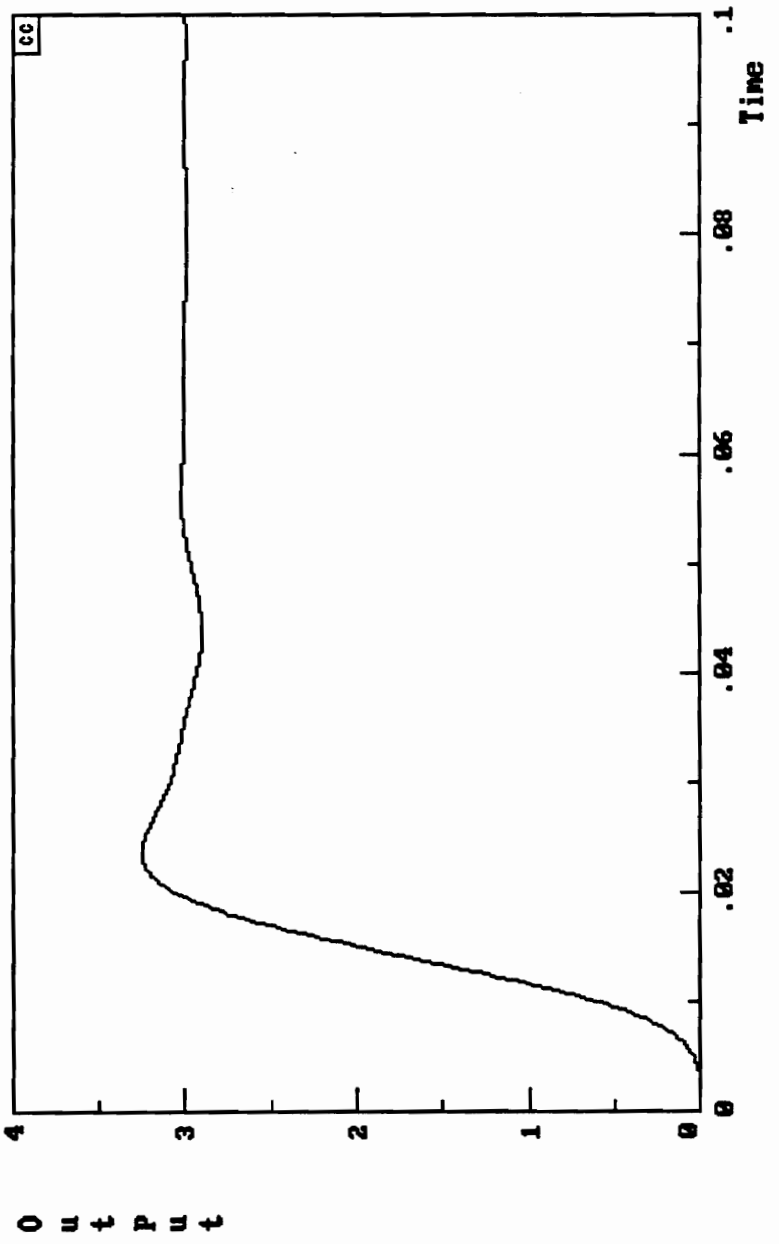

Figure A.14. Vertical Axis System Closed Loop Step Response.

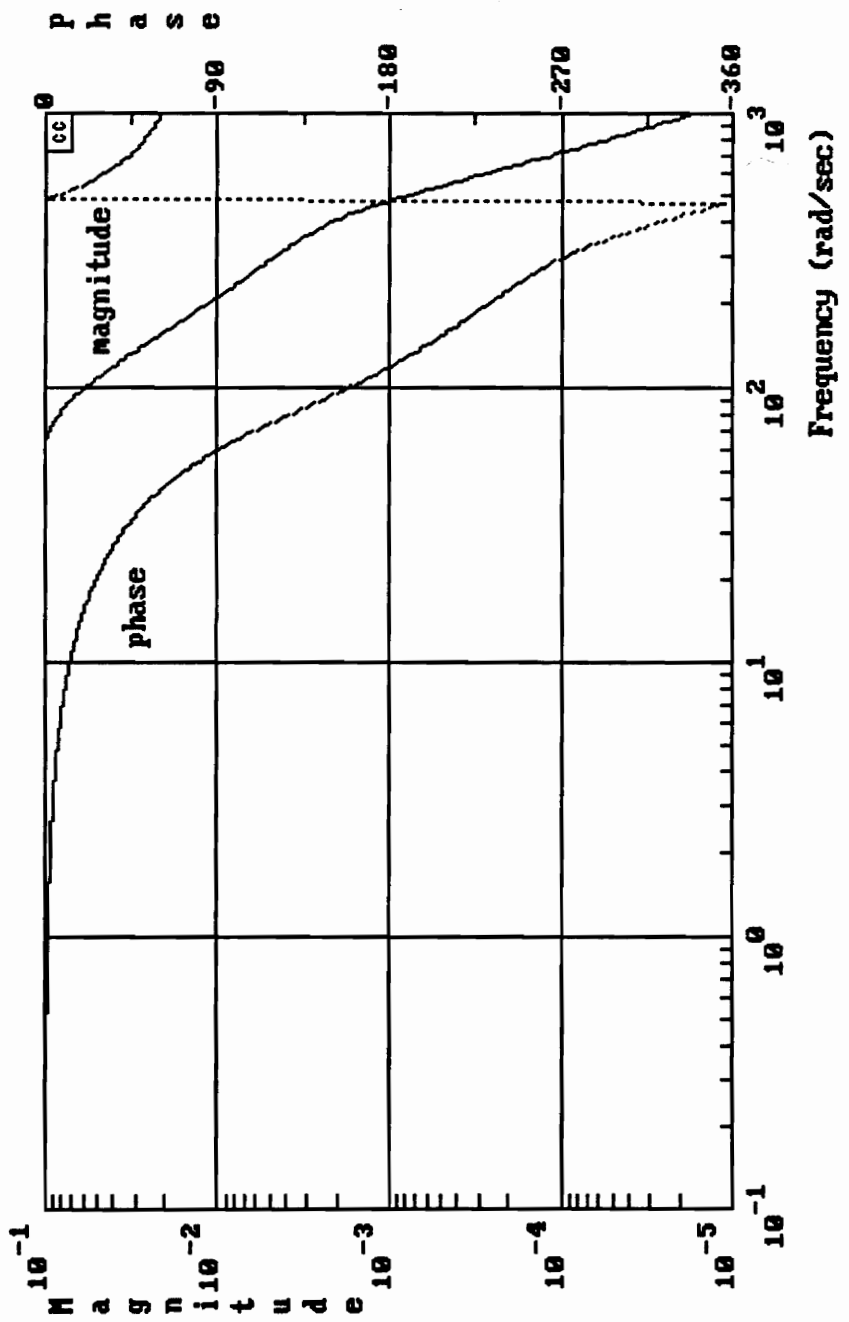

Figure A.15. Pitch Axis System Bode Plot, $J = 600in - lb - sec^2$.

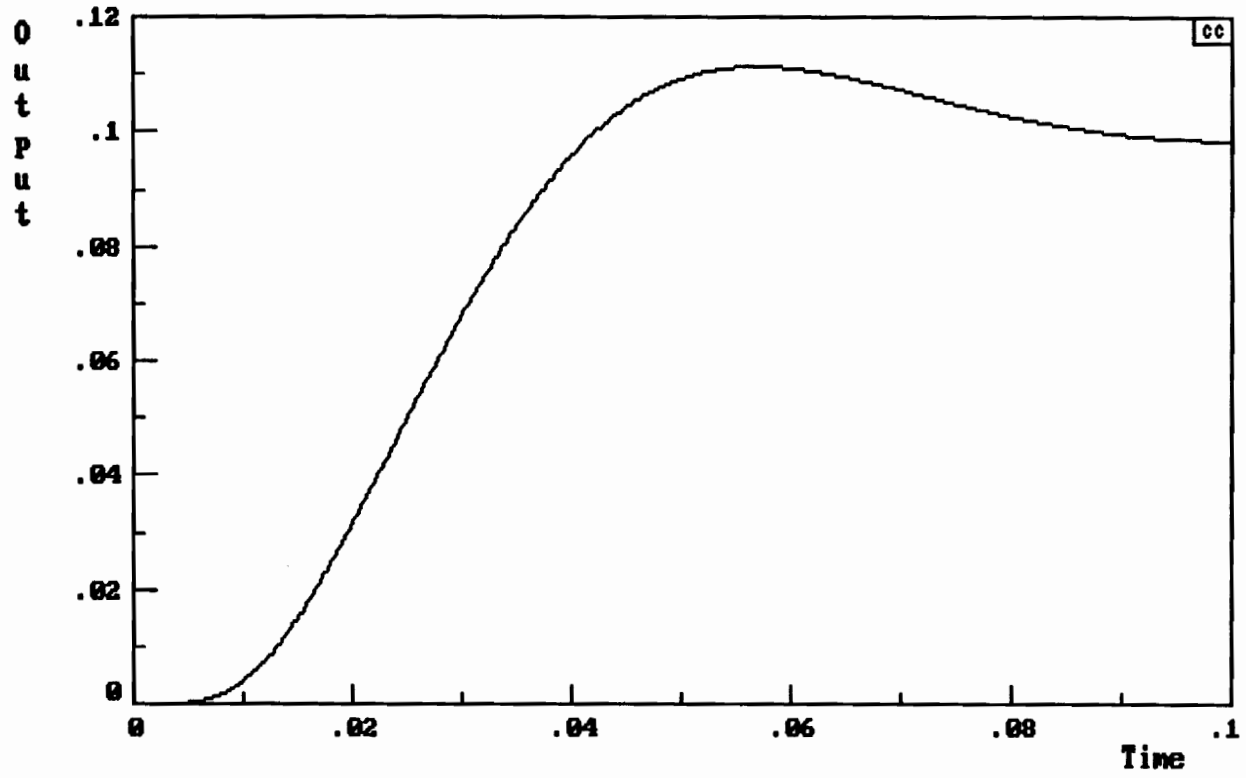

Figure A.16. Pitch Axis System Closed Loop Step Response, $J = 600in - lb - sec^2$.

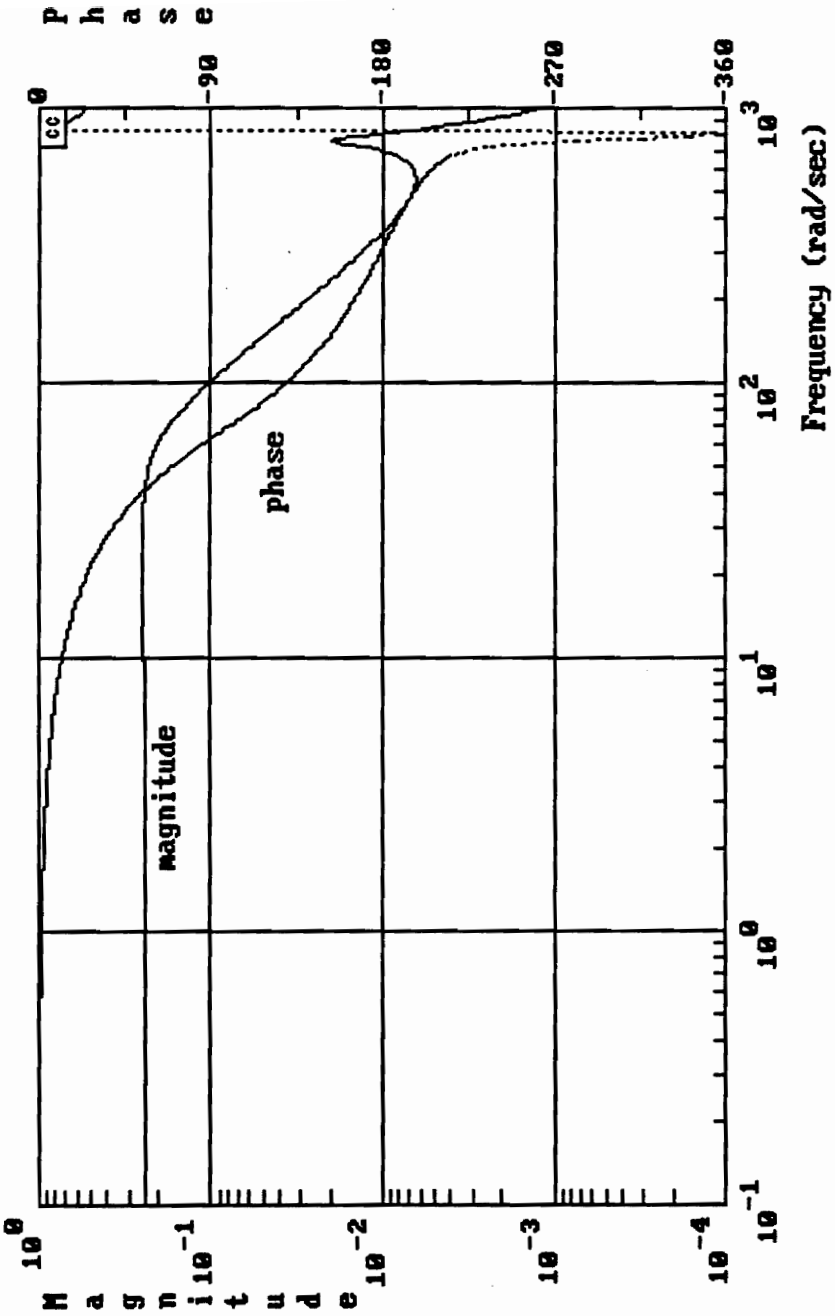

Figure A.17. Roll Axis System Bode Plot.

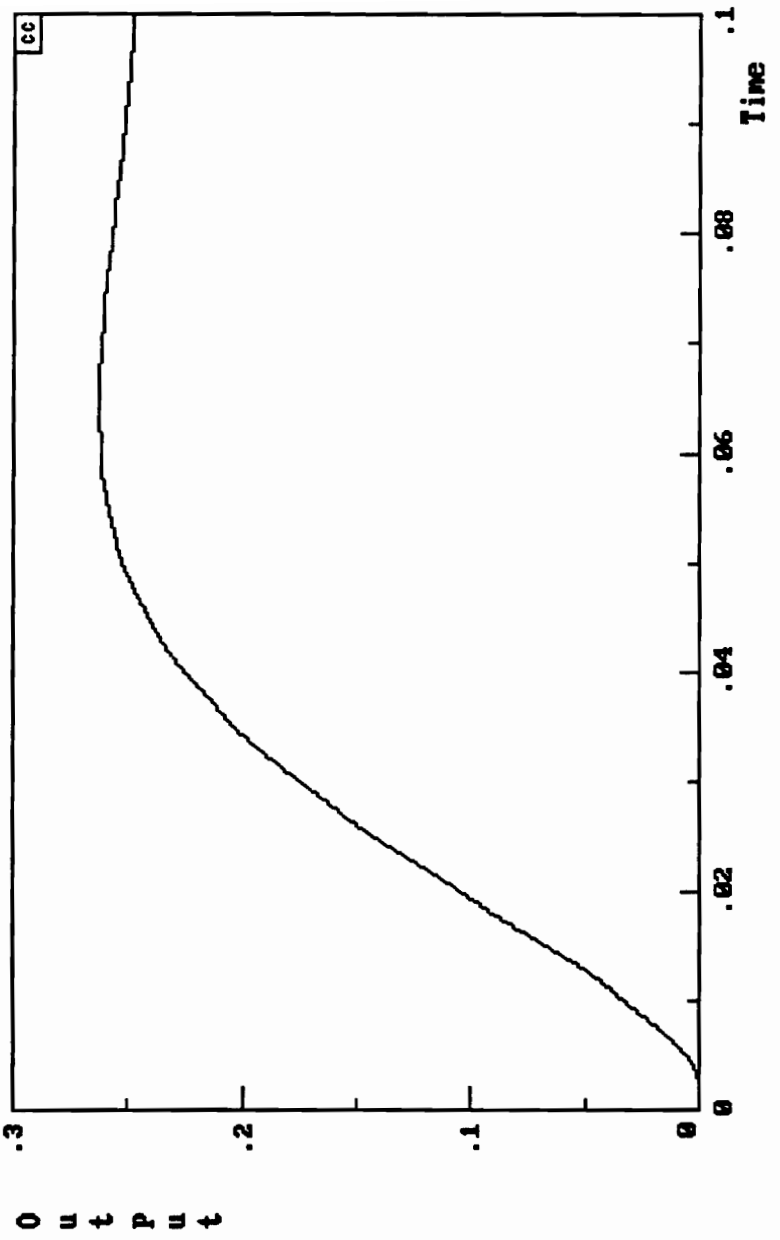

Figure A.18. Roll Axis System Closed Loop Step Response.

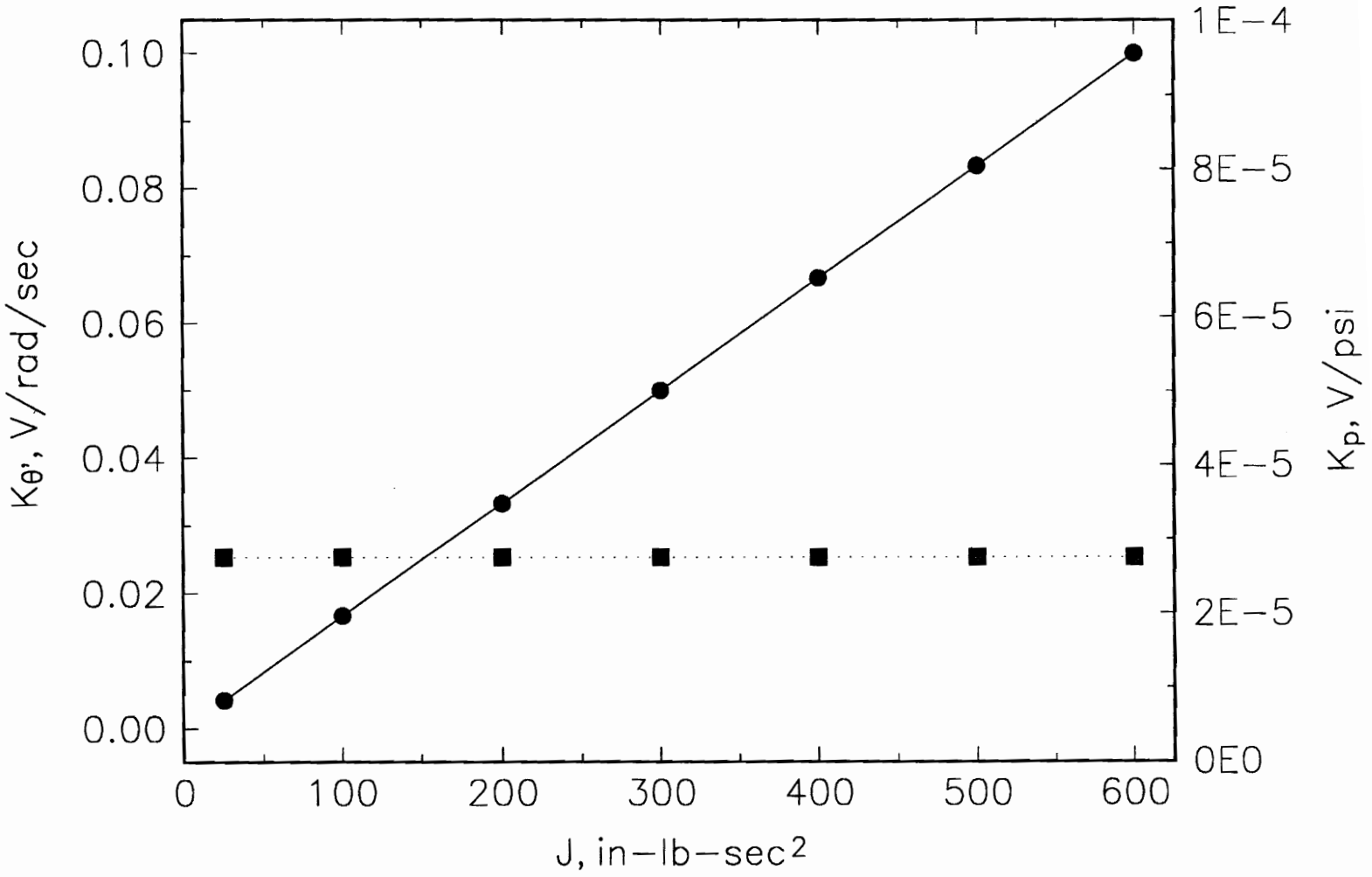

Figure A.19. Pitch Axis System Feedback Gain Adjustment Plan.

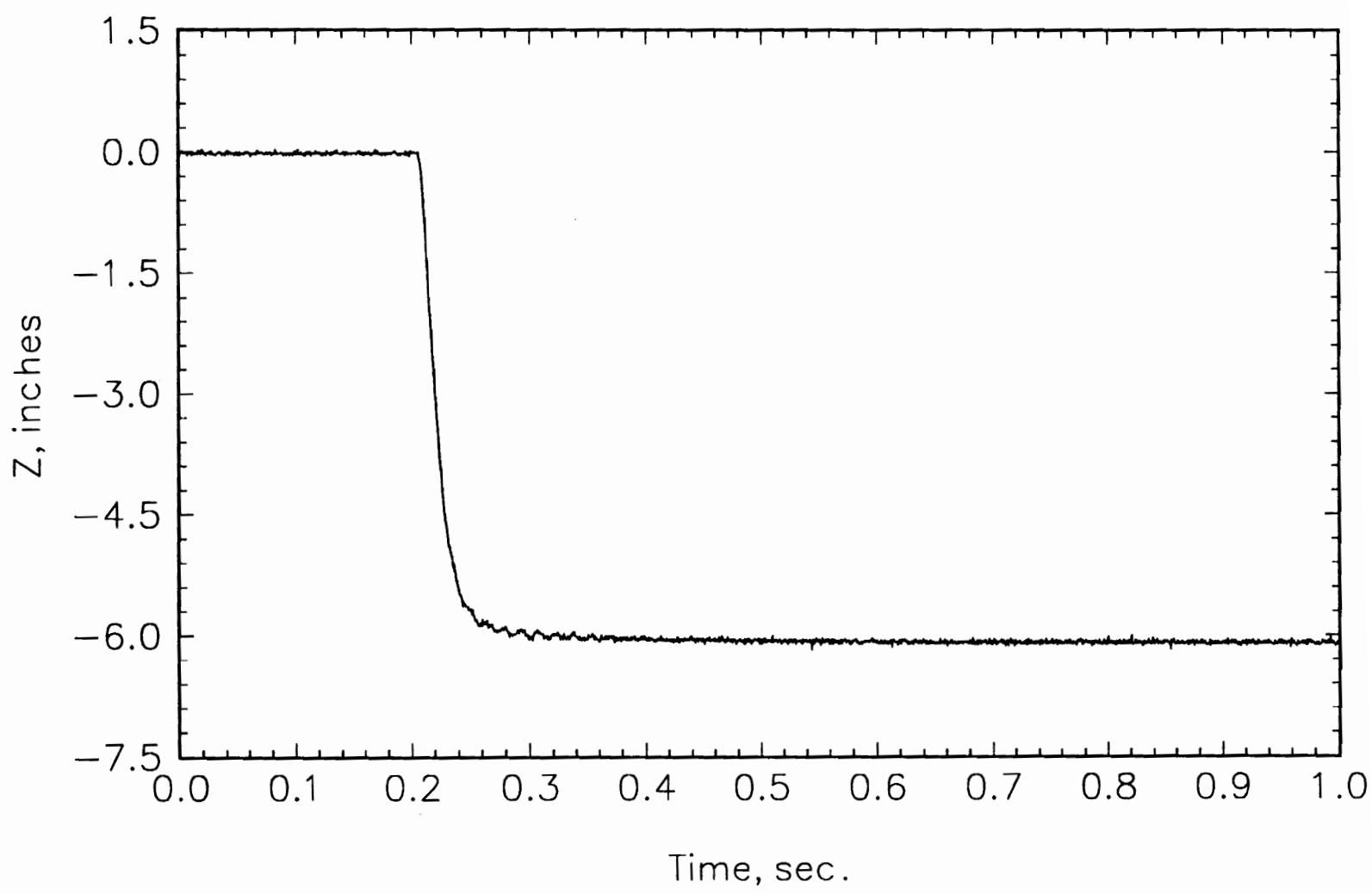

Figure A.20. Plunge Actuator Closed Loop Step Response.

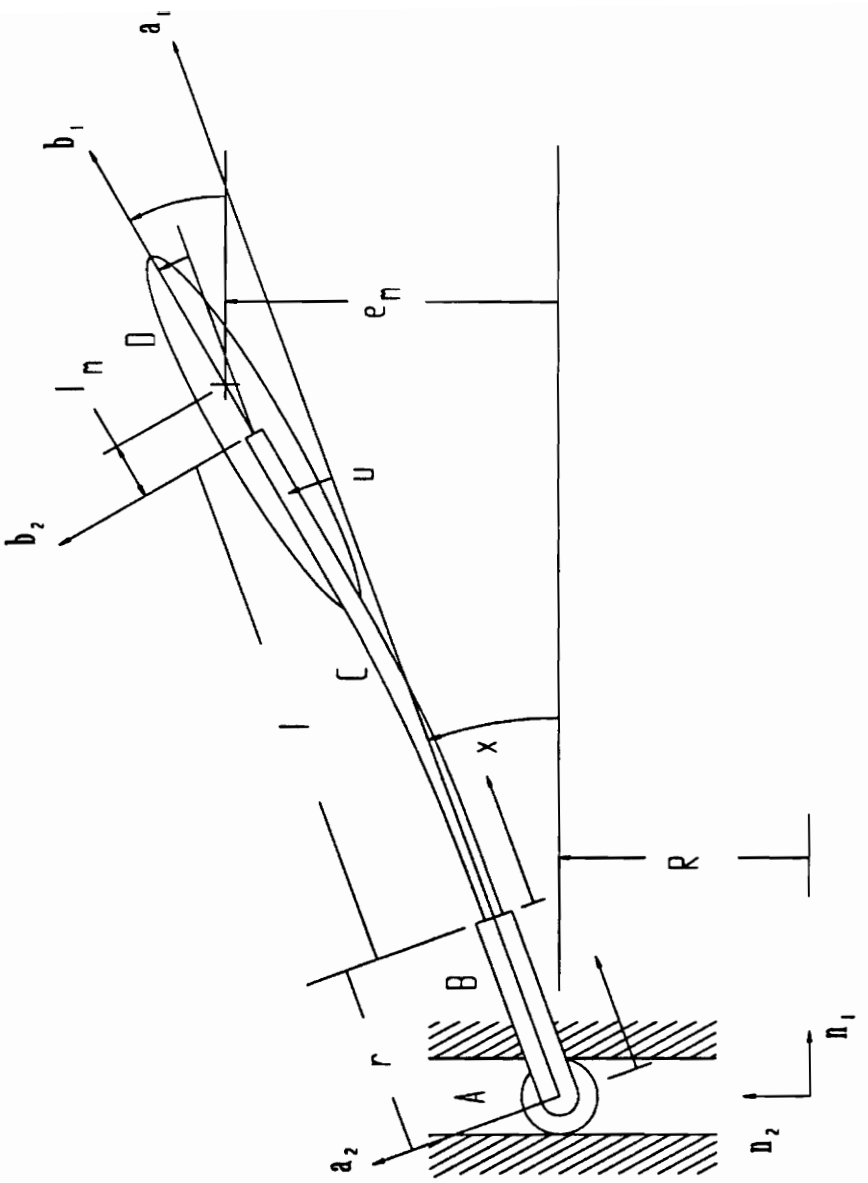

Figure A.21. Sting Deflection Correction.

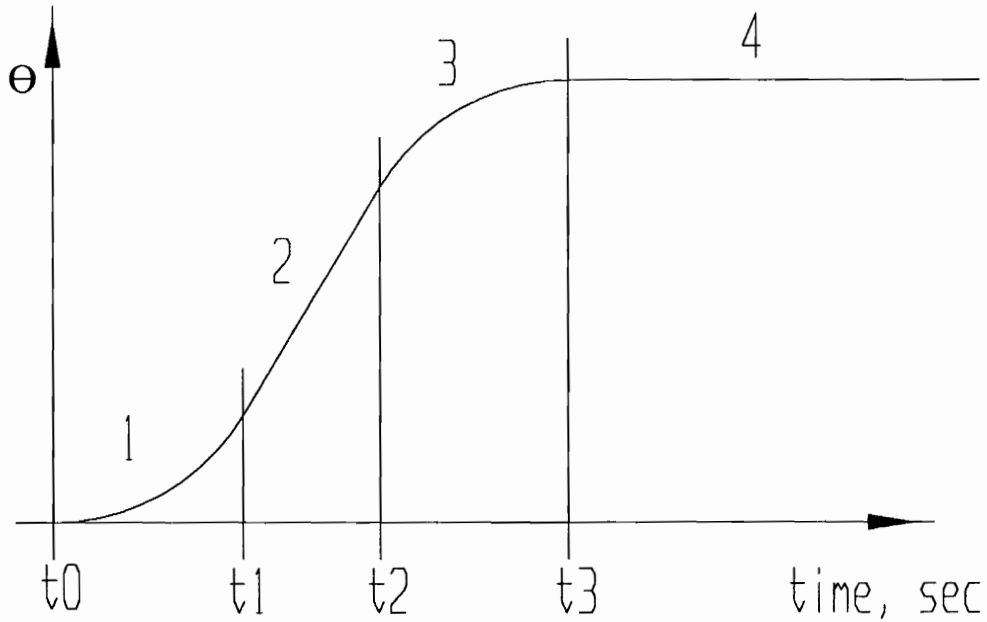

Figure A.22. Trajectory Shaping.

APPENDIX B.

SURFACE VELOCITY ON THE ELLIPSOID

SURFACE VELOCITY ON THE ELLIPSOID.

An ellipsoid with three unequal axes is the only type of truly three dimensional body for which the exact potential flow can be computed. From the approach formulated by Lamb (1945) to the useful equations of Mason (1981), there is a big gap in deriving the potential flow solution. In this section, the potential flow solution of the problem is derived in detail with the help of existing literatures (Faulkner *et al.*, 1968; Cebeci *et al.*, 1980; Band and Payne, 1980). The only onset flow considered here will be those parallel to the coordinate axes. The surface velocities of other inclinations of the onset flow can be obtained as linear combination of those for these cases. Ellipsoids have the simplifying property that the velocity at any point on the surface is simply the component tangent to the surface of the maximum surface velocity. The surface velocity vector at any other point on the surface is just the component of this maximum velocity and is obtained by subtracting from the maximum velocity vector its component along the local normal vector at the point in question. Consider an ellipsoid whose semiaxes lie along the coordinate axes. If the body is in an irrotational, incompressible uniform flow $\mathbf{U}$, it is possible to introduce a velocity potential Φ with a fluid velocity $\mathbf{V}$,

$$\mathbf{V} = \mathbf{U} - \nabla\Phi$$

The scalar function Φ satifies the Laplace's equation.

$$\nabla^2\Phi = 0$$

The boundary condition should be

- Slip condition on the surface of the body.

$$\mathbf{V} \cdot \mathbf{n} \qquad \text{or} \qquad \left.\frac{\partial \Phi}{\partial n}\right|_S = \mathbf{U} \cdot \mathbf{n}$$

  Here $\mathbf{n}$ is the local normal vector.

- At infinity, uniform flow of velocity $\mathbf{U}$.

$$\nabla \Phi = 0$$

The surface of the ellipsoid is given by the equation

$$\frac{x^2}{a^2} + \frac{y^2}{b^2} + \frac{z^2}{c^2} = 1$$

In the elliptic coordinates system λ, μ, ν defined by the relation

$$x^2 = \frac{(a^2+\lambda)(a^2+\mu)(a^2+\nu)}{(a^2-b^2)(a^2-c^2)}$$
$$y^2 = \frac{(b^2+\lambda)(b^2+\mu)(b^2+\nu)}{(b^2-c^2)(b^2-a^2)}$$
$$z^2 = \frac{(c^2+\lambda)(c^2+\mu)(c^2+\nu)}{(c^2-a^2)(c^2-a^2)}$$

the Laplacian $\nabla^2\Phi$ is expressed as follows:

$$\nabla^2\Phi = \frac{-4}{(\lambda-\mu)(\mu-\nu)(\nu-\lambda)}\left\{(\mu-\nu)k_\lambda \frac{\partial}{\partial\lambda}\left(k_\lambda \frac{\partial\Phi}{\partial\lambda}\right)\right.$$
$$\left. + (\nu-\lambda)k_\mu \frac{\partial}{\partial\mu}\left(k_\mu \frac{\partial\Phi}{\partial\mu}\right) + (\lambda-\mu)k_\nu \frac{\partial}{\partial\nu}\left(k_\nu \frac{\partial\Phi}{\partial\nu}\right)\right\}$$

Here

$$(k_\lambda)^2 = (a^2+\lambda)(b^2+\lambda)(c^2+\lambda)$$

$$(k_\mu)^2 = (a^2+\mu)(b^2+\mu)(c^2+\mu)$$

$$(k_\nu)^2 = (a^2+\nu)(b^2+\nu)(c^2+\nu)$$

The Laplace's equation in ellipsoidal coordinates can be written in the form

$$(\mu-\nu)k_\lambda\frac{\partial}{\partial\lambda}\left(k_\lambda\frac{\partial\Phi}{\partial\lambda}\right)+(\nu-\lambda)k_\mu\frac{\partial}{\partial\mu}\left(k_\mu\frac{\partial\Phi}{\partial\mu}\right)+(\lambda-\mu)k_\nu\frac{\partial}{\partial\nu}\left(k_\nu\frac{\partial\Phi}{\partial\nu}\right)=0$$

Seek a solutions of the form

$$\Phi=\alpha\chi,$$

where χ is a function of λ only. Plugging in the Laplace's equation and rearranging, we get

$$\frac{\partial}{\partial\lambda}\log\left(\frac{\partial\chi}{\partial\lambda}\right)=-\frac{2}{\alpha}\left(\frac{\partial\alpha}{\partial\lambda}\right)$$

Since the left hand side is a function of λ only, the right side must be independent of μ,ν, and therefore the proposed form of the soultion is only possible when α be such that this condition is satisfied. Thus α must be of the form

$$\alpha=\alpha_\lambda f(\mu,\nu)$$

where α_λ is independent of μ, nu and $f(\mu,\nu)$ is independent of λ. In this case (3) becomes

$$\frac{d}{d\lambda}\left[\log\left(k_\lambda\frac{d\chi}{d\lambda}\right)\right]=\frac{d}{d\lambda}\left[\log\frac{1}{{\alpha_\lambda}^2}\right],$$

which , on integration, gives

$$\chi=A\int\frac{d\lambda}{{\alpha_\lambda}^2k_\lambda}+B,$$

where A and B are arbitrary constants. Thus if α is an ellipsoidal harmonic having the postulated properties, so also are

$$\alpha\int\frac{d\lambda}{{\alpha_\lambda}^2k_\lambda}\qquad\int\frac{d\lambda}{k_\lambda},$$

the second being obtained by taking $\alpha = 1$, which is obviously the solution. Now (1) is merely Laplace's equation $\nabla^2\Phi = 0$ expressed in a particular system of coordinates. Therefore x, y, z, xy, yz, zx and in fact any spherical harmonic, are solution of (1). The values of x, y, z are already given, so that we may take

$$\alpha = (a^2+\lambda)^{\frac{1}{2}}(a^2+\mu)^{\frac{1}{2}}(a^2+\nu)^{\frac{1}{2}}, \quad \text{corresponds to x}$$

$$\text{or} \quad \alpha = (b^2+\lambda)^{\frac{1}{2}}(b^2+\mu)^{\frac{1}{2}}(b^2+\nu)^{\frac{1}{2}}(c^2+\lambda)^{\frac{1}{2}}(c^2+\mu)^{\frac{1}{2}}(c^2+\nu)^{\frac{1}{2}},$$

corresponding to yz, which both obviously satisfy (1). Rearranging,

$$\alpha_1 = \alpha_{\lambda_1} f_1(\mu,\nu) \qquad \text{where} \quad \alpha_{\lambda_1} = a^2+\lambda$$

$$\alpha_2 = \alpha_{\lambda_2} f_2(\mu,\nu) \qquad \text{where} \quad \alpha_{\lambda_2} = (b^2+\lambda)(c^2+\lambda)$$

Therefore the ellipsoidal harmonics given by the first function of (5) are

$$\Phi_x = Cx\int_\lambda^\infty \frac{d\lambda}{(a^2+\lambda)k_\lambda} \qquad \Phi_{yz} = Cyz\int_\lambda^\infty \frac{d\lambda}{(b^2+\lambda)(c^2+\lambda)k_\lambda},$$

where C is an arbitrary constant, and x, y, z are supposed expressed in terms of λ, μ, ν as above.

Consider an ellipsoid which corresponds $\lambda = 0$, moving in the direction of negative x-axis with velocity U. The boundary condition is

$$\frac{\partial\Phi}{\partial n} = U_0\cos\theta_x \qquad \text{or} \qquad \frac{\partial\Phi}{\partial\lambda} = U_0\frac{\partial x}{\partial\lambda}, \qquad \lambda = 0,$$

where θ_x is the angle normal and the x-axis. The function $\Phi = \Phi_x$ satisfies the condition $\lambda = 0, \Phi = Ux$ and $\lambda \to \infty, \Phi \to 0$. We therefore take

$$\Phi = Cx\int_\lambda^\infty \frac{d\lambda}{(a^2+\lambda)k_\lambda}.$$

Condition (2) then gives

$$U\frac{\partial x}{\partial \lambda} = C\frac{\partial x}{\partial \lambda}\int_0^\infty \frac{d\lambda}{(a^2+\lambda)k_\lambda} - \frac{Cx}{a^2 \cdot abc}, \quad \text{when} \lambda = 0.$$

From (1), $\partial x/\partial\lambda = \frac{1}{2}x/a^2$, when $\lambda = 0$, and therefore

$$C = \frac{abcU}{2-\alpha_0} \qquad \text{where} \qquad \alpha_0 = abc\int_0^\infty \frac{d\lambda}{(a^2+\lambda)k_\lambda}.$$

The constant α_0 depends solely on the semi-axes a, b, c of the ellipsoid. Its numerical evaluation requires the use of elliptic integrals. Thus, finally,

$$\Phi = \frac{abcU}{2-\alpha_0}\int_\lambda^\infty \frac{d\lambda}{(a^2+\lambda)^{\frac{3}{2}}(b^2+\lambda)^{\frac{1}{2}}(c^2+\lambda)^{\frac{1}{2}}k_\lambda},$$

and on the surface of the ellipsoid,

$$\Phi = \frac{\alpha_0 xU}{2-\alpha_0}.$$

For the ellipsoid at an incidence, the velocity components of U are $(U_0, 0, W_0)$ and the solution is obtained similar to (7) with terms analogous construction about z,

$$\Phi_c = \frac{\alpha_0 U_0}{2-\alpha_0}x + \frac{\gamma_0 U_0}{2-\gamma_0}z$$

where

$$\alpha_0 = abc\int_0^\infty \frac{d\lambda}{(a^2+\lambda)\sqrt{(a^2+\lambda)(b^2+\lambda)(c^2+\lambda)}}$$

$$\gamma_0 = abc\int_0^\infty \frac{d\lambda}{(c^2+\lambda)\sqrt{(a^2+\lambda)(b^2+\lambda)(c^2+\lambda)}}$$

Using change of variables, $\lambda = a^2/u - a^2$, then (8) becomes

$$\alpha_0 = \frac{bc}{a^2}\int_0^1 \sqrt{\frac{u}{\left[1+(b^2/a^2-1)u\right]\left[1+(c^2/a^2-1)u\right]}}du.$$

Same way for (9) with $\lambda = c^2/u - c^2$, we obtain

$$\gamma_0 = \frac{ba}{c^2}\int_0^1 \sqrt{\frac{u}{\left[1+(b^2/c^2-1)u\right]\left[1+(a^2/c^2-1)u\right]}}du.$$

For the case of prolate spheroid,

$$b = c \qquad \text{and} \qquad L = \frac{a}{b} = \frac{a}{c} = \frac{1}{t}.$$

The equation for α_0 and γ_0 are integrated and we obtain

$$\alpha_0 = \frac{t^2}{1-t^2}\left[\frac{1}{\sqrt{1-t^2}}\log\frac{1+\sqrt{1-t^2}}{1-\sqrt{1-t^2}} - 2\right]$$

$$\gamma_0 = \frac{t^2}{1-t^2}\left[\frac{1}{2\sqrt{1-t^2}}\log\frac{1-\sqrt{1-t^2}}{1+\sqrt{1-t^2}} + 1\right]$$

The problem becomes in terms of velocity components u, v, w and function of potential Φ_c on the surface of prolate spheroid.

The magnitude of the maximum surface velocities can be written in terms of α_0 and β_0.

$$\frac{V_1}{V_\infty} = \frac{2}{2-\alpha_0}$$

$$\frac{V_2}{V_\infty} = \frac{2}{2-\beta_0}$$

$$\frac{V_3}{V_\infty} = \frac{2}{2-\gamma_0}$$

And for a prolate spheroid $\beta_0 = \gamma_0$. At any point on the surface there are two perpendicular velocity components. The component V_θ around the circular cross section which lies in a plane $x = const$ and a component V_p tangent to the rotated elliptic profile at the angle θ corresponding to the point in question. Any point of the surface can be specified by two angles. The angle θ and the slope angle β between the line tangent to the elliptic profile and the positive x-axis.

The onset flow V_∞ is assumed to lie in the xy-plane and to make an angle α with the positive x-axis. Then

$$V_{\infty x} = V_\infty cos\alpha$$

$$V_{\infty y} = V_\infty sin\alpha$$

For the onset flow $V_{\infty x}$ parallel to the x-axis the surface velocity components are

$$\frac{V_p}{V_{\infty x}} = V_0(t)cos\beta$$
$$\frac{V_\theta}{V_{\infty x}} = 0$$

For the onset flow $V_{\infty y}$ parallel to the y-axis the velocity components are

$$\frac{V_p}{V_{\infty y}} = V_{90}(t)sin\beta cos\theta$$
$$\frac{V_\theta}{V_{\infty y}} = V_{90}(t)sin\theta$$

The function $V_0(t)$ and $V_{90}(t)$ are independent of position and depend only on the thickness ratio t. They are related by

$$V_{90}(t) = \frac{2V_0(t)}{2V_0(t) - 1}$$

And from eq(xxx)

$$V_0(t) = \frac{(1-t^2)^{\frac{3}{2}}}{(1-t^2)^{\frac{1}{2}} - \frac{1}{2}t^2 \log\left(\frac{1+\sqrt{1-t^2}}{1-\sqrt{1-t^2}}\right)}$$

For a given $\frac{x}{l}$, define $\xi = 2(\frac{x}{l}) - 1$ and

$$\frac{r}{l} = \frac{t}{2}\sqrt{1-t^2}$$

and

$$cos\hat{\beta} = \frac{(1-t^2)^{\frac{1}{2}}}{\left[1 - \xi^2(1-t^2)\right]^{\frac{1}{2}}}$$

where if $\xi > 0$, $\hat{\beta}$ is negative. For a given θ the surface velocity components become

$$\frac{U_e}{V_\infty} = V_0(t)cos\alpha cos\hat{\beta} - V_{90}(t)sin\alpha sin\hat{\beta}cos\theta$$
$$\frac{W_e}{V_\infty} = V_{90}(t)sin\alpha sin\theta$$

Finally, the surface pressure coefficient can be calculated by

$$C_p = 1 - \left[\left(\frac{U_e}{V_\infty}\right)^2 + \left(\frac{W_e}{V_\infty}\right)^2\right]$$

and the cross flow angle relative to the x-axis of

$$\beta = tan^{-1}\left(\frac{W_e}{V_\infty}\right)$$

APPENDIX C.

BOUNDARY LAYER TRANSITION TRIP

C.1 Boundary Layer Trip Device

It is currently impossible to simultaneously reproduce all the scaled viscous parameters in a subscale experiment. The basic state of the art of tripping techniques is summarized by Russo (1989) in his review to the AGARD Working Group 09 on "Boundary Layer Simulation and Control in Wind Tunnels". According to this report, our current knowledge of the properties of boundary layer tripping techniques, at least in terms of distributed roughness, is reasonably complete. If we can define a desired transition location, then generally a trip can be sized to assure transition at that location. It should be emphasized, however, that our working knowledge for sizing such trips is based on the data bases for zero pressure gradient flows. It is still to be determined if the pressure gradient is an important parameter in determining the trip size on these basic distributed roughness boundary layer trips.

To ensure the desired transition location, the control of the size, height, and density (or spacing) of the trip elements is really important. Moreover, repeatibility becomes a very critical issue on these boundary layer trip devices, especially the carborundum particles, which is very difficult to duplicate the same density distribution every time it is applied. The durability of carborundum trips during testing highlights one of the difficulties of carborundum grit trips, in addition to the difficulties of defining the effective height. To overcome these difficulties and get a proper control on the trip devices, every facility developed its own technique

according to their preference and situation (Russo, 1989). One of them is the disk trip element which produced as low a critical Reynolds number as the grit trips. The advantage of using the disks is that their geometry, such as trip height and spacing of the elements, is well defined and durable and its application is repeatable. Furthermore, as found by Sinclaire (Kraft, 1989), at subsonic and transonic speeds a single row of disks was as effective as multiple rows of disks.

It was found that for a Reynolds number above critical for a single three-dimensional roughness element in the absence of a pressure gradient, the behavior of the boundary layer downstream of the element is identical to that for a naturally transitioned turbulent boundary layer. In addition, it has been clearly established that for the more popular trips such as carborundum grit, ballontini balls, distributed disks, *etc.*, the boundary layer profiles downstream of the tripping device recover to a basic law of the wall turbulent profile. The effects of the distributed three-dimensional tripping elements on the boundary layer properties downstream of the trips are the same as in the case of the single three-dimensional trip element. Immediately behind the trip the velocity profile is representative of a transitional profile where as further downstream the mean velocity distribution changes into a fully developed turbulent profiles. Correspondingly, the Reynolds shear stress distribution in the fully transitioned boundary layer downstream of the trips reflects the same behavior as naturally transitioned turbulent boundary layer. Consequently, similar to the isolated roughness element, distributed three-dimensional tripping elements in the absence of a pressure gradient produce the same type of turbulent boundary layer as natural transition (Kraft, 1989). For those tripping elements that are effective in causing early transition of the boundary layer, the

displacement thickness, δ^*, and momentum thickness, θ, exhibit the typical overthickening caused by a tripping element. There is no noticeable difference in the boundary layer properties because of the difference in the tripping elements. However, it is interesting to note that the shape factor, $H = \frac{\delta^*}{\theta}$, recovers to the natural transition value, although in a shorter distance downstream. Here, the trip disk method used by the Boeing Commercial Airplane Co. (Smith, 1989) was used as a boundary layer trip device. Details are presented in the Trip Disk Generation Section.

C.2 Critical Trip Height Calculation

Assuming a condition for air at 77°F and flow speed of 100 ft/sec and 150 ft/sec, the test Reynolds numbers in the Stability Wind Tunnel become $R_N = 2.85 \times 10^6$ and 4.20×10^6, respectively. The trip height should be taylored to satisfy both these test conditions. From the power-law expression which is reasonably accurate up to a Reynolds number no greater than $Re_x = 10^7$

$$\theta = \frac{0.036x}{Re_x{}^{1/5}} \tag{C.1}$$

$$Re_x = \frac{U_\infty x}{\nu}. \tag{C.2}$$

Here $\nu = 1.684 \times 10^{-4} ft^2/sec$ at 77°F. Then the momentum thickness θ of the turbulent boundary layer based on the run length at X/L = 0.2, where the trip is to be applied, become $\theta = 0.0298$ inch and 0.0275 inch, respectively.

Following the relation of Braslow and Knox(1958), one can derive a relation for $\frac{k}{x}$ in terms of R_k and R_x. By definition

$$\eta_k = \frac{k}{2x}\sqrt{R_x}. \tag{C.3}$$

The roughness Reynolds number, on the particle height and the local flow conditions in the boundary layer at the tip of the particle, is defined

$$R_k = \frac{u_k k}{\nu_k} \tag{C.4}$$

$$= \frac{k}{x} R_x (\frac{u_k}{U})(\frac{\nu_o}{\nu_k}). \tag{C.5}$$

Equation (C.3) can be rewritten in the form

$$\frac{R_k}{\sqrt{R_x}} = (\frac{k}{x}\sqrt{R_x})(\frac{u_k}{U})(\frac{\nu_o}{\nu_k}). \tag{C.6}$$

Assuming viscosity relationship

$$\frac{\mu}{\mu_o} = C\frac{T}{T_0} \tag{C.7}$$

we get

$$\frac{\nu_o}{\nu_k} = \frac{\mu_o}{\mu_k}\frac{\rho_k}{\rho_o} = \frac{1}{C}(\frac{T_k}{T_0})^{-2}. \tag{C.8}$$

Substituting (C.8) into (C.6)

$$\frac{R_k}{\sqrt{R_x}} = \frac{1}{C}(\frac{k}{x}\sqrt{R_x})(\frac{u_k}{U})(\frac{T_k}{T_o})^{-2}. \tag{C.9}$$

For low speed flow ($M \approx 0$)

$$\frac{T_k}{T_o} = 1.0 \tag{C.10}$$

and

$$\frac{k}{x} = C(\frac{U}{u_k})(\frac{R_k}{R_x}). \tag{C.11}$$

Furthermore $T_w = T_o$ gives

$$C = \sqrt{\frac{T_w}{T_o}}(\frac{T_o + s}{T_w + s}) = 1. \tag{C.12}$$

Then the roughness height becomes

$$\frac{k}{x} = (\frac{U}{u_k})\frac{R_k}{R_x}. \tag{C.13}$$

The velocity and temperature distribution through the boundary layer, of course, is dependent upon whether the flow is of the two- or three-dimensional type. For 2-dimensional flow, we can simplify

$$\begin{aligned}\frac{u_k}{U} &\simeq (0.6344)\eta \\ &= (0.30)\frac{k}{x}\sqrt{R_x}. \end{aligned} \tag{C.14}$$

Finally, with (C.14), the equation (C.13) reduces to

$$\frac{k}{x} = [(R_x)^{-3/2}(\frac{R_k}{0.3172})]^{\frac{1}{2}} \tag{C.15}$$

which agrees quite well with the Figure 3.a of Braslow and Knox(1958) for the range of local Reynolds number $R_x \geq 1.0 \times 10^5$ as shown in Figure C.1.

From the above modified equation(C.15) of Braslow and Knox (1958), the roughness height k for these local Reynolds numbers become k = 0.0250 inch and 0.0184 inch for $R_k = 600$, respectively. Braslow *et al.* (1966) also found that for subsonic speed, an increase in roughness height by a factor of 2 over that indicated by $R_k = 600$ can be tolerated with very little or no drag increase. Thus the roughness height of the trip device is decided to be 0.028 inches which can satisfy both conditions and ensure boundary layer trip at this particular location. This value is also very close to the calculated momentum thickness of the turbulent boundary layer based on the run length at this location.

C.3 Trip Disk Generation

Boundary layer transition trip dots are made out of the feed holes of a N/C milling tape punched through a tape punch machine and its pattern is as shown in Figure C.1. The mylar N/C tape is laminated with 3M super 33^{+} plastic tape which is built up to the desired thickness. In order to build 0.028 inch thick trip tape, 4 layers of this 0.007 inch thick electric tape are required. After the tapes are laminated, the mylar tape is run through a tape punch machine which punches 0.046 inch diameter feed holes at 0.1 inch intervals. The electric tape is then peeled off the N/C tape and attached at the desired location for boundary layer trip. Pat-build epoxy or Bondo is applied in the holes using constant pressure. Hold a flexible sweep at an angle of about 5 to 10 degrees to the surface when sweeping the pat-build into the tape holes. Then, after it is cured, sand the disks flush to the tape using fine sand paper about No. 150. The model surface should be throughly cleaned before the trip tape is applied and the disks should not be installed on top of a pencil or ink mark for the trip position.

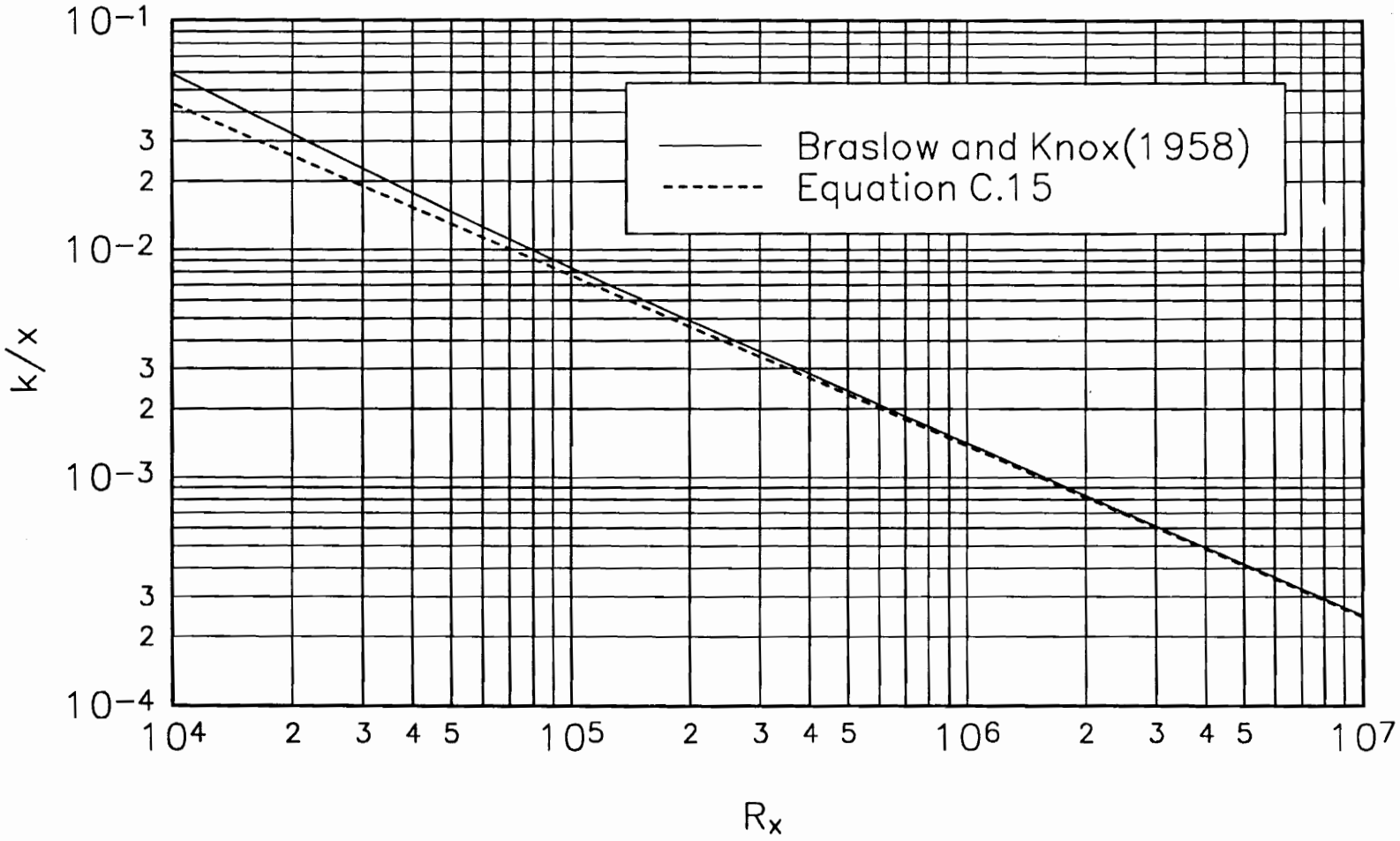

Figure C.1. Roughness Height k/x for $R_k = 600$.

APPENDIX D.

DESIGN, FABRICATION, AND CALIBRATION OF 5-COMPONENT INTERNAL BALANCE

D.1 General Design Considerations

In general circumstances the measurement even of static forces is a difficult and complex task. The problem is in choosing a system with adequate sensitivity for each mode and a minimum interaction between measured components. Additional restrictions must also be considered such as overall deflection should be kept minimum not to alter the configuration. Since the early development of the internal balances (Hansen, 1956(a); Hansen, 1956(b); Moor, 1961), continued effort has been made to improve the linearity and minimize interaction problems (Fussey, 1974; Ewald, 1979; Dubois, 1981; Edwards, 1983; Johnson, 1983; Sjörs, 1983; Ringel and Levin, 1985; Ewald and Krenz, 1986; Ewald and Graewe, 1987; Schnabl, 1987). The need to support the body undergoing test within the fluid with a minimum of flow disturbance from the support resulted in a sting mounting. Even in a steady measurement with a minimum disturbance from the support, the sting with the model at its end undergoes transverse vibration when the flow is unsteady and so the balance responds to the corresponding inertia loads. This sting vibration becomes much more complex when the model undergoes an inexorable motion. Not only the flow but also the motion itself becomes unsteady. Other vibration modes associated with the flexures of the balance, the inertia of the model, and the other parts of the balance may also be excited, so that the response of the measuring system is a very complicated function of all these modes. These resonances must be removed if the input forces are to be determined from

the responses. One way to avoid this problem is to design the balance such that all the natural frequencies are outside of the 'critical range'. This critical frequency band is the one corresponding to the harmonic component of the input forces. High- and low-pass electronic filters can be used, but attention must also be paid to phase-shift.

Tcheng (1980) studied the dynamic characteristics of a 5-component balance and found that the balance is a band limited device with a bandwidth lower than the first natural frequency of the system. This means that the natural frequency of the balance should be much higher than the frequency range of interest. The natural frequency of a beam is proportional to the stiffness as follows;

$$\omega_n = \sqrt{\frac{k}{m}}$$

where, k is the system spring constant and m is the system mass. Rarely are all the force components of similar order of magnitude, so that for an internal balance a simple cantilever beam is machined to improve the sensitivity for some components. In many situations the load range of the axial force component is an order of magnitude smaller than that of the normal force component and much weaker flexure is required to achieve adquate sensitivity. This, in turn, results in a lower stiffness and natural frequency. Due to a rather high and repeated inertia load generated by the finite mass of the model undergoing severe dynamic conditions, several different types of design were considered. Of the types considered, simple 'moment beam' type and cylindrical 'can' type (Coutler and Buchanan, 1980; Coutler and Marquart, 1982) were found to be adequate for the circumstances. These two types of design approach were compared in several different aspects of requirements such

as load range for a given size, deflection under load, ease of machining, gage application, balance weight, and model interface. Dominant advantage of the 'can' type design over the beam type design is the reduction of the stiffness problem of the model. But, the balance itself might weigh more than the savings of model weight due to its size. Besides, the balance diameter $d \approx 5$ inch is rather too large to be used in the future applications. Even though the rolling moment sensitivity of the beam type design is rather low compared to the 'can' type design and an extra stiffner is required inside of the model, the moment beam type design shows superiority over the 'can' type design in all the aspects considered. The stiffner of the model can also be taken off from the model to give enough space and volume for the future applications such as LDV measurements.

D.1.1. Material and Design Strain

The usual design level of strain gage for good bond life and output linearity is about 1000 microinch per inch (Perry and Lissner, 1955). Strain is related to the Young's modulus of a material by

$$\epsilon = \frac{S}{E}$$

where, ϵ = strain in inches per inch

S = stress, psi

E = Young's modulus

17-4 PH stainless steel is selected for the balance material due to several characteristics of the material. 17-4 PH precipitation hardened stainless steel which has Young's modulus of $E = 29.0 \times 10^6$ has excellent characteristics for transducers

due to its good elastic qualities, ease of machining, little deformation during the heat treating, low machining stress, and good fatigue life at an ultimate tensile strength of 190 Ksi (ARMCO; 1986). It can be machined to its final dimensions in Condition A without allowance for scaling or distortion because the final hardening temperatures are low. It also has a fatigue strength of 90 Ksi at 10 million cycles and 73 Ksi at 100 million cycles after heat treated to condition H900. Heat treating to an ultimate tensile strength F_{tu} of 190 Ksi will allow a sufficient factor of safety based on a design maximum strain of 1000 microinch per inch.

Factor of safety can be defined as

$$F.O.S. = \frac{F_{tu}}{S_d}$$

where, $S_d = E\epsilon_d$. For the material and design strain selected

$$S_d = 0.001 \times 29.0 \times 10^6$$

$$F.O.S. = \frac{190,000}{28,500} > 5.0$$

D.1.2. Gage selection

Good number of resistance strain gages are available for transducer applications. Since most balances are considered as permament equipment, the gage must be selected not only for their initial characteristics but also for long term durability such as fatigue characteristics. Small transverse sensitivity, good output linearity, and small thermal effects are some of the other requirements to be considered.

Measurement Group MM SK-01-050AH-350 350 Ohm foil type strain geges are used for the bridge elements due to its long fatigue life (Measurement Group; 1990). These gages are bonded with M-bond 610 and temperature compensated for the working temperature of $40F \sim 100F$. The gages were then coated with MM Gage coat No. 8. The 30-ft long balance lead wires are made of 7-40 AWG 32 twisted pairs to minimize electric noise.

For a four active arm bridge, the bridge output can be written as

$$E_0 = E_{in}(G.F.)\epsilon$$

where, E_0 = bridge output voltage

E_{in} = bridge excitation voltage

$G.F.$ = gage factor

ϵ = average bridge strain

The gage factor of the selected gages is arround 2.0. The design strain value,ϵ, is 0.001 inches per inch. Excitation voltage in excess of about 10 V should be avoided due to the local heating which may cause nonlinear characteristics in the gage itself as well as output instability. So, the excitation voltage of 5V was chosen which gives 0.010V output at maximum loading condition.

D.2 Structural Design and Stress Analysis

The design load ranges of the balance are as follows.

- Normal Force 1400 LB.
- Side Force 800 LB.
- Pitching Moment 3000 in-LB.
- Yawing Moment 1500 in-LB.
- Rolling Moment 600 in-LB.

Several design examples can be found but Moor (1961) gives a through design procedure. Even though it is for the multi-piece balance, It was closely followed here for the NF and SF sections. Torsional spring design was employed for the RM section design (Pope and Goin; 1966). The design is of a conventional moment beam type and cruciform type flexure, main web with two side webs, is used for the rolling moment measurement.

D.2.1 Forward and After Bending Moment Measuring Section

From the procedure given by Moor (1961), the distance from the balance centerline to the line of action of normal force is

$$\sum M_C: 1500d = 3000$$

$$d = \frac{3000}{1500} = 2.0 \quad \text{(inches)}$$

The distance from the line of action of the maximum normal and side forces to the bending moment sections are limited by the maximum section modulus of

the cross-section. For a circular cross-section of $\phi = 2.0$ inches,

$$I = \frac{\pi r^4}{4}$$
$$z = \frac{I}{c} = \frac{\pi r^3}{4}$$
$$S_d = 28,500 \quad (\text{psi}) = \frac{M}{z}$$
$$M = \frac{(28,500)(3.1416)(1.0)^3}{4}$$
$$= 22,383 \quad (\text{in-lb})$$

Where M is the maximum moment at the design stress S_d. The maximum separation distance, d, of the point of application is

$$d = \frac{22,383}{1500} = 14.9 \quad (\text{inches})$$

Then the maximum separation of the two moment section is

$$2 \times (14.9 - 2.0) = 25.8 \quad (\text{inches})$$

A distance of 6.0 inches will be enough for the bridge wiring and for the space to locate the rolling moment section in between.

From the bending moment diagram shown in Figure D.1, the bending moment at each measuring section due to the design normal force and pitching moment is

$$M_z = \pm 1500 \times (3.0 + 2.0) = \pm 7500 \quad (\text{in-lb})$$

By similar analysis for the side force and yawing moment,we get

$$M_y = \pm 800 \times (3.0 + 2.0) = \pm 4000 \quad (\text{in-lb})$$

The two equations for the bending moment measuring section become

$$S_d = \frac{M_z C_z}{I_x} = \frac{M_z}{z_x}$$
$$S_d = \frac{M_y C_y}{I_y} = \frac{M_y}{z_y}$$
$$\frac{1}{z_x} = \frac{c_z}{I_x} = \frac{h/2}{I_x} = \frac{6}{bh^2}$$
$$\frac{1}{z_y} = \frac{c_y}{I_y} = \frac{h/2}{I_y} = \frac{6}{hb^2}$$

Solving these equations and with a few adjustments, we get

$$h = 1.400 \quad \text{(inches)}$$

$$b = 0.800 \quad \text{(inches)}$$

for a rectangular cross section which fits in 2-inch diameter circular section as shown in Figure D.2.

For this section, we have

$$I_x = \frac{1}{12} bh^3 = 0.1829 \quad (in^4)$$
$$I_y = \frac{1}{12} hb^3 = 0.0597 \quad (in^4)$$
$$c_x = \frac{h}{2} = 0.700 \quad \text{(inches)}$$
$$c_y = \frac{b}{2} = 0.400 \quad \text{(inches)}$$
$$M_x = S_d z_x = S_d \frac{I_x}{c_x}$$
$$= 7446 \quad \text{(in-lb)}$$
$$M_y = S_d z_y = S_d \frac{I_y}{c_y}$$
$$= 4253 \quad \text{(in-lb)}$$

at $S_d = 28,500$ psi.

D.2.2 Rolling Moment Measuring Section

The Rolling Moment can be written by the following equation for a cruciform section shown in Figure D.3.

$$RM = E\epsilon_R \alpha_m b_m {c_m}^2 \left[1 + 2\frac{\beta_s}{\beta_m}\frac{b_s}{b_m}\left(\frac{c_s}{c_m}\right)^3 \right]$$

where b_m, c_m, b_s and c_s are the height and witdh of the main web and side webs, respectively. α and β are constants related to the height and width ration of webs,

For the rolling moment section, the design stress was chosen to be $750\mu\epsilon$ instead of $1000\mu\epsilon$ because of the possible nonlinear effects of the web under torsion. This resulted in, after some iteration, the following geometry.

$$b_m = 1.600 \quad \text{(inches)}$$

$$c_m = 0.200 \quad \text{(inches)}$$

$$b_s = 0.400 \quad \text{(inches)}$$

$$c_s = 0.200 \quad \text{(inches)}$$

which gives maximum Rolling Moment of 575 in-lbs. The section modulus become

$$I_x = 0.0688 \quad (in^4)$$

$$I_y = 0.0608 \quad (in^4)$$

The area moments of inertia of the designed sections are as shown in Table D.1. The final balance configuration designed after attaching the 12 to 1 taper joints at both ends is as shown in Figure D.4.

D.2.3 Stress analysis

In order to ensure that the balance designed should have sufficiently high factor of safety, through stress analysis should be performed. The factor of safety usually has a value of 3 to 5 and it is assumed that all five forces and moments are applied at the same time. From the above design, we have

$$I_{yy} = 0.1814 \quad (in^4)$$

$$I_{zz} = 0.0582 \quad (in^4)$$

At balance station 3.500,

$$M_y = PM + NF(3.500) = 7900 \quad \text{(in-lb)}$$

$$M_z = YM + SF(3.500) = 4300 \quad \text{(in-lb)}$$

The stress at the surface of the measuring section becomes

$$\begin{aligned} f_b &= Mc/I_y + Mc/I_z \\ &= 7900(0.70)/0.1814 + 4300(0.4)/0.0582 \\ &= 60,038 \quad \text{(psi)} \end{aligned}$$

The factor of safety becomes

$$F.O.S. = 190,000/60,038 = 3.16$$

At station 3.000 where the strain gage is bonded,

$$M_y = PM + NF(3.500) = 7200 \quad \text{(in-lb)}$$

$$M_z = YM + SF(3.500) = 3900 \quad \text{(in-lb)}$$

The maximum strain at this location becomes $975\mu\epsilon$ and $941\mu\epsilon$ respectively. The stress at the surface of the strain gage section becomes

$$\begin{aligned} f_b &= Mc/I_y + Mc/I_z \\ &= 7200(0.70)/0.1814 + 3900(0.4)/0.0582 \\ &= 54,588 \quad \text{(psi)} \end{aligned}$$

The factor of safety becomes

$$F.O.S. = 190,000/54,588 = 3.42$$

Factor of Safety over 3 is achieved for both cases.

Since the rolling moment section was weakened by cutting the material out to maintain high sensitivity, this section will show the minimum factor of safety. At station 1.00 where the roll flexure joins to the main body of the balance,

$$M_y = PM + NF(1.000) = 4400 \quad \text{(in-lb)}$$

$$M_z = YM + SF(1.000) = 2300 \quad \text{(in-lb)}$$

Total stress at this location becomes

$$\begin{aligned} f_b &= Mc/I_y + Mc/I_z \\ &= 4400(0.80)/0.0688 + 2300(0.8)/0.0608 \\ &= 81426 \quad \text{(psi)} \end{aligned}$$

Then the factor of safety is

$$F.O.S. = 190,000/60038 = 3.42$$

D.3 Balance Calibration

The purpose of the balance calibration is to determine the sensitivity and interaction characteristics of each component including second order or combined loading effects.

D.3.1 Static Calibration

The balance was loaded at 3 different locations, namely, moment center, forward gage station, and after gage station. Normal forces were loaded at 200 lb increament up to full scale range and the side forces were loaded at 100 lb increament. Rolling moments were loaded at 100 in-lb increament with a constant 28.8 lb of normal force. Each loading is consisted of increasing and decreasing load to check the hysterisis of the flexure and both positive and negative loadings were performed by changing the roll angle of the balance and the calibration body.

Since the balance designed utilizes two bending moment sections, forward and after, to measure normal force and pitching moment, the relationship between forces and moments generated at two descrete locations on a cantilever beam are expressed as follows:

$$NF = \frac{M_2 - M_1}{\Delta x}$$

where, M_1 and M_2 are moments measured by the forward and the after sections, respectively, and Δx is the distance between M_1 and M_2. M_1 and M_2 are proportional to the bridge electrical outputs, R_1 and R_2, the above equation can be expressed by

$$NF = \frac{K'_2 R_2}{x_2 - x_1} - \frac{K'_1 R_1}{x_2 - x_1}$$

where, x_1 and x_2 are the corresponding bridge stations. If

$$K_2 = \frac{K'_2}{x_2 - x_1} \qquad \text{and} \qquad K_1 = \frac{-K'_1}{x_2 - x_1},$$

then

$$NF = K_1 R_1 + K_2 R_2$$

$$\text{or} \quad NF = N_1 + N_2$$

Here N_1 is a force measured at the x_2 location and N_2 is a force measured at x_1 location for a moment balance. Calibration stations near the electrical bridge center may be used for x_1 and x_2 provided that interaction of N_1 on N_2 and N_2 on N_1 are evaluated. Magnitude of these terms will dependent on the location of calibration stations relative to the strain gage bridge stations. Pitching moment referenced to the balance center or any reference station is given by the equation

$$PM = N_1 \times (Ref.STA - x_2) + N_2 \times (Ref.STA - x_1)$$

The side force and yawing moment equations are expressed in similar manner

$$SF = S_3 + S_4$$

$$YM = S_3 \times (Ref.STA - x_4) + S_4 \times (Ref.STA - x_3)$$

Rolling moment is directly measured as

$$RM = K_5 R_5$$

First order interaction on NF, PM, SF, and YM are evaluated as being linear whereas interactions on RM is considered to be nonlinear. If we do not account for the second order combined load interactions and expand RM equation in order

to account for the nonlinear interactions, the balance equations take the following form.

$$N_1 = K_1R_1 - A_2N_2 - A_3S_3 - A_4S_4 - A_5RM$$

$$N_2 = K_2R_2 - B_1N_1 - B_3S_3 - B_4S_4 - B_5RM$$

$$S_3 = K_3R_3 - C_1N_1 - C_2N_2 - C_4S_4 - C_5RM$$

$$S_4 = K_4R_4 - D_1N_1 - D_2N_2 - D_3S_3 - D_5RM$$

$$\begin{aligned} RM = {} & K_5R_5 - E_1N_1 - E_2N_2 - E_3S_3 - E_4S_4 \\ & - E_{11}{N_1}^2 - E_{22}{N_2}^2 - E_{12}N_1N_2 \\ & - E_{33}{S_3}^2 - E_{44}{S_4}^2 - E_{34}S_3S_4 \end{aligned}$$

During the calibration, the tare weight of the calibration body was not considered in the evaluation of the constants. The calibration result obtained through the primary loading conditions mentioned above shows maximum deviation less than 0.15% of full scale range and the standard deviation of each component based on all loads was within 0.25% of full scale range. The interaction terms were evaluated for each component for a different loading component and are presented in Table D.2. The balance statis calibration coefficients are tabulated in Table D.3.

D.3.2 Dynamic Calibration

As the separated flows are highly nonlinear (Ericsson, 1986), higher harmonic components are introduced at multiples of the first harmonic frequency. To correct and verify the effect of these higher harmonics, dynamic calibration of the 5-component balance was performed. In order to obtain a frequency response function, single frequency sine wave can be used as an input (Bendat and Piersol,

1986). But this method needs a large number of test points to cover the frequency range of interest and a large number of averages in order to get a reasonable accuracy in the phase information. To avoid this problem, a multichannel FFT analyzer was used with an impact hammer as an input source. The test setup is shown in Figure D.5. 5 independent records were averaged to achieve a reasonable accuracy in Frequency Response Function and Phase information. The main objectives of the dynamic calibration are to determine the natural frequencies, frequency response function, and the order of the dynamic interactions between the measured components. Since a balance is an elastic medium which acts as a linear system for a small deflection, small force about the order of 0.5 lb was applied even though the full scale range is much larger.

Typical frequency response functions are as shown in Figures D.6 to D.10 for each component which has 512 points up to 160 Hz. Well below the first natural frequency, the amplitude response is flat. The first mode natural frequencies of each component , which are shown in Table D.3, are much higher than the theoretical one-dimensional beam analysis. As found by Tcheng (1980) dynamic interactions as well as bridge sensitivities are frequency dependent and it is not possible to set up a simple method to correct the interactions in frequency domain. Besides, the interactions are amplitude, or applied force, dependent and the situation gets much more complicated than the static case. The dynamic interactions are as shown in Table D.4 which show almost one order of magnitude higher than the static case shown in Table D.2.

Since the frequency response functions are flat up to first mode natural frequency ω_n and can cover up to 3rd harmonics of the expected test frequencies, it

is assumed, with minor sacrifice of the accuracy, that static calibration holds even for the dynamic case.

TABLE D.1.

Section Moment of Inertia (unit in in^4)

Section	I_{xx}	I_{yy}
Fwd Measuring Section	0.1829	0.0597
Roll Section	0.0688	0.0608
Aft Measuring Section	0.1829	0.0597

TABLE D.2.

Balance Static Interaction

Applied Component	% interaction N_1	N_2	S_3	S_4	RM
N_1	-	1.99	1.19	-	0.33
N_2	2.21	-	-	1.38	0.74
S_3	1.85	-	-	2.34	2.84
S_4	-	0.88	2.44	-	3.31
RM	-	-	-	-	-

Interactions less than 0.25% are neglected.

TABLE D.3.

Balance Coefficients

$K_1 =$	-.1236E+00	$C_1 =$	-.6815E -02	$D_1 =$	.6331E -03
$K_2 =$	.1201E+00	$C_2 =$	.6714E -03	$D_2 =$	-.7820E -02
$K_3 =$	-.7289E -01	$C_4 =$	-.2437E -01	$D_3 =$	.2370E -01
$K_4 =$	.7040E -01	$C_5 =$	-.2396E -03	$D_5 =$	-.1206E -04
$K_5 =$	.7012E -01				
		$E_1 =$	.1585E -03		
$A_2 =$	-.2240E -01	$E_2 =$	-.1662E -02		
$A_3 =$	.3210E -01	$E_3 =$	-.1974E -01		
$A_4 =$	.4562E -03	$E_4 =$	-.2345E -01		
$A_5 =$	.2350E -02				
		$E_{11} =$	.9700E -06		
		$E_{22} =$	.8753E -06		
$B_1 =$	.2017E -01	$E_{12} =$	.1873E -05		
$B_3 =$	.2288E -02	$E_{33} =$	-.1950E -05		
$B_4 =$	.1522E -01	$E_{44} =$	.1483E -05		
$B_5 =$	-.2981E -02	$E_{34} =$	-.3419E -05		

TABLE D.4.

1st Harmonic Natural Frequency, ω_n

Component	Calibration Body(28 lb)	Model(56 lb)
N_1	54 Hz	27 Hz
N_2	56 Hz	28 Hz
S_3	71 Hz	36 Hz
S_4	48 Hz	24 Hz
RM	48 Hz	24 Hz

TABLE D.5.

Balance Dynamic Interaction (average value)

Applied Component	% interaction N_1	N_2	S_3	S_4	RM
N_1	-	8.64	8.89	7.75	9.56
N_2	7.98	-	11.32	4.18	6.13
S_3	3.98	3.39	-	9.395	7.925
S_4	7.97	8.99	9.32	-	9.30
RM	3.02	3.67	≈ 10	3.01	-

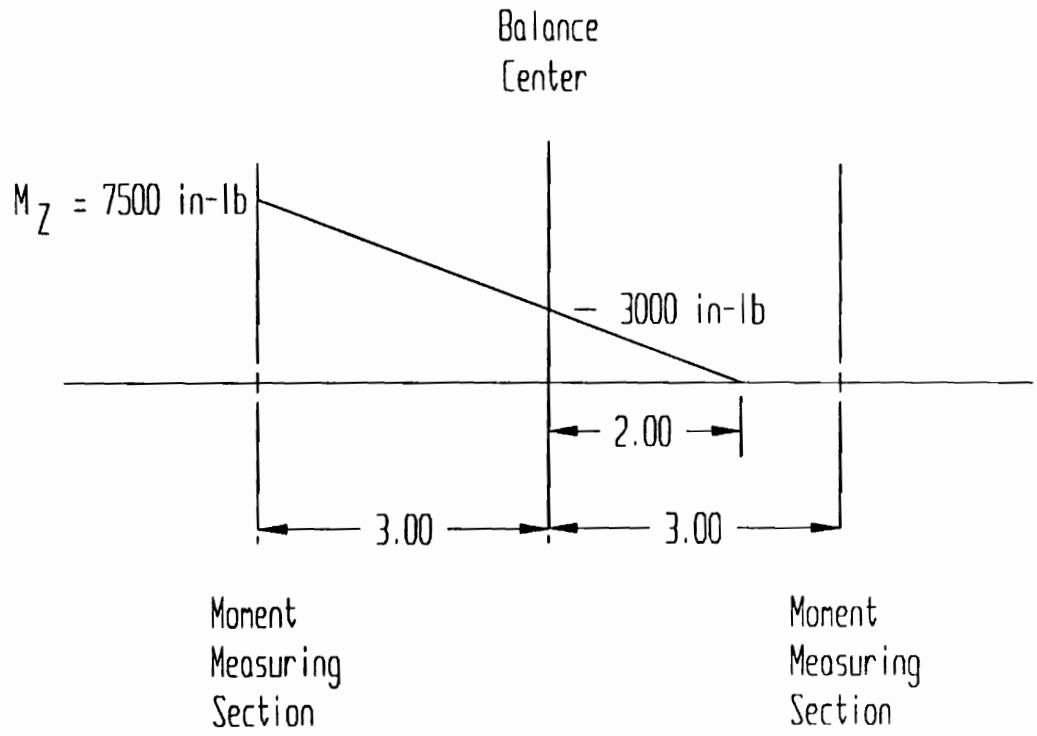

Figure D.1. Normal Force Measuring Section Moment Diagram.

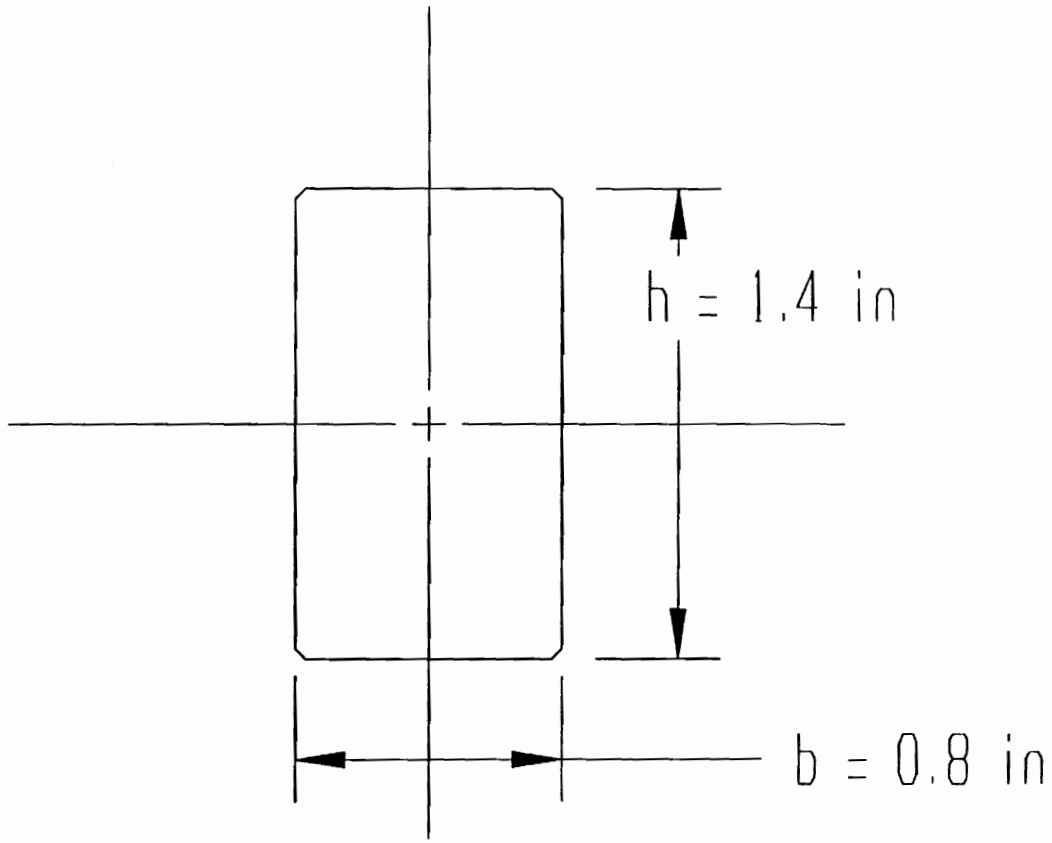

Figure D.2. Moment Measuring Section for Normal and Side Forces.

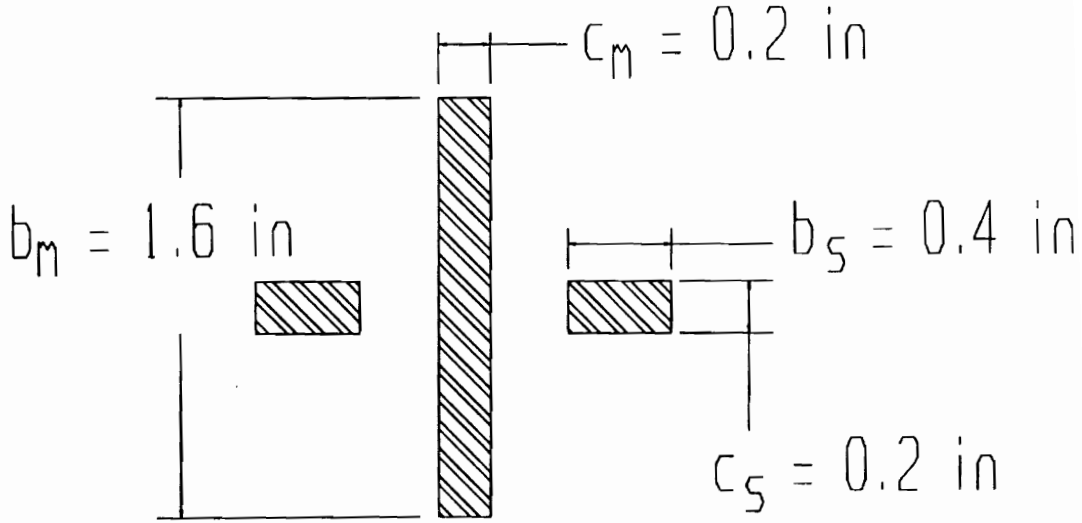

Figure D.3. Cruciform Element for the Rolling Moment Measuring Section.

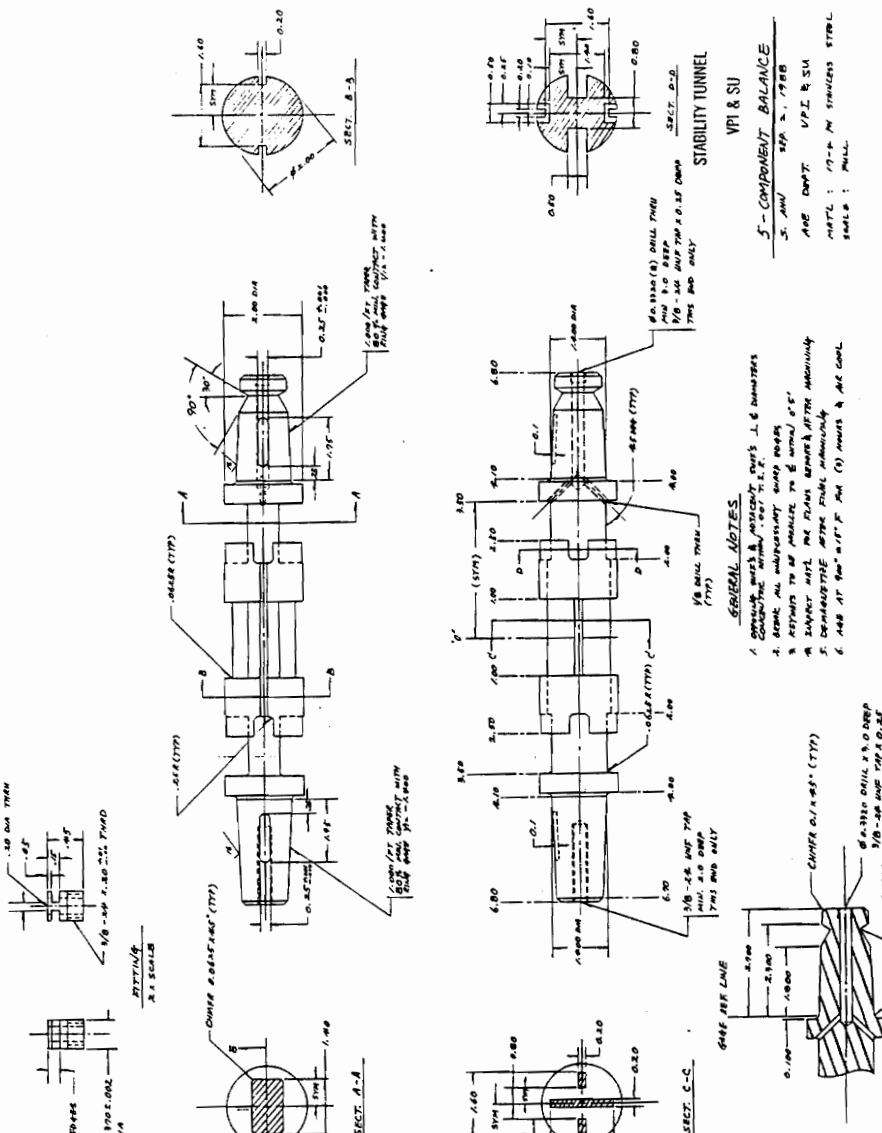

Figure D.4. 5-Component Internal Balance.

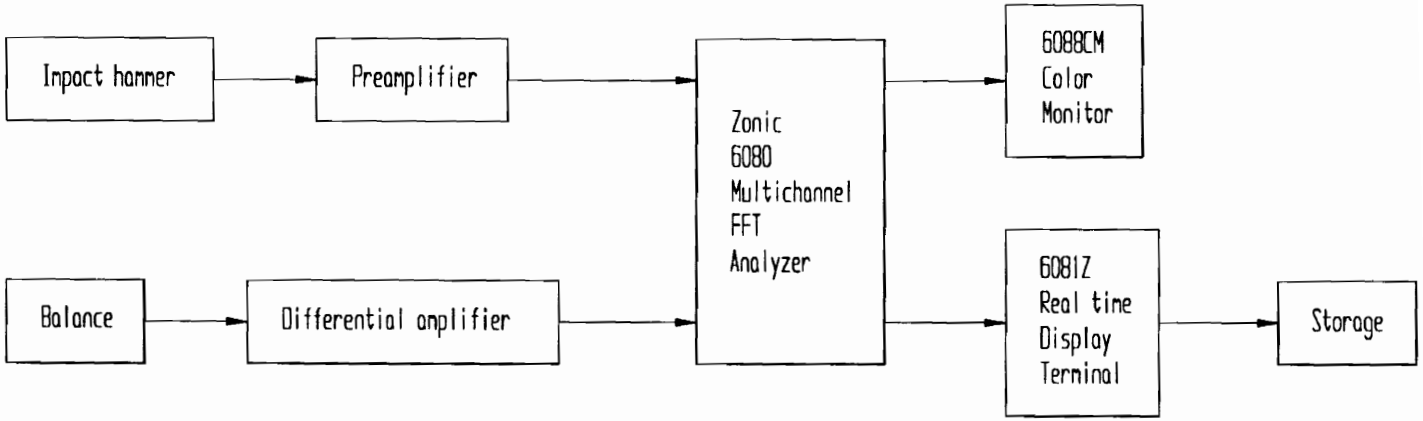

Figure D.5. Balance Dynamic Calibration Set-up.

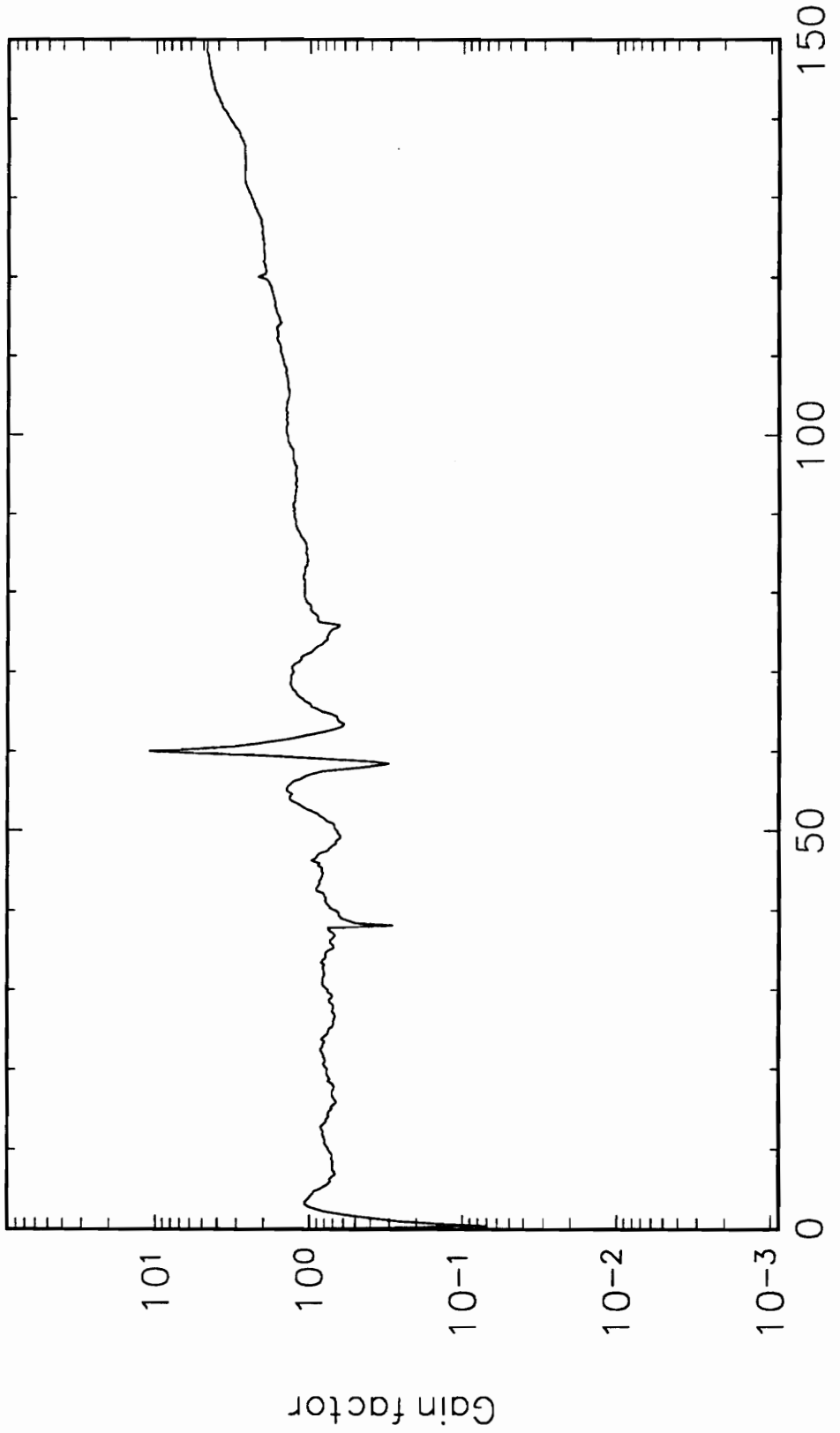

Figure D.6. Frequency Response of Gage N_1.

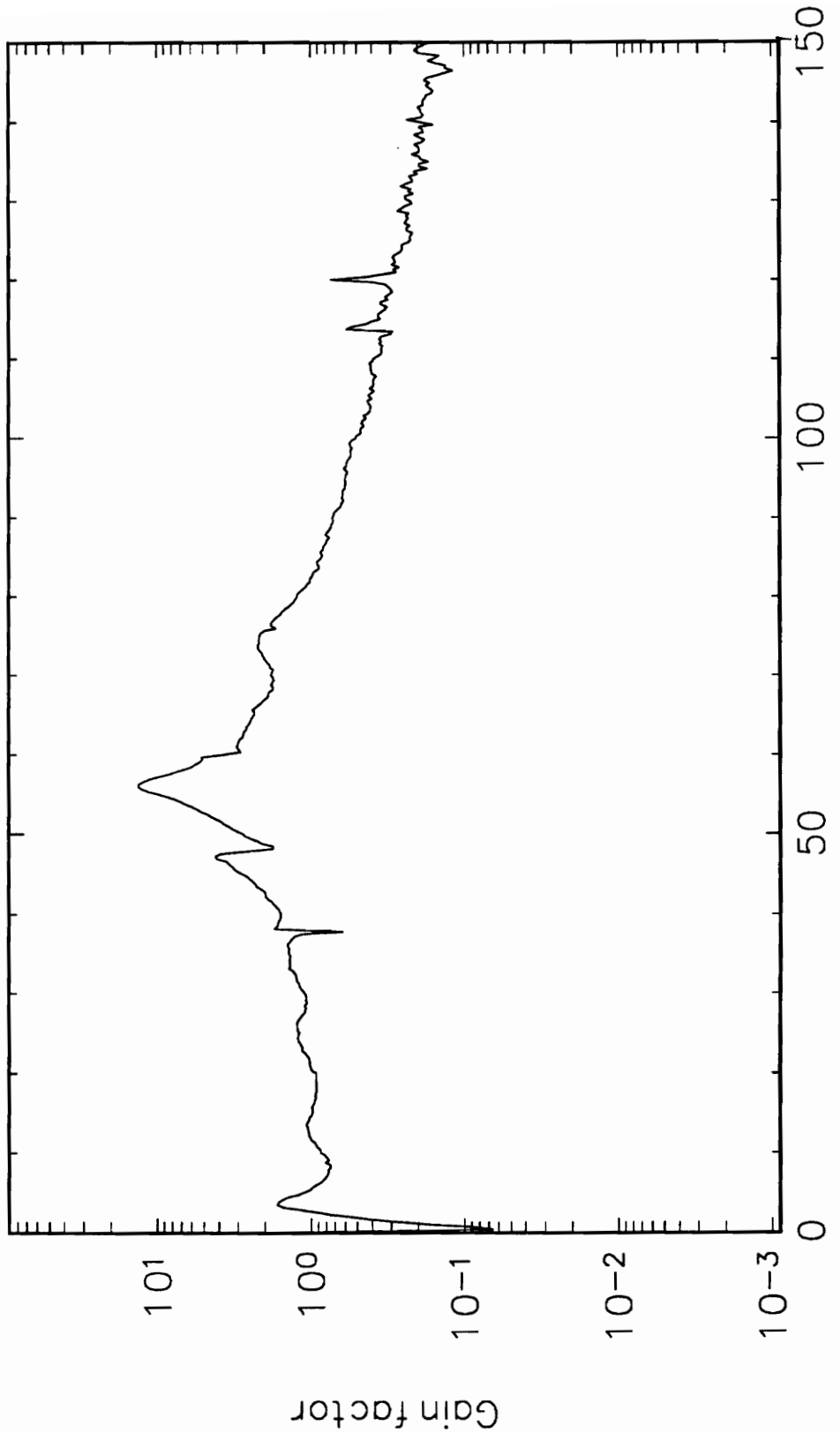

Figure D.7. Frequency Response of Gage N_2.

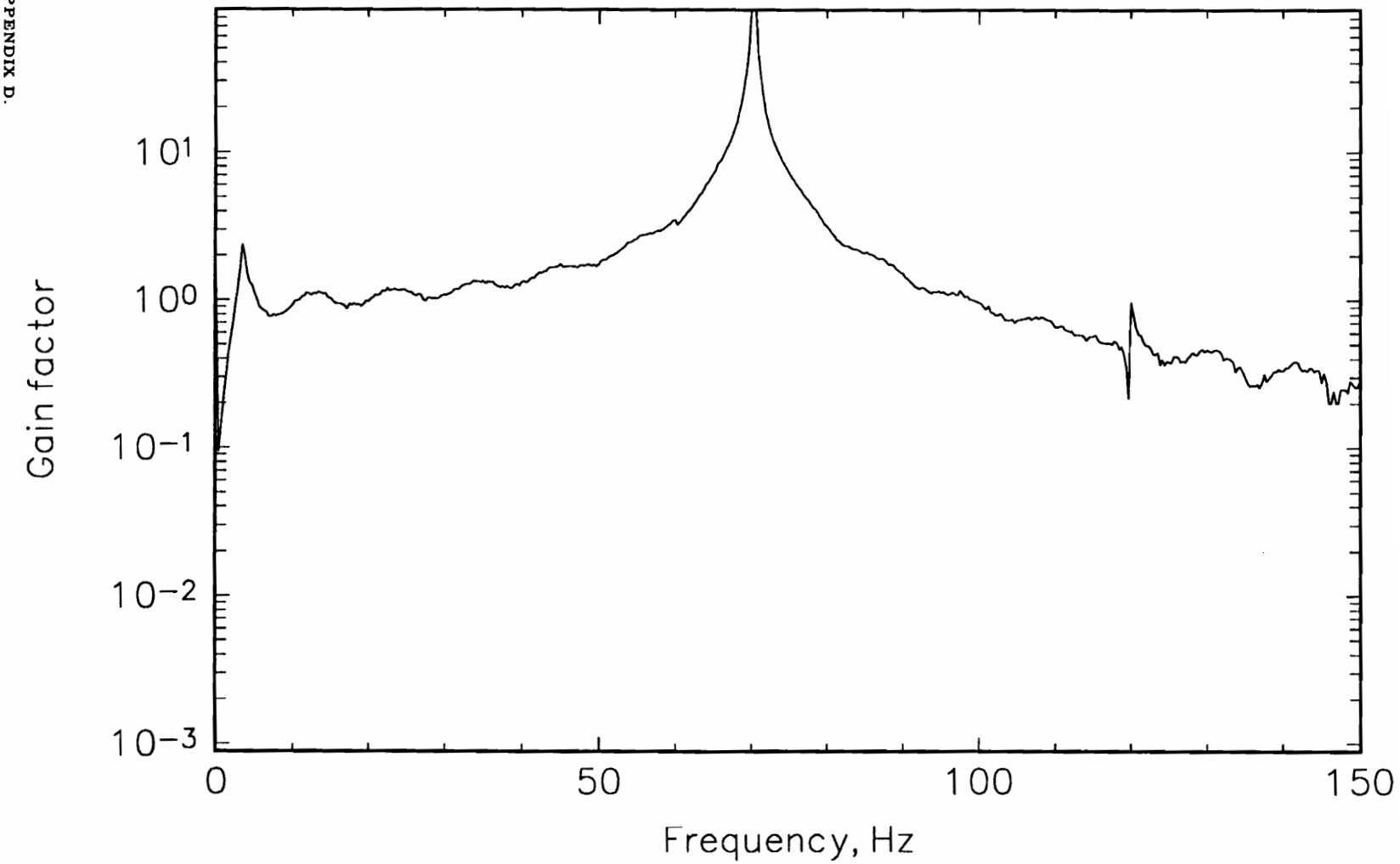

Figure D.8. Frequency Response of Gage S_3.

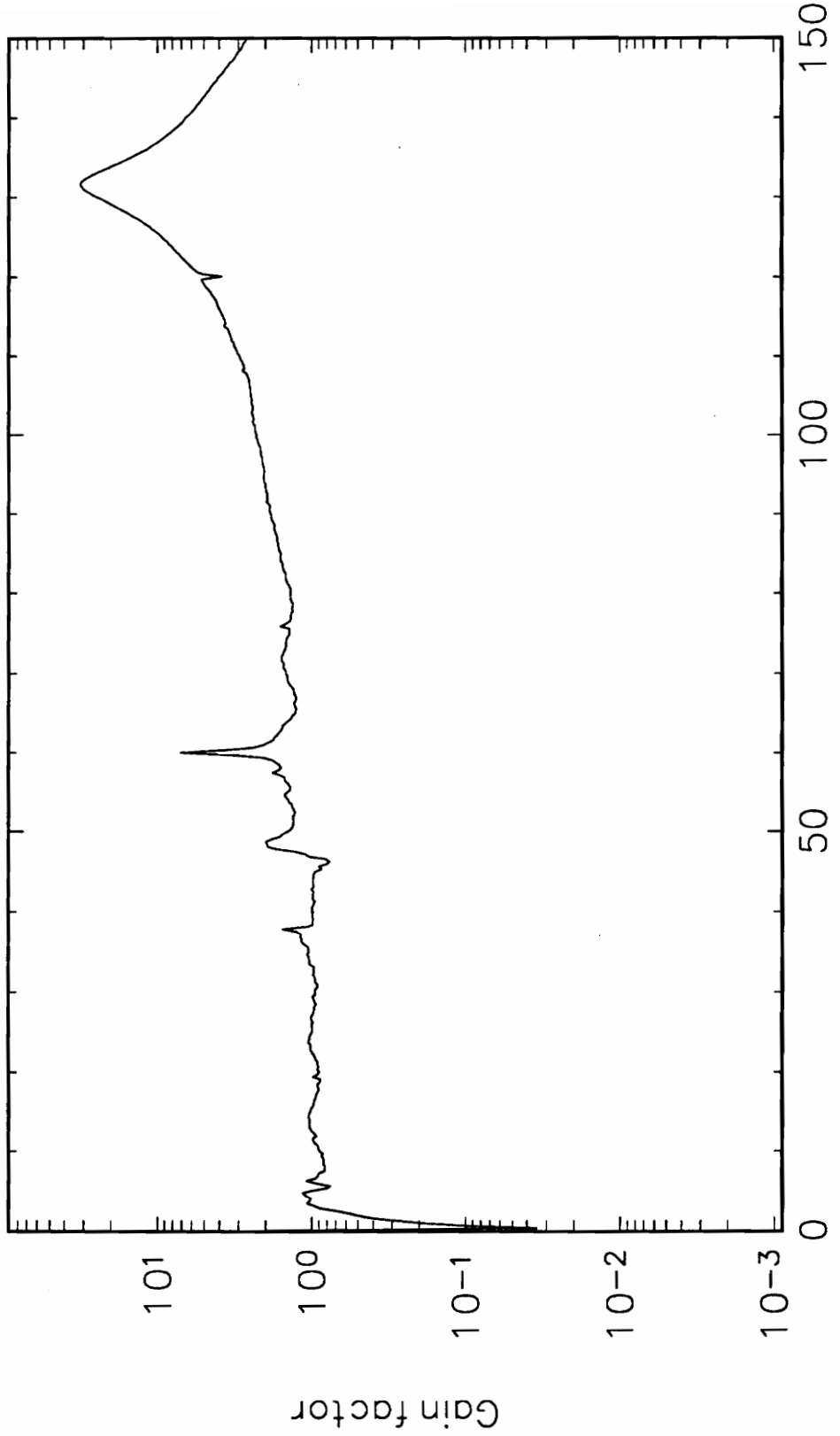

Figure D.9. Frequency Response of Gage S_4.

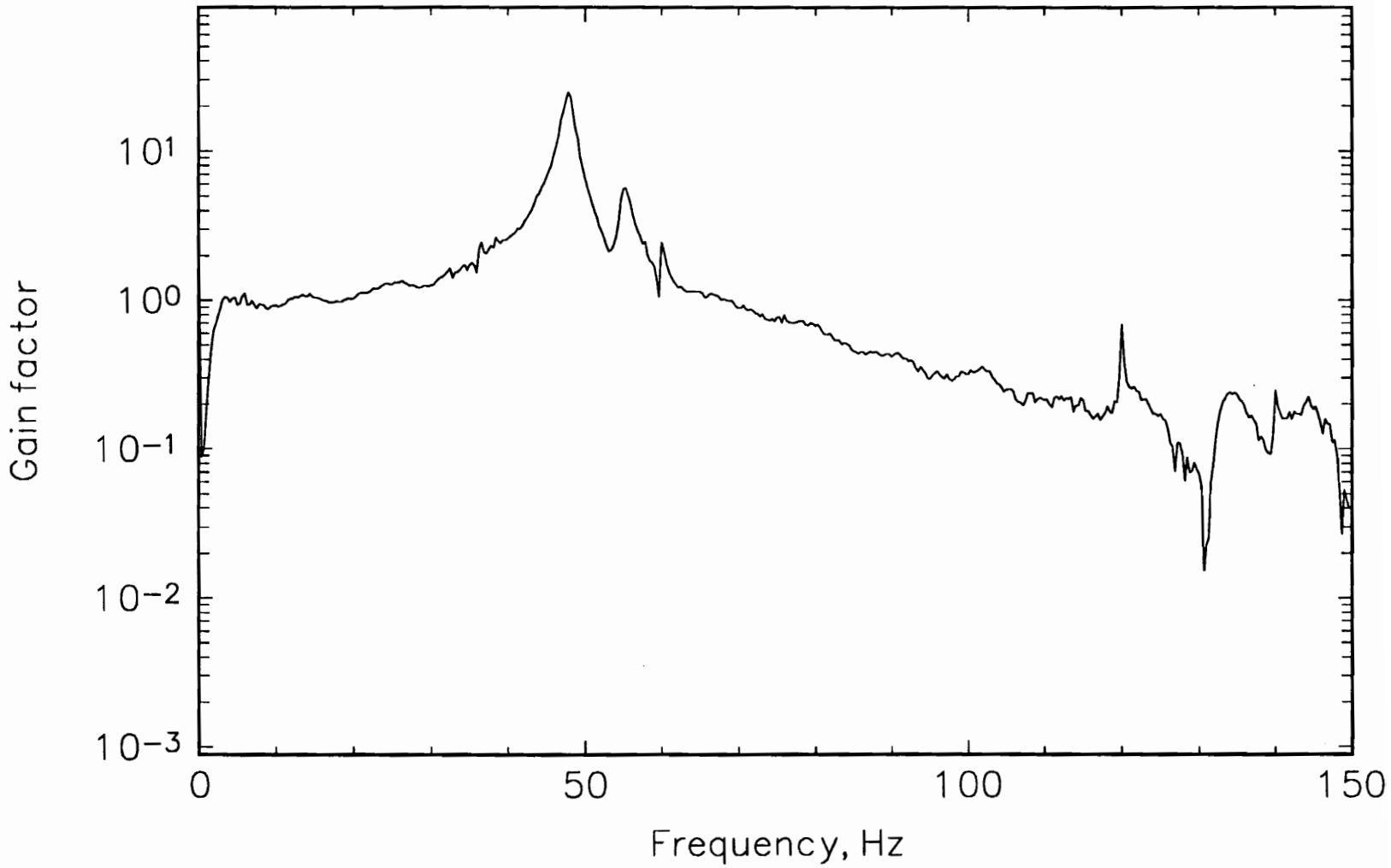

Figure D.10. Frequency Response of Gage RM.

APPENDIX E.

WALL INTERFERENCE CORRECTIONS

E.1 Introduction

Wind tunnel provides well controlled flow environment. Due to the existence or absence of the wall to provide this well controlled flow field, which does not exist in real flight, there is an interference effect. Pope and Harper(1966) point out that there are several influences due to the presence of the tunnel walls, or in the case of an open jet, the lack of the tunnel walls. One influence, longitudinal buoyancy, is the effect caused by the longitudinal pressure gradient along the test section axis. This effect is usually small in the closed test section and negligible in open jets. Other effects due to the presence of the lateral boundaries , as listed by Pope and Harper, on the flow around the model are

- Solid blockage - a lateral constraint to the flow pattern about a body. Placing the model in the test section locally reduce the tunnel cross-section area. In a closed wind tunnel the solid blocking is the same as an increase in the tunnel dynamic pressure and increase of the forces and moments at a given incidence angle. It is usually negligible with an open test section, since the air stream is free to expand.
- Wake blockage - Constraint to the flow around the wake. This effect is almost same as the solid blocking.
- An alteration to the local angle of attack along the span.
- An alteration to the streamline curvature of the flow about the wing, which causes changes in lift, moment and angle of attack of the wing.

- A change in down wash which gives an erronous measurements in lift, drag, tail setting, hinge moment, and static stability.
- A change in the level of flow assymetry due to the assymetric loading of the wing.
- Other additional effects such as flow angularity, local variation of flow velocity, and support interference.

E.2 Correction Methods in Use

Recognizing the difficulty of modeling separated flows, Maskell proposed an alternative, semi-emprical approach based on careful measurements of flows over flat plates placed normal to the stream. His method is well established for such flows but its extension to partially-separated flows such as those over stalled wings has a less certain foundation, since it relies on an assumption concerning the character of the separated flow. Evidence presented later shows that this method overestimates the blockage correction for a wing body model.

It has been recognized for some time that wall-pressure measurements can assist in the calculation of the wall interference in solid-wall tunnels. Present developments using the increased power of modern computers, have sought to exploit this idea more fully, placing greater emphasis on the measurements of the flow near the walls and generalizing the concept to other types of wind tunnel. These methods may be conveniently divided into two groups; One, called model representation

method, requiring the simulation of the model perturbation flow field and needing a relatively limited number of static pressure measurements at a close to the walls and the other, called two component method, not requiring a model representation but calling for knowledge of two component of flow velocity at the outer boundary. These components are that normal to the boundary and that in the streamwise direction.

There are other methods such as using panel pethods (e.g. PMARC) to account for the presence of the tunnel wall. Or using adjustable walls to eliminate the pressure gradient generated by the presence of the model in the tunnel. But, the size of the model is small compare to the size of the test section and because of its simple geometry it is assumed to be enough to apply only classical correction method for the body of revolution.

E.3 Contribution to Corrections.

Corrections due to Pope and Harper(1966). For a body only, the corrections become simple and only solid blockage and wake blockage are to be corrected. For solid blockage,

$$\epsilon_{sb,B} = \frac{\Delta V}{V_u} = \frac{K_3 \tau_1 (\text{body volume})}{C^{3/2}}$$

where, K_3 = body shape factor, $d/l \approx 0.167$

τ_1 = tunnel test section shape factor ≈ 0.82

C = tunnel cross-section area

$$\epsilon_{sb,B} = \frac{0.93 \times 0.82V}{36^{3/2}}$$

$$V = \frac{4}{3}\pi ab^2$$

$$= 1.32536 ft^3$$

$$\epsilon_{sb,B} = 0.00468 = \frac{\Delta V}{\delta V_u}$$

Thom's short form gives

$$\frac{\Delta V_{sb}}{\delta V_u} = \epsilon_{sb,B} = \frac{K(vol)}{C^{3/2}}$$

$K = 0.9$ for wing

$= 0.96$ for a body of revolution

Wake blockage can be expressed as follows.

$$\Delta V = \frac{Q}{2Bh}$$

$$\epsilon_{wb,B} = \frac{\Delta V}{\delta V_u} = \frac{S}{4C} C_{Du}$$

$$\Delta C_{DB} = \frac{K_3 \tau_1 (\text{volume})}{C^{3/2}} C_{Dou}$$

$$\approx 0.00468 C_{Dou}$$

Assuming

$$C_{Dou} \approx 0.25$$

$$\Delta C_{DB} \approx 0.00117 (0.1\%)$$

For example,

- Closed test section of $6' \times 6'$.
- Longitudinal pressure gradient of 0 per ft.
- Jet speed is 200 mph.
- Displacement thickness 0.5 inches.

- Model Maximum cross-section area 0.44179 ft^2.
- Maximum Diameter 0.75 ft.
- Model Volume 1.32536 ft^3.

For the conditions given above, the blockage correction has been applied. Effective tunnel area is

$$6 \times 6 - (0.5/12)(24) = 35(ft^2)$$

The solid blockage of the body is

$$K_3 = 0.93$$

$$\tau_1 = 0.809$$

$$\begin{aligned} \epsilon_{sb,B} = \frac{\Delta V}{V_u} &= \frac{K_3 \tau_1 (\text{body volume})}{C^{3/2}} \\ &= \frac{(0.93)(0.809)(1.32536)}{(35)^{1.5}} \\ &= 0.00482 \end{aligned}$$

The wake blockage is, assuming $C_{Du} \approx 0.030$,

$$\epsilon_{wb,B} = \frac{1}{4}\frac{0.44179}{35} C_{Du} \approx 0.0001$$

The total blockage becomes

$$\epsilon_t = 0.00482 + 0.0001 = 0.0049235 C_{Du}$$

As a Reference, from eq. (6.38) of Pope and Harper (1966),

$$\epsilon_t = 0.00316$$

The necessary corrections applied are as follows:

$$\epsilon = \epsilon_{sb} + \epsilon_{wb}$$

$$V = V_u(1 + \epsilon)$$

$$q = q_u(1 + \epsilon)$$

$$R_N = R_{Nu}(1 + \epsilon)$$

No other correction are to be made than the aerodynamic quantities listed above.

Corrections taken from Garner, *et al.*(1966) are as follows. For a body of revolution, the necessary correction is

$$\epsilon = \epsilon_{sb} + \epsilon_{wb}$$

By Thompson for $\frac{1}{2} < \frac{b}{h} < \frac{1}{2}$ and a spuare tunnel of $\tau = 0.809$,

$$T = (0.36)\left[\frac{b}{h} + \frac{h}{b}\right]$$

$$= 0.72$$

And then the solid blockage becomes

$$\epsilon_{sb} = T\left(\frac{1}{bh}\right)^{3/2} V$$

The wake blockage effect is far less important for small three-dimensional model than an airfoil. For an imcompressible flow

$$\epsilon_{wb} = \frac{1}{4}\left(\frac{S}{bh}\right) C_{D0}$$

For closed rectangular tunnel and for bodies only

$$\lambda = \lambda_3$$

$$G = 1 + 0.4\beta/f = 1.0$$

$$\epsilon_{sb} = T\left(\frac{1}{bh}\right)^{3/2} VG = 0.00461$$

$$\epsilon_{wb} = \frac{1}{4}(\frac{S}{bh})C_{D0} = 0.0001$$

$$\epsilon_t = \epsilon_{sb} + \epsilon_{wb} = 0.00471$$

The corrections to the stream quantities become

$$\Delta U = (\epsilon_{sb} + \epsilon_{wb})U = \epsilon_t U$$

$$\Delta p_\infty = -\rho U^2 \epsilon_t$$

$$\Delta C_p = 2[1 - C_p]\epsilon_t$$

Compare to the high degree of change expected from a wing model, the effect from the body of revolution is insignificant.

APPENDIX F.

FREQUENCY RESPONSE FUNCTION OF PRESSURE TRANSDUCER AND PIN HOLE CAP ASSEMBLY

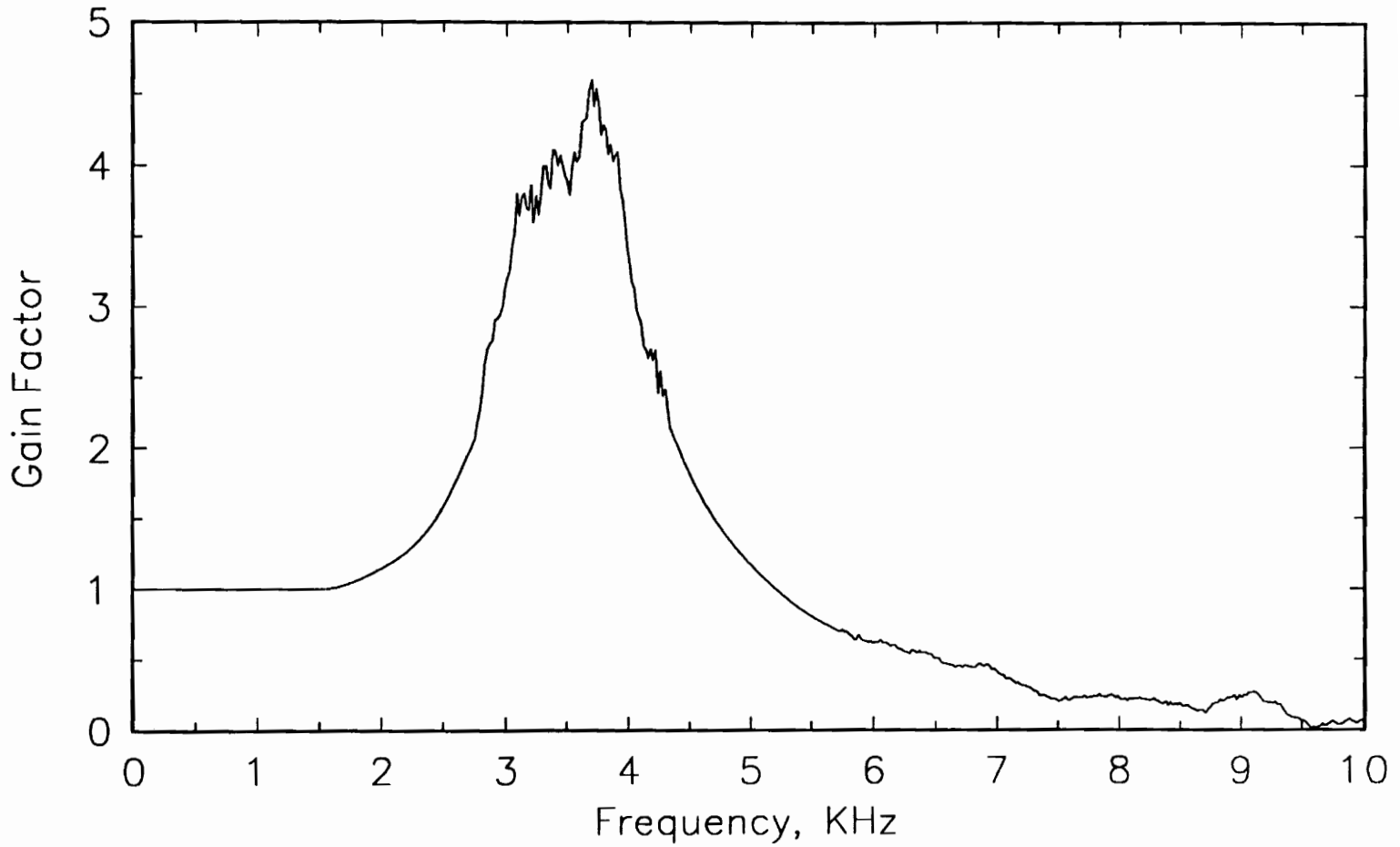

Figure F.1. Frequency Response Function of Pin-Hole Cap and Pressure Transducer S/N A36N, x/L = 0.0000.

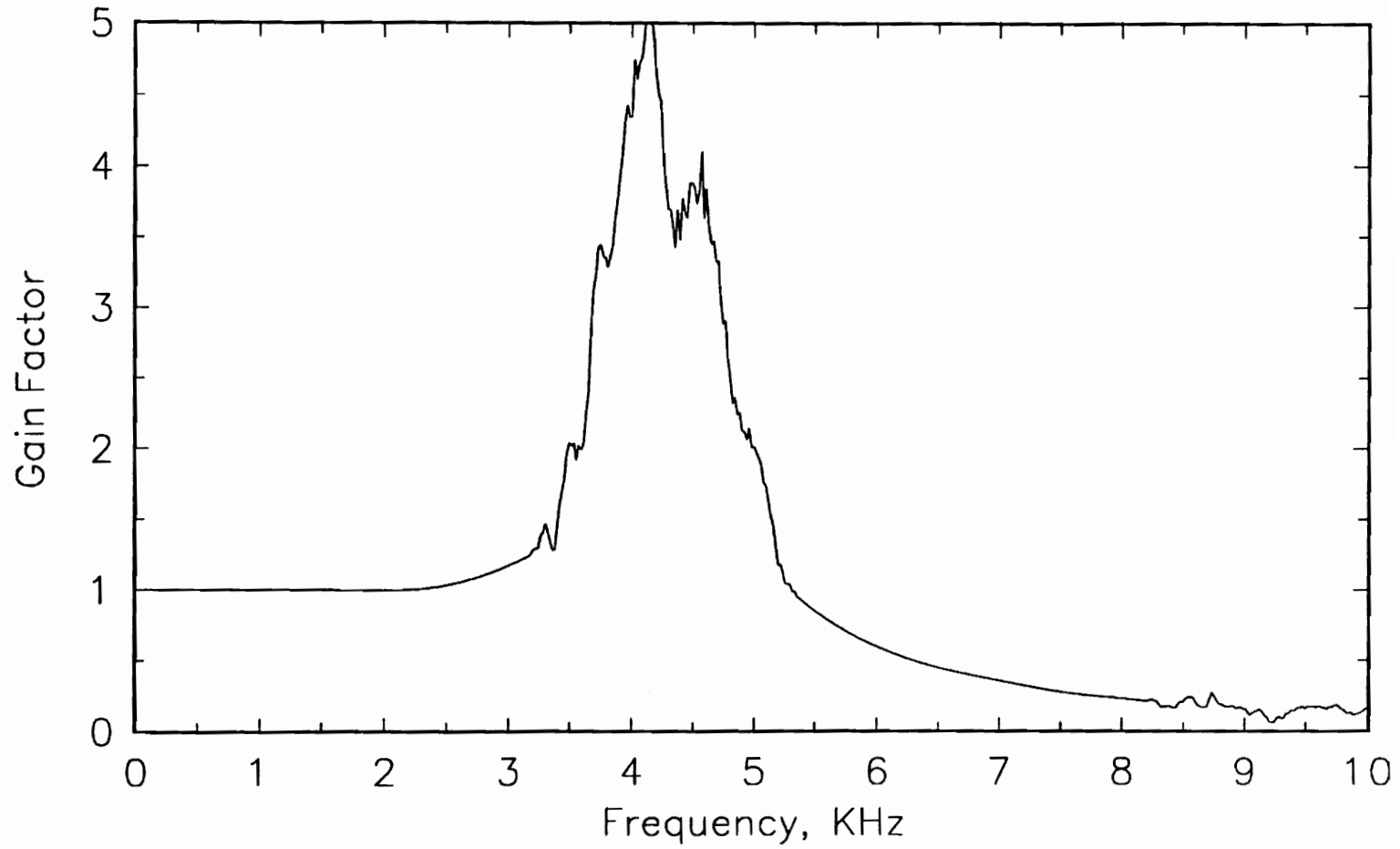

Figure F.2. Frequency Response Function of Pin-Hole Cap and Pressure Transducer S/N B38M, x/L = 0.1079.

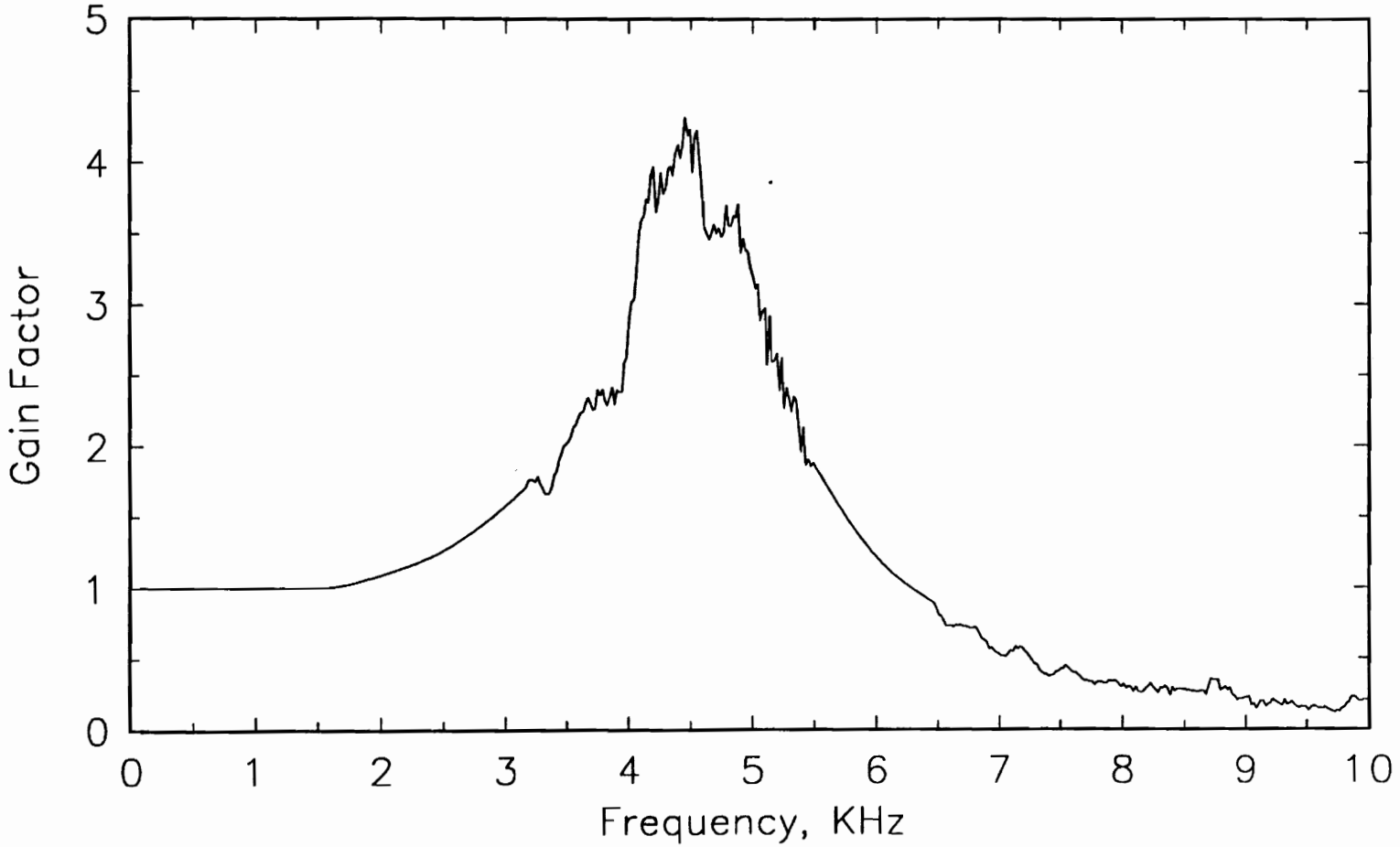

Figure F.3. Frequency Response Function of Pin-Hole Cap and Pressure Transducer S/N B36M, x/L = 0.2315.

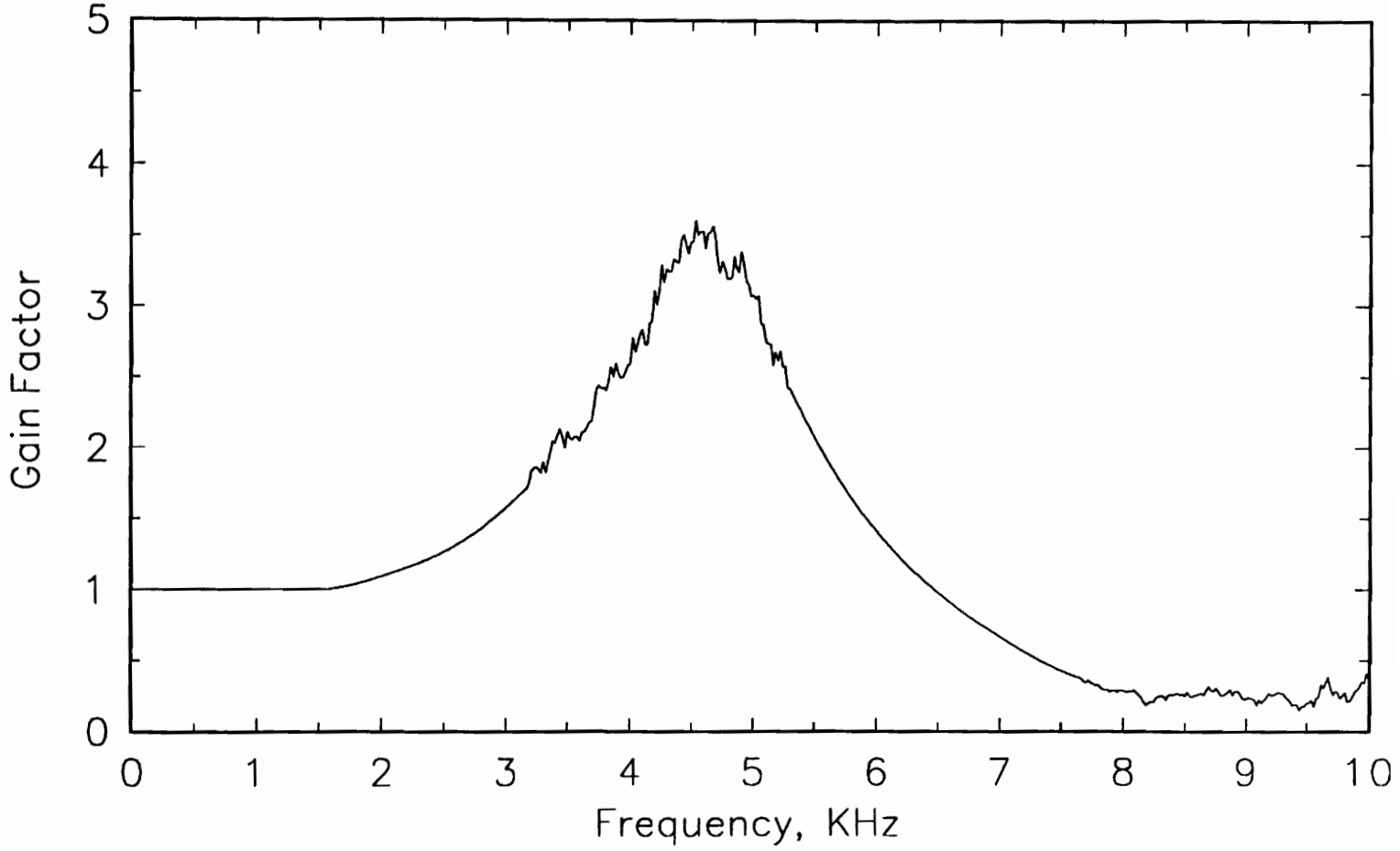

Figure F.4. Frequency Response Function of Pin-Hole Cap and Pressure Transducer S/N B42M, x/L = 0.3145.

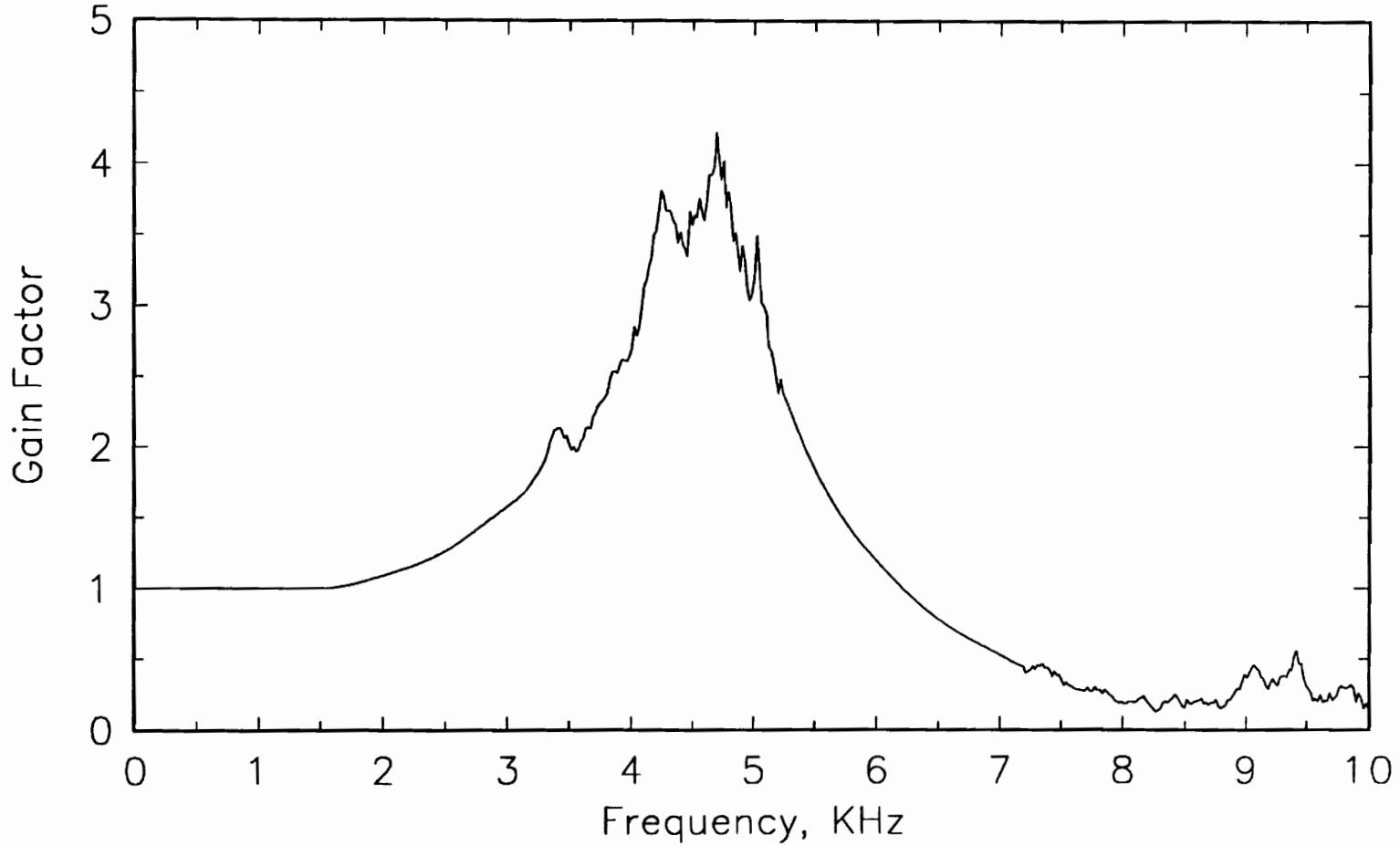

Figure F.5. Frequency Response Function of Pin-Hole Cap and Pressure Transducer S/N B08L, x/L = 0.4396.

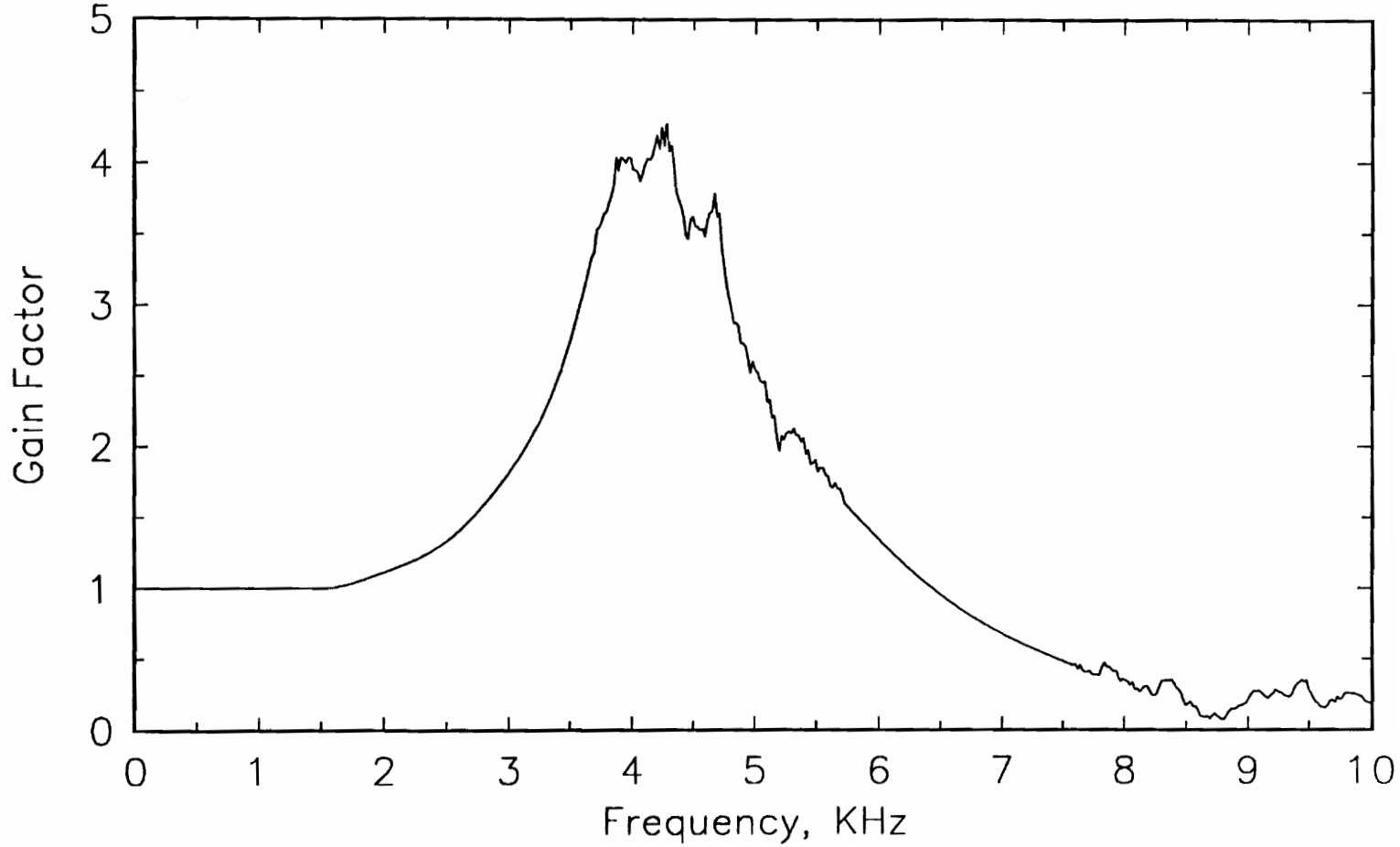

Figure F.6. Frequency Response Function of Pin-Hole Cap and Pressure Transducer S/N B19M, x/L = 0.5646.

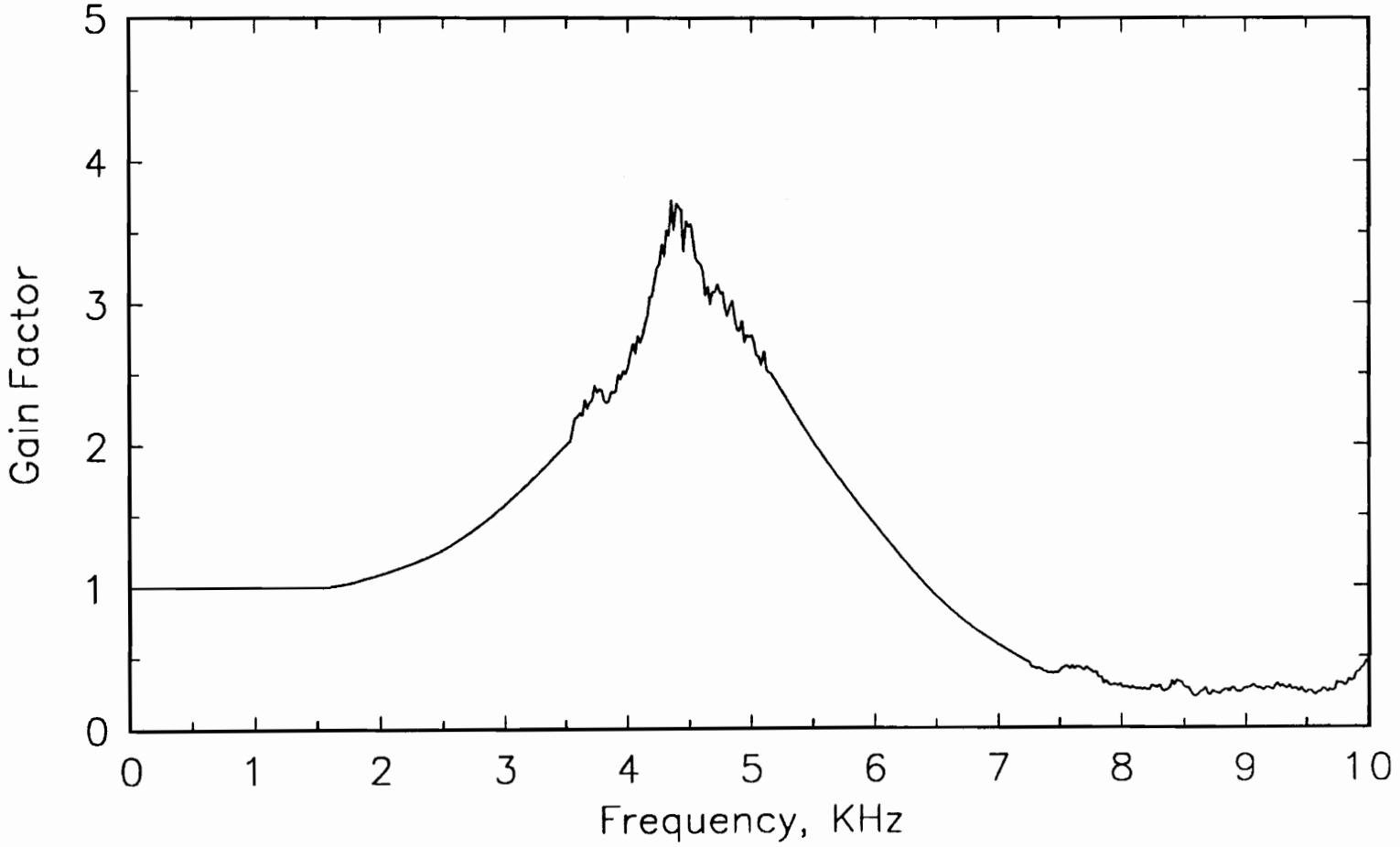

Figure F.7. Frequency Response Function of Pin-Hole Cap and Pressure Transducer S/N B30M, x/L = 0.6892.

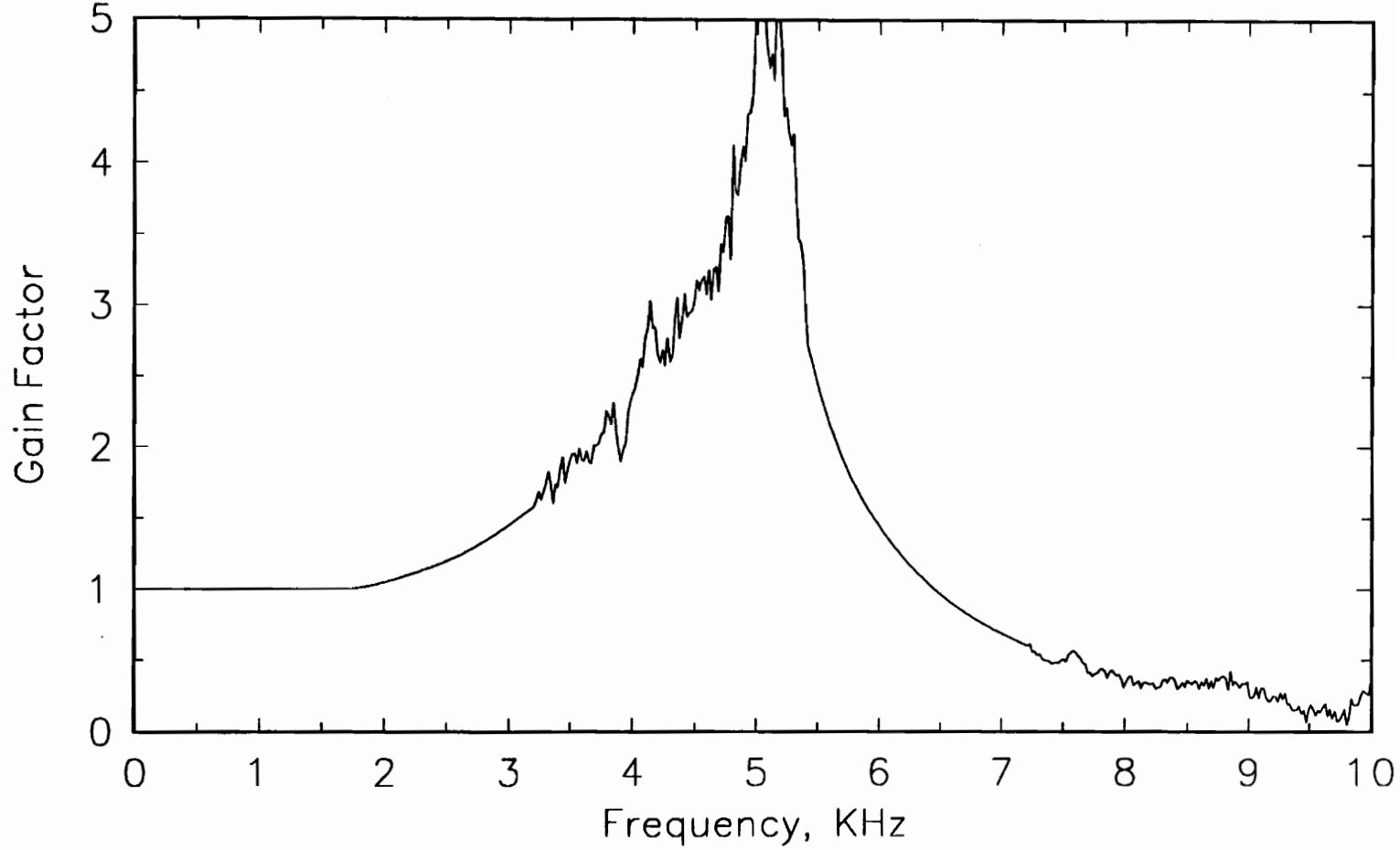

Figure F.8. Frequency Response Function of Pin-Hole Cap and Pressure Transducer S/N C13B, x/L = 0.7725.

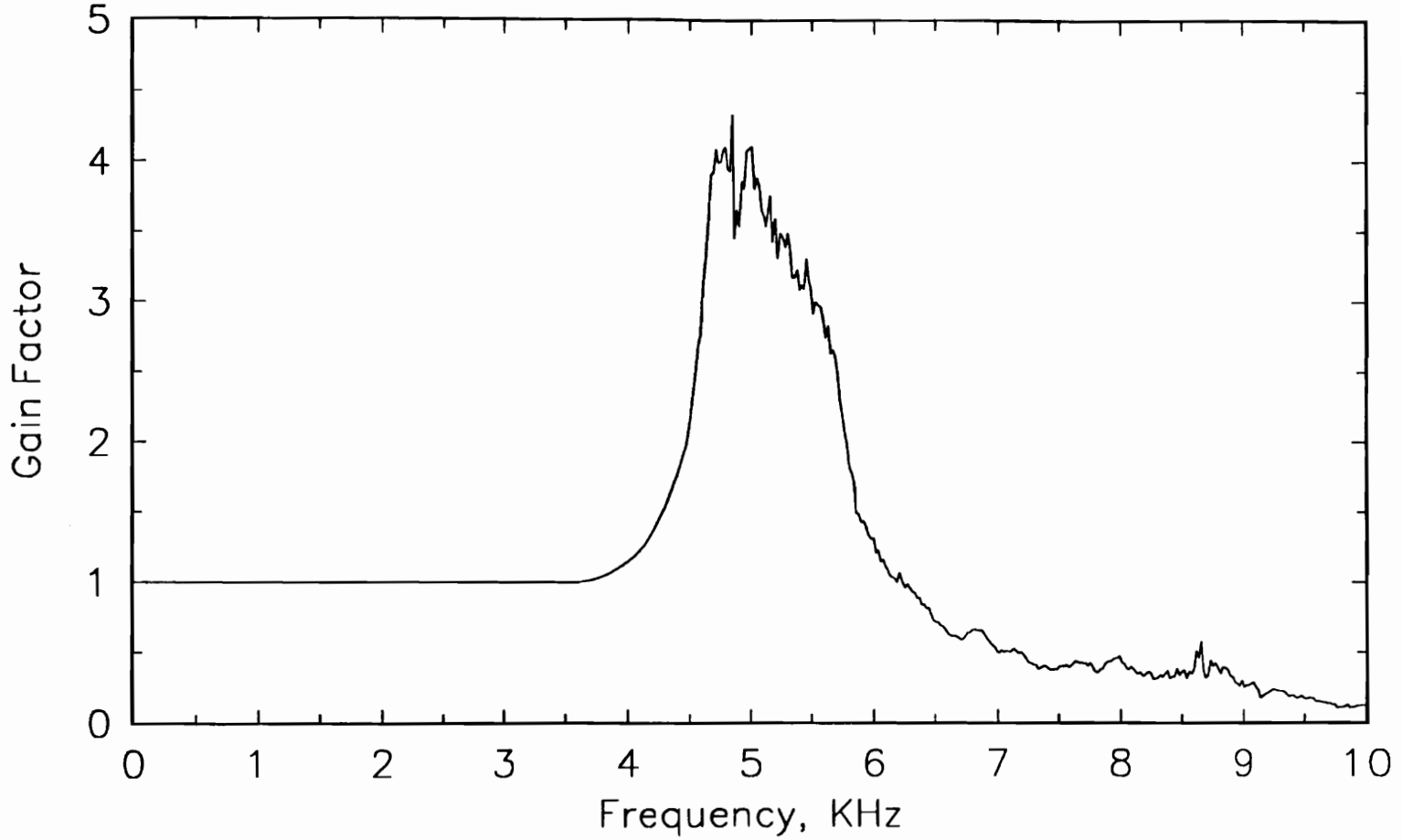

Figure F.9. Frequency Response Function of Pin-Hole Cap and Pressure Transducer S/N B45M, x/L = 0.8346.

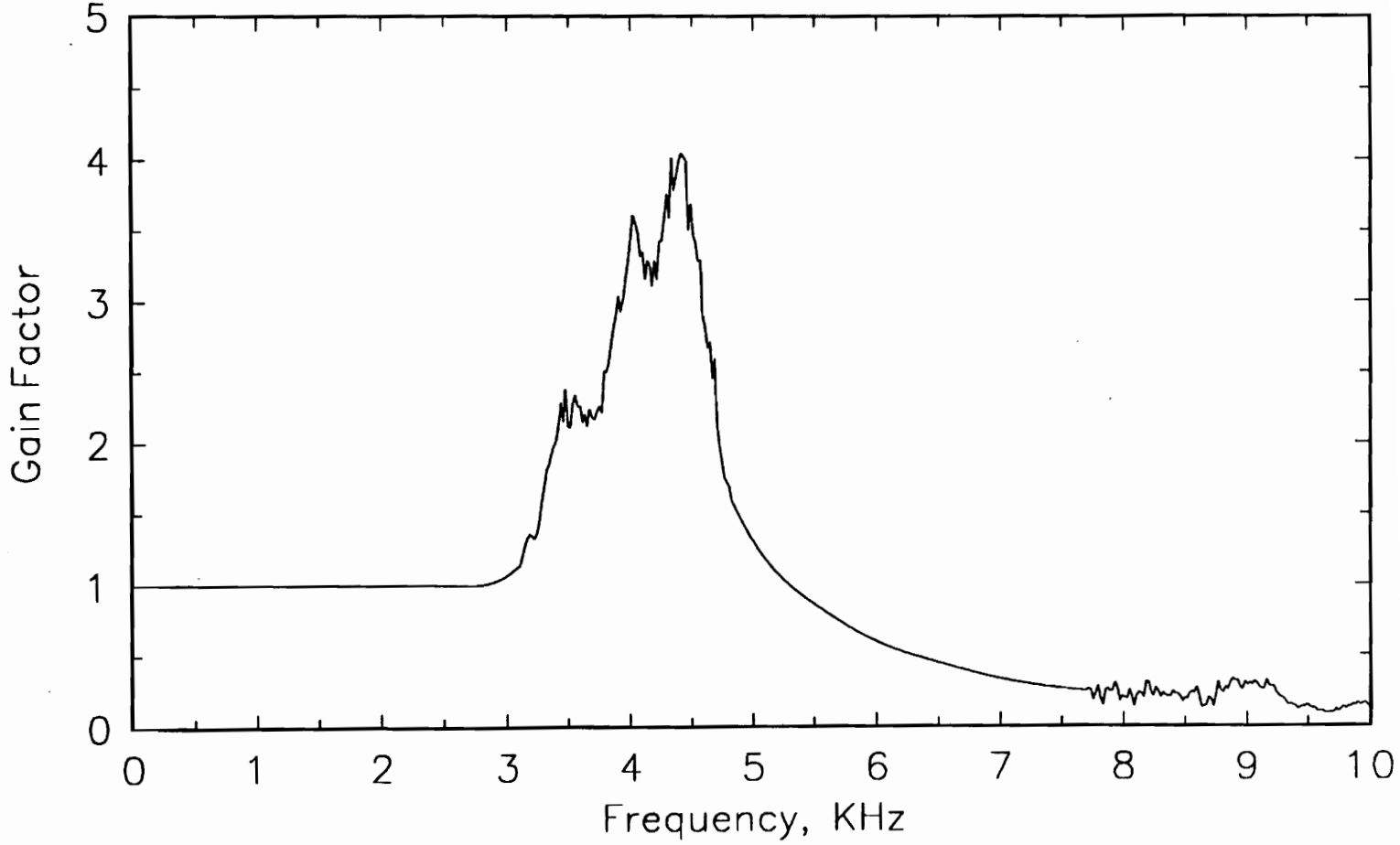

Figure F.10. Frequency Response Function of Pin-Hole Cap and Pressure Transducer S/N 90YM, x/L = 0.8962.

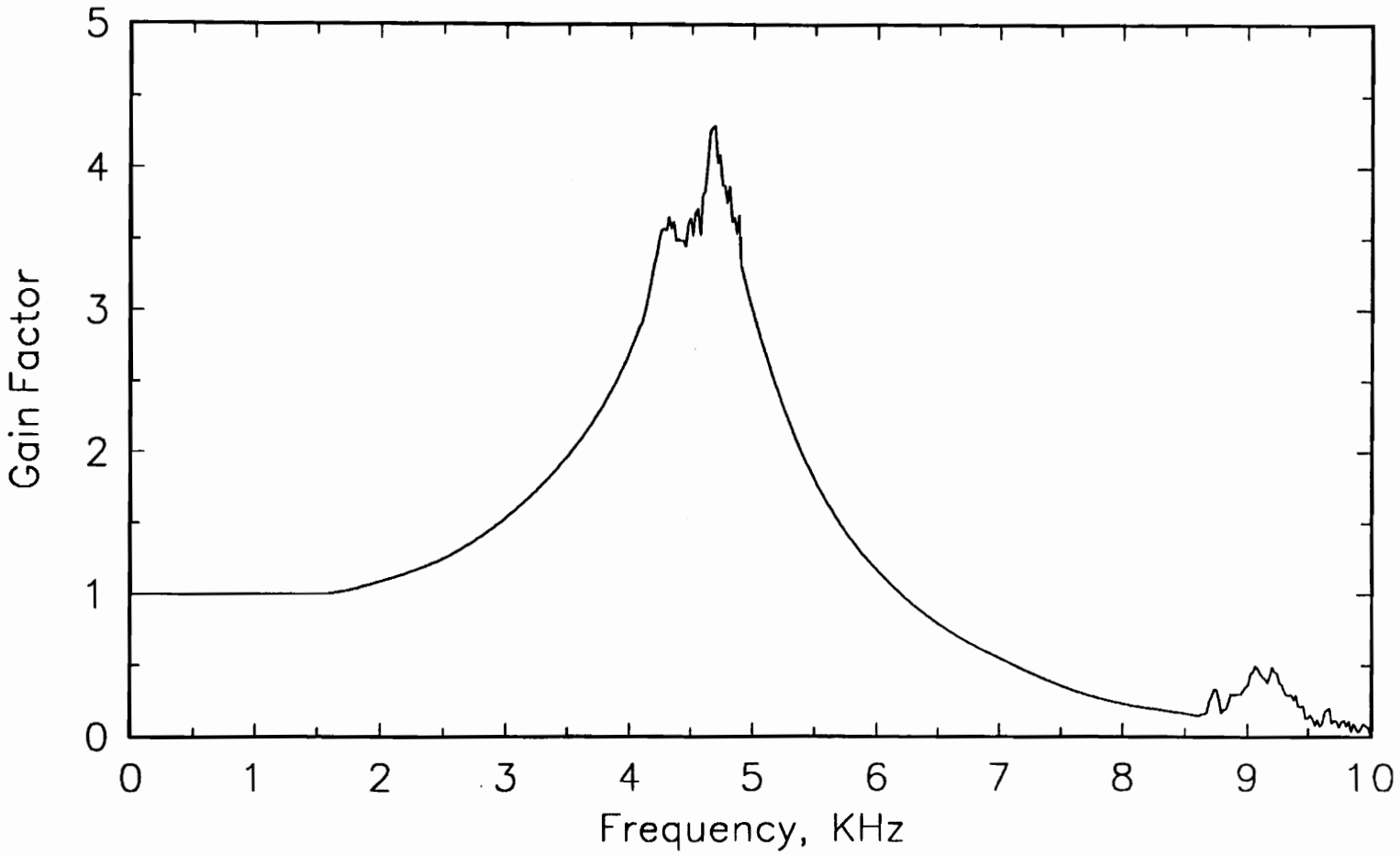

Figure F.11. Frequency Response Function of Pin-Hole Cap and Pressure Transducer S/N B22L, x/L = 0.5646, 45 degree off-set.

VITA

The author was born on March 2, 1954 in Korea. He earned his B.S. degree in Aeronautical Engineering in February, 1976, from the Seoul National University, Seoul, Korea. Upon graduation, he joined the Agency for Defense Development for Korea and practiced engineering in the Experimental Aerodynamics Group until he joined the Aerospace and Ocean Engineering Department, Virginia Polytechnic Institute and State University in 1984. After finishing his M.S. in Aerospace Engineering in July, 1986, he continued to study for his PhD in Aerospace Engineering.

In 1978, he served as an exchange engineer at the Air Force Flight Dynamics Lab., Wright-Patterson Air Force Base, Dayton, Ohio. He took aircraft design course at the Cranfield Institute of Technology, England, in 1979. He is currently a member of AIAA.